Integrated Material and Device Engineering Towards Reliable, High-Performance Perovskite Solar Cells

Adharsh Rajagopal

A dissertation

submitted in partial fulfillment of the

requirements for the degree of

Doctor of Philosophy

University of Washington

2019

Reading Committee:

Alex Jen, Chair

Hugh Hillhouse

Fumio Ohuchi

Program Authorized to Offer Degree:

Materials Science and Engineering

University of Washington

Abstract

Integrated Material and Device Engineering Towards
Reliable, High-Performance Perovskite Solar Cells

Adharsh Rajagopal

Chair of the Supervisory Committee:
Alex Jen
Department of Materials Science and Engineering

Organic-inorganic hybrid perovskites are a diverse, versatile, and multifunctional material class that have soared to prominence because of their application in solar cells. Perovskite Solar Cells (PVKSCs) are promising candidates for addressing the scalability challenge of solar based renewable energy as they combine merits of high-power conversion efficiency with facile manufacturability and low cost. The dynamically evolving research field has made immense progress in capitalizing on amazing structure-property-processing-performance traits of hybrid perovskites. At this point, research efforts for solving material and device level challenges of PVKSCs are vital in their progression towards commercialization.

The unifying research objective for works presented in this doctoral dissertation is improvement of PVKSC reliability and performance. I have utilized and integrated a wide-range

of material and device perspectives for attaining better comprehension of inherent challenges, solving key issues, and facilitating advancement of PVKSCs. Chapter 1 (Introduction) provides an overview of PVKSCs including hybrid perovskites material characteristics, multifaceted roles of interfaces in device engineering, evolution of PVKSC research landscape, and an outlook of scalability-durability-sustainability challenges in their path towards commercialization.

Subsequently, the subject matter in this dissertation is broadly categorized into three parts: investigation of complex hysteresis instability in PVKSCs (Part A: Chapters 2-3), development of perovskite tandem solar cells (Part B: Chapters 4-5), and progression towards next generation perovskite tandem solar cells (Part C: Chapters 6-7). Chapter 2 comprises a case study to understand how interfaces mediate hysteresis behavior in PVKSCs. Chapter 3 comprises a case study to understand how perovskite compositional modification influences hysteresis behavior in PVKSCs. Chapter 4 illustrates an approach to alleviate the issue of photoinduced phase segregation in large bandgap PVKSCs. Chapter 5 illustrates design of perovskite tandem solar cells, approach to minimize the photovoltage loss in small and large bandgap PVKSCs, and fabrication of monolithic (2-Terminal) tandem devices. Chapter 6 demonstrates an approach to overcome the photovoltage bottleneck in large bandgap PVKSCs. Chapter 7 investigates the impact of compositional modification on bandgap bowing and optoelectronic quality in Pb-Sn hybrid perovskites to identify the optical composition for small bandgap PVKSCs.

Chapter 8 (Conclusion) concludes this dissertation with summary of results, highlights of extensions through collaborative work, intellectual merits, research impact, and products of lasting value, and perspectives for continued development of perovskite tandem solar cells. Research results in this dissertation have been reported through the associated publications.[1–20]

TABLE OF CONTENTS

LIST OF FIGURES

LIST OF TABLES

ABBREVIATIONS

2-T – 2-terminal

4-T – 4-terminal

ABX_3 or AMX_3 – General formula for 3-dimensional halide perovskites, where A = +1 organic or inorganic cation (MA, FA, GA, Cs, Rb), B or M = +2 metal cation (Pb, Sn), and X = -1 halide anion (I, Br, Cl)

AIPL – Absolute intensity photoluminescence

AM – Air mass

CBM – Conduction band minimum

CIGS – Copper indium gallium selenide

DCB – *o*-dichlorobenze

DMF – *N*,*N*-dimethylformamide

DMSO – Dimethyl sulfoxide

DOS – Density of states

E_b – Binding energy

E_g – Bandgap

EPBT – Energy payback time

EQE – External quantum efficiency

ETL or ETM – Electron-transport layer or material

FA – Formamidinium, $[H_2N\text{-}CH{=}NH_2]^+$

FB – Forward bias

FF – Fill factor

FWHM – Full width half maximum

GA – Guanidinium, $[(H_2N)_2\text{-}C{=}NH_2]^+$

GBL – γ-butyrolactone

HF – Hysteresis factor

HP or PVK – Hybrid perovskite

HTL or HTM – Hole-transport layer or material

ICBA – Indene-C_{60} bis-adduct

IPA – Isopropyl alcohol

ITO – Indium tin oxide

J – Current density

J_{ph} – Photocurrent

J_{sc} – Short-circuit current density

LCA – Life-cycle assessment

LCOE – Levelized cost of energy

L_d – Diffusion length

MA – Methylammonium, $[CH_3NH_3]^+$

MPP – Maximum power point

NA – Numerical aperture

ND – Neutral density

OC – Open-circuit

OIHP – Organic-inorganic hybrid perovskites

OPV – Organic photovoltaic

PB – Photo-bleach

PCBM – Phenyl-C_{61}-butyric acid methyl ester

PCE – Power conversion efficiency

PEA – Phenylethylammonium $[C_6H_5\text{-}(CH_2)_2\text{-}NH_3]^+$

PEDOT:PSS – Poly(3,4-ethylenedioxythiophene)-poly(styrenesulfonate)

PL – Photoluminescence

PTAA – Polybis(4-phenyl)(2,4,6-trimethyl-phenyl)amine

PTFE – Polytetrafluoroethylene

PV – Photovoltaic

PVKSCs – Perovskite solar cells

QFLS – Quasi-fermi level splitting

QY – Quantum yield

R2R – Roll-to-roll

RB – Reverse bias

SC – Short-circuit

s-PCE – Stabilized power conversion efficiency at maximum power point

SQ – Shockley-Queisser

STH – Solar-to-hydrogen

TAS – Transient absorption spectroscopy

TrPL – Transient photoluminescence

UV-vis – Ultraviolet-visible

VBM – Valence band maximum

V_{oc} – Open-circuit voltage or photovoltage

W-H – Williamson-Hall

XRD – X-ray diffraction or X-ray diffractometry

ACKNOWLEDGEMENTS

This dissertation was made possible because of the support from several individuals. First, I extend gratitude to my doctoral advisor Prof. Alex Jen for believing in me and providing the opportunity to be a member of his research group in University of Washington. Interdisciplinary and competitive nature of Jen research group offered me an environment for accelerated learning and expand my skill-sets. Prof. Jen's high expectations and ambitions have pushed me to consistently keep challenging myself to improve and develop the drive to accomplish bigger. His trust in me to give enormous freedom in pursuing my research as well as getting me involved and take responsibility for things beyond research helped me to thrive and evolve in multiple dimensions. I thank Prof. Hugh Hillhouse for being a constant source of encouragement over the years and supporting me to work with several students from his research group. He has enriched my learning by offering critical evaluation of results and valuable suggestions. I also acknowledge other committee members Prof. Fumio Ohuchi and Prof. Qiuming Yu for their time and interest.

Current and former Jen group members have played an important part in successful completion of my doctoral research. I am thankful to Dr. Chu-Chen Cheuh and Dr. Nathan Cernetic for their willingness to help me settle in during the initial stages of my PhD. Working extensively with Dr. Spencer Williams, Dr. Zhibin Yang, and Dr. Sae Byeok Jo on several projects at different stages were instrumental for achieving successful research outcomes and they have provided an invaluable comradeship in my PhD. Dr. Po-Wei Liang, Ting Zhao, and Francis Lin have been great colleagues and made significant contributions to my research. I thank Dr. Ian Braly, Dr. Alexander Uhl, and Ryan Stoddard from Hillhouse research group for contributing in collaborative works through their complementary research expertise and perspective. I thank all my co-workers, who have aided me to work on challenging problems at the forefront of a dynamic research field.

Several experiments were conducted at the Molecular Analysis Facility and Washington Nanofabrication Facility, a National Nanotechnology Coordinated Infrastructure site at the University of Washington. Specifically, I thank Dr. Darick Baker at the Washington Nanofabrication Facility for training me to perform sputter deposition and spectroscopic ellipsometry characterization, and Dr. Liam Bradshaw at the Molecular Analysis Facility for assistance in x-ray diffraction measurements.

My research works were funded by several grants from the National Science Foundation, the Office of Naval Research, the Asian Office of Aerospace R&D, and the Department of Energy SunShot. I also thank financial support from the Stoebe Fellowship and the University of Washington Clean Energy Institute Graduate Fellowship.

Finally, I express gratitude to my family and friends. My dad, mom, and sister have been great pillars of support for me to succeed in graduate school. Their belief about my abilities helped me to overcome hardships and be determined throughout the process. This thesis is dedicated to them.

DEDICATION

To my Dad, Mom and Sister

Chapter 1. INTRODUCTION

1.1 Perovskite Solar Cells (PVKSCs) based Photovoltaic (PV) Technology

The environmental burden and resource scarcity of fossil fuel-based electricity generation make fossil fuels non-sustainable for meeting our soaring energy demand. Solar power has been one of the most promising renewable energy sources in the pursuit for alternatives over the past few decades. Despite the massive potential and incredible technological progress, photovoltaics (PVs) contribute only to a miniscule (<2%) fraction of global energy consumption.[21,22] The widespread deployment of PV is hindered by hefty financial requirements and the challenge of intermittency associated with renewable energy technologies.[21,23] PV based electricity generation is several folds more expensive than using fossil fuels, and its competitiveness is hugely reliant on government policies and subsidies.[15] A major share (90%) of the PV industry is dominated by silicon PVs, a technology that has inherently high manufacturing and installation costs.[21,23] Though the cost of silicon PV is expected to be reduced in the future based on empirical predictions from experience curves (cost reduction with accumulation of experience), its inherent technological limitations in terms of absorption (indirect bandgap), material requirements (high purity and high temperature processing), and form factor (bulky and rigid modules) impose constraints on realizable module efficiency and system costs.[21,23–25] Thus, to make PV ubiquitous through a sustainable subsidy-free market model, it is crucial to develop alternate technology with higher efficiency potential and easier manufacturability.

Perovskite solar cells (PVKSCs) are a potentially transformative PV technology that employs cheap and easily processible organic-inorganic hybrid perovskite semiconductors as an absorber material.[22,26–33] It combines distinct merits of several predecessor PV technologies (**Figure 1.1**): high efficiency (bulk crystalline silicon PV), lightweight and flexibility (GaAs,

CdTe, and CIGS inorganic thin film PVs), scalable low temperature solution processability and color tunability (organic, dye-sensitized and quantum dot based thin film PVs).[34] The important optoelectronic aspects (absorption coefficient, energy loss, electronic properties, power-per-weight) and environmental impacts (assessed by life-cycle assessment, LCA studies[35–37]) of PVKSCs compared to other thin film PVs are illustrated in **Figure 1.1**.

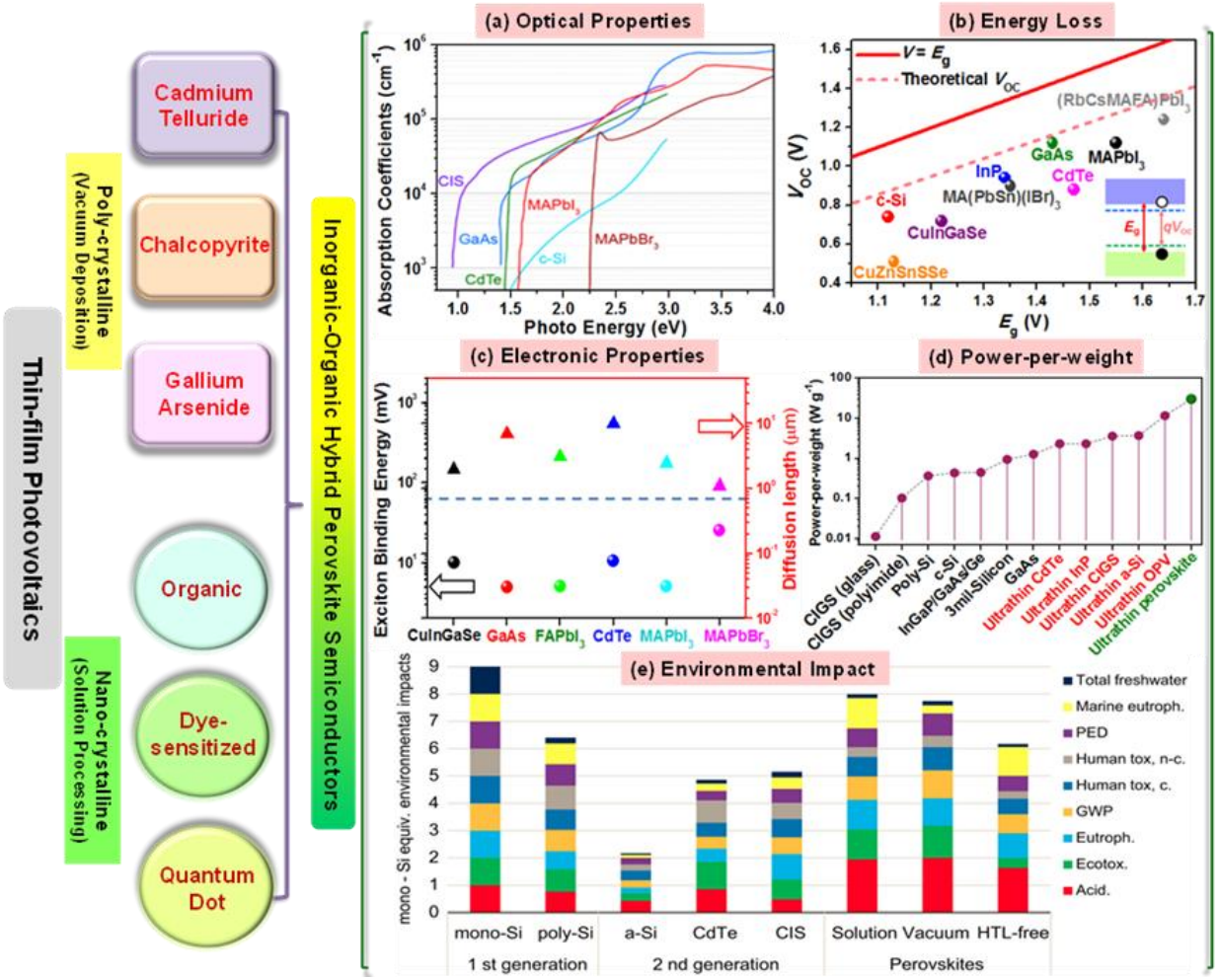

Figure 1.1. Optoelectronic aspects and environmental impact of thin film photovoltaic (PV) technologies. (a) Absorption coefficient of various PV materials.[38] (b) Open-circuit voltage, V_{oc} deficit for various commercial PV technologies (best values reported so far[34]). Theoretical maximum for V_{oc} of a solar cell is given by bandgap, E_g dependent Shockley–Queisser limit; device V_{oc} is governed by absorber quasi-fermi level splitting, shown in figure inset. (c) Binding energy, E_B and diffusion length, L_d of various PV materials; for perovskites, I choose the lowest (E_b) and highest (L_d) reported values for thin-films in literature. d) Comparison of power-per-weight of leading lightweight solar cells.[39] (e) Environmental impact (for selected impact categories) of PVKSCs in comparison with commercial PV technologies.[40] Here, GWP and PED represent global warming potential and primary energy demand, respectively; for each impact, values for different technology were normalized by corresponding values of mono-Si, setting the standard bar height as one for every category. A key assumption is same 30-year lifetime for all technologies except PVKSCs, where an average value of 5 years was assumed.

Massive research efforts over the past 6 years have led to an unprecedented growth of PVKSCs and lab-scale demonstrations have reached impressive efficiencies.[22,31,32,41] At this juncture, long-term PVKSC durability concerns are the key roadblock in the path towards commercialization, and these concerns have become the major focus of research in the field.[27,32,42,43] Parallel efforts to solve challenges associated with scaling up and demonstrating large scale modules[15,26] have begun through a cooperation between academia and industry. In the short term, enabled by its low capex and short energy payback time (EPBT), PVKSCs will enter the PV market through short-lifetime products for off-grid niche applications (portable and wearable devices useful in fields like electronics, aviation, military, and medicine).[35] In the long term, with resolution of stability issues, PVKSCs will eventually join other on-grid PV technologies for terawatt scale PV deployment.

1.2 Fundamental Background and Overview

1.2.1 Organic-Inorganic Hybrid Perovskites: Material Characteristics

Organic-inorganic hybrid perovskite is a diverse, versatile, and multifunctional material class, which offers flexibility in terms of structure, properties, processing, and performance. Below, I provide an overview of these fundamental material characteristics along with references that serve as resources for readers interested in greater detail. The material tetrahedron in **Figure 1.2** is a convenient summary of perovskite characteristics relevant for PV application.

Structure: Hybrid perovskites (also referred to as halide perovskites) are structurally and compositionally versatile.[29,30,44,45] They have a characteristic $A^{+1}B^{+2}X^{-1}_3$ perovskite crystal structure, where A^{+1} is a larger organic cation, B^{+2} is a smaller metal cation, and X^{-1} is a halide anion. Typically, metal cations are in 6-fold octahedral coordination surrounded by halide anions with organic cations in 12-fold cuboctahedral coordination sites between corner-shared BX_6

octahedra. Ionic radii (r_A, r_B, r_X) requirements for estimating the formability of such a 3D perovskite framework can be estimated via the Goldschmidt tolerance factor ($t = (r_A + r_X) / (\sqrt{2}[r_B + r_X])$) and the Octahedral factor ($\mu = r_B / r_X$). For halide perovskites, empirical observations show that t and μ lie within 0.813-1.107 and 0.442-0.895, respectively.[46] Material composition and temperature determine actual crystal symmetry.[47] A wide range of A^+ cations (methylammonium – MA^+, formamidinium – FA^+, cesium – Cs^+, rubidium – Rb^+, ethylammonium – EA^+, guanidinium – GA^+), B^{2+} cations (lead – Pb^{+2}, tin – Sn^{+2}, germanium – Ge^{+2}) and X^- anions (iodide – I^-, bromide – Br^-, chloride – Cl^-) have been employed in the exploration of 3D halide perovskites thus far.[48–51] The relaxed structural requirements for lower dimensional (2D, 1D, 0D) perovskites open up the compositional window and provide a broader toolbox for functional material design.[44,45]

Properties: The structural versatility and huge compositional space of hybrid perovskites enable realization of an exceptional range of functional properties (magnetic, dielectric, electrical, optical, charge storage).[44,45] The characteristic hybrid perovskite, methylammonium lead iodide ($MAPbI_3$), has an optical bandgap (E_g) of 1.6 eV which is easily tunable from 1.2 to 3.0 eV by engineering chemical composition.[50] These materials are direct gap semiconductors with excellent optical absorption (high absorption coefficients, α and sharp onset with low Urbach energy, E_u) and emission (high and narrow photoluminescence). Direct generation of free charge carriers (electrons and holes) under photo-excitation (due to small exciton binding energy, E_B), high point-defect tolerance (shallow defect levels), and excellent ambipolar charge carrier transport properties (large mobility (μ), long lifetime (τ), and diffusion length (L_d)) are characteristic electronic aspects of these materials. Such excellent properties (representative values presented in **Figure 1.2**) make them desirable for application as solar cell absorbers. It is important

to note that optoelectronic properties (light absorption, charge generation and extraction capabilities) are strongly dependent on material form, processing, microstructure, and composition. A detailed account of the physical origin of these exceptional properties can be found elsewhere.[29,30,33,52–57]

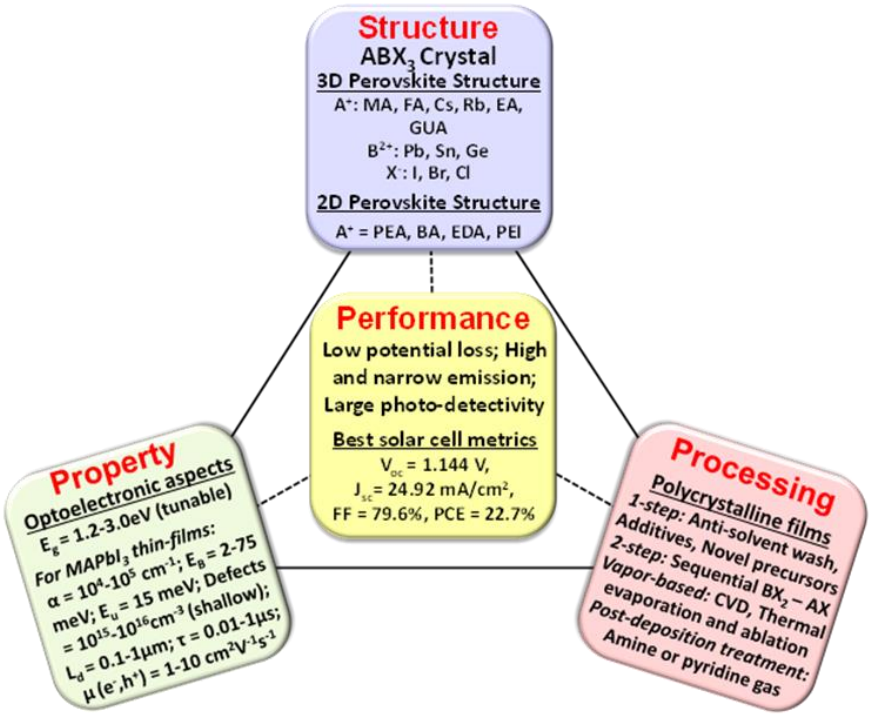

Figure 1.2. Organic-inorganic hybrid perovskite material tetrahedron, specifically focused on relevant aspects for solar cell application; values and metrics presented were taken from literature.[52,56,58] Definition of abbreviations and terms are provided in the corresponding text.

Processing: Due to low formation energies, hybrid perovskites readily self-assemble from their molecular components in the solution or vapor state without stringent processing requirements.[59–61] The control of precursor composition and solution chemistry enables realization of versatile perovskite forms (nanocrystals, polycrystalline thin films, and macroscopic single crystals) and modulation of associated material properties.[33,59,62,63] Numerous processing routes like one-step solution deposition (anti-solvent wash, additive incorporation, and precursor engineering), two-step sequential deposition (fabrication of metal halide complexes in the first step followed by solution or vapor phase treatment with organic halides), vapor deposition (dual source thermal

evaporation, single source thermal ablation or flash evaporation, and chemical vapor deposition), and post deposition vapor treatment (amine or pyridine gas assisted recrystallization) have been developed for realizing high quality perovskite thin films essential for high performance PVKSCs.[27,64–70] Low temperature solution processing routes provide enormous flexibility and enable use of low cost printing approaches (spray coating, inkjet printing, screen printing, blade coating, and slot die roll-to-roll (R2R) coating) for manufacturing PVKSCs at scale with ease.[15,26,71,72]

Performance: The exceptional material attributes of hybrid perovskites translate to numerous functional device possibilities with commendable performance metrics. Notable applications include photovoltaics,[27,32] photonic sources (light-emitting diodes, lasers),[53,73,74] photodetectors,[75] transistors,[33] batteries,[63] piezoelectrics,[76,77] synapse and memory devices.[76,77] Hybrid perovskites have been brought to prominence by the rapid rise in power conversion efficiency (PCE) of PVKSCs.[32,34,41] Typical PVKSCs employ superstrate configuration, where a glass substrate provides a window for incident light and holds the device stack constituting of a perovskite absorber sandwiched between charge (hole- and electron-) selective contacts, capped by a transparent electrode on one side and a reflective electrode on the other side. Efficiency of PVKSCs are typically evaluated using PCE determined from PV performance metrics (V_{oc} = open-circuit voltage, J_{sc} = short-circuit current density, FF = fill factor), which are strongly reliant on the quality of materials and interfaces. The facile bandgap tunability aids construction of multijunction PV to surpass performance limits of single junction PV. Low temperature processability enables flexible solar cells for niche applications. A combination of high performance characteristics with low cost potential for hybrid perovskites could thus fuel the necessary paradigm shift in the PV and electronic fields in general.

1.2.2 Organic-Inorganic Hybrid Perovskites: Material-Level Challenges

Despite their attractive structure-property-processing-performance traits, hybrid perovskites have certain inherent material-level challenges. In spite of their high defect tolerance, polycrystalline perovskite films have a non-negligible level of trap density due to point defects and extended defects such as grain boundaries, interfaces, and surface disordering. Defect density also scales with thin film area. These defects are electronically active and act as non-radiative recombination loss pathways for charge carriers.[52,54,55,78,79] The soft ionic nature of these materials favors low activation energies for lattice distortion as well as migration of intrinsic point defects and extrinsic defects. Dynamic ionic migration under solar cell working conditions induces current-voltage (*I*-*V*) hysteresis instability and activates multiple degradation pathways.[27,80–82] The volatility and polarity of organic cations lead to rapid perovskite degradation in the presence of moisture or heat.[61,83,84] The research field has been working collectively towards addressing these inherent challenges and the severe limitations they impose on PVKSC performance and durability.

1.2.3 Multifaceted Roles of Interfaces in PVKSC Device Engineering

In this section, I explain the multifaceted roles of interfaces in PVKSCs for non-specialists in the field through a discussion of the impact of interfacial engineering on perovskite film formation, defect passivation, interfacial charge dynamics, and device stability.

A. Perovskite Film Formation

Formation of perovskite thin film is a major determinant of the morphology and a pivotal step in fabricating PVKSCs. Interfacial engineering provides an important handle for controlling the crystallization (nucleation and growth) of perovskite thin films both on the macroscopic and the microscopic level, regardless of the processing route. On the macroscopic level, smooth

perovskite films with homogenous coverage of the underlying layer is imperative for preventing shorting between electrodes and enabling functional solar cells. On the microscopic level, structure and orientation of grains control the optoelectronic quality (trap state density, charge carrier lifetime and mobilities) of perovskite thin films and their efficacy as an absorber in solar cells. Recent studies have shown that larger grains (fewer grain boundaries) are beneficial for realizing lower intrinsic defect density, slower moisture-induced degradation, and lesser diffusion of ionic defects responsible for *J-V* hysteresis.[85–88] Further, the correlation of heterogeneity in trap states with different crystal grains and facets shows strong effect of microstructural features on the photo-response and the device performance.[89–92]

Here the impact of interfacial engineering on film formation is broadly grouped into three categories based on the aspect modulating morphology: underlying interlayers, interfacial modifiers, and interlayer additives.

Underlying Interlayers: The crystallization of perovskites through any solution-based routes proceeds through nucleation and growth. Nucleation is controlled by interfacial free energy and wetting contact angle of the precursor solution on the surface beneath (typically bottom interlayer). As given by the Gibbs free energy for heterogenous nucleation ($\Delta G_{het} = \Delta G_{hom} * f(\theta)$, where $f(\theta)$ is a function dependent on contact angle and ΔG_{hom} is the Gibbs free energy for homogenous nucleation), the ease of nucleation increases with lowering of the contact angle (increased wettability). Accordingly, with increase in hydrophilicity of the bottom interlayer, the wetting of perovskite precursor solution (employing polar solvents) is improved and results in formation of perovskite films with high coverage, uniformity, and crystallinity. Molecular approaches like introduction of polar functional groups on the polymer side-chains and inclusion of glucose additives have been successfully employed to render the polymeric interlayers with wetting surface

required for high quality perovskite deposition.[93–95] The dense nucleation and reduced grain boundary mobility on wetting surfaces however limit the grain growth, and result in compromised grain sizes. Alternatively, utilization of a hydrophobic bottom interlayer with non-wetting surface lifts the limitation on grain growth and increases the grain size. The use of a non-wetting surface could result in issues with film coverage, which can be alleviated by deposition of hot precursor solution.[88] This is less of an issue when vapor deposition is used for the perovskite formation.[96] Poly(bis(4-phenyl)(2,4,6-trimethylphenyl)amine) (PTAA) is a widely employed non-wetting interlayer for realization of large grains with high aspect ratio.[88,97]

Interfacial Modifiers: Functional modifications of perovskite growth surface also impact the film formation and the resultant morphology. Monolayer treatments are commonly employed to mitigate defects at the surface of metal oxide interlayers to improve the nature of contact and interfacial charge dynamics with the above grown perovskite films. The favorable interaction of terminal group in the monolayer modified oxide surface with species in perovskite precursor solution aids film assembly. Surface treatments like diethanolamine or 4-bromobenzoic acid (on NiO_x),[98,99] 4-aminobenzoic acid or 5-ammoniumvaleric acid iodide (on TiO_2),[100,101] and 3-aminopropaniac acid (on ZnO)[102] have been demonstrated to be beneficial in forming pinhole free, highly crystalline perovskite films. Such surface treatments have also been effective in improving the crystal growth and quality of the perovskite network within mesoporous metal oxides.[100,101,103] The incorporation of reduced graphene oxide as an interfacial modifier has resulted in larger perovskite crystallites due to increased hydrophobicity of the growth surface.[104,105] In addition, interfacial modifier enables morphological control via realization of the deterministic nucleation process. Branch shaped perylene has been used as a seed-mediated underlayer to crystallize perovskite films with fabric morphology, which provides enhanced

absorption due to the improved light scattering effect.[106] A recent study uses Au islands as the nucleation promoter to control nucleation sites and densities; impressively large grains up to 100 μm with little size variation across the film has been realized by adjusting the separation distance between neighboring Au islands.[107]

Interlayer Additives: Incorporation of interlayer materials as an additive to the perovskite precursor solution is another useful strategy for maneuvering film formation. Addition of fullerene derivatives (typically <0.5 wt%) to either perovskite precursor solution (for one-step processing route) or PbI_2 solution used in the first step (for two-step processing route) results in compact pinhole free films with larger grains (500-1000 nm) and higher crystallinity.[53,108–111] Improved film quality can be attributed to mobile fullerenes, which reduce the compressive stress induced by volume expansion during film evolution and fill the empty spaces across the film.[53,111] In contrast, addition of inorganic materials (NiO, Cu(thiourea)I) result in higher material quality (lower intrinsic defects) due to a stronger chemical interaction between the interlayer material and perovskite.[112,113] Incorporation of nitrogen-doped reduced graphene oxide (N-RGO) enhances the grain size and the optoelectronic quality of resultant perovskite films due to a slower crystallization process (attributed to strong interaction between basic nitrogen group and organic cation in the precursor solution).[114] Besides controlling the film formation, interlayer additives have other merits including defect passivation, enhancing charge carrier dynamics, and improving stability of perovskite thin films (discussed below).

B. Perovskite Defect Passivation

Hybrid perovskites are relatively soft ionic solids and have a non-negligible level of unintentional defects in the solution processed polycrystalline thin films. Defects affect the nature of bulk material as well as interfaces (**Figure 1.3a**) and have a significant impact on the charge

recombination processes, charge-transport, band alignment, and electrical stability of PVKSCs.[52,54,55,78] Interfacial engineering provides an unparalleled handle for defect passivation, which is critical to improve the absorber optoelectronic quality and suppress the recombination losses at interfaces arising from the variability of contacts. Localized point defects are prominent in the bulk, whereas extended defects occur at surfaces and grain boundaries. Surface defects dominate bulk defects in terms of their detrimental impacts and significantly limit the charge carrier lifetimes in thin films due to a very high surface recombination velocity.[115–117] Elimination of defects to realize higher quality perovskite absorbers with long-lived photo-induced charge carriers is fundamentally required for pushing the V_{oc}, J_{sc}, and PCE of PVKSCs close to the thermodynamic limit. Although, improved perovskite processing and post treatment approaches have shown success in increasing the grain size and decreasing the grain boundary / bulk defect density, the top and bottom film surfaces still act as a major sink for charge carriers.[117]

Here, I discuss how interfacial material employed in PVKSCs facilitate defect passivation, grouped into two categories: surface passivation through interfacial interaction, bulk passivation through perovskite-interlayer blends, and interfacial modification strategies.

Surface Passivation Through Interfacial Interactions: Depending on the material choice and structural design, multifunctional interlayers facilitate passivation of surface / GB defects, in addition to their basic function of selective charge extraction and transport. Favorable chemical interaction between the perovskite and adjoining interlayers results in the reduction of number of trap sites at the top and bottom surfaces. Several different interlayers have been developed in this direction with defect passivation capabilities. For instance, small molecule and polymer interlayers designed with electron rich (Lewis base) side groups effectively coordinates with electron deficient trap sites (like under-coordinated Pb ions and clusters) on the perovskite surface and mitigates trap

density (**Figure 1.3b**).[118–122] On the other hand, fullerene or its derivatives commonly used as the electron-transporting layer (ETL) in PVKSCs are good electron acceptors (Lewis acid) and facilitates defect passivation of the coupled perovskite surfaces through co-ordination with the negatively charged defects (Pb-I antisite defects PbI_3^- or undercoordinated halide ions).[123–126] Elimination of different non-radiative recombination loss channels through interaction at interfaces thus improve the interfacial coupling and result in an enhanced photocurrent / photovoltage for PVKSCs.

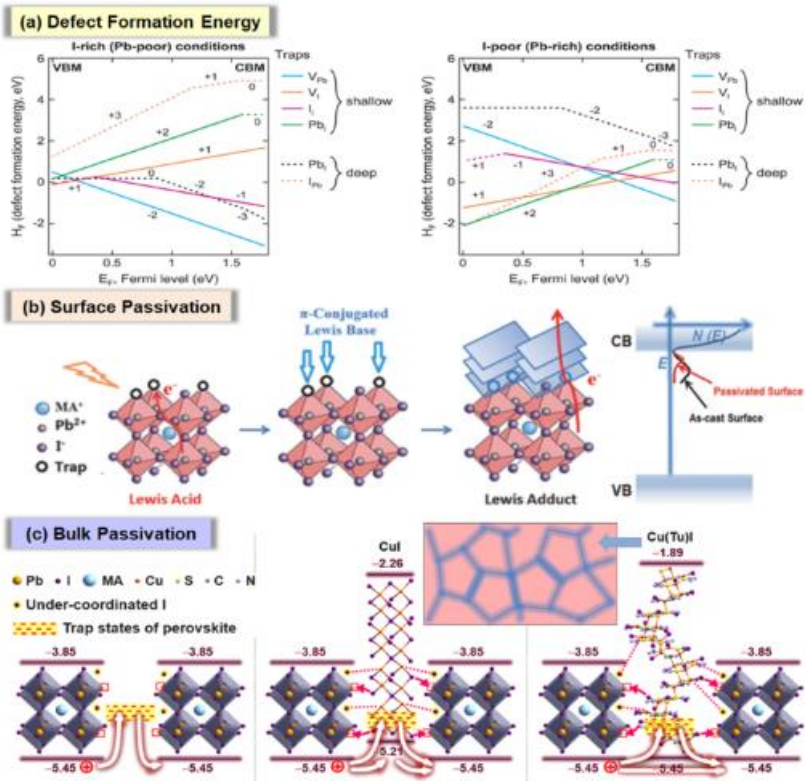

Figure 1.3. Perovskite defect passivation facet of interfacial engineering. (a) Theoretical calculations showing defect formation energies (H_F) as a function of Fermi level (E_F) position between the valence band maximum (VBM) and conduction band minimum (CBM) for native point defects in $MAPbI_3$ calculated under iodine-rich or iodine-poor growth conditions.[127] (b) Schematic of interaction between π-conjugated Lewis base and perovskite surface defects, along with an illustration for trap passivation.[118] (c) Schematic illustration of defect passivation mechanism for incorporating p-type conductor (Cu(Tu)I and CuI) in perovskite bulk; p-type conductor can effectively passivate trap states via interacting with the under-coordinated metal cations and halide anions at perovskite crystal surfaces.[113]

Bulk Passivation Through Perovskite-Interlayer Blends: The effect of defect passivation through interfacial interaction discussed above is restricted to perovskite thin film surfaces and planar

interfaces with the adjoining interlayers. It is also important to passivate defects within the bulk for lowering the overall trap densities of polycrystalline thin films closer to the level of single crystals. A viable strategy to mitigate bulk defects is to form heterojunction blends, where interfacial materials possessing defect passivation capabilities are incorporated within the perovskite layer. Diverse range of n-type and p-type materials have been demonstrated to improve the perovskite quality through interlayer blends. Direct mixing of perovskite and fullerene precursor solutions results in the formation of perovskite-fullerene bulk heterojunction (BHJ), where homogenous distribution of fullerenes fill pinholes and vacancies between perovskite grains. Marked improvements in transport (mobility and diffusion length) of charge carriers within active layer led to gains in J_{sc} and *FF*.[108,128] The favorable chemical interaction (donor-acceptor bonding) in perovskite-fullerene BHJ ties up halide defects resulting in reduced recombination losses, immobilized ions, and suppressed hysteresis in PVKSCs.[129,130] Alternately, dropping of the fullerene solution *in-situ* during perovskite solution spinning results in the perovskite-fullerene graded heterojunction (GHJ), where a gradient distribution of fullerene is formed near the surface of perovskite layer. In addition to improved material characteristics (enlargement of grain sizes and passivation of GB trap states), the gradient fullerene distribution also enhances the charge extraction efficiency due to a favorable band alignment for spatial separation of electron-holes and results in rise of all photovoltaic parameters (V_{oc}, J_{sc} and *FF*).[131,132] Similar integration of other electron-deficient heteroatom-doped polycyclic aromatic hydrocarbons (hexaazatrinaphthylene (HATNA) and bisthiadiazole-fused tetraazapentacenequinone (DCL97)) in the anti-solvent step also passivates the halide defect sites and improves the perovskite optoelectronic quality.[133] In contrast, incorporation of Cu(thiourea)I (a p-type conductor) into the perovskite effectively passivates trap sites through a concurrent interaction with the under-coordinated metal cations and

halide anions at crystal surfaces (**Figure 1.3c**); the resultant p-i (Cu(Tu)I-perovskite) BHJ with an increased depletion width reduces the charge carrier recombination and accelerates the hole extraction.[113]

C. Interfacial Charge Dynamics

Photoinduced charge generation and extraction form the basis for operation of PV devices. The foremost priority of engineering interfaces is to facilitate favorable interfacial charge dynamics and minimize carrier losses. Attributes of the perovskite and interfacial contacts together determine the efficacy of PVKSCs. Steps in charge generation and recombination process are illustrated in **Figure 1.4**.[134]A complete picture of photo physical processes in PVKSCs is still being unraveled and recent reviews provide an overview of the current understanding.[52,56,135–139]

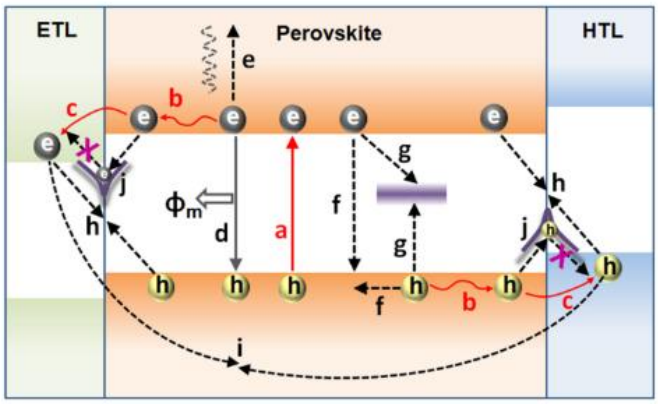

Figure 1.4. Charge transfer and recombination processes in a typical perovskite solar cell: **a** - photo-excitation of the perovskite to generate excitons, which immediately dissociate into free carriers (holes and electrons); **b** - charge diffusion; **c** - injection of photo-generated electrons into ETL and holes into HTL; **d** - radiative decay leading to photoluminescence at interface (ϕ_m = quantum yield for emission); **e** - auger recombination; **f** - bimolecular recombination; **g** - trap-assisted non-radiative monomolecular recombination (due to intrinsic defects and impurities in perovskite); **h** - back charge transfer at CTL/PVK interface; **i** – non-radiative charge recombination at direct contact between ETL and HTL interface; **j** - surface recombination caused by trap states at interface and grain boundaries. The recombination processes of (g-j) can be avoided and depressed by interfacial optimization. Time scales for charge injection, charge transport recombination and back charge transfer are (>1 ps to 1 ns), (>1 ns to 1 μs) and (>1 μs to 1 ms), respectively.

Optoelectronic characteristics of perovskite absorber govern the initial part of the photovoltaic process that includes light absorption, dissociation of exciton into free charge carriers (electrons and holes), and transport of carriers. Hole- and electron-selective interfacial contacts

govern the subsequent part of the process that includes preferential charge carrier flow, transfer, and collection at the respective electrodes. Important considerations in design of charge transporting materials (CTMs) include, (1) wide bandgap (to minimize parasitic absorption); (2) suitable energy levels (to selectively extract charge carriers); (3) high carrier mobility (to mitigate charge transport losses); (4) no defect induced loss pathways (to eliminate non-radiative recombination); and (5) controlled interfacial coupling with perovskite (to prevent charge accumulation losses). A wide-range of time-resolved laser spectroscopies (transient absorption, terahertz absorption, photoluminescence, and microwave conductivity), small perturbation spectroscopies (electrochemical impedance, intensity-modulated photocurrent and photovoltage), electrical transient techniques (charge extraction by linearly increasing photovoltage and time-of-flight), and steady-state methods (Hall effect, field-effect transistor, and space charge limited current) have been employed to understand the charge carrier dynamics at all levels from neat films to complete solar cells.[139,140]

Here, I provide a contextual discussion to elucidate the importance of interfacial charge dynamics in PV functionality, categorized into three parts: charge extraction governing photocurrent, charge recombination governing photovoltage, and charge accumulation governing hysteresis behavior.

Charge Extraction Governing Photocurrent: Perovskite semiconductors are semi-intrinsic in nature due to the doping arising from several intrinsic (defect formation chemistry) and extrinsic (film processing environment and interlayer interaction) mechanisms.[54,56] As the unintentional intrinsic self-doping (**Figure 1.3a**) is difficult to control in perovskite films, interlayers (p- and n-type) sandwiching the perovskite absorber play a crucial role in the origin of the photovoltaic action. Interlayers establish the built-in electric field (V_{bi}) necessary to provide the driving force

for charge separation (drift of electron and holes in the opposite directions towards interfacial contacts). The competition between interfacial charge transfer and recombination processes determine the fate of photo-generated carriers, and a large discrepancy in the dynamics of these processes is thus desired for efficient photocurrent extraction.[134,141,142] Dynamics of charge transfer and transport can be boosted to outcompete the recombination processes through suitable alignment of interfacial energy levels with perovskite, high conductivity of interlayers, and low levels of interfacial defects. A high carrier-collection efficiency is favored in PVKSCs because of the ultrafast charge generation, separation, and transfer processes compared to the free-carrier lifetime.[134]

Diffusion of carriers to contacts preceding the interfacial charge transfer takes ~200 ps to few ns depending on the thickness of perovskite films.[143] In the common mesoporous-type architecture, the interfacial charge transfer (electron and hole injection from perovskite to TiO_2 and spiro-OMeTAD, respectively) occurs on ps timescales, which is ~10^6 times faster than the pertinent recombination processes (μs range).[134] Compared to spiro-OMeTAD and TiO_2, charge transfer from $MAPbI_3$ to other p-type (P3HT, PTAA) and n-type (C_{60}, PCBM) organic transport materials is 3-4 orders of magnitude slower, just sufficient enough to overcome the recombination processes for charge extraction.[144,145] For oxide CTMs (TiO_2, NiO_x), interfacial defects and poor bulk conductivities can limit the charge extraction despite the high charge transfer rates (sub-ps).[146,147] Higher interfacial contact area, surface passivation, doping and energy level tailoring are approaches that have been employed to improve the charge extraction yield for interlayers with limitations. An illustration of the extraction yield as a function of ETL carrier density is shown in **Figure 1.5a**. Mitigation of the heterogeneity in interfacial charge extraction and the associated recombination losses are key for future performance improvements.[92,148]

Charge Recombination Governing Photovoltage: The thermodynamic limit for V_{oc} considering 100% radiative recombination is: $V_{oc,rad} = \frac{k_B T}{e} \ln\left(\frac{J_{sc}}{e\Phi_{em,0}} + 1\right)$; $\Phi_{em,0} = \int a(E)\varphi_{BB}(E)\,dE$, where $V_{oc,rad}$ is the radiative limit for V_{oc}, $a(E)$ is the material absorptance as a function of photon energy E, and $\varphi_{BB}(E)$ is the black body spectrum. Using the reciprocity between absorption and emission, a solar cell V_{oc} can be expressed as: $V_{oc} = V_{oc,rad} - \Delta V_{oc,non-rad}$; $\Delta V_{oc,non-rad} = \frac{k_B T}{e} \ln EQE_{EL}^{-1}$, where $\Delta V_{oc,non-rad}$ accounts for losses due to the non-radiative recombination and is quantified by the electroluminescence quantum yield (EQE_{EL}).[55,149] The correlation between EQE_{EL} and V_{oc} for PVKSCs with different ETLs are shown in **Figure 1.5b**. To make the solar cell highly luminescent and maximize V_{oc}, the quality of absorber material and interfacial contacts are crucial. Defects in the perovskite (dependent on the film composition and morphology) and the surface recombination (dependent on the interfacial contacts) are common non-radiative recombination channels that limit PVKSC performance.[150] The intimate link between surface recombination and photovoltage is evident in HTM- and/or ETM-free PVKSCs, where the less regulated interfaces result in severe V_{oc} loss.[151]

In PVKSCs, V_{oc} originates from the photo-generated electrochemical potential (quasi-fermi level splitting) in perovskite, which is dependent on the bandgap and charge carrier densities sustained under illumination.[55] Significantly higher V_{oc} loss is therefore observed when the surface recombination is dominant, as in the case of PVKSCs employing PEDOT HTL.[55,152] Carrier losses by surface recombination can be controlled by tuning the interfacial energetics, charge extraction, and defect passivation. Interfacial energy level alignment is important in the sense that they are strongly correlated with the V_{bi} driving charge carrier separation and the recombination losses due to back charge transfer at contacts. Improved charge selectivity and reduced interfacial

recombination enabled by tailoring the interlayer or introduction of ultrathin insulating layers have successfully improved V_{oc}.[153–156] Recently it has also been identified that dopants employed to improve HTL (spiro-OMeTAD, PTAA) conductivity act as recombination centers and are detrimental to V_{oc}. Accordingly, the reduction of dopant concentration increases V_{oc} up to 1.23 V, which is inching closer to the corresponding $V_{oc,rad}$ limit (1.33 V).[157] Furthermore, contact passivation mitigates electronically active interfacial defects to suppress non-radiative surface recombination and provides significant V_{oc} gain.[158–160]

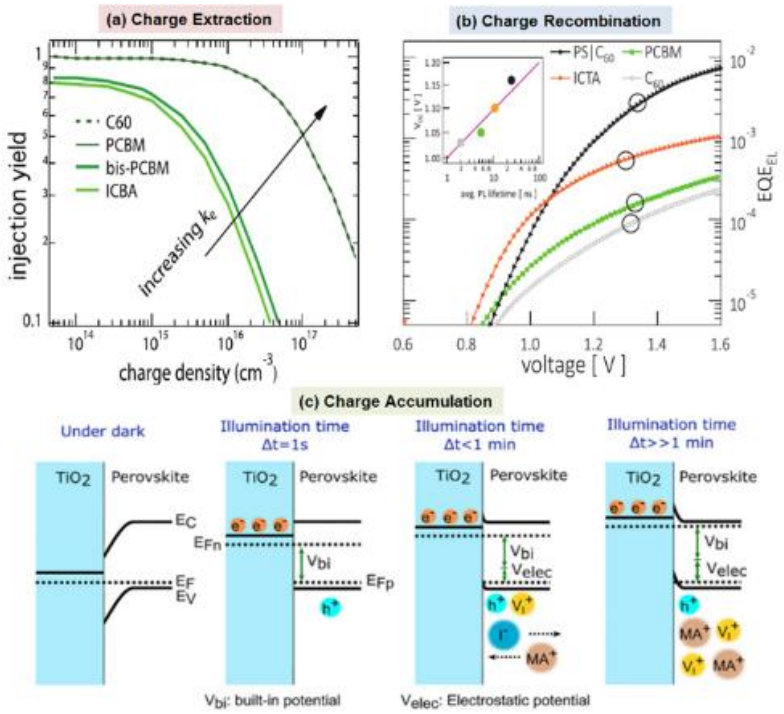

Figure 1.5. Effect of interfacial charge dynamics on solar cell device performance. (a) Extraction yield as a function of charge carrier density for different electron transport materials (ETMs).[145] (b) EQE_{EL} as a function of applied forward bias for PVKSCs with different ETMs; circles indicate values at injection current densities equivalent to J_{sc} under 1 sun illumination. Inset shows device V_{oc} versus average fluorescent lifetime, with linear line as a reference.[154] (c) Illustration of energetic landscape at the TiO_2/Perovskite interface at four different stages; band bending results from an increase in the hole concentration at the interface associated with ionic accumulation, which forms an electrostatic potential (added to V_{bi}) due to the electric field across the interface.[161]

Charge Accumulation Governing Hysteresis Behavior: The mixed electronic-ionic nature of hybrid perovskites has strong implications on their functional properties.[162,163] Facile vacancy-assisted ion migration with low activation energies (0.1-0.6 eV) results in significant ionic

conductivities under conditions relevant to the solar cell operation.[82,163] Sandwiching perovskite between CTMs as in PVKSCs facilitates the electronic transport but blocks the ionic transport across interfaces, inevitably causing ionic accumulation and excess low frequency capacitance. This significantly influences the electrode polarization (piling up of space charge near interfaces[164,165]), interfacial energetics (doping or dipole formation by ionic defects[165–167]), built-in electric field (compensating ion-induced electric field[168]), and functionality (tunneling mediated by ions[16,169]). Impacts associated with the charge accumulation are illustrated in **Figure 1.5c** using TiO_2/Perovskite interface as an example. The resultant PVKSCs are plagued by complex hysteresis behavior, where *I-V* characteristics are distorted by the additional voltage-dependent capacitive (due to light and electric field driven ionic/electronic charge redistribution) and non-capacitive (due to interfacial reactivity) current components with a slow (seconds to minutes) transient response.[27,80,81,151,170] They manifest as the change in PV performance metrics and shape of *I-V* characteristics with scan direction as well as the operational instability at maximum power point. In addition, the ionic migration and accumulation makes PVKSCs strongly sensitive to environmental exposure, illumination, and biasing history.[171,172]

Interfaces play an important role in mediating the ion accumulation and hysteresis behavior, which are inherently tied to the interfacial interaction, diffusivity, charge extraction, recombination, and perovskite structural/chemical changes.[27,151] In this regard, fullerene-based interlayers are most influential because of multiple aspects such as passivation of defects,[123,129] inhibition of ion migration,[130] minimization of charge accumulation,[173] and improvement of charge extraction,[124] facilitated by the chemical reaction with perovskite (anion-induced electron transfer).[174,175] Hysteresis instabilities in PVKSCs have been mitigated through fullerene incorporation in numerous ways: interlayers, interfacial modifications, and blends with

perovskite.[125,126,176] Engineering interfaces to reduce the charge accumulation by control of the interfacial electric field, ionic permeability, and ionic reactivity also suppresses hysteretic effects.[177–179] On the whole, improved interfacial charge dynamics (fast charge transfer, low non-radiative recombination, and less charge accumulation) alleviates hysteresis and improves performance of PVKSCs.[27,81,151]

D. Device Stability & Durability

The promising rise of PVKSCs is hampered by the unstable nature of hybrid perovskites. Tailored charge transporting interlayers have added capabilities of a barrier layer to protect the perovskite from external contaminants and interfacial modifications modulate the chemical reactivity of perovskite with adjoining layers.

External factors like humidity, temperature, pressure, light, electric field, and chemical environment strongly influence the perovskite absorber characteristics and its functionality. Overcoming impediments in the material and device stability is thus crucial for commercial deployment. Schematic illustrations of different degradation pathways in PVKSCs are provided in **Figure 1.6**. The degradation of hybrid perovskites is intrinsically related to their structural instability and soft nature. Presence of volatile organic components and prevalence of mobile ionic defects result in sensitivity to external factors and interaction with associated layers, which are ultimately responsible for majority of degradation pathways (**Figure 1.6a-d**). Reactivity with H_2O, O_2 and I_2 vapors also permanently render the perovskite material less useful for photovoltaic conversion.[84,180,181] Detailed account of degradation mechanisms and approaches for perovskite design to circumvent stability issues can be found elsewhere.[27,84,182] Beyond intrinsic material nature of hybrid perovskites, interfaces also play a crucial role in influencing the device stability and durability (**Figure 1.6e-f**).

In this section I discuss critical roles of interfaces in modulating instabilities induced by intrinsic perovskite degradation, ionic migration, and other device components. The discussion summarizes interface pertinent degradation pathways and points out the promise of interfacial engineering strategies for improving the PVKSC durability.

Instability Induced by Intrinsic Perovskite Degradation: Studies have shown that even though alternate perovskite formulations with organic cation modifications show better resilience than typical $MAPbI_3$, the mechanism and principles of degradation are fundamentally similar to those established with earlier studies based on $MAPbI_3$.[47,180,183,184] Degradation of $MAPbI_3$ results in disintegration of the material into PbI_2 and volatile products. Boundary conditions of the degrading perovskite determine the specific degradation pathway and the nature of volatile products (CH_3NH_2, HI, NH_3, I_2, CH_3I). Humidity exposure causes severe degradation due to the aqueous solubility of organic component in hybrid perovskites.[185,186] Water molecules diffused into perovskite films form hydrogen bonds with the volatile organic components and result in a reversible monohydrate phase; however, excessive moisture exposure subsequently result in an irreversible dihydrate phase and permanent loss of organic molecules (**Figure 1.6a**).[181,185,187,188] When coupled with light / heat, the degradation due to moisture ingress is faster because of the accelerated formation of PbX_2 phases (**Figure 1.6b**).[189] Application of an electric field in the presence of water also quickens degradation, due to the drift of loosely bound cations in the hydrated phase that results in destabilization of the perovskite structure.[171] Utilization of hydrophobic interlayers is an internal line of defense that resist the attack of moisture and alleviate the above-mentioned impacts of moisture.[190] Besides moisture, a combination of light and oxygen initiates a much severe degradation due to the formation and reaction of superoxide (O_2^-) with the organic moiety in perovskites (**Figure 1.6c,d**).[191–194] Since O_2^- species result from the interaction

of photoexcited electrons with the molecular O_2, efficient interfacial charge extraction is crucial for mitigating the impact of light and oxygen induced degradation.[194] Charges trapped at interfaces and grain boundaries is another irreversible degradation trigger, where the induced local electric field results in the deprotonation of organic cations and permanent decomposition of perovskite.[183] Appropriate selection of electron- and hole-transporting interlayers which possess hydrophobic properties and facilitate efficient charge extraction are thus imperative for preventing intrinsic perovskite degradation.

Instability Induced by Ionic Migration: Degradation of CTMs and electrodes happen due to their undesirable reactivity with profoundly migrating ionic point defects (both within the perovskite and across interfaces). Factors like electric field, moisture, and thermal stress prevalent during device operation have a catalytic effect on the ionic migration and result in a faster decay of PVKSC performance. Chemical reaction between spiro-OMeTAD$^+$ and the migrating I^- ions progressively reduces conductivity and hinders functionality of the HTL.[195] Migration and accumulation of I^- ions at the internal surface of Ag electrode leads to the generation of a AgI barrier for charge collection. The oxidation of Ag to AgI (yellow coloration) and the associated performance decay is not only observed when exposed to air, but also observed in N_2 atmosphere when the PVKSC is stressed under operating conditions.[196] Other metal electrodes like Al, Cr, Yb induce device degradation due to the redox reactions between Pb^{2+} in perovskite and the neutral metal contact.[197] When Au electrodes are employed, diffusion of Au through spiro-OMeTAD into the perovskite (**Figure 1.6f**) deteriorates all PV parameters due to the introduction of shunting pathways and deep trap sites.[198] Employment of robust interlayers and barrier layers at electrode contacts have minimized the ionic reactivity and alleviated the associated degradation pathways.

Beyond degradation of contacts, ionic migration and accumulation at interfaces is the major culprit behind widely observed *I-V* hysteresis instabilities in PVKSCs.

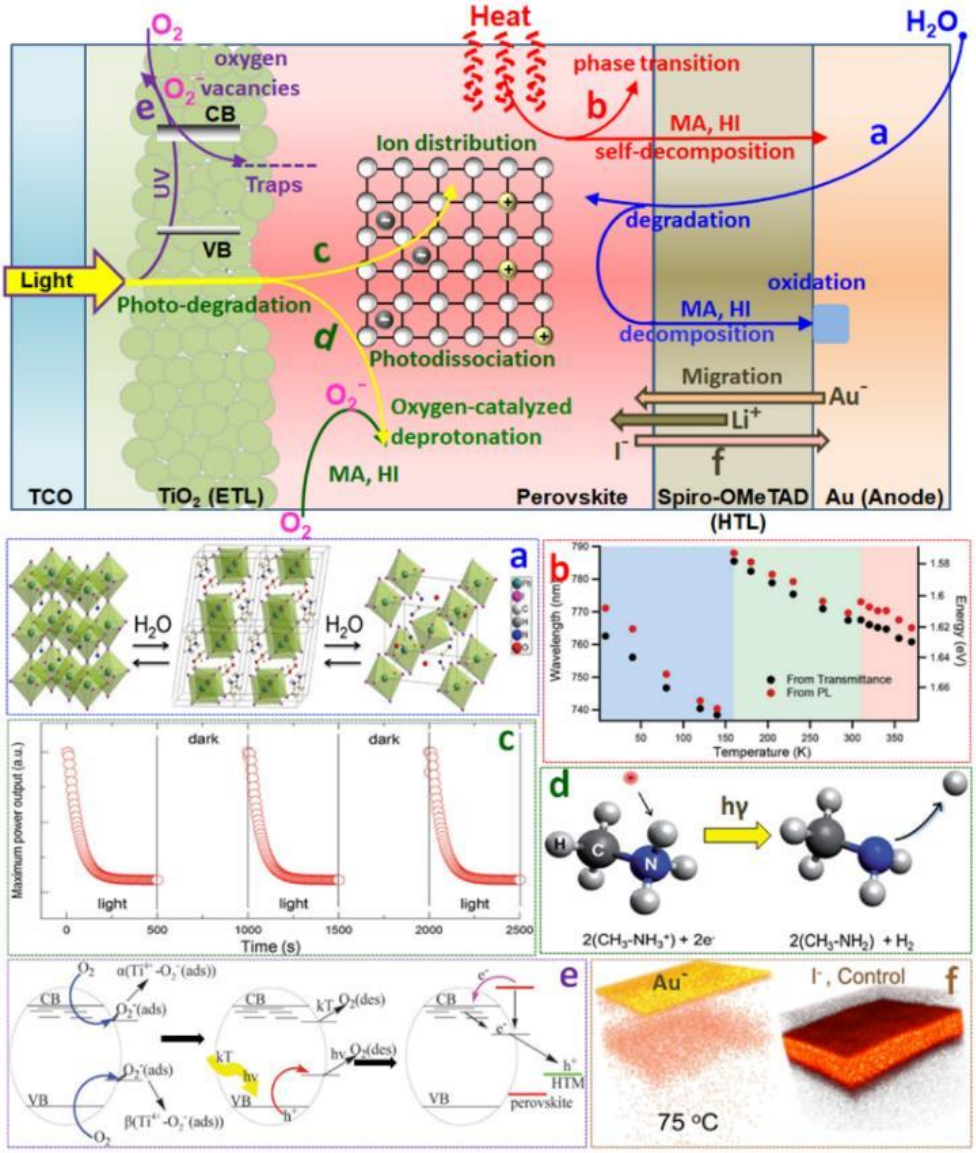

Figure 1.6. Top figure schematically illustrates six representative degradation pathways induced by moisture, heat, and light in regular (n-i-p) architecture PVKSCs. Figures below (a-f) provide descriptive information pertinent to each of those degradation pathways: (a) Hydration scheme for $MAPbI_3$ - initial hydration results in formation of monohydrate and subsequent hydration results in formation of dihydrate along with PbI_2.[181] (b) Variation of photoluminescence (PL) peak wavelength and absorption band-edge wavelength (energy) as a function of temperature.[189] (c) Modeled maximum power conversion efficiency (with fast halide and slow cation vacancy migration) over 3 cycles of light and dark shows similar (non-quantitative) reversible performance losses.[171] (d) Schematic depiction of dissociation mechanism of MA^+ due to the capture of a photo-generated electron.[172] (e) Oxygen induced formation of deep trap states at mesoporous TiO_2 surface / interface under UV illumination.[84] (f) Reconstructed elemental 3D maps for Au^- and I^- ions traced in the depth profile (by ToF-SIMS) demonstrates ionic diffusion across the device.[198] First four pathways (a-d) of degradation can be slowed down by tailored interlayer choices, whereas the last two pathways (e-f) of degradation can be eliminated via interfacial modifications.

Instability Induced by Other Device Components: Degradation of other device components (interlayers, electrodes) and permanent damage triggered by their reactivity with the perovskite absorber also result in PVKSC instability. In terms of ETL, the commonly employed TiO_2 suffers from photo-instability due to the photocatalytic activity under UV light exposure (**Figure 1.6e**). The unoccupied deep surface trap sites in TiO_2 (generated by the reaction between photo-generated holes and oxygen radicals) induce oxidation of the perovskite layer and promote formation of PbI_2, resulting in increased recombination losses.[199,200] The ZnO ETL suffers from thermal instability due to the basic nature of its surface. Proton-transfer reactions at the ZnO/perovskite interface result in loss of the organic cation and decompose the perovskite to PbI_2.[201–203] Alternate ETL materials and different interfacial modifications have been employed to alleviate instability at the ETL/perovskite interface. On the other hand, for HTL, the most popular candidate spiro-OMeTAD is often doped with 4-tertbutylpyridine (tBP) and bis(trifluoromethane)sulfonimide lithium salt (Li-TFSI) to improve the formability and conductivity. However, the sophisticated oxidation procedure associated with the doping process, the corrosive action of tBP on perovskite, and the redistribution of Li-TFSI under the action of electric field or ambient exposure make PVKSCs with spiro-OMeTAD extremely unstable and not reliable in the long term.[204,205] Alternate organic HTL choices like poly[bis(4-phenyl)(2,4,6-trimethylphenyl)amine] (PTAA) and PEDOT:PSS are also not intrinsically stable because of their sensitivity to moisture and oxygen. Development of next generation organic or inorganic p-type interlayers with better intrinsic properties will be pivotal to mitigate the HTL instability.

1.2.4 Perovskite Solar Cell Research Landscape

Efficiency, stability, scalability, and cost are four cornerstones pivotal for PVKSC development and its successful laboratory-to-industry translation.

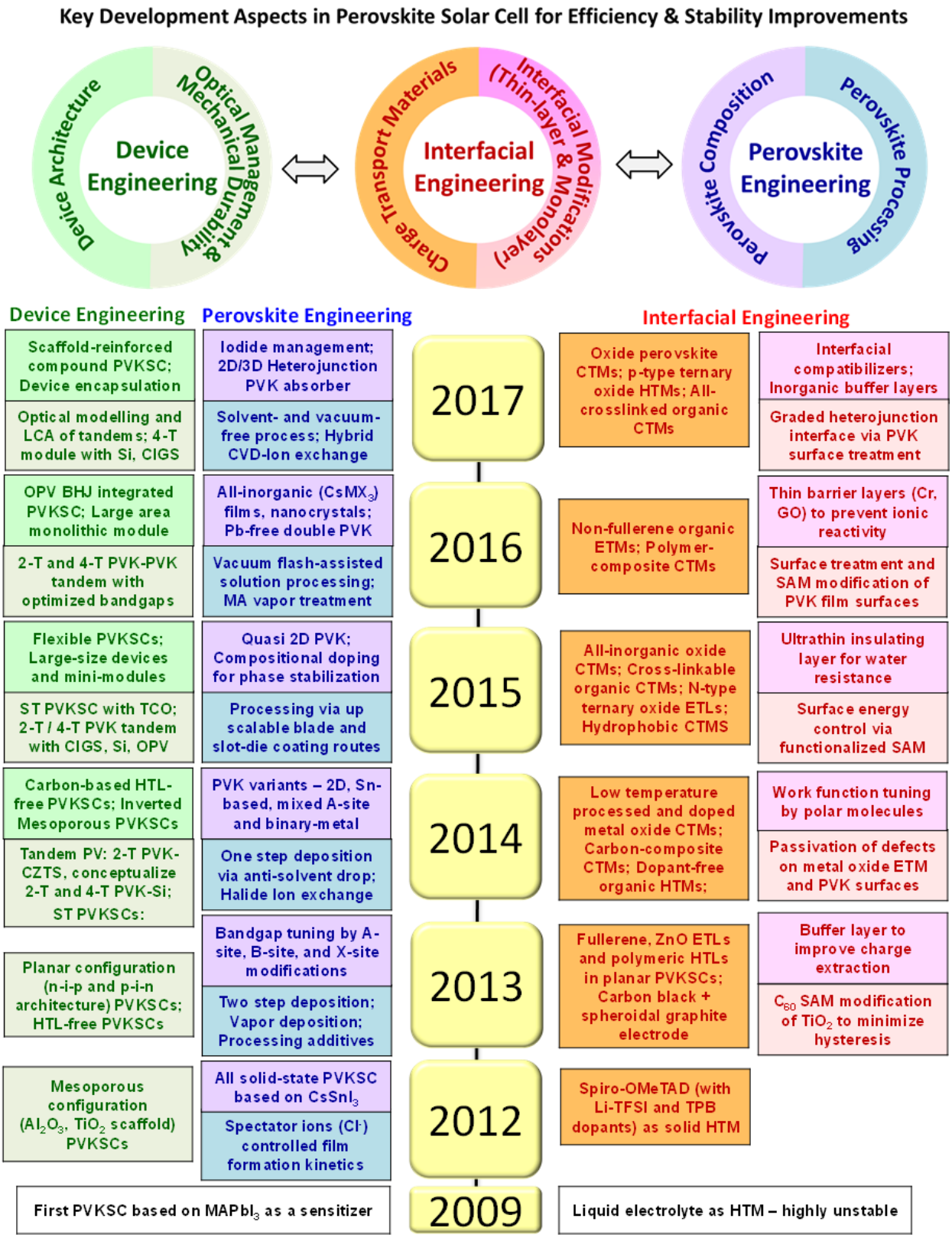

Figure 1.7. A timeline summarizing the onset of key developments in PVKSC field for efficiency and stability improvements (until 2017), grouped into three categories: Device Engineering, Interfacial Engineering, and Perovskite Engineering.

Since the inception of the PVKSC field, improvement of device efficiency and stability have been the major research focal points, with increasing effort towards solving scalability challenges and reducing costs over the last two years. Synergetic material characterization, theoretical studies, and experimental studies have led to a better understanding of fundamental issues and the development of innovative approaches to overcome them. Best practices for measurements / calculations of material properties and device performance are being established to avoid reproducibility and accuracy issues arising from complexities inherent to PVKSCs.[206–209] PVKSC development can be broadly categorized into three fronts: device, interfacial, and perovskite engineering. The evolution of the PVKSC field up until 2017 on all three of these fronts is depicted in **Figure 1.7** with a timeline summarizing the onset of key developments. Reviews of PVKSC development from perovskite and device engineering fronts can be found in several recent articles.[27,28,43,48–51,57,59,65,66,210–212] Review focused on the interfacial engineering front of PVKSC development can be found in my recent publication,[6] where I have presented an exhaustive summary of the progression of the entire field from the perspective of interfaces.

1.3 Outlook Toward Commercialization

With progression in lab-scale device efficiency and stability, scaling up fabrication of PVKSCs is becoming increasingly relevant. To replace commonly used spin-coating and enable scalable deposition, a wide range of processing techniques including but not limited to electrodeposition, spray coating, inkjet printing, screen printing, blade coating, and slot-die roll to roll (R2R) coating are being explored. A summary of key characteristics, merits and demerits associated with each technique being used is provided in **Table 1.1**.

Table 1.1. Summary of roll-to-roll compatible techniques for perovskite deposition.

Technique	Key characteristics
Electro-deposition	▪ Established industrial technique already being utilized for functional coatings and inorganic thin film solar cells ▪ Promising for fabrication of inorganic mesoporous scaffold and epitaxial films, which can be coupled with liquid or vapor based treatments for conversion to perovskite ▪ Large amount of liquid bath used in the process is concerning in terms of solution wastage and disposal
Spray coating	▪ Utilization of low solid concentration in solution compared to spin coating on laboratory scales ▪ Impractical on large scale due to low resolution patterning and excessive restrictions on the boiling points of solvent used
Inkjet printing	▪ Programmable fabrication enables precise control of patterns and interfaces. Multiple channels can ease compositional engineering of perovskite via in situ mixing of ink from separate cartridges ▪ Speed limitations and restrictions on ink properties limits the utility of printing all layers in R2R compatible device fabrication
Screen printing	▪ Effective in formation of nanostructured scaffolds and very thick layers (10-500 μm) for use as interlayers and electrodes ▪ Expensive when transferred to flexible substrates for high throughput processing via rotary screen printing
Blade coating	▪ Convection facilitated drying leading to slower film formation favoring realization of large crystalline domains and photonic nanostructures for efficient and colorful perovskite solar cells ▪ Efficient materials usage and high throughput deposition for a wide variety of perovskite chemistries ▪ Difficulty in fabrication of thin interface layers
Slot-die R2R coating	▪ Unique crystallization kinetics controllable via solution feed, drum speed and temperature eases efficient printing of well-defined stripes for solar module fabrication ▪ Desired thickness and properties of perovskite and interlayers can be achieved via ink, surface and interface modifications ▪ Economically viable because of its effective material usage for printing few meters per minute with minimal dead space

Several scalability-durability-sustainability challenges lie ahead in the path towards commercialization of PVKSCs. Below I briefly highlight these challenges with reference to current efforts. It is important to begin accounting for these considerations comprehensively in future research directions on all fronts (perovskite, interfacial and device engineering), to enable in parallel advancement of PVKSCs and minimize the gap for their translation from laboratory to industry.

Scalability

- **Ambient Processing:** For deployment of large scale printing approaches in PVKSC manufacturing, transformation of perovskite film formation from spin coating inside glovebox to R2R coating outside in ambient atmosphere is a key task. This is complicated by sensitivity of perovskite formation to moisture and other process parameters, requiring a re-optimization of growth under conditions relevant to R2R coating.[15] Approaches like thermodynamically limited film growth facilitated by control of solution / interfacial chemistry, regulated growth within mesoporous scaffolds via carbon-based device architecture, and enhanced moisture resistance enabled through modulation of precursor composition, additive formulation, or design of multidimensional perovskite composites show promise in this direction.[15,213–215]
- **Module Design:** Individual solar modules are comprised of series-connected cells, with additional considerations. During fabrication, it is required to realize uniform pin-hole free perovskite films on large area, utilize low-loss interconnects, and minimize dead area between cells for high geometrical fill factor. New scalable processing routes and post-patterning via laser scribing are avenues for improving module efficiency.[216,217] During operation, partial shading induces mismatch losses and additional stresses because of the shadowed cells being operated under reverse bias. Reverse bias breakdown in PVKSCs occurs via tunneling mediated by interfacial ionic accumulation; design at device (interfacial characteristics) and module (bypass diodes) levels are thus critical to circumvent operational breakdown.[16,169]
- **Economics:** Capitalizing on PVKSCs potential for low levelized cost of energy (LCOE) and short energy payback time (EPBT) necessitates judicious choice of materials and processes overall. With consideration of high-throughput and low capex manufacturing (R2R) processes, raw materials account for a major fraction (>75%) of perovskite module cost.[35] High

temperature requirements and multi-step synthesis protocols impose additional burden in terms of cost / energy demand. New material and process developments (encompassing reduced production complexity, low temperature processability)[218,219] critically refined through assessment by LCA studies[35,220] are important to ensure economic edge of PVKSCs right from the development stage.

Durability

- **IEC Tests:** International Electrotechnical Commission (IEC) has established IEC 61646 test certification to assess long-term durability of thin film terrestrial PV modules. It includes three types of accelerated ageing tests: Temperature cycling (-40° C to +85° C for 200 cycles), Humidity Freeze (-40° C to +85° C & 85% RH for 10 cycles), and Damp Heat (+85° C & 85% RH for 1000 hours).[221,222] PVKSCs ability to survive these tests evaluate their progress towards 25 years operational lifetime. Current test specifications have been established based on knowledge from inorganic PVs; specific test standards for PVKSCs are expected in future with further understanding of their degradation pathways.
- **Thermomechanical Reliability:** During thermal fluctuations under operation, the differential thermal expansion within device stacks inevitably induce mechanical stresses. Due to the mechanical fragility (low fracture energies) of PVKSCs, additional stresses result in delamination and device failure.[223,224] This issue with thermomechanical stresses compounds at scale and is a huge liability. Advances in terms of cross-linking techniques for better cohesion of constituent layers (perovskite absorber and interlayers) and interfacial compatibilizers for better adhesion between layers is useful to improve intrinsic fracture energies. Alternate scaffold based device designs with extrinsic reinforcement and shielding enhance mechanical robustness of PVKSCs.[223,225]

- **Encapsulation:** Glass-glass encapsulation including polymeric encapsulants and edge sealants is an industry-standard packaging method to protect PV modules from environmental stresses. Contemplations regarding processing necessities (stack handling, temperature-pressure-time profile) and cost tally (glass and balance of module components factor for >90% of material cost)[35] are vital for implementing PVKSC packaging. Replacement of reactive-metal electrode by TCO empowers PVKSC to survive packing process; such packaged cells have passed IEC Damp Heat test.[226] Moving forward to withstand mechanical stresses during temperature cycling / flexible applications, flexible encapsulant and electrode development need to keep up.[227,228] R2R-process compatible flexible lamination encapsulation is attractive for scalability and flexible PVKSCs.[229]

Sustainability

- **Environmental Toxicity:** Use of Pb-based absorbers has raised debate regarding applicability of PVKSCs and associated environmental / toxicological implications. On one hand, high aqueous solubility product of PbI_2 (10^{-8}) compared to other heavy metal compounds like CdTe (10^{-34}) poses severe risk of Pb accumulation with food-chain.[230–232] On the other hand, 100% reliable and robust encapsulation of PVKSCs could prevent leaching out of Pb into water sources during operation / after module failure.[230,231] Judicious packaging and rigorous protocols thus become critical for PVKSC implementation. Alternatively, current search for discovery of Pb-free variants show promise to altogether mitigate Pb-toxicity issue: Sn-based perovskites and double perovskites are prominent directions.[51,232,233]
- **Green Solvent Processing:** Several solvents that are toxic (*N*,*N*-dimethylformamide, *N*-methyl-2-pyrrolidone, chlorobenzene) and skin-penetrating (dimethyl sulfoxide) are utilized in PVKSC fabrication. They have adverse environmental impacts and are incompatible with

ambient R2R processing. For perovskites, direct use of green solvent selection guide[234] to find solvent replacement is hard because of convoluted relationship between complexation in precursor solution, film formation and material quality.[62,235,236] Engineering of non-hazardous solvent systems[237,238] and novel processing routes with greener solution chemistry[239] are intriguing with enormous scope. Recent identification of 'Mayer Bond Order' as a solvent selection metric enables accelerated developments via computational screening possible.[240]

- **Recycling and End-of-life:** Careful end-of-life management strategies for handling Pb containing perovskite modules is significant to mitigate toxicity and environmental impacts. Proof-of-concept demonstration for facile dismantling of PVKSC shows immense potential for recovery / reuse of all major components to facilitate efficient recycling of degraded cells.[241] Dissolution and electrodeposition approach will allow recycling and recovery of Pb.[242] In case of disposal, incineration approaches are more sustainable compared to landfill.[243] Currently its premature for comprehensive end-of-life analysis; future module development coupled with complete cradle-to-grave analysis will provide better picture about the sustainability of perovskite modules.

Immense technological potential and ongoing vigorous efforts directed toward commercialization are encouraging. PVKSCs could eventually be poised to play a major role in the solar revolution aspiration for displacing fossil fuels as the next-generation energy source.

1.4 Dissertation Outline

The unifying research objective for works presented in this doctoral dissertation is improvement of PVKSC reliability and performance. I have utilized and integrated a wide-range of material and device perspectives for attaining better comprehension of inherent challenges,

solving key issues, and facilitating advancement of PVKSCs. The subject matter here is broadly categorized into three parts **(Figure 1.4**) as follows.

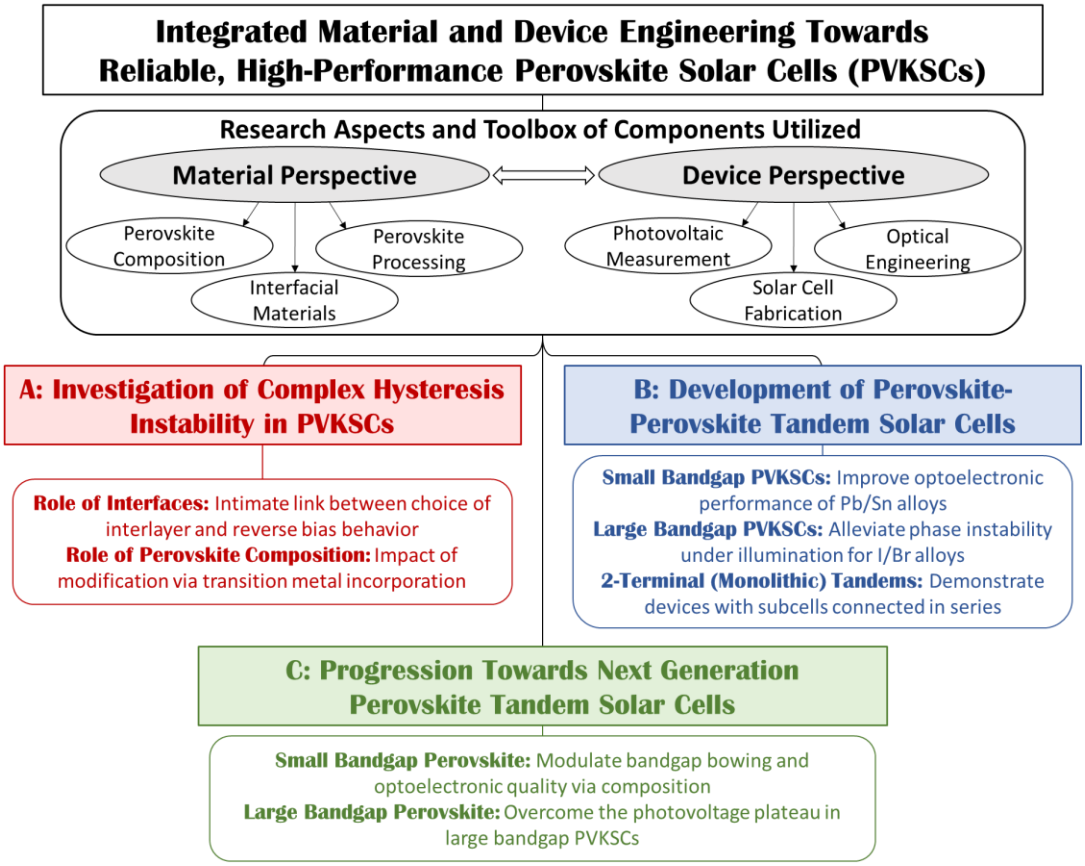

Figure 1.8. Dissertation outline along with research aspects and toolbox of components utilized.

1) **Part A (Chapters 2 and 3)** is focused on the investigation of complex hysteresis instability in perovskite solar cells.

   - *Chapter 2* comprises a case study to understand how interfaces mediate hysteresis behavior in PVKSCs. Sections of this chapter were adapted with permission from the associated publication.[16] Copyright 2016, American Chemical Society.
   - *Chapter 3* comprises a case study to understand how perovskite compositional modifications influence hysteresis behavior in PVKSCs. Sections of this chapter were adapted with permission from the associated publication.[19] Copyright 2017, The Royal Society of Chemistry.

2) **Part B (Chapters 4 and 5)** is focused on the development of state-of-the art perovskite-perovskite multi-junction (tandem) solar cells.

- *Chapter 4* illustrates an approach to alleviate the issue of photoinduced phase segregation in large bandgap PVKSCs. Sections of this chapter were adapted with permission from the associated publication.[13] Copyright 2016, American Chemical Society.
- *Chapter 5* illustrates design of perovskite tandem solar cells, approach to minimize the photovoltage loss in small and large bandgap PVKSCs, and fabrication of monolithic (2-Terminal) tandem devices. Sections of this chapter were adapted with permission from the associated publication.[20] Copyright 2017, Wiley-VCH.

3) **Part C (Chapters 6 and 7)** is focused on the progression towards next generation perovskite tandem solar cells.

- *Chapter 6* demonstrates an approach to overcome the photovoltage bottleneck in large bandgap PVKSCs. Sections of this chapter were adapted with permission from the associated publication.[7] Copyright 2018, American Chemical Society.
- *Chapter 7* investigates the impact of compositional modification on bandgap bowing and optoelectronic quality in Pb-Sn hybrid perovskites to identify the optical composition for small bandgap PVKSCs. Sections of this chapter will be used to prepare the manuscript for a separate publication.[12]

Finally, **Chapter 8** concludes this dissertation with summary of results, highlights of extensions through collaborative work, intellectual merits, research impact, and products of lasting value, and perspectives for continued development of perovskite tandem solar cells. Certain sections in *Chapter 1* and *Chapter 8* were adapted with permission from the associated publication.[6] Copyright 2018, Wiley-VCH.

PART A: INVESTIGATION OF COMPLEX HYSTERESIS INSTABILITY IN PEROVSKITE SOLAR CELLS

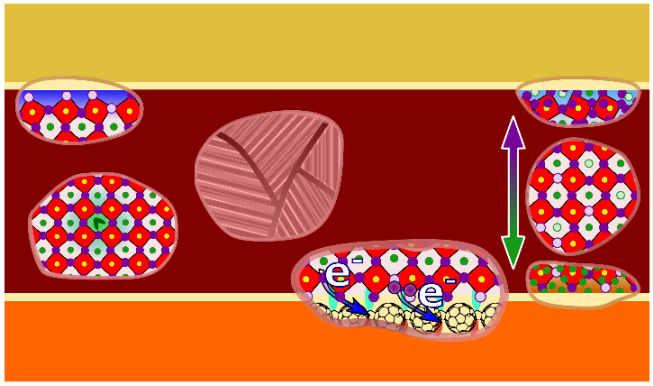

Schematic of a PVKSC depicting perovskite absorber and both charge transporting layers, with representation of different material and interfacial aspects (such as surface defects, perovskite composition and microstructure, interfacial interaction, ion migration and accumulation) tied to complex hysteresis instability in PVKSCs.

Chapter 2. UNDERSTANDING THE INTIMATE LINK BETWEEN INTERFACES AND REVERSE BIAS INDUCED ABNORMAL CURRENT-VOLTAGE HYSTERESIS

2.1 Introduction

Organic-inorganic hybrid perovskite solar cells (PVKSCs) are being extensively studied because they combine inherently facile processability with high power conversion efficiencies.[244–247] Despite these advantages, PVKSCs are plagued by complex hysteresis that differs greatly from the capacitive charging typically observed in photovoltaics.[248,249] Extensive studies have linked hysteresis in PVKSCs to a slow transient process within the material itself, which modifies electric field profile during *I-V* measurement.[168,250] Progressively, more accumulated evidences demonstrate the relationship between *I-V* hysteresis and ion motion. Key physical aspects of the process, namely time scale and activation energy, strongly implicate ion motion as the source of transient changes within perovskite responsible for anomalous hysteresis.[163,251,252] Thus, significant efforts have been directed toward device and material design to alleviate hysteresis.[129,253–255]

Hysteresis in PVKSCs has been widely observed for both conventional and inverted device configurations. Relationships between charge extraction, ion motion and hysteresis have highlighted the importance of interlayer selection in PVKSCs.[251,256,257] The absence of any significant hysteresis over a wide range of scan rates in the ITO/PEDOT:PSS/$CH_3NH_3PbI_3$/PCBM/Ag system serves as an excellent example for the importance of interfaces in modulating hysteresis; however, the interplay between perovskite interfaces and hysteresis is not yet clearly understood.[173,258] Precise and comprehensive *I-V*

measurements are thus pivotal in understanding the influence of device modifications on hysteresis. Studies have shown that absence of hysteresis at a particular set of scan parameters doesn't indicate its complete elimination.[250] The sensitivity of hybrid perovskites toward light, electric field bias, history and measurement conditions makes definitively establishing the cessation of the transient process behind hysteresis difficult.[250,259–261] Therefore, compared to other PV technologies special attention must be paid to the selection of scan parameters used for *I-V* measurement of PVKSCs.[207] Scan rate (step size and delay time), scan direction, pre-conditioning and scan range are key parameters in *I-V* measurement. Unger *et al.*[250] have demonstrated that PVKSC hysteresis is observed only at a particular characteristic scan rate closely associated with the time scale of the transient process in question. Further, Tress *et al.*[168] and Eames *et al.*[163] have demonstrated that the transient process influences net electric field distribution within the device, leading to hysteresis during *I-V* measurement. Thus, the starting and ending point of the scan could potentially influence *I-V* behavior because of the time dependent response of this process. At present, no systematic study on the influence of scan range in *I-V* measurements currently exists.

Herein, the influence of *I-V* scan range and scan rate on p-i-n, planar heterojunction PVKSCs are investigated to compare electronic consequences of commonly used hole transport layers (HTLs), PEDOT:PSS and nickel oxide (NiO_x). Strikingly different behavior is observed between these two systems. PEDOT:PSS based devices show stable *I-V* behavior independent of scan parameters contrary to NiO_x based devices, which show abnormal *I-V* characteristics when the scan is started from reverse bias (RB). The Cu:NiO_x HTL based devices used here show same abnormal behavior as NiO_x HTL based devices. Measurements of external quantum efficiency (EQE) under various RB reveal that the key difference between PEDOT:PSS/$CH_3NH_3PbI_3$ and

$NiO_x/CH_3NH_3PbI_3$ interfaces is the presence of an additional compensating electric field in devices with NiO_x interfaces. This manifests that the $NiO_x/CH_3NH_3PbI_3$ interface is responsible for abnormal *I-V* characteristics. Through exploring these systems, we propose that divergence from typical *I-V* characteristics and its dependence on scan range is linked to the formation of a transient tunnel junction at the $NiO_x/CH_3NH_3PbI_3$ interface during *I-V* measurement. This study provides understanding important for navigating complexities of PVKSC *I-V* behavior and demonstrates the ability of interfaces to modulate the ion motion intrinsic to perovskites.

2.2 Experimental Methods

Precursor Solution Preparation: NiO_x and $Cu:NiO_x$ precursor solutions were prepared according to previously reported procedures.[262–264] Methylammonium lead iodide ($CH_3NH_3PbI_3$) precursor solution were prepared by dissolving 1:1 molar ratio of CH_3NH_3I and PbI_2 in mixed solvent (40 wt%) of dimethylsulfoxide and γ-butyrolactone (3:7 by volume), and then stirred at 60 °C for 12 hours. All the solutions were at room temperature and filtered with 0.45 μm PVDF filters before spin-coating.

Solar Cell Device Fabrication: Solar cell devices were fabricated using procedures similar to our group's previous publications.[124,264] Cleaned ITO coated glass substrates were used for device fabrication. Except hole transport layers, all the layers were processed inside a N_2-filled glovebox. PEDOT:PSS (Baytron PVP AI 4083) films were spin coated at 5000 rpm for 30 s and annealed at 150 ^{0}C for 10 min. NiO_x and $Cu:NiO_x$ films were spin coated at 3000 rpm for 60 s and annealed at 400 ^{0}C for 1 h. Dual HTL films were obtained by spin coating PEDOT:PSS on $Cu:NiO_x$ film using same conditions. Perovskite ($CH_3NH_3PbI_3$) films were prepared using solvent washing method: spin coating (1000 rpm for 15 s, then 4000 rpm for 45 s) with 700 μl of toluene dropped

in the last 15-20 s and annealed at 100 ^{0}C for 15 min. $PC_{61}BM$ (15 mg/ml in chlorobenzene) films were spin coated at 1000 rpm for 60 s and annealed at 100 ^{0}C for 5 min. Fullerene surfactant, Bis-C_{60} (2 mg/ml in IPA) was spin coated at 3000 rpm for 30 s. Silver (Ag) electrodes were deposited by thermal evaporation under a vacuum pressure of 9 x 10^{-7} Torr with an evaporation rate of 2.0 Å/s; shadow masks were used to define the device area (3.14 mm^2).

Thin film Characterization: Film thickness were measured using Bruker DektakXT stylus profiler. SEM characterization was performed using a FEI XL 30 Sirion scanning electron microscope. AFM measurements were done in tapping mode using Digital Instruments Multimode Nanoscope Illa scanning probe microscope (Veeco Instruments, plainview, NY).

I-V Characterization: Solar cells were tested under AM 1.5 spectrum obtained using a Class A solar simulator (Solar light 16S-300), in compliance with general measurement procedures in ASTM E-948. A NIST certified Si-photodiode with KG5 filter was used to calibrate 1 Sun intensity (100 mW/cm^2). *I-V* scans under dark and illumination were measured using a SMU (Keithley 2400) at different scan rates, by varying the delay times at constant step size (0.01 V). *I-V* measurements were performed inside a N_2-filled glovebox and were generally done within 3 days from device fabrication, unless specified. Devices were kept in dark without application of any external bias (short circuit condition) post device fabrication and between measurements. For all *I-V* scans under illumination, the shutter was opened just (2-3 s) before start of measurements. *I-V* hysteresis was studied using an uninterrupted sequence of forward and reverse scans (RB/SC→FB→RB/SC) for a given scan range, unless specifically mentioned. For scans started from RB, the devices were held at 0 V (SC) just before the jump to RB starting point as the measurement was initiated. Dark measurements were done in fresh devices which were not exposed to any prior illumination to avoid the influence of unintentional preconditioning. Series

and shunt resistance were calculated using the slope of *I-V* curve near open circuit and short circuit respectively.

External Quantum Efficiency Measurements: Bias (DC-voltage) dependent external quantum efficiency (EQE) measurements were performed using a setup consisting of a xenon lamp (Oriel, 300 W) as a light source, monochromator (Newport Cornerstone 130), a chopper with a frequency of 100 Hz, lock-in amplifier (Stanford Research Corp SR830), a SMU (Keithley 2400) and a NIST certified Si-photodiode (Thorlabs FDS 100-CAL) for calibration. The setup provided the absolute photoresponse at 0 V and different RB. White light bias was applied using a 50 W LED fiber optic illuminator; no change was observed in the EQE measurements with and without white light bias. The EQE spectrum was integrated over AM 1.5G photon-flux to attain photocurrent density. The fluctuation of xenon arc lamp source was within 5 % during the entire period of measurement.

2.3 Results and Discussion

2.3.1 Interface Dependence of Reverse Bias Induced Abnormal Hysteresis

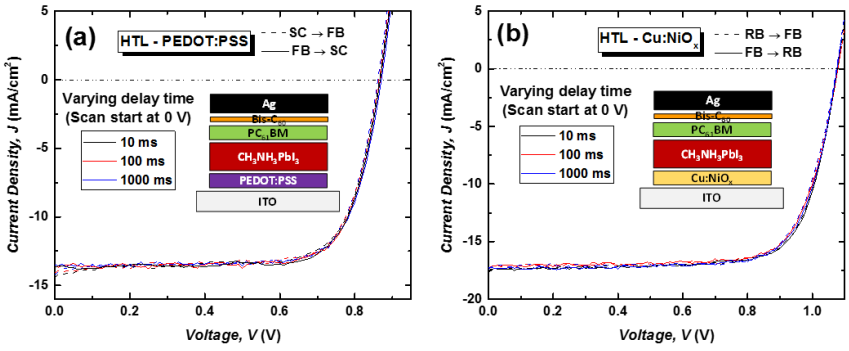

Figure 2.1. *I-V* behavior of $CH_3NH_3PbI_3$ based solar cells with (a) PEDOT:PSS and (b) Cu:NiO_x HTL, measured at different delay times (scan rates) and constant scan range (0 V to 1.1 V), with corresponding device architectures shown in insets.

PEDOT:PSS and NiO_x are commonly used organic and inorganic p-type interlayers to achieve high-performance PVKSCs.[265,266] To investigate the electronic consequences of these

interlayers, device architectures similar to our group's previous studies[124,264] were used (insets of **Figure 2.1**). Throughout this study, a **"standard *I-V* scan"** is defined as a scan from 0 V (short-circuit, SC) to 1.1 V (slightly beyond open circuit) with a scan rate of 0.1 V/s (delay time – 100 ms and step size - 0.01 V) without any pre-conditioning. This standard *I-V* scan is used to evaluate device performance. Scan direction plays a key role in the *I-V* measurements presented herein, so **forward scan** (RB/SC to forward bias (FB)) and **reverse scan** (FB to RB/SC) are concisely represented as **RB→FB** and **FB→RB**, respectively. **Figure 2.1a-b** show the *I-V* scan of devices with PEDOT:PSS and Cu-doped NiO_x (Cu:NiO_x) HTL at 10 ms, 100 ms and 1000 ms delay times. For both device architectures, *I-V* behavior is independent of scan rate and no significant hysteresis is observed when characterized with a standard *I-V* scan. The Cu:NiO_x HTL is similar to NiO_x HTL, but can yield an improved PCE due to its higher conductivity.[264] The power conversion efficiencies (PCEs) of the PEDOT:PSS and Cu:NiO_x devices used in this study are 9.2±0.5 % and 13.4±0.8 %, respectively, which are consistent with the stabilized current under illumination at maximum power point (**Table 2.1**). Further, it is important to note that the $CH_3NH_3PbI_3$ films fabricated on PEDOT:PSS and NiO_x by solvent washing method have similar bulk morphology as reported in our previous studies.[124,264] This can be attributed to the in-situ quenching step of adding non-polar solvent during spin coating, which effectively minimize the influence of different surface energy on perovskite crystallization.

Table 2.1. Performance metrics of $CH_3NH_3PbI_3$ based solar cells with PEDOT:PSS and Cu:NiOx HTLs; statistical data correspond to at least 16 devices of each type.

HTL	V_{oc} [V]	J_{sc} [a)] [mA/cm^2]	J_{sc} [b)] [mA/cm^2]	*FF* [%]	PCE [%]	*Stabilized* PCE [%]	R_s [Ω.cm^2]	R_{sh} [Ω.cm^2]
PEDOT:PSS	0.86 ± 0.01	14.20 ± 0.33	13.86 ± 0.31	75 ±1	9.2 ± 0.5	9.5	8.7 ± 0.1	1550 ± 229
Cu:NiO_x	1.07 ± 0.01	16.81 ± 0.89	16.80 ± 0.66	74 ±2	13.4 ± 0.8	13.3	9.1 ± 0.8	2246 ± 277

[a)] From *I-V* measurements; [b)] From integration of EQE spectrum with AM 1.5G photon-flux

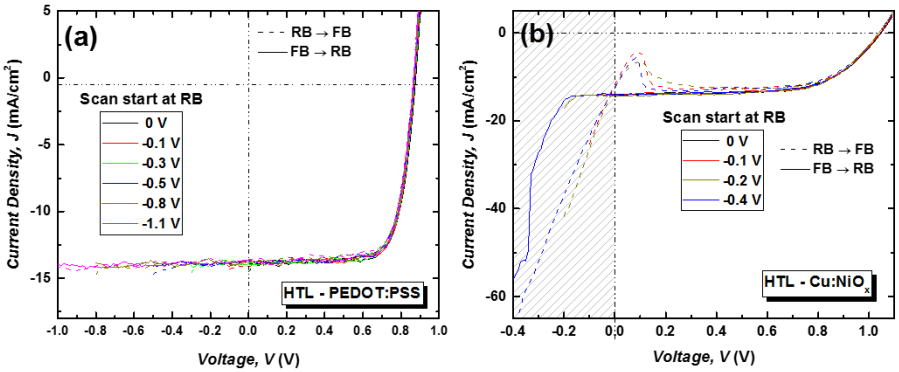

Figure 2.2. Comparison of forward and reverse (RB→FB→RB) *I-V* scans under illumination for $CH_3NH_3PbI_3$ based solar cells with (a) PEDOT:PSS and (b) Cu:NiO_x HTL, starting at 0 V and different points in reverse bias (RB).

Figure 2.2 shows *I-V* behavior of the above devices measured with different scan ranges by varying starting point in RB. PEDOT:PSS based devices show identical *I-V* behavior for all starting points in RB ranging from 0 V to -1.1 V and thus *I-V* behavior is independent of the scan range (**Figure 2.2a**). Surprisingly, Cu:NiO_x based devices showed a strikingly different *I-V* behavior when scanned from RB as shown in **Figure 2.2b**. The RB→FB scan shows huge leakage current combined with an inflection in the FB, and this is consistent for all scans starting at RB (**Figure 2.2b**). In contrast, a FB→RB scan displays *I-V* behavior typical of a photodiode until a threshold voltage around -0.2 V, beyond which a breakdown-like event is observed and eventually leakage current matches with that of the RB→FB scan. This threshold voltage is fairly consistent even in the standalone FB→RB scan starting at 1.2 V (**Figure 2.3a**), and the stabilized current at RB voltages matches with corresponding values in the *I-V* scan. Interestingly, the peak point of inflection in FB decreased with increasing delay time and ultimately disappears for delay times larger than 1000 ms, as shown in **Figure 2.3b**. The point at which the RB→FB scan recovers *I-V* behavior typical to a photodiode shifts closer to 0 V as delay time increases. All reported observations are repeatedly reproducible over several batches of devices.

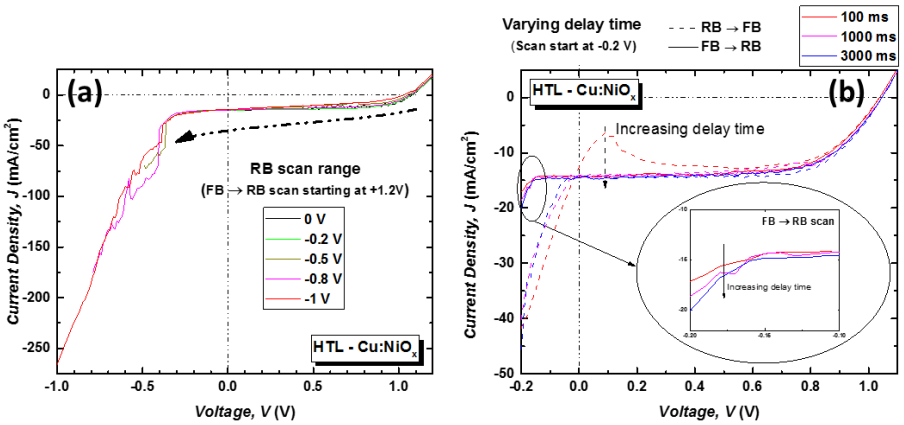

Figure 2.3. Characteristics of anomalous behavior in $CH_3NH_3PbI_3$ based solar cells with Cu:NiO_x HTL. (a) Standalone FB→RB (reverse) *I-V* scans starting at +1.2 V (FB) and ending at different points in reverse bias (RB). (b) Variation of the FB inflection in RB→FB *I-V* scans (-0.2 V to 1.1 V) measured at different delay times; 100 ms , 1000 ms and 3000 ms delay times correspond to scan rates 0.1 V/s, 0.01 V/s and 0.003 V/s respectively; inset shows the zoomed in region of FB→RB scans.

To establish that abnormal *I-V* behavior is associated with the HTL/$CH_3NH_3PbI_3$ interface, a PEDOT:PSS layer was inserted between Cu:NiO_x and $CH_3NH_3PbI_3$. As can be clearly seen in **Figure 2.4**, the resultant *I-V* behavior was independent of scan range, which is quite consistent with the behavior of PEDOT:PSS based devices discussed above. The device structure, performance metrics and *I-V* scans for Cu:NiO_x/PEDOT:PSS dual HTL based devices are also shown in **Figure 2.4**. When Cu:NiO_x was replaced by NiO_x as HTL, the characteristic abnormal *I-V* behavior was still observed in RB→FB scans. This eliminates potential redox chemistry involving Cu and I as a possible cause of this abnormal *I-V* behavior. Thus, we infer that the abnormal *I-V* behavior is directly associated with the NiO_x/$CH_3NH_3PbI_3$ interface. The scan rate and scan direction dependence of *I-V* behavior in NiO_x based devices observed here is uniquely different from the resistive switching effect reported in memory devices based on organic-inorganic hybrid perovskites.[267,268] Further, the observed interlayer dependence of abnormal hysteresis and the disappearance of the phenomenon at slow scan rates eliminates the possibility of "filamentary" conduction.[269–272]

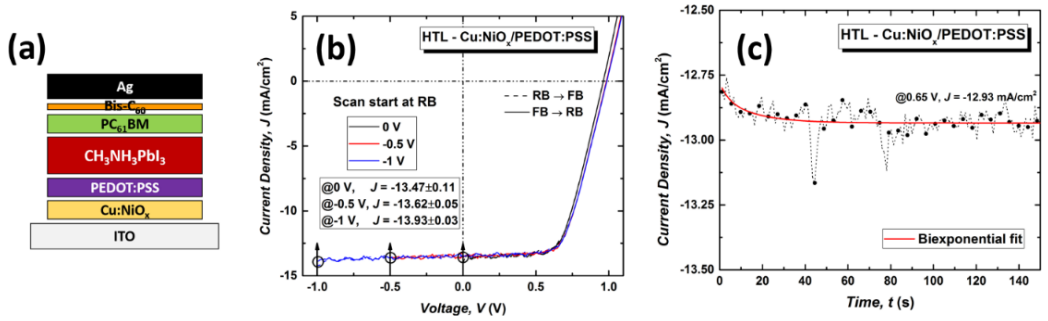

(d)

V_{oc} (V)	J_{sc} (mA/cm²)	FF (%)	PCE (%)	Stabilized PCE (%)	R_s (Ω.cm²)	R_{sh} (Ω.cm²)
1.00±0.02	13.47±0.11	60±3	8.2±0.3	8.4	21.1±0.4	1931±390

Figure 2.4. $CH_3NH_3PbI_3$ based solar cells with Cu:NiO_x/PEDOT:PSS dual HTL. (a) Device structure. (b) *I-V* behavior for scans starting at 0 V, -0.5 V and -1 V. (c) Bi-exponential fit of stabilized current under illumination at maximum power point. (d) Statistical data of photovoltaic performance metrics.

The thickness of PEDOT:PSS and NiO_x interlayers are 25 ± 5 nm and 20 ± 3 nm respectively. **Figure 2.5** shows the morphology (SEM and AFM) for ITO glass before and after spin coating of PEDOT:PSS or NiO_x layers. The change in morphology along with the decrease in surface roughness after deposition of PEDOT:PSS (R_{RMS} = 2.20 ± 0.06 nm) and NiO_x (R_{RMS} = 3.33 ± 0.11 nm) compared to ITO glass (R_{RMS} = 5.12 ± 0.13 nm) ensures good film quality and complete coverage of ITO surface by HTLs.

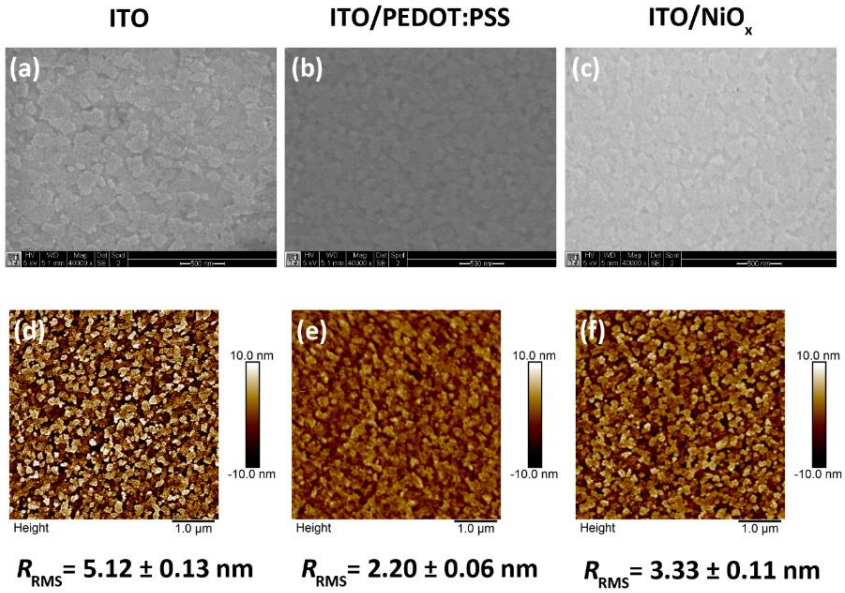

Figure 2.5. SEM and AFM morphologies of (a) & (d) ITO glass; (b) & (e) PEDOT:PSS spin coated on ITO glass; (c) & (f) NiO_x spin coated on ITO glass, respectively. The calculated RMS value of roughness (R_{RMS}) for different surfaces is specified below their corresponding AFM images. Scan parameters were kept unaltered during measurement of different surfaces; scale bars in SEM and AFM images denote 500 nm and 1 µm respectively.

As noted in **Table 2.1**, PEDOT:PSS and Cu:NiO_x based devices have similar series and shunt resistance, indicating that the breakdown-like event observed in NiO_x devices is not due to leakage from poor film properties. Further, the influence of scan direction on threshold voltage for anomalous breakdown (**Figure 2.2b**), the scan rate dependent inflection in the FB region (**Figure 2.3b**), and the preserved device function after anomalous breakdown demonstrate that the observed behavior cannot be attributed to a simple, irreversible junction breakdown.[273,274]

2.3.2 Characteristics of Transient Process Associated with Abnormal Hysteresis

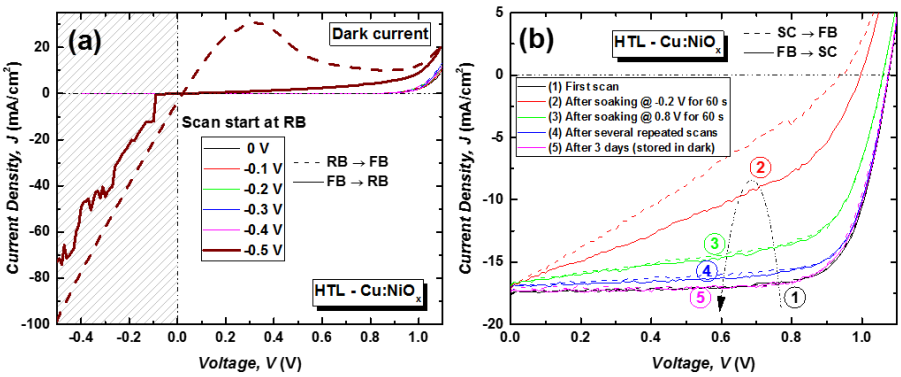

Figure 2.6. Effect of illumination and electric field bias on the *I-V* behavior of $CH_3NH_3PbI_3$ based solar cells with Cu:NiO_x as HTL. Dependence of (a) dark *I-V* characteristics on scan range with different starting points in reverse bias (RB) and (b) Standard *I-V* scans (0 V to 1.1 V, 100 ms delay time) on different device pre-conditioning; numbers 1-5 refer to the order of standard *I-V* scans.

To understand the nature of the anomalous breakdown and associated abnormal hysteresis in our NiO_x based devices, a series of comprehensive *I-V* measurements were performed. **Figure 2.6a** shows that under dark, no leakage is observed for scans starting in RB anywhere between 0 V to -0.4 V. However, when starting from -0.5 V, the observed behavior is similar to that under illumination even for scans starting at -0.1 V, dramatically different from the threshold voltage of around -0.5 V required to trigger anomalous breakdown in the dark. To characterize the role of light, we soaked the device in SC under 1 sun illumination for 0 to 60 min and performed RB→FB scans starting at -0.3 V. With increased light soaking, the peak point of inflection increases and typical *I-V* behavior takes progressively larger FB to restore (**Figure 2.7a**). Moreover, the

abnormal *I-V* behavior can be amplified (~1 min) more quickly by applying RB (-0.2 V) during light soaking (**Figure 2.7b**). From this, it is clear that the process responsible for anomalous breakdown and recovery is responsive to electric field and is accelerated and amplified by light.

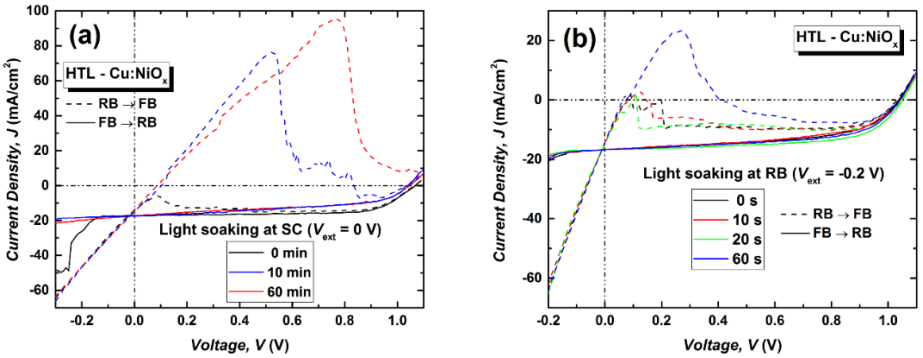

Figure 2.7. Dependence of abnormal *I-V* behavior on light (1 Sun illumination) soaking at (a) short circuit, SC (V_{ext} = 0 V) and (b) reverse bias, RB (V_{ext} = -0.2 V) for $CH_3NH_3PbI_3$ based solar cells with Cu:NiO_x HTL.

To define the transient process responsible for anomalous breakdown and its dependence on illumination and bias soaking, a series of standard *I-V* scans with different device pre-conditioning was conducted (**Figure 2.6b**). The first scan corresponds to a PCE of 14 % without any hysteresis as mentioned above. Since the process under scrutiny is triggered in RB, we soaked the device at -0.2 V for 60 s under 1 Sun illumination. The subsequent standard *I-V* scan showed considerably lower *FF* and V_{oc} with huge hysteresis between forward and reverse scans. After further soaking at +0.8 V for 60 s, the ensuing standard *I-V* scan showed hugely recovered device performance without significant hysteresis. This recovery progressively continued with repeated standard *I-V* scans. After storing one day in a dark, inert environment, the standard *I-V* scan matched exactly with the initial scan conducted the previous day with no hysteresis.

The above series of preconditioning scans (**Figure 2.6b**) coupled with step *I-V* scans (**Figure 2.8a-b**) demonstrate a compelling link between the phenomenon responsible for anomalous breakdown and the transient process responsible for *I-V* hysteresis in PVKSCs. A growing wealth of research reveals that the transient process behind *I-V* hysteresis in PVKSCs is

motion of charged defects within $CH_3NH_3PbI_3$ in response to the dynamically changing electric field within a device under operating conditions.[162,163,165,251,257,275,276] Relationships between anomalous breakdown and device hysteresis demonstrated above suggest that ion motion and consequent ion accumulation at the $NiO_x/CH_3NH_3PbI_3$ interface plays an intimate role in the unique current response of NiO_x based devices studied herein.

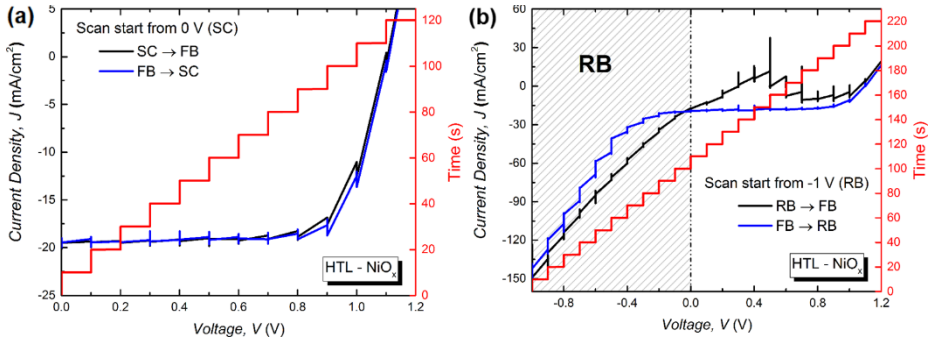

Figure 2.8. Step *I-V* scans under illumination for $CH_3NH_3PbI_3$ based solar cells with as NiO_x HTL. (a) Scan start from 0V (SC) and (b) Scan start from -1 V (RB).

If interfacial ion accumulation and associated change in space charge are responsible for the RB triggered abnormal *I-V* characteristics of NiO_x devices, there should be a corresponding change in efficiency of photocurrent collection[251,257,275] in the RB. To evaluate this, we measured EQE under different RBs. In general, for thin film photovoltaics it is expected that under increased RB, EQE will remain constant or increase depending on device charge collection efficiency.[277] Shown in **Figure 2.9a-c** is the EQE at different RB for devices with PEDOT:PSS, $Cu:NiO_x$ and $Cu:NiO_x$/PEDOT:PSS HTLs respectively. The EQE at varied RB for devices with PEDOT:PSS or $Cu:NiO_x$/PEDOT:PSS as HTL are as anticipated and reveals that under increasing RB EQE remains constant. This indicates that applied external field (E_{ext}) in RB supplements built-in field (E_{bi}) for collection of photo-generated carriers. Integrated current density (J_{Int}) from EQE at RB matches well with *I-V* measurements for devices with PEDOT:PSS HTL (**Figure 2.9d**). This substantiates our observation that PVKSCs with a $PEDOT:PSS/CH_3NH_3PbI_3$ interface behave like conventional photodiodes without any *I-V* hysteresis irrespective of scan parameters.

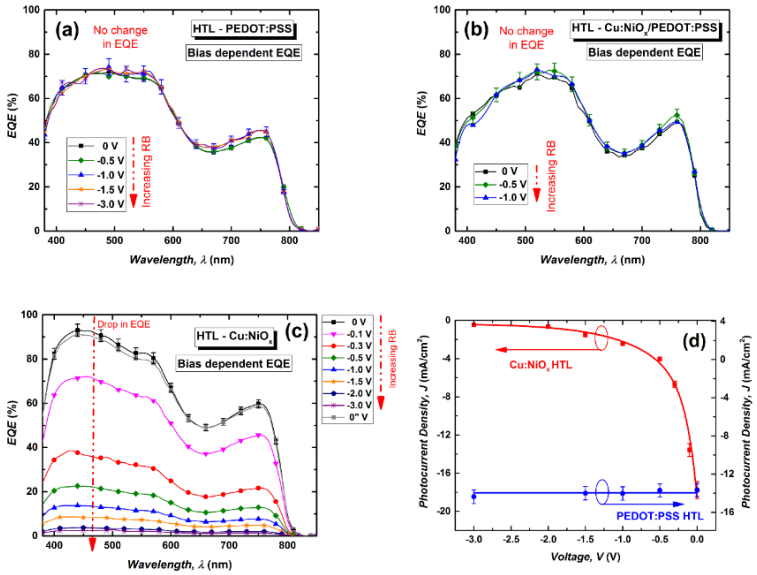

Figure 2.9. Electric field bias dependent external quantum efficiency. Spectral dependence of EQE at 0 V (SC) and different reverse bias (RB) for $CH_3NH_3PbI_3$ based solar cells with (a) PEDOT:PSS as HTL, (b) Cu:NiO_x as HTL and (c) Cu:NiO_x/PEDOT:PSS as HTL; 0 V and 0" V refer to measurements at SC before and after all RB measurements. (d) Comparison of variation in photocurrent density with voltage (RB) for $CH_3NH_3PbI_3$ based solar cells with PEDOT:PSS and Cu:NiO_x as HTL. Error bars indicate less than 5 % variation in the measurements.

Enormously different behavior was observed for devices without the PEDOT:PSS interlayer, in which Cu:NiO_x directly contacts $CH_3NH_3PbI_3$. Under increasing RB ranging from 0 V to -3 V, EQE continuously decreased (**Figure 2.9b**). The consistency of EQE measurements at 0 V before and after all RB measurements (denoted as 0 V and 0" V respectively in **Figure 2.9b**), demonstrates that the decrease in EQE with increasing RB is not because of degradation or other irreversible processes. The associated decrease in J_{Int} with increasing RB is shown in **Figure 2.9d**. Throughout this decrease, the spectral dependence of the EQE remains constant with applied voltage. This clearly implies that the EQE drop is due to electrical losses rather than optical losses. Thus, the uncharacteristic decrease of EQE with increasing RB in NiO_x based devices is associated with reduced charge collection, which is an indication of the E_{bi} being counteracted by an electric field induced by the applied potential in RB. The dependence of J_{Int} on RB suggests that a compensating electric field increases with increasing RB, resulting in a gradually diminishing driving force for photo-generated carrier collection compared to the SC condition.[163,261] This

observation is consistent with previous studies demonstrating the presence of a compensating electric field and its potential association with ion motion and *I-V* hysteresis under PVKSC operating conditions.[163,168,278] Based on the above EQE results, we establish that the presence of a compensating electric field is a key factor differentiating devices with $NiO_x/CH_3NH_3PbI_3$ and PEDOT:PSS/$CH_3NH_3PbI_3$ interfaces. Further, this observation of an interlayer dependent compensating electric field emphasizes the potential of interfacial engineering as an approach to effectively address hysteresis in PVKSCs.

2.3.3 Elucidation of Transient Tunnel Junction Formation in PVKSCs

The abnormal *I-V* behavior of RB→FB scans can be divided into four regions (**Figure 2.10**): breakdown in RB (Region I), increasing and decreasing current response with voltage in FB (Region II and III respectively) and conventional diode behavior (Region IV). The negative resistance (NR) in Region III coupled with distinctive peak and valley points in FB for a typical RB→FB scan in NiO_x based devices are remarkably similar to the well-known tunnel diode (Esaki diode) *I-V* characteristics.[273,279] The characteristics of RB→FB scan measured under illumination are similar to the RB→FB dark scan, with an added contribution of photocurrent (**Figure 2.10a**). The compensating electric field identified in devices with $NiO_x/CH_3NH_3PbI_3$ interfaces through bias dependent EQE (**Figure 2.10c**) implies changes in interfacial space charge[168,278] under RB conditions. The widely observed illumination and electric field dependent ion accumulation[174,276,278,280,281] intrinsic to $CH_3NH_3PbI_3$ is the likely origin of this compensating field as well as the correlated *I-V* characteristics indicative of transient tunnel junction formation at the $NiO_x/CH_3NH_3PbI_3$ interface. Further, observation of typical photodiode *I-V* characteristics in NiO_x based devices for scans starting at 0 V (**Figure 2.10a**) emphasize that transient tunnel junction formation is triggered by RB. Devices containing a permanent combination of a

photodiode and a tunnel diode, such as multi-junction photovoltaics, have *I-V* characteristics without anomalous breakdown and independent of scan direction, with the exception of slight hysteresis for very high series resistance (50 Ω) or under high optical concentration (10^3 suns).[282–284]

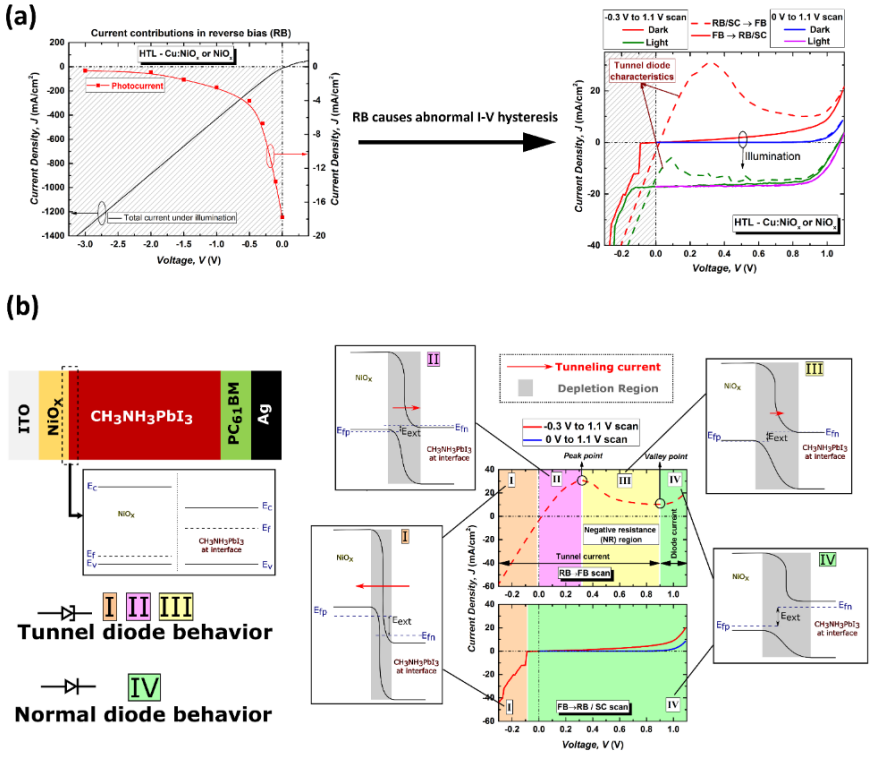

Figure 2.10. Mechanism for transient tunnel junction formation in NiO_x based PVKSCs. (a) A consequence of transient tunnel junction formation at the $NiO_x/CH_3NH_3PbI_3$ interface is a coupled effect between increased tunneling current and decreased photocurrent under RB, which subsequently causes abnormal hysteresis in dark and light *I-V* characteristics when the scan is started from -0.3 V (RB); the RB→FB behavior is remarkably similar to the tunnel diode *I-V* characteristics and no hysteresis is observed in *I-V* scans started at 0 V (SC). (b) Different regions and characteristic features in *I-V* scans under dark started at RB and SC are distinguished along with corresponding band diagrams (similar to an Esaki tunnel diode[273]) showing shifts in energy landscape within narrow regions on either side of the interface. Shaded areas in band diagrams indicate depletion width at HTL interface; sizes of red arrows indicate relative magnitudes of tunneling current between different regions.

However, in NiO_x based PVKSCs studied here, tunnel junction formation is dependent on electric field bias and coupled with photodiode function by virtue of the compensating electric field restricting photocurrent collection under RB. The transient process responsible for the creation of the tunnel junction is the same process that impedes collection of photo-generated carriers. The result of this coupled effect is pronounced abnormal hysteresis and a strong dependence on

preconditioning in photodiode and transient tunnel diode contributions to observed *I-V* characteristics (**Figure 2.10a**). Based on the results presented herein, we recommend that caution be taken for the measurements in RB necessary for devices like $CH_3NH_3PbI_3$ photodetectors, as without specific identification of photocurrent, the measured current response may be dominated by the formation of a tunnel junction.[285,286] The tunneling phenomenon in devices with NiO_x interfaces is portrayed via band diagrams in **Figure 2.10b**.

The difference in compensating electric field between devices with PEDOT:PSS/$CH_3NH_3PbI_3$ and NiO_x/$CH_3NH_3PbI_3$ interfaces characterized through bias dependent EQE (**Figure 2.9**) point toward a difference in space charge accumulation[168,278] at interfaces. This difference is unsurprising because of the disparate interfacial chemistry and capacitance between PEDOT:PSS and metal oxide interlayers in PVKSCs.[84,173,276,287,288] Several studies have revealed changes in morphology at the HTL/$CH_3NH_3PbI_3$ interface[173] and electrical properties like doping between PEDOT:PSS and $CH_3NH_3PbI_3$,[287,289] which could potentially mediate ion accumulation at the interfaces. Although the exact mechanism responsible for the difference we observe between PEDOT:PSS and NiO_x systems remains an object of active investigation, it implicates interfacial interaction as a key factor controlling the electronic consequences of ion accumulation. Based on several recent literature reports,[163,174,287,290–292] an explanation for the observed HTL-dependent *I-V* behavior is postulated and presented in **Figure 2.11**. The ~0.3 eV difference in valence band position[293] between NiO_x and PEDOT:PSS may impact *I-V* behavior and its relationship to transient processes within $CH_3NH_3PbI_3$. However, the strong dependence of carrier tunneling on depletion width rather than potential barrier height at the tunnel junction[274] leads us to exclude differences in valence band position as a primary determinate of the difference between the two systems. In general, depletion width is a strong function of charge density,[273] which is the most

widely varying parameter in $CH_3NH_3PbI_3$ at interfaces[165,257] under device operating conditions. Thus, the doping induced by ion accumulation within $CH_3NH_3PbI_3$ noted by Xiao *et al.*[165] and Frolova *et al.*[166] likely plays an important role.

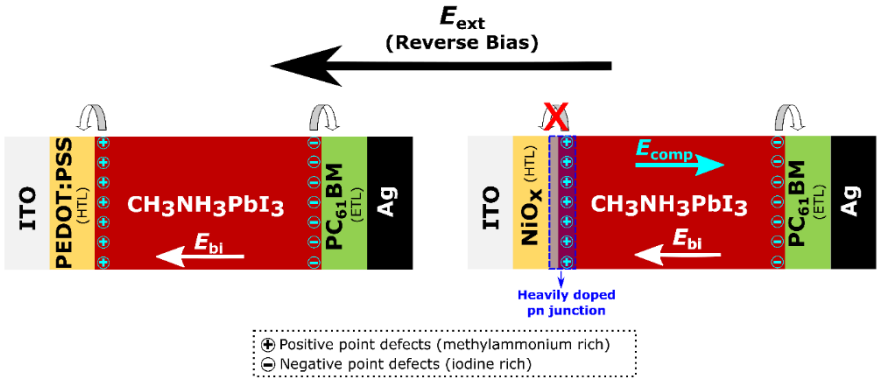

Figure 2.11. Hypothesis for hole transport layer (HTL) dependent *I*-V behavior in $CH_3NH_3PbI_3$ based solar cells. The electric field due to applied external reverse bias (E_{ext}) coupled with built-in electric field (E_{bi}) would induce accumulation of positive and negative point defects at HTL/$CH_3NH_3PbI_3$ and ETL/$CH_3NH_3PbI_3$ interfaces respectively.[163] Recently reported interactions[287] between PEDOT:PSS and $CH_3NH_3PbI_3$ could possibly relieve ion accumulation at the PEDOT:PSS/$CH_3NH_3PbI_3$ interface. However, non-interacting nature of metal oxides could withhold ion accumulation[290–292] near HTL and subsequently induce a compensating electric field[163,168,278] (E_{comp}) and accompanying doping of $CH_3NH_3PbI_3$ in proximity to NiO_x, ultimately responsible for the observed tunnel junction behavior; the direction of E_{comp} counteracts E_{bi} and E_{ext} in RB. The curved arrow at ETL/$CH_3NH_3PbI_3$ interfaces highlight the possibility of I^-/PCBM interaction as demonstrated recently.[174]

The postulated mechanism responsible for transient tunnel junction formation at the NiO_x/$CH_3NH_3PbI_3$ interface is presented in **Figure 2.10** along with band diagrams showing corresponding shifts in energy landscape. Initial fermi level (E_f) positions are drawn schematically from previous studies regarding the p- and n-type nature of NiO_x[293] and $CH_3NH_3PbI_3$[294] respectively. Based on the relationship between E_{bi} and E_{ext} and current understanding, ion accumulation at interfaces increases under RB and decreases under FB, inducing interfacial n- and p-doping of $CH_3NH_3PbI_3$.[163,165,278] Correspondingly, depletion width at interfaces is dependent both on net electric field and the extent of ion accumulation. Therefore, when a scan is started from RB, an added current contribution due to tunneling is observed until the depletion width falls below the threshold necessary for tunneling (Regions I to III). Under sufficiently large FB, tunneling current becomes zero and conventional photodiode behavior is eventually restored (Region IV).

Conversely, for a FB→RB scan normal diode behavior (Region IV) is preserved until sufficient RB (~ -0.2 V), at which point breakdown (Region I) attributed to tunnel junction formation is observed. For a scan with delay time of 100 ms and step size of 0.01 V, time from SC to 1.1 V is ~11 s which matches predicted time scales for ion motion[163,252] in $CH_3NH_3PbI_3$, reinforcing the proposed mechanism rationalizing differences between forward and reverse scans.

2.4 Conclusion

In summary, through comprehensive *I-V* characterization and biased EQE a new type of *I-V* hysteresis is identified in PVKSCs employing Cu:NiO_x or NiO_x HTLs caused by transient tunnel junction formation under RB. Comparison of this system to devices with PEDOT:PSS/$CH_3NH_3PbI_3$ interfaces demonstrates both that transient tunnel junction formation occurs at the NiO_x/$CH_3NH_3PbI_3$ interface and that the phenomenon is correlated with a compensating electric field under RB. In light of the current understanding of $CH_3NH_3PbI_3$, this implicates ion accumulation induced doping[165,166] and consequent reduction in depletion width as the culprit of transient tunnel junction formation in NiO_x based PVKSCs. The lack of tunnel junction formation, detectable *I-V* hysteresis, and compensating electric field under RB in PVKSCs with a PEDOT:PSS/$CH_3NH_3PbI_3$ interface demonstrates a compelling link between interfacial chemistry and the degree to which transient processes inherent to $CH_3NH_3PbI_3$ perturb ultimate device function. By virtue of relationships between illumination, electric field and tunneling characteristics, this work provides first steps toward a new kind of metrology for analysing complex transient processes within $CH_3NH_3PbI_3$. Ultimately, this work demonstrates that given appropriate interfacial conditions, RB alters how $CH_3NH_3PbI_3$ contributes to the functional nature of derived device.

Chapter 3. UNDERSTANDING THE IMPACT OF PEROVSKITE MODIFICATION VIA TRANSITION METAL INOCORPTAION ON CURRENT-VOLTAGE HYSTERESIS

3.1 Introduction

The recent development of hybrid perovskite solar cells (PVKSCs) has received very significant attention from academia and industry because the power conversion efficiency (PCE) of methylammonium lead iodide ($CH_3NH_3PbI_3$) based devices have soared from 3% to above 20% in just a few years.[254,295,296] The meteorically rising efficiencies in hybrid perovskites combined with their excellent solution processability and semiconductor quality poise them to transform the solar energy sector. It has recently been shown that PVKSCs energy payback time (EPBT) can be as low as 0.22 years compared to ~2.4 and ~0.7 years for crystalline silicon and thin film PV technologies, respectively.[37] However there remains measured skepticism about its ultimate impact because of intrinsic toxicity and instability. In order to realize the full potential of PVKSCs, present issues related to toxicity, degradation and current-voltage (I-V) hysteresis have to be addressed.[15]

Complex hysteresis behavior of $CH_3NH_3PbI_3$ based photovoltaic devices makes performance extremely sensitive to operation conditions, including illumination, electric field bias, and environmental exposure.[168,297] This unreliability not only creates a significant challenge for commercialization, but also harms the progression of the field in terms of poor reliability, inadvertently misleading device characterization, and artificially high efficiencies.[207] Understanding and addressing this is a unique challenge for $CH_3NH_3PbI_3$ and its derived devices because of the complexity of its growth from solution, and the corresponding difficulty of

establishing robust structure-property relationships. In photovoltaic devices, hysteresis manifests as a change in the shape of *I-V* characteristics between forward and reverse scans. In most PV technologies, hysteresis is observed at very fast scan rates (15-300 V/s) and can be eliminated at slower scan rates.[249,298] This is characteristic of capacitive charging. When hysteresis in perovskite solar cells (PVKSCs) was first noted by Snaith *et al.*,[299] it was observed that slower voltage scan rates anomalously exacerbate hysteresis. In addition to this anomalous dependence on scan rate, *I-V* hysteresis in perovskite devices depends sensitively on voltage scan range, electrical bias, pre-bias conditions, and light soaking.[168,297]

This anomalous hysteresis indicates the existence of a complex transient process. This has motivated vigorous research in the field exploring the origins of hysteresis (**Figure 3.1**), such as (i) interfacial defects,[256,300,301] (ii) ferroelectricity,[302,303] (iii) cation rotation,[304,305] (iv) light induced phase transformations,[306,307] and (v) ion motion.[162,163,165,257]

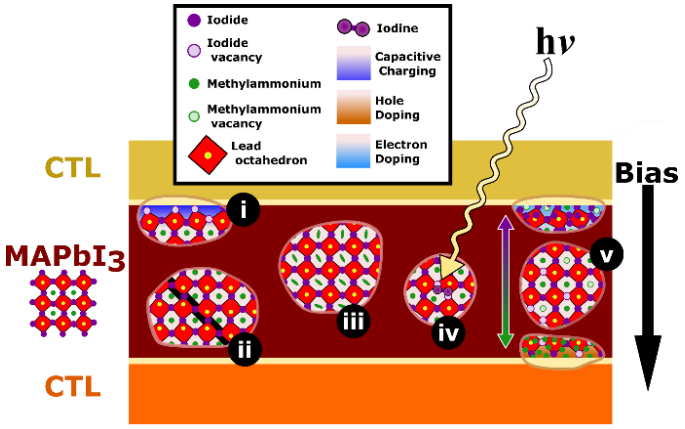

Figure 3.1. Schematic representation of a PVKSC depicting both charge transporting interlayers (CTLs) and $CH_3NH_3PbI_3$. Within $CH_3NH_3PbI_3$ most rationalizations for widely observed device hysteresis are represented. This includes (i) interfacial defects, (ii) ferroelectricity, (iii) cation rotation, (iv) light induced phase transformations, and (v) ion motion.

The general implication of these investigations is a fundamental link between hysteresis and dynamically changing electric field profiles within the perovskite layer and at its interfaces.[168] While there is still fierce argument surrounding this issue, identifying the troublesome processes

at play comes down to understanding the time scales they operate on and their activation energies. Current results indicate that the activation energy for hysteresis in PVKSCs is ~0.6 eV, which is close to the energy required for iodide and methylammonium vacancy migration in $CH_3NH_3PbI_3$.[163,308,309] As charged point defects like these diffuse, the distribution of space charge and the electric field profile within the absorber shifts, both in the perovskite bulk and more dramatically at its interfaces. The typical timescale of ion migration also fits with the timescale associated with device hysteresis.[163]

In crystalline solids, atomic diffusion must occur through distortion of the lattice, and in most systems defect generation and motion are intimately tied to the process. Lattice distortion and defect generation come at an energetic cost defined by the nature of the nearby atoms and bonds. To control ion migration at the atomic level, alterations to the crystalline lattice itself are necessary. This can be accomplished by alterations in short and long-range order within the crystal (*microstructure*) as well as the introduction of foreign species and changes in stoichiometry (*composition*). To preserve the properties that make $MAPbI_3$ ideal for solar absorption, any alterations to microstructure and composition must be slight enough to preserve the symmetry and semiconducting quality intrinsic to the material. In the case of $MAPbI_3$, substitution by a foreign species can occur on the halogen anion,[310] organic cation[311], or metal cation[312] sites and its stoichiometry can shift depending on growth conditions.[313] $MAPbI_3$ composition has been directly linked to hysteresis in several studies.[254,309] This is unsurprising as lattice composition defines energy required for both defect generation and migration. This indicates that tuning composition and growth of $MAPbI_3$ and its solid solutions, the process of ion motion can be controlled at the most fundamental level.

Herein, we study how a set of closely related transition metals (Mn, Fe, Co, and Ni) modify $CH_3NH_3PbI_3$ functionality and properties by first identifying what primary controlling variables determine the nature of material growth and resulting morphology. Through this effort we develop mechanistic insight into how both DMSO and this class of transition metal affect growth and morphology, allowing us to ultimately deconvolute the compositional and morphological influences of these transition metals and directly analyze their compositional impact on $CH_3NH_3PbI_3$ properties.

3.2 Experimental Methods

Materials: All precursors and solvents were purchased from Sigma-Aldrich and used without further purification, unless specified. Methylammonium iodide (CH_3NH_3I) and surfactant Bis-C_{60} were synthesized using our previously reported procedures.[314,315]

Solution Preparation: All perovskite precursor materials were stored and weighed in a nitrogen filled glove box. Molarity of perovskite precursor solutions was defined as the total molarity of metal ions in solution, percent Fe was defined as atom percent Fe relative to total metal ions (Fe / (Fe + Pb)), and stoichiometry of methylammonium was varied as noted in the main text (x = 1, 0.9, & 0.8). After weighing out the appropriate amount of starting material, DMSO was added and the solution was stirred at 60 °C for 1 h. Solutions were then aged for a minimum of two days before filtration and use. Notably, we used a 1 to 1 ratio between total metal ions in solution and methylammonium iodide to fabricate perovskite solutions for the work that precedes the stoichiometric optimization. For the remainder of the work, and optimized stoichiometry of 0.1 TI_2 : 0.9 PbI_2 : 0.9 CH_3NH_3I. All solutions were at room temperature and filtered with 0.45 µm PVDF filters before spin-coating.

1-step deposition for Transition metal-incorporated Perovskite films: The precursor solutions (~30 µl per substrate) were spin coated (5000 rpm, 60 s). For the data discussed in **Figures 3.4**, films were immediately annealed at 90 °C for 15 min. For the vast majority of the other data discussed, films were first annealed at room temperature for 60 min followed by 90 ^{o}C for 10 min. The one exception to this is for the final data presented (**Figure 3.12-3.14**), a shorter room temperature annealing time of 20 minutes was used simply to allow the more efficient fabrication of a larger number of films. Films of different thicknesses were achieved by varying solution concentration from 0.6 M to 1.2M. Glovebox atmosphere was periodically purged to avoid back-conversion issues from DMSO interaction. Also to limit the deleterious impact of DMSO, we used only ~30 uL per sample and only 1 to 2 samples per batch.

Solvent wash for Standard $CH_3NH_3PbI_3$ films: Precursor solutions were prepared by dissolving 1:1 molar ratio of CH_3NH_3I and PbI_2 in mixed solvent (40 wt% / 1M) of dimethyl sulfoxide and γ-butrylactone (3:7 by volume); the mixture was then stirred at 60 ^{o}C for 12 h. Subsequently, they were spin coated (1000 rpm for 15 s, then 4000 rpm for 45 s) with 700 µL of toluene dropped in the last 15−20 s and annealed at 100 °C for 15 min.

Perovskite growth under magnetic fields: Ceramic (ferrite) block magnets were purchased from Master Magnets, Inc. (item no. 07044, ~0.2 T). Two conditions were used for perovskite growth: low field and high field (**Figure 3.7a**). Magnets of opposite orientations were placed side by side to increase field strength without increasing the height of the stack. For growth under both low and high fields, perovskite films were exposed to the appropriate field for the entire duration of growth which includes room temperature annealing, thermal annealing, and cooling to room temperature. Because ferrite is a thermal insulator, we preheated magnet stacks for at least an hour at a temperature above 100 °C to accommodate any thermal gradient. Exact annealing conditions

vary as discussed in the main text (room temperature annealing vs. thermal annealing). Thermal annealing for all samples in this work was accomplished with an Isotemp heated magnetic stir plate (model number 11-100-16sh).

Photovoltaic Device Fabrication: Solar cells used here employed a device structure of Glass / ITO / PEDOT:PSS / "*Perovskite"* / $PC_{61}BM$ / Bis-C_{60} / Ag and were fabricated using procedures similar to those in our previous publications.[16,124] After cleaning the ITO-coated glass substrates, PEDOT:PSS (Baytron PVP Al 4083) films were spin coated (5000 rpm, 30 s) and annealed (150 ^{o}C, 15 min) in ambient atmosphere. All the subsequent layers were processed in a N_2-filled glovebox with relatively low O_2 levels (<10 ppm). Appropriate perovskite layers (choice of precursor solution and processing condition) were fabricated using the corresponding procedure mentioned above. $PC_{61}BM$ (15 mg/mL in chloroform) films were spin coated (4000 rpm, 60 s) and annealed (100 °C, 5 min) on top of perovskite. Subsequently, surfactant Bis-C_{60} (2 mg/mL in IPA) were spin coated at 3000 rpm for 30 s. Silver (Ag) electrodes (150 nm) were deposited by thermal evaporation under a vacuum pressure of 9×10^{-7} Torr with an evaporation rate of 2.0 Å/s; shadow masks were used to define the device area (3.14 mm^2).

Thin film characterization, microscopy, and X-ray diffraction: Thin film absorption measurements were performed using a UV-Vis spectrophotometer (Agilent Cary 5000). Film thicknesses were measured using a stylus profiler (Bruker DektakXT). The thickness of films deposited from 0.6 M, 0.8 M, 1 M and 1.2 M solutions were 80 ± 10 nm, 165 ± 9 nm, 230 ± 10 nm and 320 ± 8 nm respectively. An FEI Sirion scanning electron microscope was used for all SEM based characterization with 5 kV used for imaging and 20 kV used for EDS. A Bruker D8 Discover 2-D XRD with a Cu Kα source was used for all X-ray diffraction measurements. All XRD data that is directly compared in any given figure is integrated from 2D scans with identical

integration parameters to allow quantitative comparison of peak heights and peak height ratios. All XRD peaks were indexed by hand. Lattice parameters were characterized with a minimum of 15 clearly analyzable peaks. The evolutionary algorithm in the Solver package of Excel was used to minimize the sum of residuals squared produced between measured and calculated plane spacings to arrive a lattice parameters providing the best fit for the data assuming a tetragonal Bravais lattice.

I-V Characterization: Standard *I-V* measurements were performed using a SMU (Keithley 2400) with a fixed scan rate (0.01 V step size, 100 ms delay time). For varying scan rate, the step size was unchanged (0.01 V) and the delay time was changed from 10 ms to 1000 ms. Every measurement ensued an uninterrupted sequence of forward and reverse scans (reverse bias (RB) → forward bias (FB) → RB) and the scan range was fixed as -0.2 V to 1 V, unless specifically mentioned. The devices were stored and measured inside a N_2-filled glovebox to avoid any complications from potential degradation issues. For light I-V characteristics, AM 1.5 solar illumination was obtained using a Class A solar simulator (Solar light 16S-300). A NIST-certified Si-photodiode with KG5 filter was used for 1 Sun (100 mW/cm^2) calibration. Stabilized power output was obtained by applying a constant voltage corresponding to the maximum power point and measuring the current response as a function of time. A minimum of 8 devices were used to calculate statistics for solar cell parameters. For consistency, the best device in a given condition was used to determine *Hysteresis Factor (HF)* using a previously reported procedure.[179] Illumination intensity (*G*) dependent measurements were performed using a set of neutral density filters. *I-V* characteristics were measured under seven different intensities ranging between 0.5 mW/cm^2 to 100 mW/cm^2. A slight difference in V_{oc} and J_{sc} dependence on *G* was observed between forward and reverse because of the persistent hysteresis in *I-V* curves. However, the

reported trends (**Figure 3.8-3.9**) are true regardless of scan direction. For consistency and clear interpretation, reverse scan data were used for all the analysis reported in this work, unless specifically mentioned. The linear fits of data had high degree of accuracy, with the R^2 values generally being in the range of 0.96 – 1. The analysis and interpretation of illumination intensity dependent I-V data are in accordance to previously reported solar cell device physics related literature.[56,277,316–324]

Transfer Matrix Optical Modeling: The real (*n*) and imaginary (*k*) part of the refractive index for different layers in device stack were obtained using Spectroscopic Ellipsometry (Woollam-M-2000). Custom-made Matlab program was used to perform transfer matrix optical simulations for obtaining the active layer absorption as a function of thickness. Theoretical J_{sc} corresponding to different active layer thicknesses were calculated using the modelled absorption, assuming 100% internal quantum efficiency (no electrical losses).

Impedance Spectroscopy Characterization:[325–330] Impedance spectroscopy were performed with CHI660e electrochemical workstation at frequency between 10Hz to 1MHz. To simulate recombination-dominant working condition, all devices were characterized under open circuit condition: the devices were illuminated by solar simulator (AM 1.5, 100mW/cm^2) with an applied bias voltage close to internal field. The recombination resistance was calculated from low frequency arc in the Nyquist plots, modeled with parallel circuit comprising recombination resistance and chemical capacitance. The tail observed at larger Z' is characteristic of Warburg diffusion commonly observed in organic-inorganic hybrid perovskites. Rapid decrease of recombination resistance under increasing electric bias (from 0.2 V to 0.7 V) shown in **Figure 3.11d** supports that the dominant frequency response of the devices were from the charge recombination. Furthermore, similar dominant characteristic frequency (Bode plot in **Figure**

3.11c) in combination to evident change in recombination resistance (**Figure 3.9e**) for different thickness of photoactive layers suggest that the chemical capacitance (related to the intrinsic capability of charge storing by hetero-interfaces and density of states (DOS) in active layers) is highly dependent on the Fe inclusion. Fe-induce trap state as well as magnetic-field induced morphological evolution effectively broadened the distribution of DOS and thus trap-assisted recombination pathway prevailed during the device operation.

Photoluminescence Spectroscopy and Modeling: TrPL was taken by using the Libra laser system (50 fs FWHM at 1kHz repetition rate, 1mJ/cm^2, 800 nm fundamental wavelength) combined with collection optics, spectrometer and streak camera (Hamamatsu model C-10627). Streak camera and laser source were synchronized through synchronous delay generator (C-10647) and jitters were regulated by delay unit (C1097-05). The minimum time resolution is around 20 ps. The excitation fluence was modulated by 2 consecutive neutral density filters. The diameter of spot size is 1 mm. The samples for trPL were all encapsulated with glass slides and epoxy.

We assumed band structure were dominated by the invariant metal halide framework in perovskite alloys, in which direct bandgap facilitates radiative bimolecular recombination.

$$\frac{dn}{dt} = -k_1 n - k_2 n^2 \; ; \frac{I(t)}{I_0} = k_2 nN + k_2 n^2$$

where k_1 is total monomolecular decay rate through both non-radiative (k_1^{nr}) and radiative decay (k_1^r) pathway; $k_1 = k_1^{nr} + k_1^r N$. k_2, n and N correspond to the product of initial photocarrier density (n_0) and bimolecular recombination rate ($\overline{k_2}$), normalized carrier density of electron and holes with respect to n_0 and the relative density of the emissive monomolecular recombination center, respectively. n_0 was calculated by Beer-Lambert's law, $n_0 = (I_{ex}\lambda/hc)(1 - e^{-\alpha L})/ L \sim I_{ex}\lambda/Lhc)$, where I_{ex} is fluence at wavelength λ, α is absorption coefficient at λ and L is thickness. The differential equation was numerically solved with parametric optimizations to fit

the decay data. Assuming the dominance of bimolecular recombination in emission at the excitation fluence near the onset of amplified spontaneous emission, the characteristic lifetime (τ) and PL quantum yield (QY) can be acquired as follows, $\tau = \frac{1}{k_1+\overline{k_2}n_0}$; $QY = \frac{\overline{k_2}n_0}{k_1+k_2^0 n_0}$.

Provided that initial carrier densities n_0 are almost identical for all films (complete absorbance) and the non-radiative relaxations are the major decay pathway, relative change of decay rate and QY indicate intrinsic difference of bimolecular recombination, possibly originating from carrier mobility, dielectric environment as well as the change of density of state and band structure.

3.3 Results and Discussion

Use of metal halides as starting materials is key for studying impact of compositional modification because the use of spectator ions like Cl^- and $CH_3CO_2^-$ create complexities like spectator ion based intermediate formation and spectator ion / excess methylammonium volatilization.[60,314,331] We chose pure DMSO as solvent because of its ubiquitous use in perovskite growth and its ability to mutually solvate PbI_2 and transition metal iodides. Aprotic solvents like DMSO tend to encourage solvation of molecular transition metal halide units in a process reminiscent of complex ion formation during PbI_2 solvation[314,332] making DMSO ideal in the solution state, regardless of its potential impact in the solid state. Solutions containing 5 at%, 10 at%, and 25 at% of each foreign element were fabricated, where *at% = moles of transition metal ions / moles of total metal ions*. Because of the ambiguity in exactly what site these transition metals occupy in $CH_3NH_3PbI_3$, we will adopt a new way of writing a formula for these perovskite alloys. We will refer to this class of transition metal perovskite alloy with the formula $AM(T)_yX_3$ where (T) is the transition metal and y is its stoichiometry relative to Pb. **Table 3.1** shows how each composition in at% translates to a $AM(T)_yX_3$. We continue to use an amount of CH_3NH_3I

directly proportional to total moles of metal (i.e. PbI_2 + FeI_2) until we optimize methylammonium iodide stoichiometry directly.

Table 3.1. The corresponding formula for each at% discussed in this chapter, where T is transition metal which in this case is Mn, Fe, Co, and Ni. Stoichiometry of the transition metal (**y**) is rounded to two significant figures.

at% T at% = [mol TI_2 / (mol PbI_2 + mol TI_2)]	Formula $CH_3NH_3Pb(T)_yI_3$	y = $(T)_y$
0%	$CH_3NH_3PbI_3$	y = 0
5%	$CH_3NH_3Pb(T)_{0.053}I_3$	y = 0.053
10%	$CH_3NH_3Pb(T)_{0.1}I_3$	y = 0.1
15%	$CH_3NH_3Pb(T)_{0.18}I_3$	y = 0.18
20%	$CH_3NH_3Pb(T)_{0.25}I_3$	y = 0.25
25%	$CH_3NH_3Pb(T)_{0.33}I_3$	y = 0.33

3.3.1 Role of DMSO in $CH_3NH_3PbI_3$ growth

Perovskite films fabricated *via* the commonly used solvent washing technique right after fabrication, after sitting in the resulting DMSO rich glovebox environment for 15 min, and then again after another round of thermal annealing for 15 min are shown in **Figure 3.2a**. Bleaching observed in **Figure 3.2a** is reversible and due to formation of the CH_3NH_3I-PbI_2-DMSO phase (identified in **Figure 3.2b** via XRD[333,334]). This same phase is evident in drop cast $CH_3NH_3PbI_3$ films annealed at a temperature too low to ensure complete conversion to perovskite (**Figure 3.2c**). We note that this film bleaching is not apparent when toluene is used in sufficient quantities to make it a significant component of the glovebox atmosphere. Thus not only is CH_3NH_3I-PbI_2-DMSO readily thermodynamically accessible from either the solvated or solidified $CH_3NH_3PbI_3$ phase,[335] but also the use of toluene during perovskite growth retards CH_3NH_3I-PbI_2-DMSO regeneration. This is likely achieved both by removing solvent from the system before intermediate formation and slowing recursion of solvent vapor into the film, consistent with the work of Zhou *et al.*[336] who implement solvent-solvent extraction to facilitate large-scale $CH_3NH_3PbI_3$ growth. Film bleaching is impeded in films grown with 10 at% FeI_2 (**Figure 3.2b & d**).

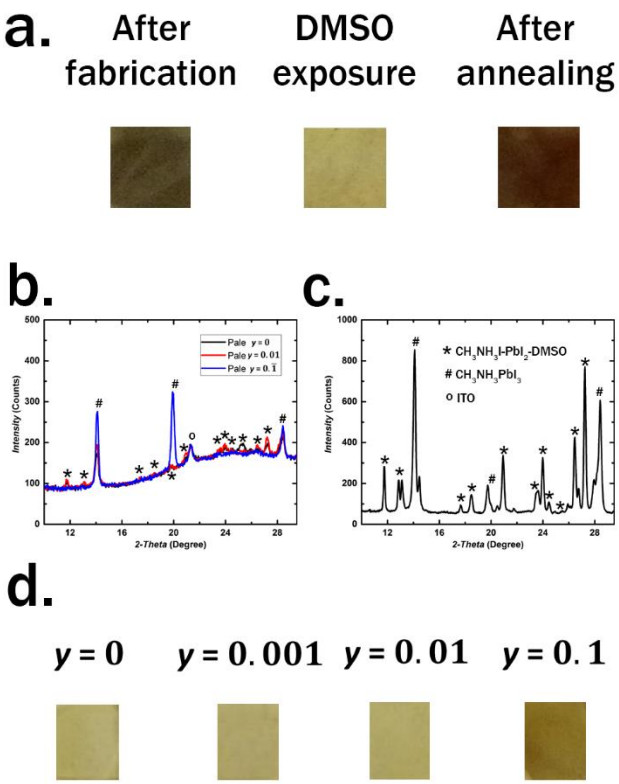

Figure 3.2. (a) Photographs showing a pure Pb, solvent washed film after fabrication, after bleaching by DMSO, and after another round of annealing at 90 C. (b) and (c) compare XRD of thin films that have been exposed to DMSO of varying iron contents with the XRD of a partially transformed drop cast film. ITO, $CH_3NH_3PbI_3$, and CH_3NH_3I-PbI_2-DMSO. (d) shows photographs of films in the bleached state with differing amounts of iron demonstrating that 10 at% Fe films are uniquely robust.

While 10 at% Fe films resist CH_3NH_3I-PbI_2-DMSO reformation (**Figure 3.2d**), back conversion is not forbidden. In **Figure 3.3a-c**, we compare 10 at% Fe films fabricated sequentially with 35 µl each to illustrate how CH_3NH_3I-PbI_2-DMSO formation impacts microstructure. The photograph in **Figure 3.3g** illustrates how this manifests macroscopically. 2D XRD in **Figure 3.3d-f** show (200) reflections disappearing upon back conversion demonstrating clearly that the ingress of even small quantities of DMSO into the highly-ordered lattice formed naturally through direct perovskite nucleation (**Figure 3.3f**) leads to a rapid degradation of short range (**Figure 3.3d-e**) and long range (**Figure S5a-b**) order.

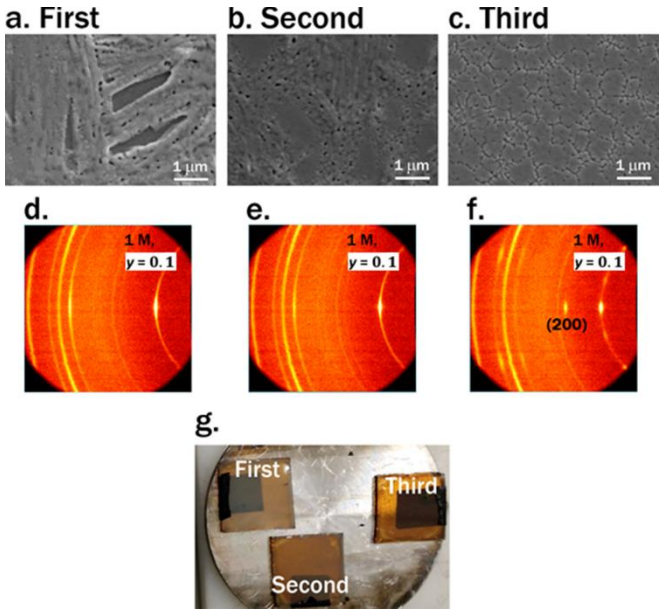

Figure 3.3. Morphological influence due to back conversion under a DMSO atmosphere shown via (a-c) SEM micrographs, (d-f) 2D XRD showing crystal orientation and (g) photographs; First, Second and Third correspond to the order of spin coating with samples being exposed to varying DMSO amounts resulting from subsequent film fabrication.

This shows that other synthetic conditions like atmospheric composition, solution concentration, and annealing profile modify the balance between these competing growth routes (**Figure 3.2-3.4**). Transformation through direct perovskite nucleation in the presence of transition metal is encouraged through low solution concentrations and room temperature annealing (**Figure 3.4**), while DMSO in the atmosphere aggressively encourages CH_3NH_3I-PbI_2-DMSO formation (**Figure 3.3**). Thus, to study how these transition metals impact properties, we used relatively low solution concentrations, room temperature annealing before brief thermal annealing, and control of atmosphere (details in **Section 3.2**).

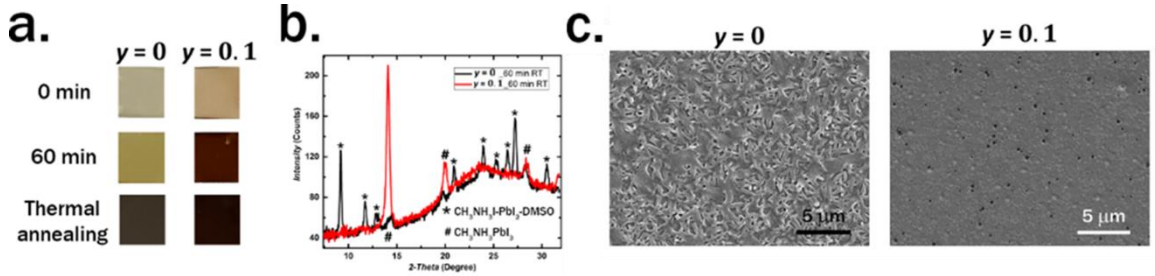

Figure 3.4. Characterization of the two competing transformation pathways *via* (**a**) photographs, (**b**) XRD of films mid transformation (60 min of room temperature annealing), and (**c**) SEM images of final film morphologies. Films were made from 1 M solutions.

3.3.2 Morphological Aspects of Transition Metal Inclusion Influencing Diode Behavior

Impact of CH_3NH_3I Stoichiometry: While our growth optimization enabled $CH_3NH_3Pb(Fe)_{0.1}I_3$ films on PEDOT:PSS for photovoltaic study, these films exhibited unstable, poorly defined diode *I-V* curves before stoichiometric optimization of CH_3NH_3I (**Figure 3.5a**). While otherwise dark and reflective, under the solar simulator these films appeared bright white **(Figure 3.6a)**. This suggested the existence of a physical inhomogeneity within the bulk of the film acting as a scattering centre. If transition metals are indeed becoming incorporated through competing mechanisms, then there is likely a slight excess of methylammonium and iodide. In the kinetic extreme of spin coating, this excess may create disorder at a scale too small to readily be characterized by XRD or SEM.[337,338] To account for this issue, we tuned $CH_3NH_3^+$ and I^- stoichiometry by reducing the CH_3NH_3I in precursor solutions (*x* CH_3NH_3I:0.9 PbI_2:0.1 FeI_2, where *x* = relative moles of CH_3NH_3I).

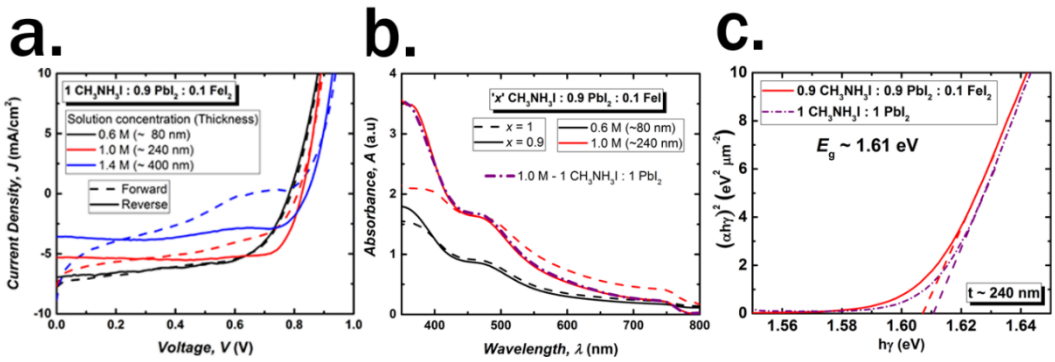

Figure 3.5. (a) Unstable and poorly defined *I-V* characteristics for devices made with stoichiometric (1:1 ratio between CH_3NH_3I and metal halides) precursor composition. (b) Absorbance of $CH_3NH_3Pb(Fe)_{0.1}I_3$ perovskite films with varied CH_3NH_3I stoichiometry vs. pure $CH_3NH_3PbI_3$ fabricated by standard solvent washing with toluene. (c) Tauc plot showing the band gap of optimized $CH_3NH_3Pb(Fe)_{0.1}I_3$ films.

CH_3NH_3I reduction[338] resulted in elimination of internal scattering under solar simulator light (**Figure 3.6a**) and more defined absorption features (**Figure 3.5b**).[208,339] In contrast to most compositional modifications of $CH_3NH_3PbI_3$, band-gap is unchanged by Fe inclusion (**Figure 3.5c**) and absorption features are identical to pure Pb, solvent washed films. PV devices made with varied CH_3NH_3I stoichiometry (*x* = 0.8, 0.9, 1) show that *x* = 0.8 and 0.9 devices have more well-

defined diode curves (**Figure 3.6b**). The overall stoichiometry represented by $x = 0.9$ equates to an exact stoichiometry of $CH_3NH_3Pb(Fe)_{0.1}I_3$. This formula is now exact with regard to the stoichiometry of all species in the precursor solution.

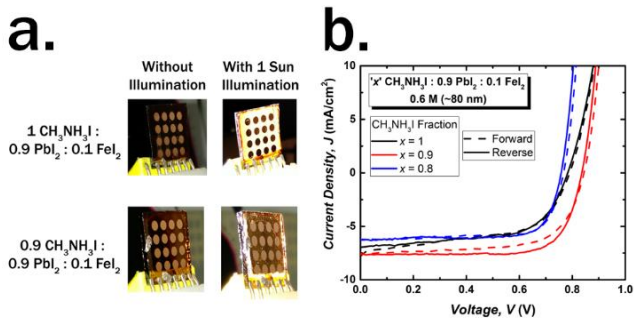

Figure 3.6. (a) Photographs showing the otherwise hidden difference between films made from solutions with differing CH_3NH_3I stoichiometry revealed by the intense light of the solar simulator. (b) *I-V* characteristics of $CH_3NH_3Pb(Fe)_{0.1}I_3$ solar cell devices with varying fractions of CH_3NH_3I. All devices show significant hysteresis between forward (short circuit (SC)→open circuit (OC)) and reverse (OC→SC) scans.

Impact of Magnetic Field: Beyond composition, we began to suspect that the magnetic stir-bar in our hot plate affects film formation. To explore this, $CH_3NH_3Pb(Fe)_{0.1}I_3$ films were grown under magnetic fields of different strengths (**Figure 3.7a**). Magnetic field encourages high quality film growth with larger grains and better coverage (**Figure 3.7b**), but linear and highly oriented features appear. These features are indicative of magnetostriction induced twinning, a tendency common in oxide perovskites and often occurs in material systems with a high to low symmetry phase transformation.[340,341]

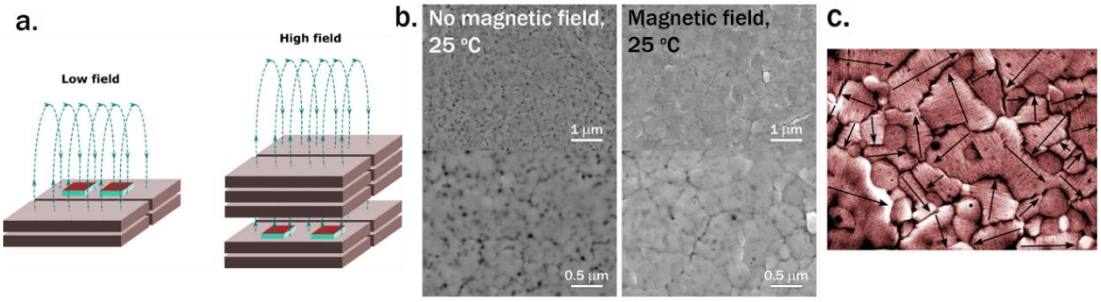

Figure 3.7. a) Schematic illustrations of how perovskite growth under external magnetic field was accomplished. Grey boxes represent individual ferrite block magnets. Red films represent how substrates are arranged in the field. Blue lines illustrate the orientation of the magnetic field with arrows signifying the direction. The space between magnet stacks in the high field case was created with stacked glass spacers that are not shown. b) SEM images comparing growth of $CH_3NH_3Pb(Fe)_{0.1}I_3$ films both without and with a magnetic field at room temperature. c) Direct replication of SEM data in Figure 3.7b (with magnetic field) with increased contrast to show the twin like features. Vectors are superimposed perpendicular to periodic, linear morphological features to aid the eye in identifying them.

Recently, twinning has been observed as an important intrinsic part of $CH_3NH_3PbI_3$ functionality regardless of compositional modification.[342] Previously, highly oriented, periodic grain boundaries have been identified in pure $CH_3NH_3PbI_3$[343] as an existent but minor contributor to overall grain structure. However, in this alloyed material grown under a magnetic field this feature is ubiquitously present. These features have a significant impact on optoelectronic quality (**Figure 3.8**) and the presence of external magnetic fields presents an important diminishing return. Herein we minimize their deleterious impact on morphology by shutting off magnetic stirring during annealing.

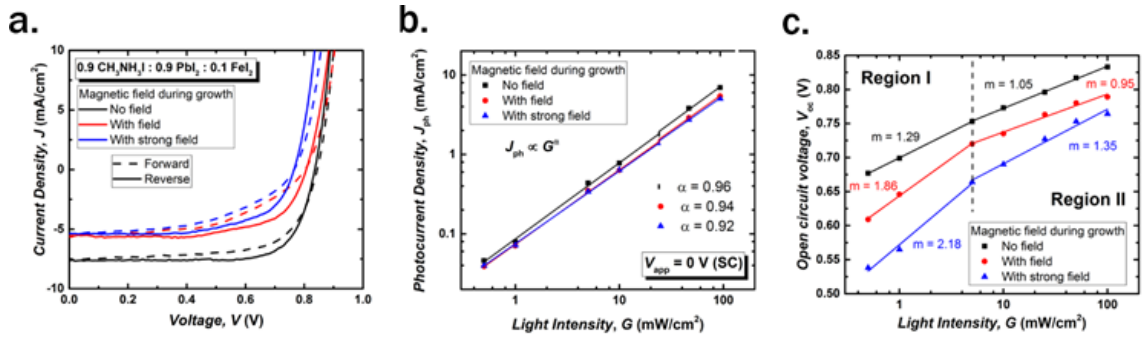

Figure 3.8. Influence of magnetic field during growth of $CH_3NH_3Pb(Fe)_{0.1}I_3$ films shown via (a) *I-V* characteristics of solar cells devices; light intensity dependence of (b) photocurrent density at short circuit condition (V_{app} = 0 V) and (c) open circuit voltage. The light intensity dependence of J_{ph} and V_{oc} clearly illustrates an increased trap-assisted recombination with increased field strength during growth.

3.3.3 Compositional Impact of Transition Metal Inclusion on Hysteresis Behavior

Through our deep morphological study and device optimization we systematically eliminated the impact of nonidealities on material performance including the poor film quality caused by CH_3NH_3I-PbI_2-DMSO formation (**Figure 3.3**), the disorder induced by excess methylammonium iodide (**Figure 3.5-3.6**), and the morphological impact of magnetic field (**Figure 3.8**). Before expanding our investigation to all species in this study (Fe, Mn, Co, and Ni), we first closely analyze the impact of transition metal incorporation on recombination using Fe perovskite alloys as a model system.

Impact of Fe inclusion: $CH_3NH_3Pb(Fe)_{0.1}I_3$ films preserve optical properties of $CH_3NH_3PbI_3$ (**Figure 3.5b-c**). While band-gap remains unchanged, these transition metals invariably introduce valence d-orbitals that may alter recombination kinetics despite the preservation of optical properties.[344,345] The absorption of $CH_3NH_3Pb(Fe)_{0.1}I_3$ films scale with perovskite thickness as expected (**Figure 3.9a**), but performance does not (**Figure 3.9b**).

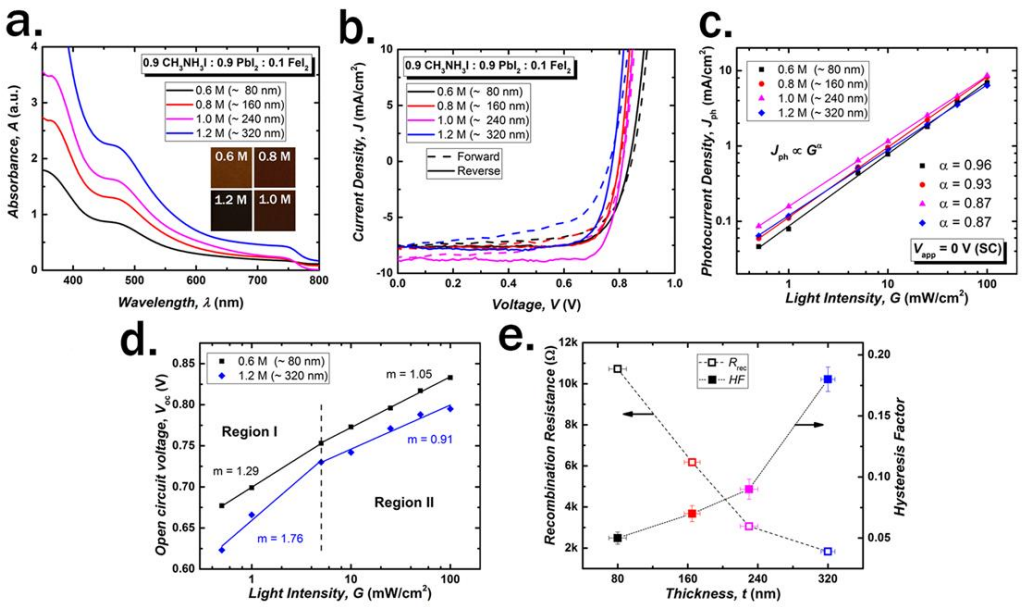

Figure 3.9. Optoelectronic characterization of $CH_3NH_3Pb(Fe)_{0.1}I_3$ films with varying thickness *via* (a) UV-vis absorption spectra (photographs inset) and (b) *I-V* characteristics of solar cell devices. (c)-(e) Recombination analysis for different thicknesses of $CH_3NH_3Pb(Fe)_{0.1}I_3$ films *via* light intensity dependence of (c) photocurrent density at short circuit condition (V_{app} = 0 V) and (d) open circuit voltage; (e) variation of recombination resistance and hysteresis factor with thickness.

Specifically, J_{sc} does not proportionately scale with absorption (**Figure 3.10a**) and V_{oc} decreases with increasing thickness which parallels *FF* trends (**Table 3.2**). The ideality factor (η) of 1.6 – 1.8, calculated with dark *I-V* characteristics (**Figure 3.10b**), indicates dominant monomolecular recombination.[44] Comparable series and shunt resistances among these devices (**Figure 3.9b**) implicates this recombination as the cause of *FF* trends with thickness.

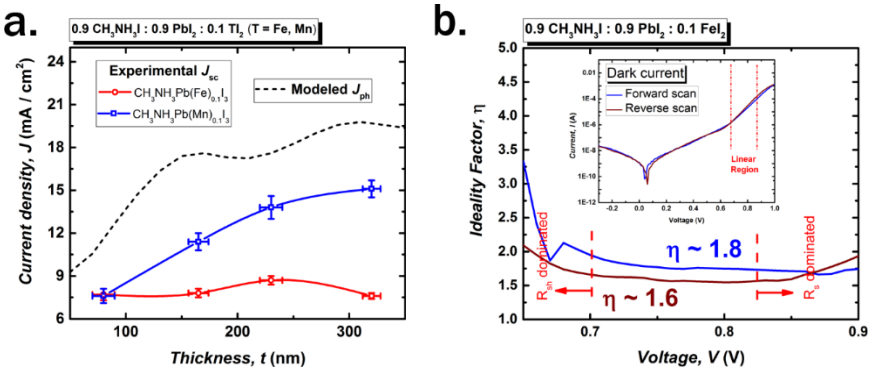

Figure 3.10. (a) Comparison of experimental short circuit current density for different film thickness to the theoretical maximum predicted from absorption profile obtained by transfer matrix modeling. We show both the J_{sc} exhibited by Fe and the later discussed Mn devices to underscore the comparison that is touched on in the analysis of all alloy systems addressed in the last part of this chapter. (b) Dark ideality factor for solar cell devices with $CH_3NH_3Pb(Fe)_{0.1}I_3$ films.

Light intensity (G) dependent I-V measurements (**Figure 3.9c-d**) were performed to identify the nature, extent, and origin of this monomolecular recombination. Low exciton binding energies[56] eliminate geminate recombination. Accordingly, slight variation in photocurrent (J_{ph}) with voltage can be linked to ineffective charge transport resulting from trap-assisted recombination. At SC, $J_{ph} \propto G^{\alpha}$ where α is related to extent of recombination. The degree of sub-linearity in $J_{ph}(G)$ is thus an indication of the extent of recombination losses. This metric (α) decreases with increasing thickness (**Figure 3.9c**) pointing towards recombination centres/trap sites within the perovskite bulk explaining the J_{sc} trend (**Figure 3.10a**). To verify the origin of recombination, we investigated V_{oc} dependence on G to determine light ideality factor (m)[323] using $\partial Voc/\partial \log G = (mk_BT)/(2.303q)$. V_{oc} vs. G plots (**Figure 3.9d**) showed different slopes at low and high light intensities, a trend characteristic of intensity dependent recombination.[316] A transition region around 5 mW/cm^2 (0.05 Sun) defines a boundary between trap-dominated recombination at low G (higher slopes) and bimolecular recombination at high G (lower slopes). At low light intensities, thinner films have low slopes (m = 1.29) compared to thicker films (m = 1.76), but at higher light intensities slopes become comparable (m ~ 1). This trend is consistent with trap-assisted recombination within the perovskite bulk and likely results from trap filling at increased light

intensities. Slight differences between dark and light ideality factors (*n* and *m*) are due to inherent differences between recombination resistance in the dark and under illumination.[322,323]

Table 3.2. Solar cell device performance metrics for different film thickness of $CH_3NH_3Pb(Fe)_{0.1}I_3$ with optimized precursor stoichiometry.

Thickness (Concentration)	Scan Direction	V_{oc} (V)	J_{sc} (mA/cm^2)	FF (%)	PCE (%)		Hysteresis Factor
					Average	Highest	
80 ± 10 nm (0.6 M)	**Forward**	**0.84 ± 0.01**	**7.7 ± 0.4**	**66 ± 1**	**4.28 ± 0.22**	**4.69**	**0.05**
	Reverse	**0.83 ± 0.01**	**7.7 ± 0.4**	**77 ± 1**	**4.88 ± 0.24**	**5.30**	
165 ± 9 nm (0.8 M)	Forward	0.80 ± 0.01	7.8 ± 0.3	69 ± 2	4.25 ± 0.21	4.66	0.07
	Reverse	0.80 ± 0.01	7.8 ± 0.3	80 ± 1	4.96 ± 0.21	5.36	
230 ± 10 nm (1 M)	Forward	0.80 ± 0.01	8.5 ± 0.4	65 ± 2	4.47 ± 0.27	4.70	0.09
	Reverse	0.81 ± 0.01	8.7 ± 0.3	79 ± 3	5.45 ± 0.40	5.94	
320 ± 8 nm (1.2 M)	Forward	0.76 ± 0.01	7.6 ± 0.1	54 ± 4	3.11 ± 0.25	3.33	0.18
	Reverse	0.77 ± 0.01	7.6 ± 0.2	78 ± 1	4.58 ± 0.07	4.69	

These findings were further confirmed by impedance spectroscopy (**Figure 3.11**). Nyquist plots of all devices irrespective of perovskite thickness (**Figure 3.11a**) have only one arc, indicative of a single dominant recombination mechanism. Zoomed in regions of Nyquist plots at low *Z*' (high frequency region) confirm the absence of significant interfacial resistance (**Figure 3.11b**).[323,346] The small shift at low *Z*' can be attributed to series resistance and it does not vary with thickness as pointed out above. Characteristic frequencies in Bode plots (**Figure 3.11c**) are around 10^5 to 10^6 Hz corresponding to a time constant of several μs, indicative of recombination within perovskite under the given experimental conditions.[86,347] The decrease in Nyquist plot arc diameter points to a decrease in recombination resistance, R_{rec}, with increasing V_{app} (**Figure 3.11d**) which further corroborates the recombination limited resistance in these devices. It can be clearly observed that R_{rec} (calculated from Nyquist plots) decreases with increasing film thickness (**Figure 3.9e**). These results agree excellently with the trap assisted recombination and consequent depressed performance identified through *I-V* analysis.

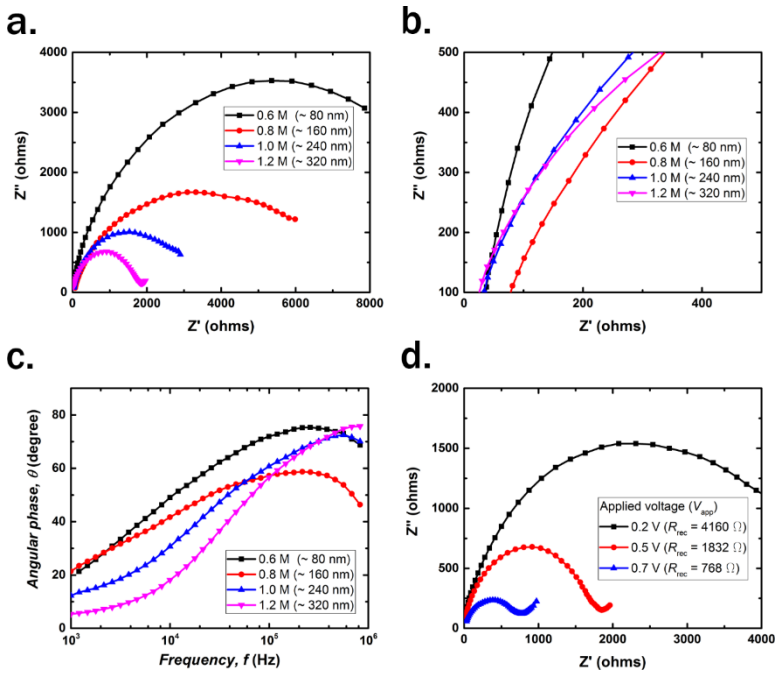

Figure 3.11. Impedance analysis of solar cell device with different thickness of $CH_3NH_3Pb(Fe)_{0.1}I_3$ films. (a) Nyquist plot, (b) zoomed in region of Nyquist plots in the high frequency region showing the absence of interfacial resistance, (c) Bode plots indicating single characteristic time constant and (d) Nyquist plots at different applied voltages implying recombination limited resistance in devices.

Overall, the above analysis shows that Fe inclusion leads to increased monomolecular recombination *via* trap states created within the perovskite bulk. The consistent hysteresis in this material system (**Figure 3.9b**) is intimately related to transition metal inclusion as hysteresis is not observed in unalloyed $CH_3NH_3PbI_3$ solar cells with PEDOT:PSS and $PC_{61}BM$ interlayers regardless of processing.[45–51] Hysteresis in perovskite solar cells is a combined effect of trap sites and ion motion.[2,50,52,53] To quantify and compare hysteresis among devices,[54] we define *Hysteresis Factor (HF)* as $HF = \left|1 - \frac{A_{\text{Forward}}}{A_{\text{Reverse}}}\right|$ where A_{Forward} and A_{Reverse} are areas under *SC→OC* and *OC→SC* scans respectively. Larger HF was observed for thicker active layers (**Table 3.2** and **Figure 3.9e**), which correlates with trends in trap assisted recombination (**Figure 3.9c-d** and **3.11**) and recombination resistance (**Figure 3.9e**). This indicates that with these alloys in this device architecture, contributions from traps most strongly determine the extent of I-V hysteresis.

Generalizing insight to characterize impact of transition metal electronic structure: While the case study of Fe provides some insight into how these transition metals optoelectronically impact perovskite, it does not probe the potential of this class of hybrid perovskite alloy. If defect states induced by the d-orbital of the transition metal are indeed leading to some of the troublesome recombination behaviour in Fe based alloys, it is possible that the differing energetics and occupancy of d-orbitals belonging to the other transition metals[348] in this study may alter these limitations. Each of the four transition metals studied (Fe, Mn, Co, and Ni) modify growth route in essentially the same manner.[19] This combined with our insight into the importance of stoichiometry (**Figure 3.5**) and the impact of environmental conditions in affecting transformation route (**Figure 3.2-3.3**) allow us to compare the compositional impacts of Fe, Mn, Co, and Ni with minimal convolution from morphological differences. This is evidenced by the consistent morphology and absorption profiles of $CH_3NH_3Pb(Mn)_{0.1}I_3$, $CH_3NH_3Pb(Fe)_{0.1}I_3$, $CH_3NH_3Pb(Co)_{0.1}I_3$, $CH_3NH_3Pb(Ni)_{0.1}I_3$ thin films made *via* optimized growth conditions and stoichiometry identified above (**Figure 3.12**). Band gaps are comparable to that of $CH_3NH_3PbI_3$ (**Figure 3.12b** and **3.5b-c**).[21,22]

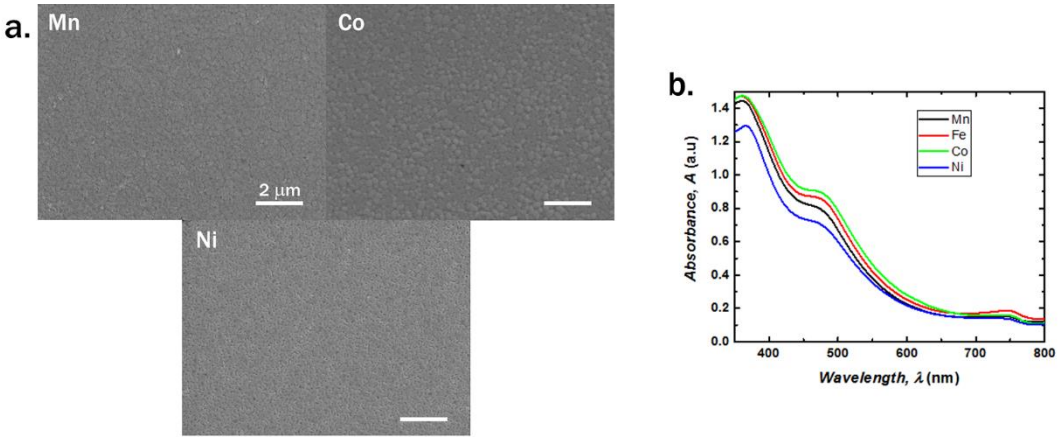

Figure 3.12. (a) SEM of $CH_3NH_3Pb(T)_{0.1}I_3$ films made with 0.6 M solutions, where T = Mn, Co, and Ni. (b) UV-Vis absorption of $CH_3NH_3Pb(T)_{0.1}I_3$ films.

Solar cell devices based on each different perovskite alloy display distinct characteristics in terms of device performance and *I-V* hysteresis (**Table 3.3** and **Figure 3.13a**). The $CH_3NH_3Pb(Ni)_{0.1}I_3$ devices show the worst performance and highest *HF*, with steadily increasing performance and decreasing *HF* as we work backwards through the periodic table from Ni → Co → Mn (**Table 3.3**). The difference in performance between Fe and Mn based devices is slight, but hysteresis that is ubiquitously present in $CH_3NH_3Pb(Fe)_{0.1}I_3$ devices (**Figure 3.9** and **Table 3.2**) is negligible in $CH_3NH_3Pb(Mn)_{0.1}I_3$ devices (**Figure 3.13a** and **Table 3.3**).

Table 3.3. Performance metrics for $CH_3NH_3Pb(T)_{0.1}I_3$ based solar cell devices, where T = Fe, Mn, Co, Ni corresponds to the transition metal incorporated.

T	Scan Direction	V_{oc} (V)	J_{sc} (mA/cm^2)	FF (%)	PCE (%)		Hysteresis Factor
					Average	Highest	
Fe	Forward	0.84 ± 0.01	7.7 ± 0.4	66 ± 1	4.28 ± 0.22	4.69	0.05
	Reverse	0.83 ± 0.01	7.7 ± 0.4	77 ± 1	4.88 ± 0.24	5.30	
Mn	**Forward**	**0.83 ± 0.01**	**7.8 ± 0.5**	**76 ± 2**	**4.95 ± 0.32**	**5.30**	**0.01**
	Reverse	**0.83 ± 0.01**	**7.4 ± 0.5**	**80 ± 2**	**5.08 ± 0.34**	**5.50**	
Co	Forward	0.77 ± 0.04	6.3 ± 0.4	57 ± 4	2.74 ± 0.34	3.02	0.07
	Reverse	0.78 ± 0.04	6.4 ± 0.4	58 ± 4	2.91 ± 0.42	3.28	
Ni	Forward	0.62 ± 0.01	2.9 ± 0.3	49 ± 1	0.89 ± 0.05	0.94	0.10
	Reverse	0.66 ± 0.01	2.9 ± 0.2	50 ± 1	0.98 ± 0.07	1.04	

To establish if this indicates that $CH_3NH_3Pb(Mn)_{0.1}I_3$ minimizes the severity of recombination caused by transition metal inclusion, we fabricated a series of devices with increasing perovskite thickness in the same fashion as in **Figure 3.9b**. In contrast to the case of $CH_3NH_3Pb(Fe)_{0.1}I_3$ (**Figure 3.9b**), the $CH_3NH_3Pb(Mn)_{0.1}I_3$ devices showed minimal increase in hysteresis with increasing thickness (**Figure 3.13b**). When looking at the data in **Figure 3.3b**, it is important to note that Mn slightly less aggressively alters perovskite transformation compared to Fe.[19] The increased tendency to transform through CH_3NH_3I-PbI_2-DMSO with increasing solution concentration becomes uniquely problematic in $CH_3NH_3Pb(Mn)_{0.1}I_3$ films deposited from

solutions above 0.8 M.[19] Morphological problems are likely the dominant cause of suppressed performance for devices with $CH_3NH_3Pb(Mn)_{0.1}I_3$ films made from 1 and 1.2 M solutions.

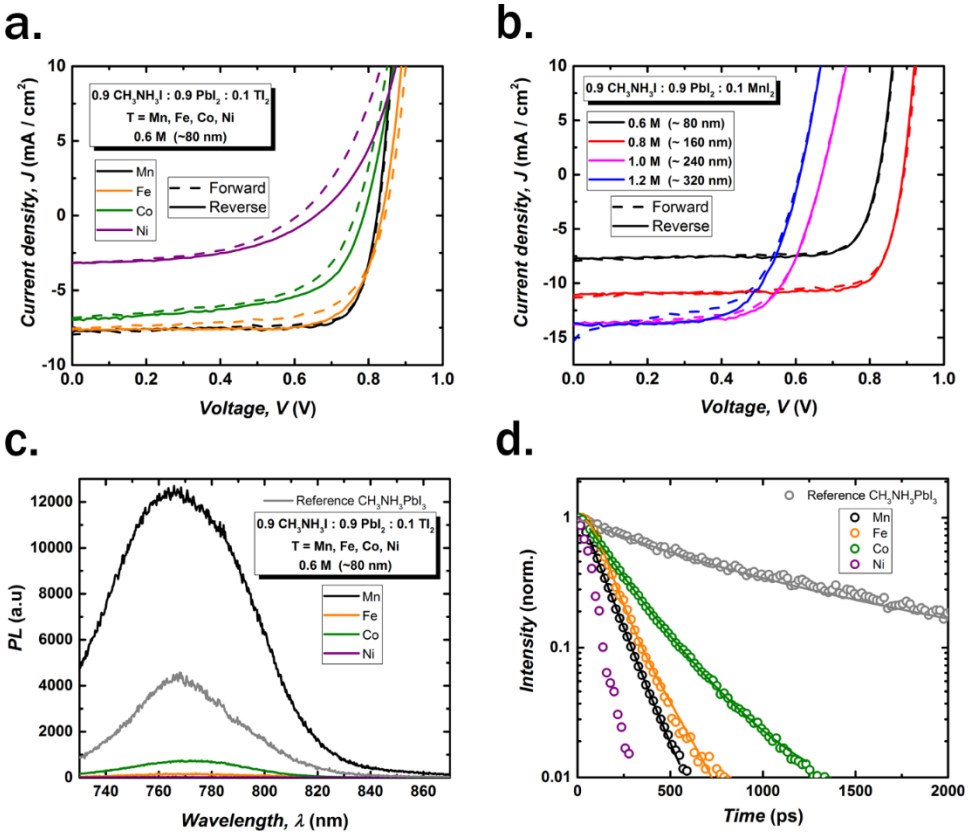

Figure 3.13. (a) *I–V* characteristics of $CH_3NH_3Pb(T)_{0.1}I_3$ solar cell devices demonstrating the influence of different transition metal inclusion (T = Mn, Fe, Co, Ni) on photovoltaic performance and hysteresis. (b) *I-V* characteristics of solar cell devices with varying film thickness of $CH_3NH_3Pb(Mn)_{0.1}I_3$; a less dramatic increase in hysteresis with thickness is observed in sharp contrast to the $CH_3NH_3Pb(Fe)_{0.1}I_3$ case discussed earlier. (c) Emission of $CH_3NH_3Pb(T)_{0.1}I_3$ alloys under 1μJ/cm^2 365 nm excitation; all spectra were corrected with respect to excitation pulse to accommodate the luminescent quantum yield. (d) Transient photoluminescence dynamics of $CH_3NH_3Pb(T)_{0.1}I_3$ alloys; the data for a ~200 nm thick $CH_3NH_3PbI_3$ film prepared by solvent washing was included for reference.

In the case of $CH_3NH_3Pb(Fe)_{0.1}I_3$, increasing perovskite thickness does not increase J_{sc} despite the observation that absorption scales appropriately with thickness (**Figure 3.9a-b**). Despite the complication with growth in thick $CH_3NH_3Pb(Mn)_{0.1}I_3$ films, the series of Mn based devices show that J_{sc} is not sharply limited as in $CH_3NH_3Pb(Fe)_{0.1}I_3$ analogues (**Figure 3.10a**). V_{oc} also increases with thickness for $CH_3NH_3Pb(Mn)_{0.1}I_3$ devices (until problems with growth set in at 1 M) compared to the monotonic decrease observed in $CH_3NH_3Pb(Fe)_{0.1}I_3$ devices (**Table 3.2** and **3.4**).

Table 3.4. Solar cell device performance metrics for different film thickness of $CH_3NH_3Pb(Mn)_{0.1}I_3$ with optimized precursor stoichiometry.

Thickness (Concentration)	Scan Direction	V_{oc} (V)	J_{sc} (mA/cm^2)	FF (%)	PCE (%)	
					Average	Highest
~ 80 nm (0.6 M)	Forward	0.83 ± 0.01	7.8 ± 0.5	76 ± 2	4.95 ± 0.32	5.30
	Reverse	0.83 ± 0.01	7.4 ± 0.5	80 ± 2	5.08 ± 0.34	5.50
~ 160 nm (0.8 M)	**Forward**	**0.87 ± 0.02**	**11.5 ± 0.6**	**76 ± 1**	**7.61 ± 0.32**	**8.54**
	Reverse	**0.87 ± 0.02**	**11.3 ± 0.6**	**80 ± 1**	**7.88 ± 0.34**	**8.79**
~ 240 nm (1 M)	Forward	0.62 ± 0.04	13.7 ± 0.7	66 ± 1	5.63 ± 0.39	6.02
	Reverse	0.63 ± 0.03	13.8 ± 0.8	69 ± 2	5.94 ± 0.32	6.20
~ 320 nm (1.2 M)	Forward	0.56 ± 0.05	15.8 ± 0.5	55 ± 1	4.85 ± 0.29	5.14
	Reverse	0.56 ± 0.05	14.4 ± 0.7	64 ± 1	5.20 ± 0.29	5.49

Thus, the $CH_3NH_3Pb(Mn)_{0.1}I_3$ device made with a ~160 nm perovskite film (0.8 M solution) yielded the highest power conversion efficiency (PCE) in this study (**Figure 3.14a** and **Table 3.4**). **Figure S3.14b** shows scan rate dependent *I-V* characteristics for a typical $CH_3NH_3Pb(Mn)_{0.1}I_3$ device made with a ~160 nm active layer demonstrating minimization of hysteresis in this alloy.

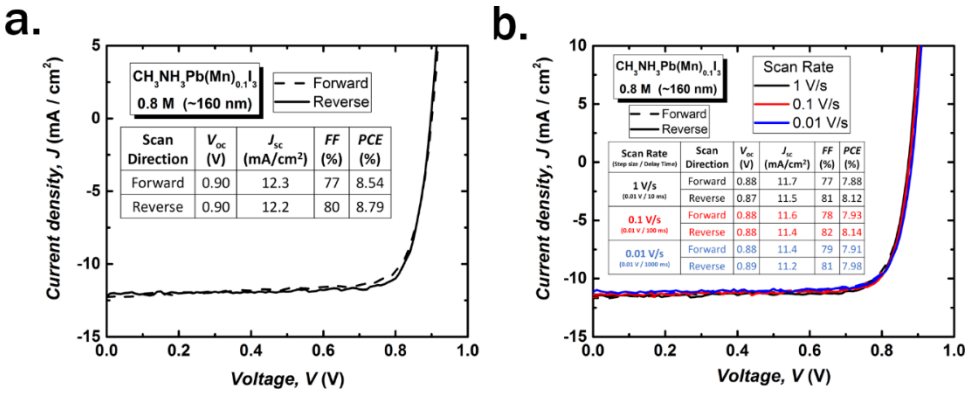

Figure 3.14. (a) *I-V* characteristics of the best device in this study utilizing a ~160 nm $CH_3NH_3Pb(Mn)_{0.1}I_3$ as photoactive layer and (b) Scan rate (0.01 – 1 V/s) dependent *I-V* characteristics for a typical ~160 nm $CH_3NH_3Pb(Mn)_{0.1}I_3$ based solar cell device. Devices show consistently negligible hysteresis and the corresponding solar cell performance metrics are provided in figure insets.

Dramatic reduction of hysteresis and elimination of the strict limit on J_{sc} and V_{oc} with thickness suggest that Mn minimizes the impact of deleterious trap-assisted recombination inherent to transition metal inclusion in $CH_3NH_3PbI_3$. To refine material insight that can be drawn from this

trend in performance, we used time resolved photoluminescence (trPL) spectroscopy to compare $CH_3NH_3Pb(T)_{0.1}I_3$ films (details in SI). **Figure 3.13c** and **3.13d** compare emission spectra and radiative decay kinetics for each alloy under 365 nm excitation with 1 μJ/cm^2 fluence. This excitation condition corresponds to a charge carrier density in the range of 10^{17} cm^{-3}, which is close to the onset of amplified spontaneous emission. Although Mn minimizes the deleterious impact of transition metal inclusion, emission did not persist the longest in this system. Rather, the dominance of fast radiative decay over non-radiative loss in this system led to a relatively short lifetime but a significant increase in quantum yield compared to all other alloyed systems, as well as pure $CH_3NH_3PbI_3$. On the other hand, despite showing lower performance and larger *HF* than both Mn and Fe based alloys, $CH_3NH_3Pb(Co)_{0.1}I_3$ clearly showed the longest carrier lifetime within this class of perovskite alloy (**Table 3.5**).

Table 3.5. PL metrics extracted from parametric optimization. Initial values for the fitting were given in ratio according to the measured QY values.

Formula $CH_3NH_3Pb(T)_{0.1}I_3$	n_0 (10^{17} cm^3)	k_1 (10^9 s^{-1})	k_2/n_0 (10^{-9} cm^3 s^{-1})	τ (ps)	*%QY (calc.)*	*%QY (meas.)*
$CH_3NH_3PbI_3$ (Ref)	3.0	0.942	0.038	314.7	1.195	< 0.50
$CH_3NH_3Pb(Co)_{0.1}I_3$	2.1	2.477	0.030	84.8	0.302	*0.062*[2)]
$CH_3NH_3Pb(Fe)_{0.1}I_3$	2.1	3.160	0.020	66.5	0.132	*0.015*[2)]
$CH_3NH_3Pb(Mn)_{0.1}I_3$	3.0	3.783	0.620	75.6	4.686	1.8
$CH_3NH_3Pb(Ni)_{0.1}I_3$[1)]	3.2	*N.A.*	*N.A.*	*N.A.*	*N.A.*	*0.004*[2)]

[1)] Decay was close to instrumental response (~20 ps); [2)] Values were below the resolution limit of the instrument and estimated by scaling PL spectra with measurable samples.

Two primary things distinguish the optoelectronic behaviour of $CH_3NH_3Pb(Mn)_{0.1}I_3$. Firstly, $CH_3NH_3Pb(Mn)_{0.1}I_3$ is much more emissive than all other materials in this class of perovskite alloy. Secondly, together with peculiar luminescence efficiency, the relatively short lifetime of $CH_3NH_3Pb(Mn)_{0.1}I_3$ strongly implies an abnormally high radiative bimolecular recombination rate rather than the fast loss of charge carrier density mediated by defective traps, in stark contrast to other alloys studied.

The inclusion of transition metals leads to fundamental alterations in recombination processes originating from modification of band structure, creation of trap sites, and/or modification of trap site populations and distributions.[349,350] Klug et al.[348] have found that transition metals can alter band positions despite invariance of band gap. Their modelling of these alloys indicated that the energy of states generated by transition metals are dependent on what metal is used,[348] possibly to the extent of moving trap states near or within bands. As we have shown, the impact that these transition metals have on perovskite growth, crystallinity, and morphology is comparable. Counterintuitive distinctions between $CH_3NH_3Pb(Mn)_{0.1}I_3$ and $CH_3NH_3Pb(Co)_{0.1}I_3$ may point to complex modifications to band structure through states Mn and Co create. Regardless, minimization of the deleterious impact of trap-assisted recombination and markedly improved quantum yield offered by $CH_3NH_3Pb(Mn)_{0.1}I_3$ make this system ideal for tuning material growth and properties for optoelectronic applications.

3.4 Conclusion

Study of a new class of hybrid organic-inorganic perovskite alloy was enabled through a deep morphological investigation revealing growth route to be the most significant variable controlling morphological evolution. Although DMSO is ideal in the solution state, we found that it causes CH_3NH_3I-PbI_2-DMSO formation which leads to the rod-like thin film morphology that a great deal of work in the perovskite field endeavors to circumvent *via* creative processing techniques like 2-step deposition and solvent washing. We found that transition metal inclusion allows direct perovskite nucleation to strongly compete with CH_3NH_3I-PbI_2-DMSO formation. Although we found that solution concentration, atmospheric composition, and annealing profile all impact the route through which transformation proceeds, CH_3NH_3I stoichiometry and magnetic

field have unique optoelectronic consequences that should be considered when studying this class of perovskite alloy.

This extensive analysis of growth allowed us to minimize convolution from morphological issues and directly analyse the compositional impact of transition metal inclusion on optoelectronic properties of $CH_3NH_3PbI_3$. With Fe based alloys as a model system, we closely studied recombination behaviour and its impact on photovoltaic performance and *J-V* hysteresis. Although this revealed that trap-assisted recombination induced by transition metal inclusion is problematic, extending this functional analysis to the other transition metals discussed revealed that Mn mitigates the impact of trap-assisted recombination inherent to this class of transition metal perovskite alloy and significantly enhances photoluminescence quantum yield. In addition to this functional analysis, this study also gives insight into other currently relevant aspects of perovskite design including the magnetic properties these transition metals impart,[351] the origin of complex *J-V* hysteresis,[81,352] the impact of morphological phenomena like CH_3NH_3I induced disorder[337,338,352] and field induced twinning,[342] and the roles of transformation route[314,331] and solvent induced intermediates[335] in determining morphology. Methodology and insights developed herein provide a general approach for navigating the complexity of perovskite compositional modification.

PART B: DEVELOPMENT OF PEROVSKITE TANDEM SOLAR CELLS

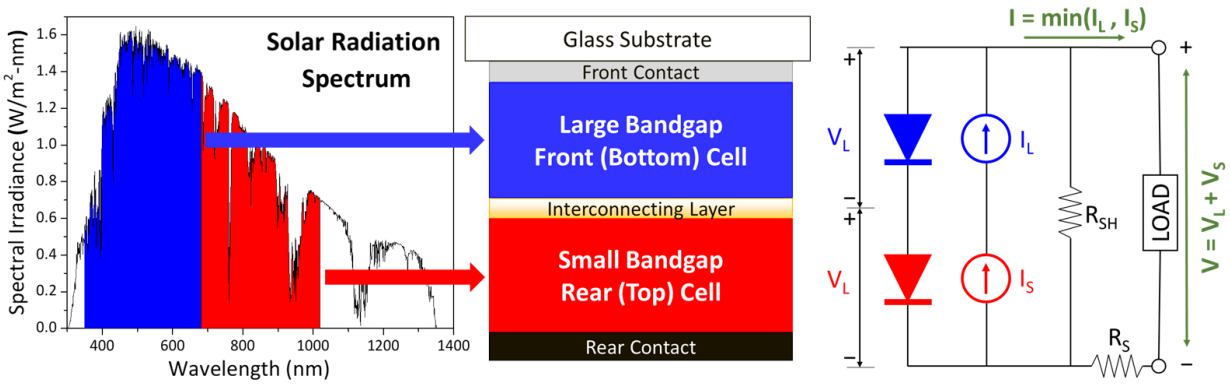

Schematic illustration of light harvesting in a perovskite-perovskite tandem solar cell along with its equivalent circuit; large bandgap front (bottom) cell absorbs the high energy photons and small bandgap rear (top) cell absorbs the low energy photons.

Chapter 4. ALLEVIATING PHOTOINDUCED PHASE SEGREGATION IN LARGE BANDGAP PEROVSKITE SOLAR CELLS BY TIN SUBSTITUTION

4.1 Introduction

Power conversion efficiency (PCE) of photovoltaics (PVs) is one of the most dominant factors determining the price per watt for solar energy generation and potential commercialization.[15] This has led to the rise and development of several competing PV technologies, with the demonstration of record efficiencies approaching that of the Shockley-Queisser limit for single junction solar cells. To date, crystalline-Si solar cells (record PCEs of 25.0%) are the most widespread PV technology that has been commercialized economically at scale.[353] Construction of multi-junction (tandem) solar cells is an effective approach to improve PCE beyond the limits of single junction devices.[254,353–355] Theoretically, PCEs greater than 30% can be achieved if a silicon solar cell is combined with a large bandgap front cell in a tandem structure.[254,353–355]

The key challenge in realizing this goal is to find a suitable large band-gap (1.7-1.8 eV) photovoltaic material that can be coupled with silicon without significantly raising the manufacturing cost. Hybrid organic-inorganic halide perovskites are excellent candidates as they represent a unique class of material that possess exceptional photovoltaic properties, facile solution processability, and tunable bandgaps.[254,353,356–361] A combination of such well-established silicon solar cells with rising perovskite solar cells (PVKSCs) is vital in the roadmap for development of transformative PV technologies.

Methylammonium lead iodide ($MAPbI_3$) which has a bandgap of ~1.58 eV is the most commonly employed semiconductor in organic-inorganic hybrid PVKSCs. The versatility of the ABX_3 perovskite structure enables bandgap tuning from 1.2 to 2.3 eV via compositional engineering of organic cations (A^+), metal cations (M^{2+}), and halide anions (X^-).[310,362–365] In general, the current development of high efficiency large band-gap (1.7-1.8 eV) PVKSCs utilizes controlled incorporation of Br into $MAPbI_3$ or $FAPbI_3$. The resultant compositionally engineered $MAPb(I_{1-y}Br_y)_3$ and $FAPb(I_{1-y}Br_y)_3$ perovskites possess tunable bandgaps of 1.57-2.29 eV and 1.48-2.23 eV, respectively.[362,363] Previously, Zhu *et al.* have developed compositionally engineered $MAPbI_2Br$ perovskite with a band-gap of 1.80 eV and achieved 10% PCE.[366] Huang *et al.* further tuned the band-gap to 1.72 eV using an optimized composition of $MAPb(I_{0.8}Br_{0.2})_3$ and combined solvent annealing to achieve a high PCE of 13.1%.[367] Recently, Jen *et al.* systematically optimized the $MA_zFA_{1-z}Pb(I_yBr_{1-y})_3$ perovskites to achieve a compositionally engineered $MA_{0.7}FA_{0.3}Pb(I_{0.8}Br_{0.2})_3$ perovskite with a bandgap of 1.69 eV and an average PCE of 15.0%.[311] Despite many reported high efficiency devices, light-induced instability was commonly observed under the operating conditions (AM1.5 illumination) for large bandgap PVKSCs employing $MAPb(I_{1-y}Br_y)_3$ and $FAPb(I_{1-y}Br_y)_3$ perovskite compositions with Br content beyond 20% ($y > 0.2$).[368] Under illumination, the complex phase segregation into iodide- and bromide-rich perovskite phases cause significant drop in photocurrent over time, raising severe concerns for stable long-term operation of these solar cells.[369,370]

Several approaches have been attempted to overcome the phase segregation and stability problems in hybrid perovskites. Huang *et al.* have recently demonstrated a stabilized large band-gap $MAPbI_{2.2}Br_{0.8}$ perovskite using a non-wetting, polybis(4-phenyl)(2,4,6-trimethyl-phenyl)amine (PTAA) as bottom hole-transporting layer to form thin and highly crystalline

perovskite films.[370] This indicates there is a link between film morphology and phase segregation, possibly a consequence of alteration in degree of ionic diffusion. However, this approach is less versatile and is limited in terms of film thickness as pointed out by the authors.[370] Recently, Snaith *et al.* have demonstrated a promising approach of incorporating Cs in $FAPb(I_{1-y}Br_y)_3$ to forbid the formation of non-perovskite yellow phase and achieve a stable single perovskite phase of $FA_{0.83}Cs_{0.17}Pb(I_{1-y}Br_y)_3$, which does not exhibit instability under continuous illumination.[355] The authors hypothesize that lattice contraction due to incorporation of smaller Cs cations (ionic radius: 1.67 Å) compared to FA cations (ionic radius: 2.53 Å) is possibly the reason for phase stabilization. Alternatively, Gratzel *et al.* propose that the increased entropic contribution due to the use of mixed A-cation results in phase stabilization.[371] These works highlight the importance of coherent tuning of perovskite morphology and composition to overcome phase segregation and stability issues.

Mechanistically, understanding of the illumination dependent phase segregation inherent to the $MAPb(I_{1-y}Br_y)_3$ system is still developing. Walsh *et al.* have demonstrated computationally that a thermodynamic miscibility gap may exist in $MAPb(I_{1-y}Br_y)_3$ due to the tendency for spontaneous ordering at temperatures below 343 K resulting in phase segregation into iodide-rich or bromide-rich phases.[372] The internal stress due to mismatch in size between iodide and bromide is the likely driving force for such phase segregation. That said, all compositions of $MAPb(I_{1-y}Br_y)_3$ are commonly realizable when not subjected to illumination unlike $FAPb(I_{1-y}Br_y)_3$, where perovskite formation is prohibited for intermediate compositions. Kamat *et al.* have empirically determined a rate constant of 0.1 - 0.3 s^{-1} for phase segregation in intermediate $MAPb(I_{1-y}Br_y)_3$ compositions and thus definitively established its link to ionic diffusion.[235] This indicates that there is an activation energy associated with the phase separation event and henceforth the

intermediate compositions are realizable by controlling the deposition kinetics or processing conditions in the absence of additional source of energy like illumination.

Reversibility of the photo-induced phase segregation under dark demonstrates that light does not just provide energy to get over this barrier, it rather causes a temporary shift in the internal material equilibrium that can, in most cases, be restored over time after illumination is removed. Light has been found to induce changes in a variety of material parameters when it comes to hybrid perovskites but, with regard to phase stability specifically, one of the most important contributions in the recent literature has been the observation of giant photostriction in the $MAPbI_3$ system.[373] Relationships between internal lattice strain and external conditions are common in both oxide and halide perovskites because of the nature of the crystal structure, but in the case of $MAPb(I_{1-y}Br_y)_3$ this may be particularly important because of the strain already created by the mixture of different sized anions in the metal halide framework.[235,372]

The existence of thermodynamic miscibility gap coupled with the prominence of photostriction in this material system thus suggests a direct link between photo-induced phase segregation and internal bonding environment. Composition engineering is one of the most elegant strategies to directly influence bonding in crystalline solids and thus alter its associated material properties. That said, the driving force for phase segregation arising from different sized anions in $MAPb(I_{1-y}Br_y)_3$ is most immediately built into the metal halide framework itself. Therefore, direct alteration of the metal site (B-site cation) could be a more immediately effective route to alter the impact of photostriction upon illumination and potentially eliminate the issue of phase segregation.

The main objective of this work is to expand and explore perovskite compositions to better comprehend factors contributing to photo-instability and develop an effective approach to

overcome phase segregation under illumination in large band-gap $MAPb(I_{1-y}Br_y)_3$ perovskites. Based on the aforementioned rationale, we have engineered the B-site cation to mitigate phase segregation instead of the previously explored A-site cation. Partial replacement of Pb^{2+} ions with smaller Sn^{2+} ions not only results in alteration of internal bonding environment required for influencing phase segregation, but also reduces the use of toxic lead.

In this work, Sn was first introduced into the highly unstable $MAPb(I_{0.6}Br_{0.4})_3$ perovskite composition to form $MAPb_{1-x}Sn_x(I_{0.6}Br_{0.4})_3$. An optimum of 25% Sn substitution was identified based on the morphology and device performance. A combination of Transient Absorption Spectroscopy (TAS) and X-Ray Diffractometry (XRD) analysis demonstrated elimination of phase segregation in $MAPb_{0.75}Sn_{0.25}(I_{0.6}Br_{0.4})_3$ and the existence of single stable phase under illumination. Introduction of Sn resulted in alteration of internal bonding environment (both crystallite size and lattice micro-strain), subsequently making the mixed halide perovskite less vulnerable to phase segregation during photostriction under illumination and thus improved photo-stability. The efficacy and versatility of this concept is further demonstrated by extending it to different Br contents in the $MAPb_{0.75}Sn_{0.25}(I_{1-y}Br_y)_3$ perovskite system. Finally, with the consideration for tandem solar cell application, a $MAPb_{0.75}Sn_{0.25}(I_{0.4}Br_{0.6})_3$ perovskite with a band-gap of 1.73 eV and stable PCE of 12.59% was demonstrated. Devices not only show constant photocurrent at maximum power point under 1 sun illumination but can also retain 95% of its original PCE after 30-day storage in inert atmosphere. It also possesses respectable thermal stability at 85 ^oC under inert atmosphere.

4.2 Experimental Methods

Materials: PbI_2, $PbBr_2$, SnI_2, $SnBr_2$ and all the solvents used in this study were purchased from Sigma-Aldrich. $PC_{61}BM$ was purchased from the American Dye Source, Inc. MAI and MABr were synthesized by a reported method.[16] Bis-C_{60} was synthesized according to our previous work.[315] Different compositional perovskite precursors (1 M) were prepared by dissolving PbI_2, $PbBr_2$, SnI_2, $SnBr_2$ and MAI and MABr with different ratio into a mixed solvent of DMSO and γ-butyrolactone (volume ratio of 3:7) and stirred at 60 ºC for 1 h.

Device fabrication: ITO glass (15 Ω sq^{-1}) was first cleaned by detergent, deionized water, acetone, and isopropanol alcohol sequentially, then by drying with a nitrogen flow. Then PEDOT:PSS (P VP AI 4083) solution was spin-coated onto the UV ozone treated ITO substrate at 5000 rpm for 40 s and annealed at 150 ºC for 10 min in ambient. Afterward, perovskite precursors (filtered with a 0.2 μm PTFE filter) were spin-coated onto the resultant substrates at 1000 rpm for 15 s and 4000 rpm for 45 s sequentially in the glove box;0.7 mL of anti-solvent (toluene) was dropped during the last 15 s of the second spin-coating step. The resulted substrates were then annealed at 100 ºC for 10 min on a hot plate. Afterward, the 15 mg/mL $PC_{61}BM$ solution and 2 mg/mL bis-C_{60} surfactant solution were spin-coated onto the perovskite films at 4000 rpm for 40 s and 3000 rpm for 60 s sequentially. Finally, silver electrode (150 nm thick) was evaporated under high vacuum ($<1\times10^{-6}$ Torr) through a shadow mask. The area of studied solar cells is 10 mm^2 (16 mm^2 cells measured by applying a shadow mask with an aperture area of 10 mm^2).

Characterization: The structure of perovskite films was characterized by SEM (FEI Sirion SEM operated at 5 kV) and XRD (Bruker F8 Focus Powder XRD). The samples for XRD measurements were all encapsulated by a thin polymethyl methacrylate layer. The absorption

spectra were measured by a Varian Cary 5000 UV-Vis-NIR spectrometer. All *J-V* curves and steady-state photocurrent of the PVKSCs were measured by a Keithley 2400 Source Meter with the illumination of a 450 W Oriel xenon lamp under an AM 1.5G condition in inert atmosphere. The light intensity was precisely calibrated with a standard Si photodiode detector that can be traced back to the standard of the National Renewable Energy Laboratory. It is worth notingthat light intensity is calibrated by a KG-5 photodiode detector to measure the $MAPbI_3$ solar cells while it was calibrated by a KG-1 photodiode detector with a mismatch factor to measure the low E_g Sn-based PVKSCs. The EQE spectra were measured by combining a monochromatic 450 W xenon lamp (Oriel) with a sourcemeter (Keithley 2400) and calculated using a calibrated Si photodiode (OSI-Optoelectronics).

Transient absorption spectroscopy: TAS was taken by using the Libra laser system (50 fs FWHM at 1kHz repetition rate, $1mJ/cm^2$, 800 nm fundamental wavelength) combined with Helios spectrometer (Ultrafast Systems). The fundamental beam was split into two lines by an 80/20 beam-splitter. The delayed probe light was generated by an optical delay stage and focused on Ti:Sapphire crystal to generate white continuum. The pump wavelength (365 nm or 500 nm) was generated by an OPerA optical parametric amplifier (Coherent, Inc.) after splitting the fundamental beam. The 365 nm and 500 nm bandpass filters were used depending on the pump wavelength to eliminate residual fundamental beam. A pump wavelength of 365 nm was used to measure the reference films without secondary excitation. Meanwhile, a 500 nm pump wavelength was used for samples measured with secondary excitation. The pump fluence was modulated by 2 consecutive neutral density filters. The diameter of spot size is 2 mm. A continuous-wave laser (CrystaLaser LC, 532 nm) was used as the secondary excitation source. The intensity of secondary excitation source was modulated by another neutral density filter. All TAS signals were monitored

at 10 ps pump-probe delay with 1 min soaking of secondary excitation. The samples for TAS were all encapsulated by a glass with epoxy.

Time resolved PL measurement: The experimental set up used for time resolved PL measurements were adapted from previous work.[369] Spectra were acquired using a modified Horiba LabRAM HR-800, a 532 nm laser diode excitation source, and a 10x objective (NA=0.25). The adjustable confocal hole before the monochromator was set at 800 um. A 150 gr/mm Czerny-Turner monochromator blazed at 1200 nm was used, and the emitted light was collected with a silicon CCD array detector. For maps, the PL collection time was set to 1 s, and the amount of time that the laser stayed at any given location was set to 1 s. This reduces the effects of any transient behavior and gives the initial condition of each perovskite composition. Spectral artifacts caused by the detector and the optical path between the sample and detector were accounted for by creating a relative correction file with a black body source (IR-301, Infrared Systems Development Corporation) set to 1050 ^{o}C. A 10 μm pin-hole was used to fix the spectral photon flux to the detector and allow an absolute photons per count calibration factor to be measured. The laser diameter was measured to be 10 μm and the FWHM of the Gaussian distributed laser intensity was measured to be 6 μm. All PL measurements were conducted with the perovskite samples in a nitrogen-filled cell (P=250 mm-Hg) with a quartz window.

The N-Suns illumination intensity: The N-Suns illumination intensity in the PL and TAS measurement was calculated by dividing the photon flux (number of photons per second per area) inside the FWHM of excitation laser by the above-bandgap (of initial perovskite) photon flux of the AM1.5 GT solar spectrum rather than comparing energy density (in W/cm^2) as previously reported. An Oriel optical power meter and beam profilometer were used to measure the illumination intensity and excitation diameter (2 mm circle), respectively, for various laser power.

Williamson-Hall analysis method: According to Williamson-Hall analysis, the line broadening (β) can be expressed as a simple sum of contributions from crystallite size (D) and micro-strain (ε). Thus we have, $\beta = \frac{\kappa\lambda}{D\cos\theta} + 2\varepsilon \tan\theta$ (where β is the line broadening at FWHM, D is the mean size of crystallite domains, ε is the micro-strain, λ is the X-ray wavelength, θ is the Bragg angle and $\boldsymbol{\kappa}$ is a dimensionless shape factor). By re-arranging the terms we have: $\beta\cos\theta = \frac{\kappa\lambda}{D} + 2\varepsilon \sin\theta$. The slope ($2\varepsilon$) and intercept ($\kappa\lambda/D$) obtained from a linear fit of $\beta\cos\theta$ vs $\sin\theta$ are expressed as strain and size contributions, respectively. The strain contribution is directly proportional to micro-strain and the size contribution is inversely proportional to crystallite size. Uniform deformation model was used based on assumption of isotropic strain.

4.3 Results and Discussion

4.3.1 Photovoltaic Characteristics of Mixed halide PVKSCs using Pb-Sn Binary Alloys

To study the phase segregation under illumination and explore compositional modification of the $MAPb(I_{1-y}Br_y)_3$ system, $MAPb(I_{0.6}Br_{0.4})_3$ was chosen as our reference. This is a highly unstable composition lying in the miscibility gap at 300 K as predicted by Walsh *et al* [372] which exhibits spontaneous phase segregation under illumination. To alter the crystal and internal bonding environment, we gradually replaced Pb^{2+} ion with a smaller Sn^{2+} ion in $MAPb(I_{0.6}Br_{0.4})_3$ to realize $MAPb_{1-x}Sn_x(I_{0.6}Br_{0.4})_3$ perovskites (**Figure 4.1a**). Sn incorporation is typically complicated by the fast crystallization rate of $MASnI_3$, which often leads to poor coverage and morphology.[312,374] However, in our recent work, we have circumvented this issue to successfully demonstrate high efficiency Pb-Sn binary alloy systems using solvent washing methodology,[1] similar to the method developed by Seok *et al*.[333] Further processing details are provided in **Section 4.2**.

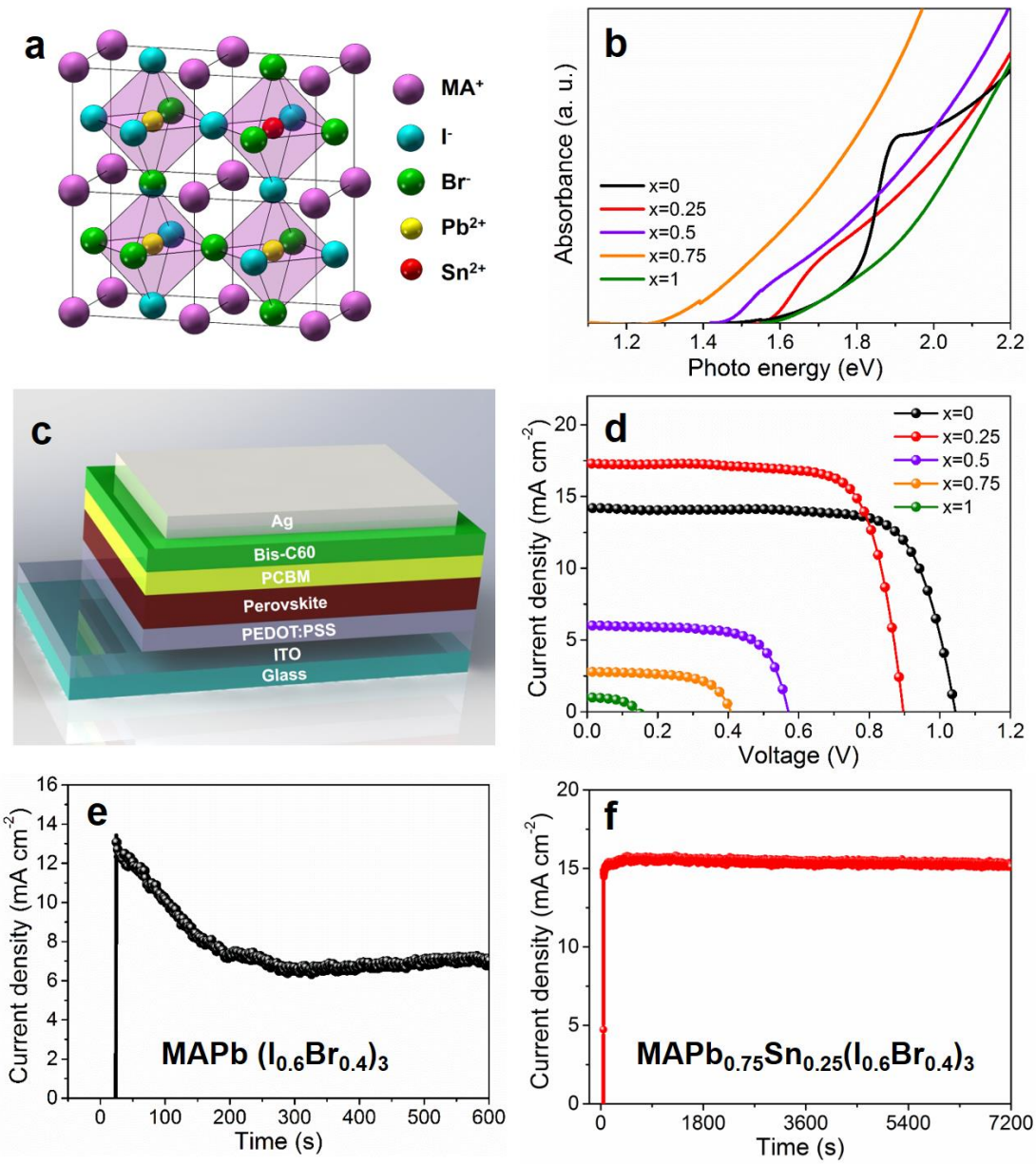

Figure 4.1. (a) Schematical illustration of lattice structure for compositionally engineered $MAPb_{1-x}Sn_x(I_{0.6}Br_{0.4})_3$ perovskites. (b) Absorption spectra of $MAPb_{1-x}Sn_x(I_{0.6}Br_{0.4})_3$ perovskites with different tin content. (c) Schematical illustration of perovskite solar cells device configuration. (d) Typical J-V characteristics of $MAPb_{1-x}Sn_x(I_{0.6}Br_{0.4})_3$ PVKSCs measured under AM 1.5 illumination with reverse scan. e and f, Steady-state photocurrent measurement of $MAPb(I_{0.6}Br_{0.4})_3$ (e) and $MAPb_{0.75}Sn_{0.25}(I_{0.6}Br_{0.4})_3$ (f) PVKSCs with an applied voltage of 0.86 V and 0.74 V at the maximum power point, respectively.

As portrayed in the Scanning Electron Microscopy (SEM) images of the $MAPb_{1-x}Sn_x(I_{0.6}Br_{0.4})_3$ perovskites (**Figure 4.2**), the $MAPb_{0.75}Sn_{0.25}(I_{0.6}Br_{0.4})_3$ perovskite (25% Sn) shows homogeneous morphology with excellent coverage similar to $MAPb(I_{0.6}Br_{0.4})_3$. Besides, SEM energy dispersive spectroscopy (EDS) mapping showed a uniform distribution of Pb, Sn, I and Br

further confirming the homogeneity of perovskite films. Increasing pinholes and inhomogeneity are apparent when the Sn content is further increased to 50%, 75% and 100% (**Figure 4.2**). The bandgap shifted from 1.80 eV to 1.35 eV when the Sn content increased from 0% to 75% and subsequently shifted back to 1.60 eV when Pb was fully replaced by Sn (**Figure 4.1b**). This anomalous nonlinear band-gap trend can be attributed to the competition between spin-orbit coupling and lattice distortion, as previously explained by Kanatzidis *et al.*[364]

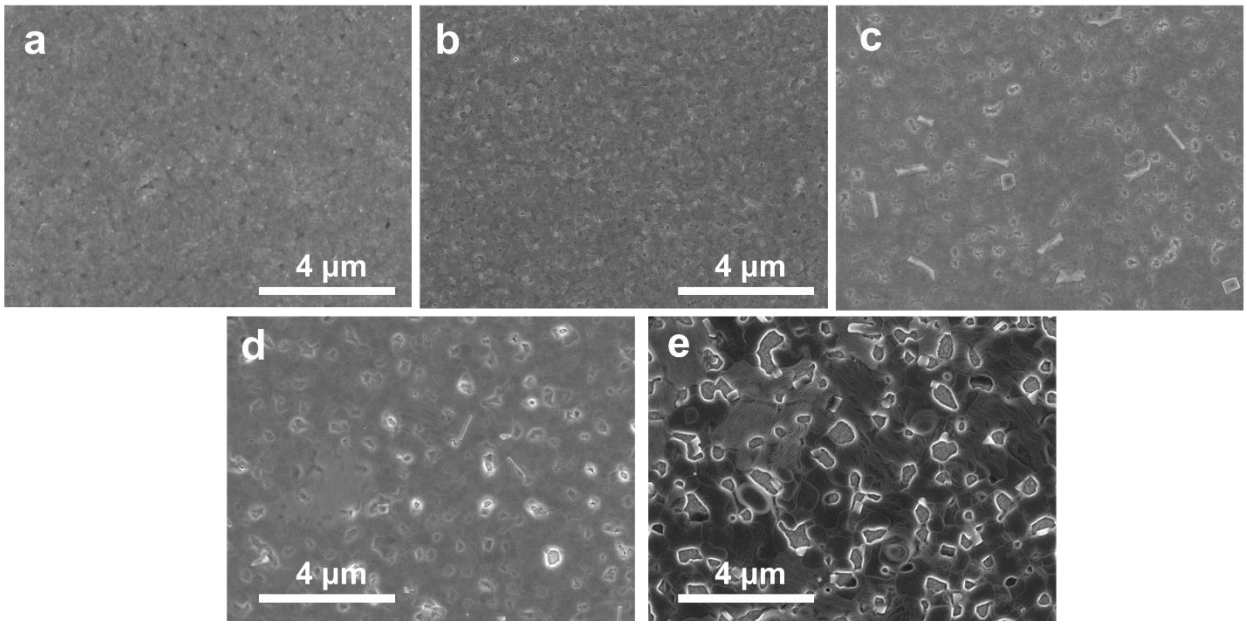

Figure 4.2. SEM images of the $MAPb_{1-x}Sn_x(I_{0.6}Br_{0.4})_3$ perovskites with Sn content of 0% (a), 25% (b), 50% (c), 75% (d) and 100% (e).

The photovoltaic performance of these perovskite films were systematically studied with a solar cell structure of ITO/poly(3,4-ethylenedioxythiophene) polystyrene sulfonate (PEDOT:PSS)/Perovskite/phenyl-C61-butyric acid methyl ester (PCBM)/bis-C_{60}/Ag (**Figure 4.1c-d**). Initially, a series of devices were fabricated using $MAPb_{1-x}Sn_x(I_{0.6}Br_{0.4})_3$ films to understand the influence of Sn content on device performance. The reference $MAPb(I_{0.6}Br_{0.4})_3$ PVKSC showed a PCE of 11.14% with an open circuit voltage (V_{oc}) of 1.05 V, a short circuit current density (J_{sc}) of 14.34 mA cm^{-2}, and a fill factor (*FF*) of 0.74. Whereas, the

$MAPb_{0.75}Sn_{0.25}(I_{0.6}Br_{0.4})_3$ PVKSC with 25% Sn had an enhanced PCE of 11.93%, with a lower V_{oc} of 0.91 V, a higher J_{sc} of 17.22 mA cm^{-2}, and *FF* of 0.76. The V_{oc} drop corresponds to the decrease in E_g, as both devices achieve 69% of their detailed balance limit for V_{oc} from Shockley-Queisser calculations. However, when Sn content is further increased to 50%, 75%, and 100%, devices show extremely low efficiency mainly due to poor morphology (**Figure 4.2**). Therefore, 25% Sn was chosen as the optimum for use in devices. Further process optimization might lead to improved morphology and device performance for Sn incorporation beyond 25%. Detailed photovoltaic parameters are summarized in **Table 4.1**.

Table 4.1. Photovoltaic parameters of the $MAPb_{1-x}Sn_x(I_{0.6}Br_{0.4})_3$ PVKSCs measured under AM 1.5 illumination.

$MAPb_{1-x}Sn_x(I_{0.6}Br_{0.4})_3$	Band gap, E_g (eV)	V_{oc} (V)	J_{sc} (mA/cm^2)	*FF*	PCE (%)	V_{oc}/V_{oc}^{SQ}
x=0	1.80	1.05±0.01	14.34±0.42	0.74±0.02	11.14±0.58	0.69
x=0.25	1.59	0.91±0.01	17.25±0.67	0.76±0.02	11.93±0.74	0.69
x=0.50	1.48	0.57±0.03	6.02±0.56	0.68±0.03	2.34±0.31	0.47
x=0.75	1.34	0.41±0.03	2.76±0.75	0.63±0.05	0.71±0.27	0.38
x=1	1.60	0.15±0.04	1.03±0.69	0.51±0.05	0.07±0.09	0.11

Average values with standard deviation. The data for each sample was obtained from 20 devices. The limit for V_{oc}, V_{oc}^{SQ}, was calculated using the ASTM G-173 standard for the AM1.5GT solar spectrum, a temperature of 298.15 K, and a perfect back reflector.

The steady-state photocurrent density of $MAPb(I_{0.6}Br_{0.4})_3$ and $MAPb_{0.75}Sn_{0.25}(I_{0.6}Br_{0.4})_3$ PVKSCs were measured at the maximum power point under AM1.5 illumination to study photo-stability (**Figure 4.1e-f**). As shown in **Figure 4.1e**, the photocurrent density of $MAPb(I_{0.6}Br_{0.4})_3$ PVKSCs decreased steadily from 13.16 to 7.08 mA cm^{-2} during 1 sun illumination for 300 s, indicating its photo-instability. The drop in photocurrent is attributed to increased trap-assisted recombination losses as a smaller bandgap phase precipitates under illumination, consistent with the rationale provided by Kamat *et al.*[235] On the other hand, $MAPb_{0.75}Sn_{0.25}(I_{0.6}Br_{0.4})_3$ PVKSCs show a stable photocurrent density of 15.69 mA cm^{-2} under 1 sun illumination for 2 hours, substantiating the phase stability of this perovskite composition under illumination (**Figure 4.1f**).

4.3.2 Evidences and Mechanism for Improved Phase stability by Tin Substitution

To reveal the difference in phase stability of $MAPb(I_{0.6}Br_{0.4})_3$ and $MAPb_{0.75}Sn_{0.25}(I_{0.6}Br_{0.4})_3$ perovskites, steady state photoluminescence (PL) measurements were initially preformed (**Figure 4.3**). For $MAPb(I_{0.6}Br_{0.4})_3$, the PL peak gradually shifted from 1.80 to 1.64 eV in 30 s under an illumination of one sun-intensity 532 nm laser (**Figure 4.3a**), indicating phase segregation as expected and observed in previous studies. However, in the case of $MAPb_{0.75}Sn_{0.25}(I_{0.6}Br_{0.4})_3$ films, extremely low PL quantum yield (PLQY) was inadequate to carry out the same systematic study with controlled light exposure. Thus, longer iteration of signals (>30 min) or high intensity exposure (>100 Sun) under continuous illumination was inevitable to get discernable signals. Accordingly, we obtained a visible PL spectra of $MAPb_{0.75}Sn_{0.25}(I_{0.6}Br_{0.4})_3$ film by soaking and iteration for 90 min under 1 sun intensity illumination (**Figure 4.3b**). A stable PL peak was observed at 1.56 eV elucidating an improved phase stability of our films with partial tin substitution.

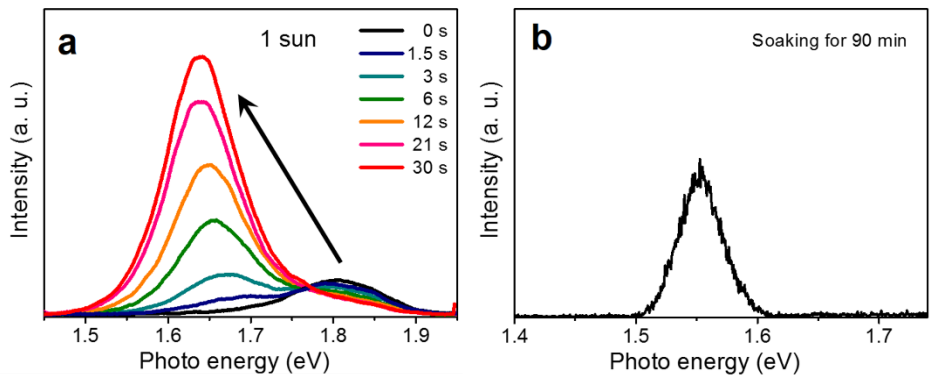

Figure 4.3. (a) Time resolved steady state PL of the $MAPb(I_{0.6}Br_{0.4})_3$ pervoskite film under an illumination of one sun-intensity 532 nm laser. (b) PL of the $MAPb_{0.75}Sn_{0.25}(I_{0.6}Br_{0.4})_3$ pervoskite film under an illumination of one sun-intensity 532 nm laser after soaking and iteration for 90 min.

To provide a more robust comparison, we use TAS to investigate phase stability of mixed halide perovskite films. TAS measurement does not suffer from extremely low PLQY of the films since it directly shows all emissive and non-emissive characteristics.[375,376] Further it has been

recently utilized to study phase segregation in perovskites.[235] A secondary excitation source of 532 nm continuous wave laser was coupled with the TAS setup to carry out this investigation. All pump fluences at 365 nm were maintained below 0.64 μJ/cm^2, roughly corresponding to a photon flux equivalent to 0.01 sun illumination to avoid any possible influence on phase segregation. The spectra was measured promptly at fixed 10 ps pump-probe delay without scanning entire transient, so that we can avoid any adverse effect of elongated exposure. As shown in **Figure 4.4a-b**, the TAS spectra of all perovskite films at 10 ps pump-probe delay exhibit characteristic photo-bleaching signals (PB2) originating from state-filling effects at the onset of steady state absorption.[377] At 10 ps delay, carrier cooling from PB1 to PB2 was completed and the additional relaxation process through energetic cascade was in the progress, so that we can observe PB2 signals from multiple phases.[235] Relative carrier cooling, relaxation and recombination dynamics were not analyzed due to largely different carrier concentrations in the presence of secondary illumination.

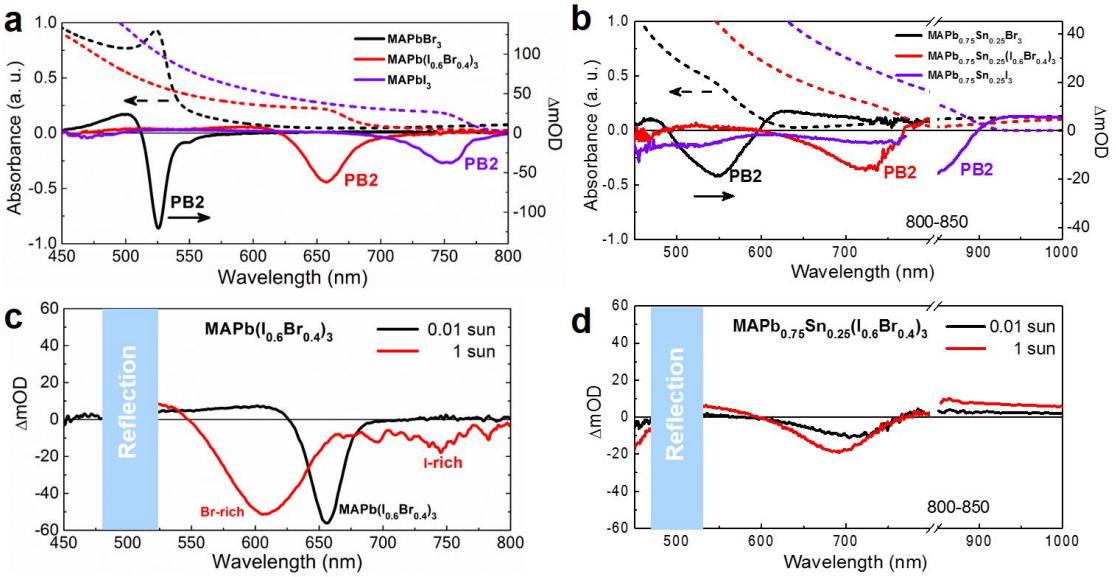

Figure 4.4. (a) Steady-state and transient absorption spectra of $MAPbI_3$, $MAPbBr_3$ and $MAPb(I_{0.6}Br_{0.4})_3$ perovskite films. (b) Steady-state and transient absorption spectra of $MAPb_{0.75}Sn_{0.25}I_3$, $MAPb_{0.75}Sn_{0.25}Br_3$ and $MAPb_{0.75}Sn_{0.25}(I_{0.6}Br_{0.4})_3$ perovskite films. (c) and (d) Transient absorption spectra of $MAPb(I_{0.6}Br_{0.4})_3$ and $MAPb_{0.75}Sn_{0.25}(I_{0.6}Br_{0.4})_3$ perovskite films measured promptly at fixed 10 ps pump-probe delay under different intensities (0.01 and 1 Sun) of secondary illumination (532 nm CW laser) after soaking for 10 minutes.

When the perovskite films were exposed to a low intensity secondary excitation (0.01 sun), PB2 signals of both $MAPb(I_{0.6}Br_{0.4})_3$ and $MAPb_{0.75}Sn_{0.25}(I_{0.6}Br_{0.4})_3$ perovskite films showed invariant absorption features (**Figure 4.4c-d**). However, when intensity of the continuous-wave (CW) laser was increased up to 1 sun, the PB2 of $MAPb(I_{0.6}Br_{0.4})_3$ gradually blue shifted towards 560-640 nm and simultaneously a new PB2 signal appeared at 700-800 nm. These results clearly indicate that $MAPb(I_{0.6}Br_{0.4})_3$ undergoes phase separation into Br-rich and I-rich phases. On the contrary, under the same 1 sun illumination, PB2 signals of the $MAPb_{0.75}Sn_{0.25}(I_{0.6}Br_{0.4})_3$ did not show any significant change and no new bleaching features corresponding to pure I-rich or Br-rich phases were observed. The slight blue-shift / broadening is related to the band-filling effect[31, 32] and possibly a broadened density of states at the band edge from a photostriction-induced disorder. This clearly demonstrates that Sn incorporation contributes to the stabilization of the I/Br mixed system under illumination.

To gain further mechanistic understanding and elucidate the role of Sn substitution in eliminating phase segregation in I/Br mixed halide system, we analyzed the change in lattice structure using XRD with and without illumination. As shown in **Figure 4.5a-b**, both $MAPb(I_{0.6}Br_{0.4})_3$ and $MAPb_{0.75}Sn_{0.25}(I_{0.6}Br_{0.4})_3$ perovskites possess a cubic structure with distinctive peaks corresponding to the {100} family of planes at room temperature without any illumination. The {100} peaks of $MAPb(I_{0.6}Br_{0.4})_3$ show only a very slight shift in 2θ values when 25% Sn was incorporated, indicating minimal change in lattice parameters. Accordingly, the calculated lattice parameters (a = b = c) (Inserted table in **Figure 4.5a-b**) for the cubic phases of $MAPb(I_{0.6}Br_{0.4})_3$ and $MAPb_{0.75}Sn_{0.25}(I_{0.6}Br_{0.4})_3$ perovskites are 6.147 Å and 6.144 Å respectively. Subsequently, we investigated the influence of illumination on lattice structure by exposing samples to a 532 nm CW laser with an intensity around 0.2 sun for 10 min.

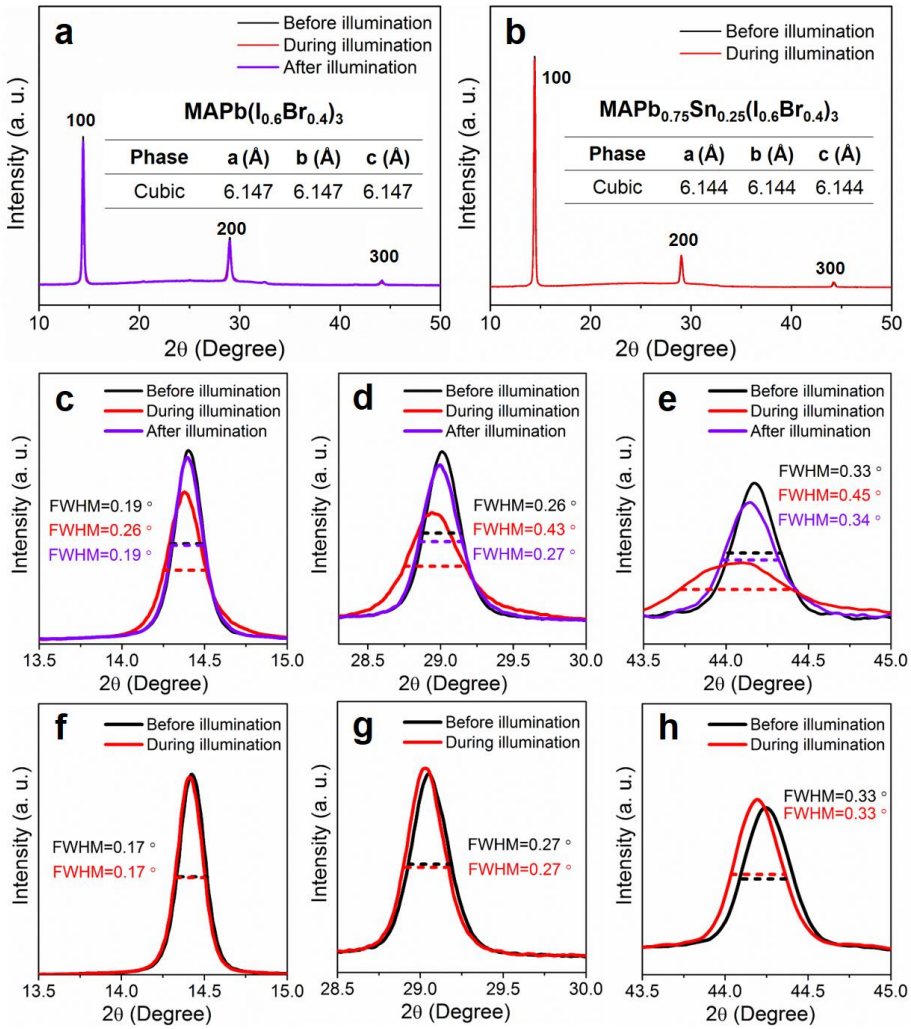

Figure 4.5. (a) and (b) XRD spectra of the $MAPb(I_{0.6}Br_{0.4})_3$ and $MAPb_{0.75}Sn_{0.25}(I_{0.6}Br_{0.4})_3$ perovskite films measured before, during and after 10 min illumination by a 0.2 sun intensity 532 nm CW laser. Lattice parameters are inserted into the figures. (c-e) Zoomed in regions in Figure 3a. (f-h) Zoomed in regions in Figure 4.5b.

As a result of illumination, for $MAPb(I_{0.6}Br_{0.4})_3$ films, we observed a decrease in the intensity of (100), (200) and (300) peaks and a concurrent increase in the full width at half maximum (FWHM) (**Figure 4.5c-e**). However, the intensity and FWHM restored back to the initial state after keeping the sample in dark for 10 min. In contrast, under similar illumination, the peak intensity and FWHM for $MAPb_{0.75}Sn_{0.25}(I_{0.6}Br_{0.4})_3$ perovskites were unaffected (**Figure 4.5f-3h**). The change in peak intensity and FWHM under illumination is thus clearly a consequence of phase-instability in $MAPb(I_{0.6}Br_{0.4})_3$ under illumination. This agrees well with the above discussed TAS results and thus corroborates the efficacy of Sn introduction to overcome the complex phase

segregation issue in I/Br mixed halide perovskites. The reduction in peak intensity and increase in FWHM is a collective consequence of decrease in crystallite size and increase in composition inhomogeneity and micro-strain under illumination. The slight shift of peaks to lower angles corresponds to a larger lattice spacing under illumination and is likely due to the photostriction induced macro-strain.

To isolate the contributions of crystallite size and micro-strain in the observed line broadening (increase in FWHM) of diffraction patterns, we employed Williamson-Hall analysis method.[378] Further details of the analysis are provided in **Section 4.2** and the size and strain contribution data are summarized in **Table 4.2**.

Table 4.2. Line broadening parameters calculated based on Uniform Deformation Model (UDM) through Williamson-Hall approach*

	Size Contribution $\boldsymbol{\kappa\lambda/D}$	**Strain Contribution** $2\boldsymbol{\varepsilon}$
$MAPb(I_{0.6}Br_{0.4})_3$ Before Illumination	0.0023	0.0080
$MAPb(I_{0.6}Br_{0.4})_3$ During Illumination	0.0036	0.0112
$MAPb(I_{0.6}Br_{0.4})_3$ After Illumination	0.0022	0.0088
$MAPb_{0.75}Sn_{0.25}(I_{0.6}Br_{0.4})_3$ Before Illumination	0.0019	0.0096
$MAPb_{0.75}Sn_{0.25}(I_{0.6}Br_{0.4})_3$ During Illumination	0.0019	0.0096

*Williamson-Hall approach: $\beta \cos\theta = \frac{\kappa\lambda}{D} + 2\varepsilon \sin\theta$ (where β is the line broadening at FWHM, D is the mean size of crystallite domains, ε is the micro-strain, λ is the X-ray wavelength, θ is the Bragg angle and $\boldsymbol{\kappa}$ is a dimensionless shape factor)

Based on this analysis, we find that Sn incorporation increases the crystallite size and micro-strain. The observation of increased crystallinity with Sn addition is in accordance to our previous work and is apparent from the XRD patterns in **Figure 4.5a-b**. Whereas, the increase in micro-strain can be interpreted as a consequence of added contribution arising from the partial substitution of Pb^{2+} by Sn^{2+}. We hypothesize that this significant alteration in the internal bonding environment (crystallite size and micro-strain) due to partial Sn substitution strongly alters the driving force for

phase segregation and increases the barrier for ionic diffusion (due to the hindrance from added strain field and increased crystallite size). Thus $MAPb_{0.75}Sn_{0.25}(I_{0.6}Br_{0.4})_3$ perovskites show less vulnerability for phase segregation under illumination compared $MAPb(I_{0.6}Br_{0.4})_3$. The increase in micro-strain and decrease in crystallite size under illumination for $MAPb(I_{0.6}Br_{0.4})_3$ is observed as result of compositional inhomogeneity due to phase segregation. No such increase is observed under illumination for $MAPb_{0.75}Sn_{0.25}(I_{0.6}Br_{0.4})_3$. Detailed analysis of internal bonding environment, compositional inhomogeneity and ionic diffusion is beyond the scope of this work and further computational studies are required.

4.3.3 General Applicability of the Approach for Entire Range of Mixed Halides

To demonstrate the applicability of Sn substitution for overcoming phase segregation in a wider range of I/Br mixtures and attain a band-gap suitable for tandem cells (1.7 – 1.8 eV), we have systematically tuned the I/Br ratio in $MAPb_{0.75}Sn_{0.25}(I_{1-y}Br_y)_3$ (**Figure 4.6**). As shown in **Figure 4.6a**, the color of the $MAPb_{0.75}Sn_{0.25}(I_{1-y}Br_y)_3$ films gradually changed from dark to light as the Br content increased from 0% to 100% indicating an increase in bandgap. Correspondingly, the onset of absorption spectra shifted linearly from 1.35 eV for $MAPb_{0.75}Sn_{0.25}I_3$ to 2.03 eV for $MAPb_{0.75}Sn_{0.25}Br_3$ (**Figure 4.6b**). Further, XRD analysis (**Figure 4.6c**) showed that the 2θ value corresponding to the {100} plane of (pseudo-)cubic $MAPb_{0.75}Sn_{0.25}(I_{1-y}Br_y)_3$ perovskites gradually shifted from 14.13^{o} to 15.02^{o} as Br content increased from 0% to 100%. This clearly depicted the existence of single phase perovskite for any combination of I/Br mixture with gradual lattice contraction as Br content is increased. Subsequently, the photovoltaic performance and stability of $MAPb_{0.75}Sn_{0.25}(I_{1-y}Br_y)_3$ PVKSCs were systematically studied using the same device structure as above (**Figures 4.6d**, **4.7a-d** and **Table 4.3**).

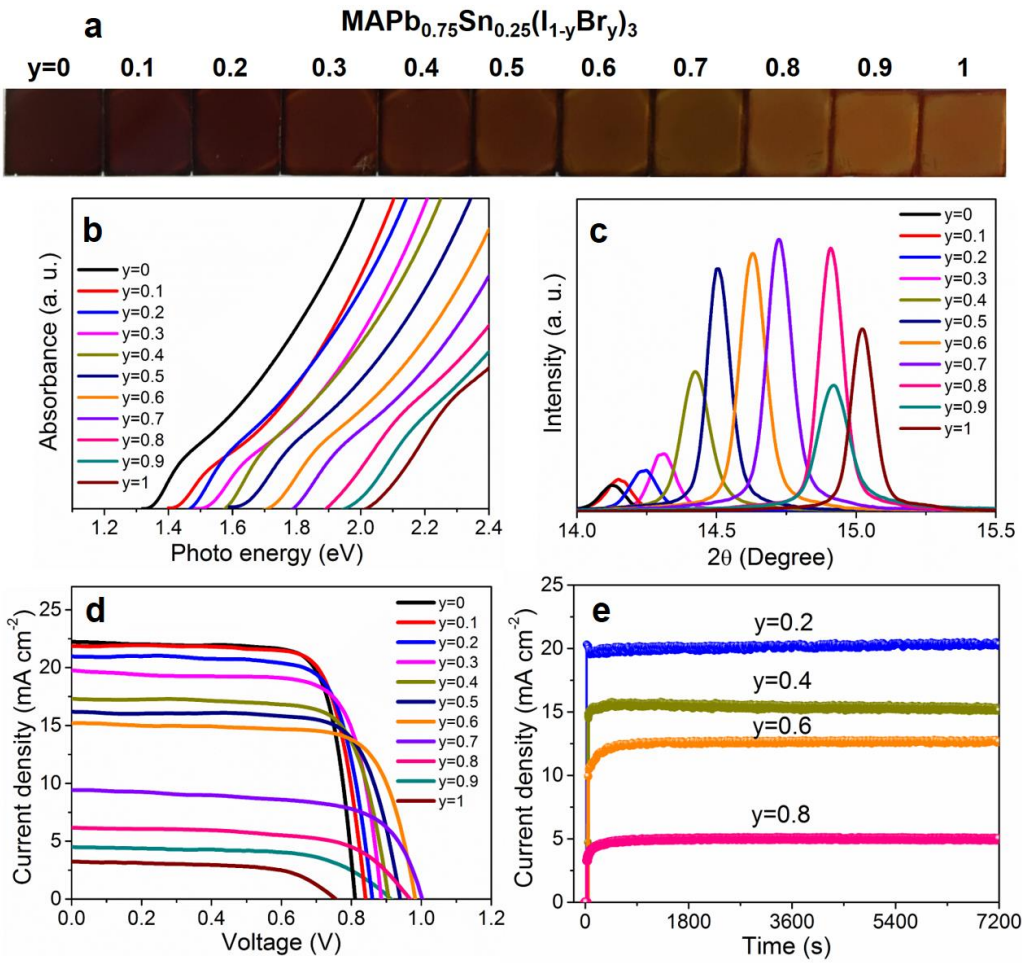

Figure 4.6. Optical images (a), absorption spectra (b) and XRD spectra (c) of $MAPb_{0.75}Sn_{0.25}(I_{1-y}Br_y)_3$ perovskites with different Br content. (d) typical J-V characteristics of $MAPb_{0.75}Sn_{0.25}(I_{1-y}Br_y)_3$ PVKSCs measured under AM 1.5 illumination. (e) The steady-state photocurrent measurement of $MAPb_{0.75}Sn_{0.25}(I_{0.8}Br_{0.2})_3$, $MAPb_{0.75}Sn_{0.25}(I_{0.6}Br_{0.4})_3$, $MAPb_{0.75}Sn_{0.25}(I_{0.4}Br_{0.6})_3$ and $MAPb_{0.75}Sn_{0.25}(I_{0.2}Br_{0.8})_3$ PVKSCs at maximum power point of 0.70, 0.74, 0.82 and 0.75 V under AM 1.5 illumination, respectively.

The V_{oc} gradually increased from 0.82 eV to 1.01 eV as Br content increased from 0% to 70% and then decreased to 0.76 V as Br content increased to 100%. Similarly, *FF* was maintained between 0.74 to 0.78 when the Br content was increased from 0% to 60% and gradually dropped to 0.61 when Br content was further increased. The non-intuitive trend in V_{oc} and *FF* is possibly a consequence of change in material quality with Br content and varying interfacial losses as a result of band edges shifting with compositional variation. The J_{sc} gradually decreased from 22.19 to 3.22 mA cm^{-2} as the Br content increased, possibly due to increased bandgap and interfacial losses. All $MAPb_{0.75}Sn_{0.25}(I_{1-y}Br_y)_3$ PVKSCs exhibit quite stable steady state photocurrent under AM1.5

illumination for 2 hours without any issues, implying a high phase stability of these compositionally tuned perovskite systems (**Figure 4.6e**).

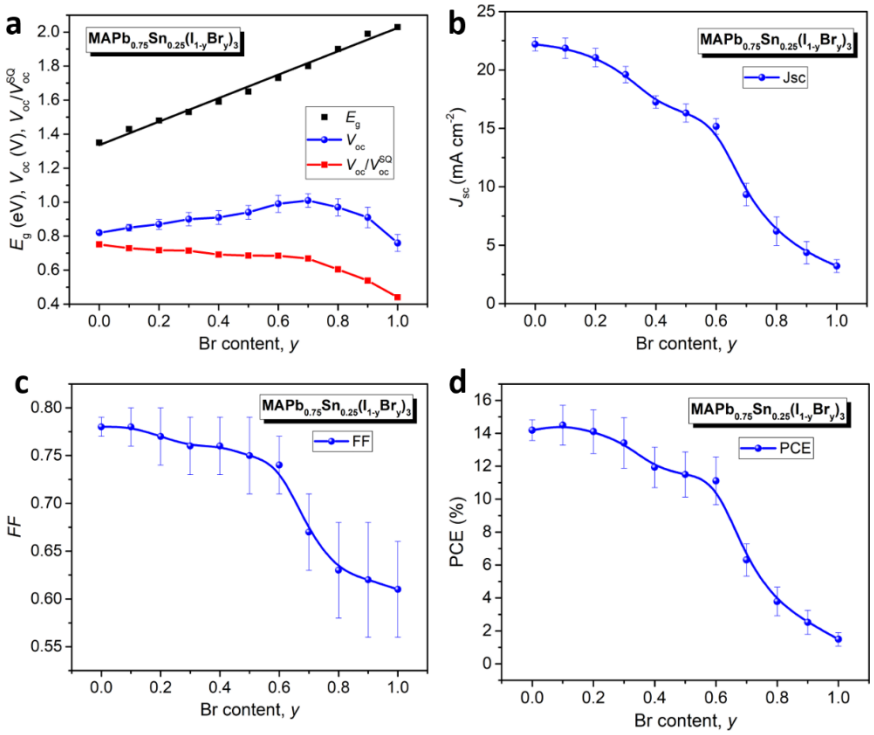

Figure 4.7. (a-d) Photovoltaic parameters of the $MAPb_{0.75}Sn_{0.25}(I_{1-y}Br_y)_3$ PVKSCs measured under AM 1.5 illumination. Average values with standard deviation; the data for each sample was obtained from 20 devices.

Table 4.3. Photovoltaic parameters of $MAPb_{0.75}Sn_{0.25}(I_{1-y}Br_y)_3$ PVKSCs measured under AM 1.5 illumination.

$MAPb_{0.75}Sn_{0.25}(I_{1-y}Br_y)_3$	E_g (eV)	V_{oc} (V)	J_{sc} (mA/cm^2)	*FF*	PCE (%)
0.0	1.35	0.82±0.01	22.19±0.56	0.78±0.01	14.19±0.63
0.1	1.43	0.85±0.02	21.86±0.87	0.78±0.02	14.49±1.21
0.2	1.48	0.87±0.03	21.05±0.79	0.77±0.03	14.10±1.32
0.3	1.53	0.90±0.04	19.60±0.69	0.76±0.03	13.41±1.53
0.4	1.59	0.91 ±0.04	17.25±0.54	0.76±0.03	11.93±1.22
0.5	1.65	0.94 ±0.04	16.31±0.77	0.75±0.04	11.50±1.37
0.6	1.73	0.99±0.05	15.16±0.67	0.74±0.03	11.11±1.45
0.7	1.80	1.01 ±0.04	9.33±0.97	0.67±0.04	6.31±0.98
0.8	1.90	0.97±0.04	6.21±1.22	0.63±0.05	3.79±0.87
0.9	1.99	0.91±0.06	4.47±0.96	0.62±0.06	2.52±0.73
1.0	2.03	0.76±0.05	3.22±0.54	0.61±0.05	1.49±0.41

Average values with standard deviation. The data for each sample was obtained from 20 devices.

As we determined that $MAPb_{0.75}Sn_{0.25}(I_{0.4}Br_{0.6})_3$ with a bandgap of 1.73 eV is an ideal candidate material for tandem solar cell application, its performance was further inspected in greater detail. During optimization, the best device showed a V_{oc} of 1.04 V, a J_{sc} of 15.52 mA cm^{-2} and a *FF* of 0.78, resulting in a PCE of 12.59% (**Figure 4.8a**). No obvious hysteresis was observed under low scan rate of 0.01 V/s. The integrated photocurrent densities from external quantum efficiency (EQE) spectra (14.82 mA cm^{-2}) matched well with the J_{sc} measured in *J-V* curves with less than 5% variation (**Figure 4.8b**).

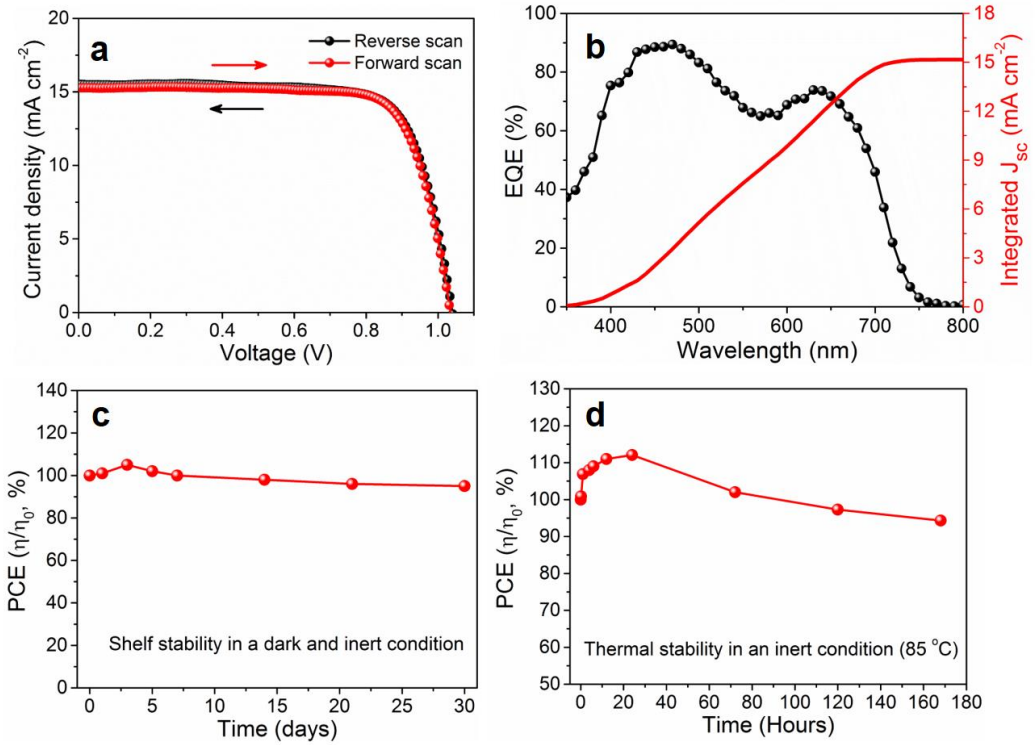

Figure 4.8. (a) J-V characteristics of the best $MAPb_{0.75}Sn_{0.25}(I_{0.4}Br_{0.6})_3$ PKVSCs measured under AM 1.5 illumination with forward and reverse scan (scan rate of 0.01 V/s). (b) EQE measurement of $MAPb_{0.75}Sn_{0.25}(I_{0.4}Br_{0.6})_3$ PVKSCs. (c) Shelf stability of $MAPb_{0.75}Sn_{0.25}(I_{0.4}Br_{0.6})_3$ PVKSCs stored in an inert and dark atmosphere. η and η_0 represent time-resolved and original efficiencies. (d) Thermal stability of $MAPb_{0.75}Sn_{0.25}(I_{0.4}Br_{0.6})_3$ PVKSCs at 85 °C in an inert atmosphere. The device was removed from hot plate during periodic J-V testing. η and η_0 represent time-resolved and original efficiencies.

Finally, the room temperature and thermal stability of devices were studied. As shown in **Figure 4.8c,** the efficiency of $MAPb_{0.75}Sn_{0.25}(I_{0.4}Br_{0.6})_3$ PVKSCs can be maintained at 95% after 30 d storage in inert atmosphere. Surprisingly, the PCE of $MAPb_{0.75}Sn_{0.25}(I_{0.4}Br_{0.6})_3$ PVKSC improve

to 112% of the initial value after annealing at 85 ^{o}C for 24 h. The performance gradually decreased to 94% of its initial PCE during the next 6 d of annealing at 85 ^{o}C (**Figure 4.8d**). The initial increase in PCE is possibly related to improved interfacial properties, specifically penetration of PCBM into perovskite and subsequent passivation of trap sites.[313] Thus, our newly developed large band-gap perovskite system possesses excellent stability and is readily transferrable for tandem applications.

4.4 Conclusion

In summary, the phase stability of $MAPb(I_{1-y}Br_y)_3$ system was found to be greatly improved by partially replacing Pb^{2+} with Sn^{2+} ions. Based on this study, we found that accounting for internal bonding environment exacerbated by photostriction under illumination is an important component for eliminating phase segregation in the $MAPb(I_{1-x}Br_x)_3$ system. Notably, $MAPb_{0.75}Sn_{0.25}(I_{1-y}Br_y)_3$ perovskites show stable and linearly tunable bandgaps from 1.35 to 2.03 eV under continuous illumination. Among them, $MAPb_{0.75}Sn_{0.25}(I_{0.4}Br_{0.6})_3$ with a bandgap of 1.73 eV shows a maximum efficiency of 12.59% with enhanced phase stability under 1 sun illumination and good thermal stability at 85 ^{o}C in inert atmosphere, making it a promising large bandgap perovskite for application in tandem solar cells.

Chapter 5. PEROVSKITE-PEROVSKITE TANDEM SOLAR CELLS REACHING 80% OF THE THEORETICAL LIMIT IN PHOTOVOLTAGE

5.1 Introduction

Organic-inorganic hybrid perovskites are chemically diverse, multifunctional semiconductors that have recently generated immense interest in the field of optoelectronics and photovoltaic industry.[28,34,44,45,53,56,63] Power conversion efficiencies (PCEs) beyond 22% have been realized for perovskite solar cells (PVKSCs), which is close to single-junction Shockley-Queisser (SQ) limit.[58,353] To further improve PCE, it is highly desirable to develop all perovskite tandem solar cells, which possess merits of solution processability and low-cost, large-scale manufacturing capability inherent to hybrid perovskites. Characteristically sharp absorption onset and low open-circuit voltage loss ($V_{oc,loss}$) makes hybrid perovskites[379] ideal material for tandem application. In addition, the versatility of hybrid perovskites[56] have enabled the development of high quality photovoltaic materials over a wide-range of bandgaps (1.2-2.3 eV), which is pivotal for building all perovskite tandem solar cells.

Perovskite-perovskite tandems can be constructed by either mechanically stacking (4-terminal, 4-T) or monolithically series integrating (2-terminal, 2-T) subcells. A 4-T configuration is relatively insensitive to bandgap (E_g) matching and primarily reliant on the efficacy of individual subcells, while precise E_g matching is required in a 2-T configuration due to the need for current matching (**Figure 5.1**). Nevertheless, the 2-T configuration is preferred over 4-T because it has minimized parasitic absorption, higher practical efficiency, and is superior from the economic point of view.[380] In perspective to hybrid perovskites, PCE of ~36% is theoretically achievable using an optimal E_g combination of 1.2 and 1.8 eV in a 2-T configuration (**Figure 5.1**). Therefore,

to further advance 2-T perovskite tandems is an exciting scientific challenge which will facilitate further hybrid perovskites development and lower the PV cost to facilitate technology translation.

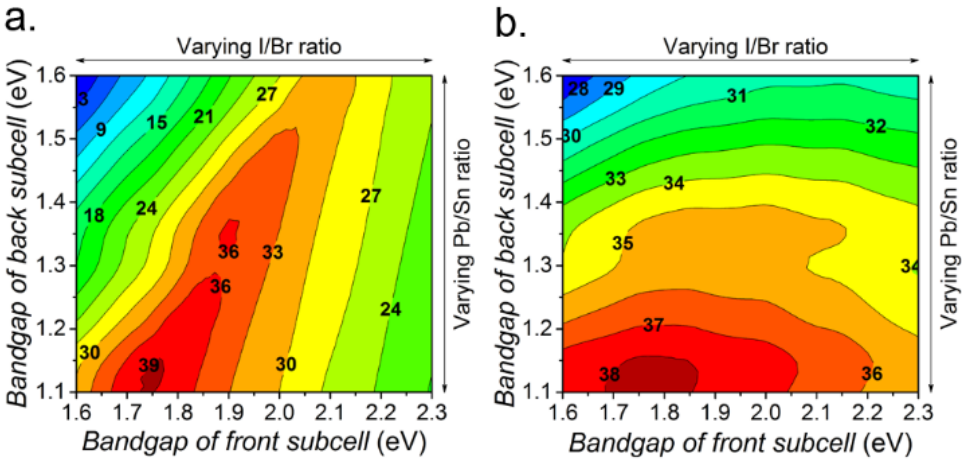

Figure 5.1. Efficiency limits for perovskite-perovskite tandem solar cells. (a) 2-terminal and (b) 4-terminal tandem configuration. Contour lines and corresponding power conversion efficiency (%) are depicted.

Earlier development of 2-T tandem PVKSCs were restricted by lacking of small E_g perovskites and difficulty in achieving orthogonal processability (PCE limited to <10%).[381,382] Although, thermal evaporation was employed to circumvent processing challenges, device performance was still limited (~15% PCE) due to non-optimized E_g combination (1.6 eV and 2 eV materials were used) and significant current-voltage (*J-V*) hysteresis.[383] Development of semitransparent PVKSCs with sputtered ITO top electrode[384] and small E_g (~1.2 eV) Pb/Sn binary perovskites[364,374,385,386] have recently enabled construction of 2-T tandems with solution processable perovskite absorbers and optimized E_g combination (1.2 eV with 1.8 eV), resulting in a PCE of ~17%.[387] However, the performance is still limited by severe photovoltage loss ($V_{oc,loss}=E_g/q - V_{oc}$).

The highest photovoltage for monolithic 2-T tandem PVKSCs with an ideal E_g combination is only ~67% of the theoretical (Shockley-Queisser) limit,[387] which is inferior to ~74% achieved in the state-of-the-art 2-T perovskite-silicon tandem (V_{oc} ~1.65 V, PCE

~23.6%)[226]. The potential of realizing high photovoltage is a distinctive advantage of such series-connected tandem architecture, however, it has not been accomplished in perovskite-perovskite tandems due to photo instability, limited V_{oc} and hysteresis of individual subcells. The theoretical limit in photovoltage for 2-T tandem is defined by the sum of $V_{oc,SQ}$ (**Figure 5.2**) for subcells, but the typical V_{oc} is lowered due to unavoidable SQ loss and avoidable non-ideal loss. Therefore, efforts to minimize non-ideal $V_{oc,loss}$ is critical for further advancement of 2-T tandem PVKSCs.

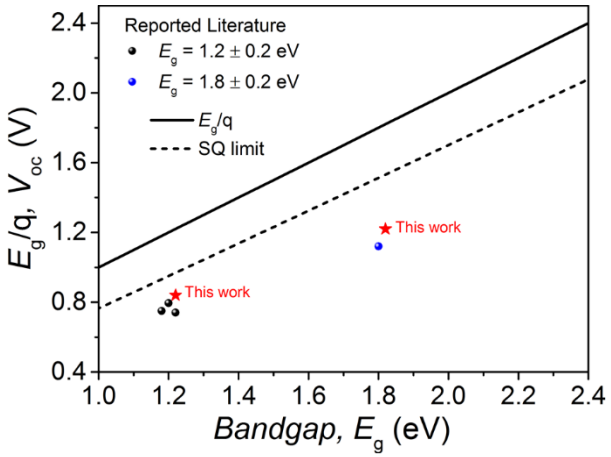

Figure 5.2. Open circuit voltage (V_{oc}) of top performing small bandgap (1.2 ± 0.2 eV) and large bandgap (1.8 ± 0.2 eV) single junction perovskite solar cells reported in literature[17,19,20] compared to this work; line corresponding to bandgap potential (E_g/q) and Shockley–Queisser limit of V_{oc} ($V_{oc,SQ}$) are also shown in the figure to provide a perspective of $V_{oc,loss}$.

In this work, we demonstrate a highly efficient ideal bandgap matched 2-T tandem PVKSCs with minimized non-ideal $V_{oc,loss}$ via improved subcell characteristics, precise current matching and engineering of tandem construction. Mitigation of non-radiative recombination centers arising from improper interfacial energetics and poor optoelectronic characteristics of absorber materials were pivotal in reducing non-ideal $V_{oc,loss}$. Enhanced quasi-fermi level splitting (QFLS) and V_{oc} realized in both small and large E_g (~1.2 and 1.8 eV) subcells were closer to the SQ limit compared to previous works (**Figure 5.2**). Optical simulations were also utilized to validate current matching criterion and identify possibilities for further improving current generation in tandem architecture. Ultimately, a stable 2-T tandem cell was demonstrated with a

high PCE of 18.5% under operating conditions with negligible *J-V* hysteresis. A high V_{oc} (1.98 V) was also realized, which is approaching 80% of the theoretical limit and by far the best for all perovskite monolithic tandem solar cells.

5.2 Experimental Methods

Materials: ITO glass (substrate: soda lime float glass with SiO_2, <15 Ω sq^{-1}) was purchased from Colorado Concept Coatings LLC. PbI_2, $PbBr_2$, SnI_2, CsI and all solvents used in this work were purchased from Sigma-Aldrich. $IC_{60}BA$ and C_{60} were purchased from American Dye Source, Inc. MAI and Bis-C_{60} were synthesized as per previously reported methods.[247,315]

Solution preparation: For large bandgap perovskites, $MA_{0.9}Cs_{0.1}Pb(I_{0.6}Br_{0.4})_3$ precursor solution was prepared by dissolving MAI (0.143 g), CsI (0.026 g), PbI_2 (0.184 g) and $PbBr_2$ (0.220 g) in mixed solvent (1 ml, volume ratio 3:7) of dimethyl sulphoxide (DMSO) and γ-butyrolactone (GBL) and stirred at 60 °C for 1 h. For small bandgap perovskites, $MAPb_{0.5}Sn_{0.5}I_3$ precursor solution was prepared by dissolving MAI (0.159 g), PbI_2 (0.254 g), SnI_2 (0.186 g) and SnF_2 (0.008 g) in Dimethylformamide (0.7 mL) and stirred at 60 °C for 1 h; additional DMSO (0.3 ml) was added into the above precursor just before use. For fullerene ETLs, C_{60} or $IC_{60}BA$ (15 mg/mL) was dissolved in dichlorobenzene and stirred at 80 °C for 2 h. For fullerene surfactant, Bis-C_{60} (2 mg/mL) in isopropyl alcohol was dissolved using sonication (typically 1 h). For NiO_x, precursor solution was prepared by dissolving Nickel (II) acetate tetrahydrate (124.4 mg) in ethanol (5 mL) and ethanolamine (30 μL) was added to it; the mixture was stirred at 60 °C for 2 h. PEDOT:PSS (Baytron PVP AI 4083) solution was allowed to reach room temperature before usage. All solutions were filtered with 0.22 μm PVDF filters before spin coating.

Device fabrication: ITO glass substrates were initially masked using Kapton tape as per the required pattern (**Figure S11**); then zinc powder was applied on the substrates which were subsequently dipped into a beaker with concentrated hydrochloric acid for 10 s and then completely washed with water. Afterwards, sequential steps of ultrasonication for 10 min in detergent, deionized water, acetone, and isopropanol alcohol was used to clean ITO glass. Cleaned ITO glass substrates were subjected to UV ozone treatment (10 min) before start of device fabrication. NiO_x precursor was spin coated onto the clean ITO glass at 3000 rpm for 60 s and annealed at 400 ^oC for 1 h in air. After this step, substrates were transferred into N_2-filled gloveboxes. $MA_{0.9}Cs_{0.1}Pb(I_{0.6}Br_{0.4})_3$ precursor solution was spin coated onto the substrate using 2-step spin program (1000 rpm for 15 s and 4000 rpm for 45 s); during the last 20-10 s of the second spin-coating step, toluene (0.7 ml) was dropped onto the spinning substrate and the substrates were annealed at 100 ^oC for 10 min using a hot plate. Subsequently, C_{60} was evaporated onto the perovskite films with a steady deposition rate (~0.2 Å/s). Then, Bis-C_{60} solution was spin coated onto at 3000 rpm for 60 s. At this stage, substrates were removed from glovebox for ITO sputtering. Around 100 nm ITO was deposited using a Lesker Sputter system (DC based magnetron sputtering) with low power (150 W) under 3 mTorr of Ar. Immediately, PEDOT:PSS solution was spin-coated on the sputtered ITO at 5000 rpm for 30 s and annealed at 100 °C for 10 min in ambient. Then substrates were transferred into glovebox again for device completion. $MAPb_{0.5}Sn_{0.5}I_3$ precursor solution was dropped on PEDOT:PSS and spin-coated at 5000 rpm for 30 s in glove box; toluene (0.7 mL) was quickly dropped onto the spinning substrate after 10 s elapse. The resulting perovskite films were annealed at 70 °C for 5 min. Subsequently, $IC_{60}BA$ or C_{60} solution was spin coated using 1500 rpm for 55 s and 4000 rpm for 5 s followed by annealing at 70 °C for 5 min. Then, Bis-C_{60} surfactant solution was spin coated on top at 3000 rpm for 60 s.

Finally, a 150 nm thick silver (Ag) electrode was evaporated under high vacuum (<1×10 $^{-6}$ Torr) through a shadow mask (14 mm^2). The entire fabrication process and electrode design for tandem cells are illustrated in detail in **Figure 5.3**. Single junction solar cells were fabricated as per device structure using the similar procedure. All single junction and tandem solar cells were characterized by applying a shadow mask with an aperture area of 10 mm^2.

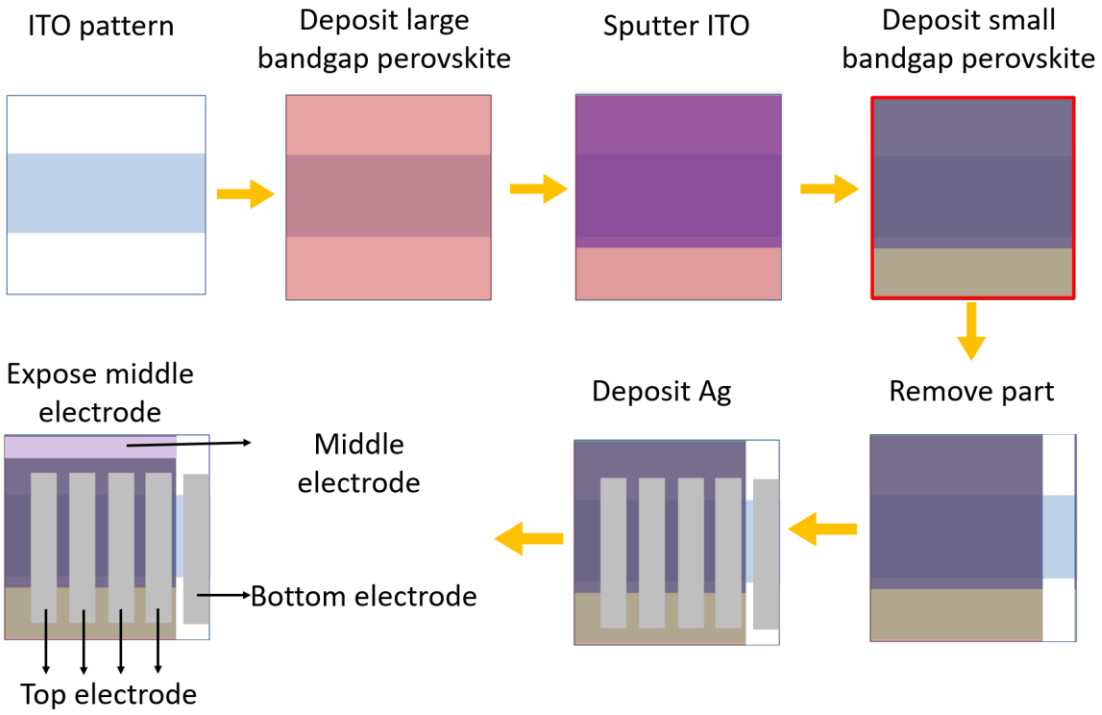

Figure 5.3. Electrode design and fabrication process for 2 terminal perovskite-perovskite tandem solar cells.

Photovoltaic characterization: Large bandgap PVKSCs were tested using Class A solar simulator (Solar light 16S-300) inside glovebox, whereas small bandgap and 2-T tandem PVKSCs were tested using Class AAA solar simulator (OAI TriSol) in ambient without encapsulation. To account for spectral mismatch factor, solar simulator was calibrated to match the integrated current calculated from corresponding EQE. A calibrated reference silicon photodiode was used to measure light intensities. *J-V* scans were measured using Keithley 2400 Source Meter at different scan rates, by varying delay times at constant step size (0.01 V); delay times of 10, 100 and 1000 ms correspond to scan rates 1, 0.1 and 0.01 V/s respectively. Typical forward *J-V* scans (short

circuit, SC → open circuit, OC) measured at 1 V/s were used to calculate solar cell performance metrics, unless specified. Hysteresis characteristics were measured using an uninterrupted sequence of forward and reverse scans (SC→OC→SC). Stabilized PCE were determined using steady-state current measurements at an applied voltage corresponding to maximum power point without encapsulation. Light intensity dependent measurements were performed using a set of neutral density filters; *J-V* characteristics were measured under eight different intensities ranging between 0.5 to 100 mW/cm^2. The linear fits of data had high degree of accuracy, with R-squared values generally > 0.98. Analysis and interpretation of illumination intensity dependent *J-V* data are in accordance to literature.[316,386,388] For all measurements under illumination, the shutter was opened just before measurement and no intentional light or electrical bias soaking was used. EQE measurements were performed using a setup consisting of xenon lamp (Oriel, 450W) as light source, monochromator (Newport Cornerstone 130), optical chopper, lock-in amplifier (Stanford Research Corp SR830), and a NIST-certified Si-photodiode (Thorlabs FDS 100-CAL) for calibration. The fluctuation of xenon arc lamp source was within 5% during the entire period of measurements. For tandem solar cells, EQE spectra were measured by contacting the middle electrode (sputtered ITO) with bottom (ITO) and top (Ag) electrodes respectively to measure front and back subcells individually. EQE spectra were integrated over AM 1.5G photon-flux to attain photocurrent density. All EQE measurements were carried out in ambient without any device encapsulation.

Thin-film characterization: A Bruker D8 Discover 2-D XRD with a Cu Kα source was used for XRD measurements; 2D scans were subsequently integrated to obtain the diffraction pattern. An FEI Sirion scanning electron microscope was used for all SEM characterization with 5 kV used for imaging. Absorption measurements were carried out using Varian Cary 5000 UV-

Vis-NIR spectrometer. Film thicknesses were measured using Bruker DektakXT stylus profiler. The UPS spectra were measured by a Kratos Axis Ultra DLD photoelectron spectrometer with an incident radiation of He I (21.2 eV).

Transient absorption spectroscopy (TAS): All spectra were taken using the Libra laser system (50 fs FWHM at 80MHz repetition rate, 800 nm fundamental wavelength) combined with Helios spectrometer (Ultrafast Systems). The fundamental beam was split into two beamlines by an 80/20 beam-splitter. Pump wavelength (365 nm) was generated by an OPerA optical parametric amplifier (Coherent, Inc.) after splitting the fundamental beam. A 365 nm bandpass filter was used to eliminate the effect of residual fundamental beam. A white continuum probe light was generated by the delayed fundamental beam focused on Ti:Sapphire crystal. The pump fluence was modulated by 2 consecutive neutral density filters. The diameter of spot size is 1 mm. All samples for TAS were prepared on glass and encapsulated by another glass with epoxy under inert nitrogen environment to avoid quenching at the air interfaces and maintain open-circuit condition. For measurements with interlayers, carrier populations were optically corrected to account for interlayer absorption.

Photoluminescence measurements: Time-resolved photoluminescence (TRPL) studies were carried out following previously reported methods.[369] PL spectra, spatial statistics of quasi Fermi-level splitting, and trends with time were acquired using a modified Horiba LabRAM HR-800, a 532 nm laser diode excitation source, and a 10x objective (NA=0.25). The adjustable confocal hole before the monochromator was set at 800 um. A 150 gr/mm Czerny-Turner monochromator blazed at 1200 nm was used, and the emitted light was collected with a silicon CCD array detector. For maps, the PL collection time was set to 1 s, and the amount of time that the laser stayed at any given location was less than 1.5 s. Spectral artifacts caused by the detector

and the optical path between the sample and detector were accounted for by creating a relative correction file with a black body source (IR-301, Infrared Systems Development Corporation) set to 1050 °C. A 10 μm pin-hole was used to fix the spectral photon flux to the detector and allow an absolute-photons-per-count calibration factor to be measured. An Oriel optical power meter and beam profilometer were used to measure the illumination intensity and excitation diameter, respectively. The N-Suns illumination intensity was calculated by dividing the photon flux inside the FWHM of the Gaussian beam by the above-bandgap photon flux of the AM1.5 GT solar spectrum. The laser diameter was measured to be 10 μm and the FWHM of the Gaussian distributed laser intensity was measured to be 6 μm. All AIPL measurements were conducted with the HP samples in a nitrogen-filled KF-flanged cell with a Kodial borosilicate glass window. Transient PL were measured using single-photon avalanche diodes based on InGaAs with home-built focusing and collection optics. Picosecond pulsed laser diodes (Picoquant PDL 800-B) at 470 nm and 640 nm wavelengths were used as an excitation source.

PL decay modelling and calculation details: We assumed that carrier dynamics after relaxation (>10 ps) is governed by monomolecular and bimolecular recombination for our excitation fluence.

$$\frac{dn}{dt} = -k_{em}n - k_2 n^2 \quad (eq. 5.1)$$

where k_{em} is effective monomolecular decay rate involving effective compensation between non-radiative losses k_{nr} and charge repopulation rate k_{rp}, k_2 is the product of initial relaxed photocarrier density (n_0) and bimolecular recombination rate ($\overline{k_2}$), and *n* is normalized carrier density with respect to n_0. Moreover, also assuming persistent direct bandgap structure of metal halide framework, PL emission is facilitated through radiative bimolecular recombination upon

excitation at wavelength below high energy band (around 520 nm) and PL intensity can be expressed as follows:

$$\frac{I(t)}{I_0} = k_2 n^2 \quad (eq.5.2)$$

In this case, n_0 was calculated by Beer-Lambert's law, $n_0 = (I_{ex}\lambda/hc)(1 - e^{-\alpha L})/L \sim I_{ex}\lambda/Lhc)$, where I_{ex} is fluence at wavelength λ, α is absorption coefficient at λ and L is thickness. Eq.5.1 and Eq.5.2 were numerically solved with parametric optimizations to fit the decay data. In this case, the characteristic lifetime (τ) and PL quantum yield (QY) can be acquired as follows, $\tau = \frac{1}{k_1 + \overline{k_2} n_0}$; $QY = \frac{\overline{k_2} n_0}{k_1 + k_2^0 n_0}$.

At perovskite surfaces, charge carriers are mostly lost through defective sub-gap states, where $k_{em} \sim k_{nr}$. With addition of C_{60} layer, the mismatched contact facilitates charge transfer to interlayer and further promotes non-radiative losses under open circuit condition. The loss comes mostly through either recombination within the interlayer or trap-assisted interfacial recombination to the ground state of perovskite. However, in case of $IC_{60}BA$, intimate contact with well-matched energy level effectively suppresses losses during the charge transfer process, so that $k_{em} \ll k_{nr}$. This behavior can account for delayed bimolecular recombination as well as reduced monomolecular recombination observed in transient absorption and emission spectroscopy. More detailed analysis is outside the scope of this work and is currently being conducted as a separate research.

Quasi-fermi level splitting calculations: Quasi Fermi-level splitting values for high and low bandgap samples were calculated using PLQY method,[4] shown in the following equation: $\Delta\mu_{QY} = \Delta\mu^{SQ}(E_g, T) + k\,T\,ln(PLQY_{Ext})$, where $\Delta\mu_{QY}$ is the quasi Fermi-level splitting, $\Delta\mu^{SQ}$ is

the detailed balance limit quasi Fermi-level splitting, E_g is the bandgap, T is the temperature, $PLQY_{Ext}$ is the external photoluminescence quantum yield, and k is the Boltzmann constant. We assume the bandgap is same as PL peak position and the temperature is 315 K.

Optical simulations: Spectroscopic Ellipsometry, SE (Woollam-M-2000) was used to measure refractive indices (*n, k*) of every layer in tandem architecture. All layers were deposited individually on glass for this measurement to enable unambiguous modeling of SE data. Spot size was ~3 mm and data was acquired in transmission mode (0°) and three different angles in reflection mode (55°, 65°, 75°). Psi and delta values obtained from SE measurements were subsequently modeled (Woollam CompleteEASE) using Kramers-Kronig (KK) consistent B-Spline model to obtain optical constants (*n, k*).[389] Data at all angles were fitted simultaneously to avoid correlation and mean squared error (MSE) values were low. Fit parameter uniqueness, specifically for thickness was checked to further establish the reliability of fit. The values were in excellent agreement with the experimentally measured thickness (using profilometer). Absorption coefficient (α) was calculated from *k* using the relation, $\alpha = 4\pi k / \lambda$. Custom-made Matlab program based on transfer matrix method (TMM)[390] was used for optical simulations. Photocurrent generated in active layers were calculated from optical simulations based on an assumption of 100% internal quantum efficiency (no electrical losses). Individual layer absorption along with reflectance and transmittance of entire device stack extracted from optical simulations were coupled with experimentally measured EQE to determine contribution of different factors for light extinction.

Efficiency simulation for tandem solar cells: Variation in power conversion efficiency as a function of subcell bandgaps for 2-terminal and 4-terminal tandem configurations shown in **Figure 5.1** were obtained based on Shockley-Queisser detailed balance calculations.[354] For 2-terminal

configuration, lowest current of two subcells was used for tandem due to the requirement for current matching. Additionally, to account for practical losses, in 2-terminal configuration we assume EQE = 90% for subcells, whereas in 4-terminal configuration we assume EQE = 90% for front subcell and EQE = 81% for back subcell due to the presence of additional substrate and electrode.

Estimation of Solar-to-hydrogen (STH) efficiency for water splitting: Connecting an electrolyzer in series with a solar cell is an indirect approach for water splitting which is highly promising for hydrogen generation and storage of solar energy.[391] The practical potential required for electrochemical water splitting is higher than the theoretical minimum (1.23 V) due to the penalty from system overpotential (electrode activation and other resistances) and is highly dependent on the choice of catalysts. Recent development of electro-catalysts for efficient evolution of hydrogen and oxygen has significantly reduced the overpotential requirements, making water splitting possible at low potentials around 1.5-1.6 V.[392–397] Accordingly, when coupled with an electrolyzer employing the state-of-the-art catalysts, the highly efficient 2-T perovskite tandem solar cells with minimized photovoltage loss ($V_{oc,loss}$) developed in this work can be used to carry out unassisted water splitting because of its high operating voltage (1.55 V) at the maximum power point.

Solar-to-hydrogen (STH) efficiency for such a photovoltaic-electrolysis system strongly depends on the conversion efficiency of solar cell (η_{sc}), Faradaic efficiency (η_F), efficiency due to overpotential (η_{ov}) and matching efficiency between the operation point and the maximum power point of solar cell (η_{op}). The resultant STH efficiency for overall water splitting can be expressed as follows:[391] $STH = \eta_{sc} * \eta_F * \eta_{ov} * \eta_{op} = \frac{\Delta_f E * J_{op} * \eta_F}{P_{sun}}$

where, $\Delta_f E$ is the minimum required voltage to produce hydrogen from water (1.23 V for the standard condition), P_{sun} is the energy of the sun light (100 mW/cm^2 for standard AM 1.5 illumination), η_F is the Faradaic efficiency and J_{op} is the operating current. Based on the assumption that the photovoltaic-electrolysis setup is operated close to the maximum power point of the 2-T perovskite tandem solar cell (V_{op} = 1.55 V and J_{op} = 12 mA/cm^2) and Faradaic efficiency is 100% (η_F = 100), we have: $STH = \frac{1.23*12*100}{100} = 14.76\%$.

5.3 Results and Discussion

5.3.1 Small Bandgap (~1.2 eV) PVKSCs

Although the early development was hindered by poor film morphologies and interfacial issues, Pb/Sn binary perovskite ($MAPb_{1-x}Sn_xI_3$) alloys have enabled the realization of the small E_g of ~1.2 eV.[364,374,398,399] A wide-range of processing techniques (solvent washing, hot casting, 2-step and anti-solvent extraction) and mixing of organic cations (methylammonium, formamidinium, cesium) were explored to attain optimal film coverage, which eventually improved PCE of the small E_g PVKSCs to 12-15%.[1,385–387,400] These works utilize commonly employed PEDOT:PSS and $PC_{61}BM/C_{60}$ as hole-transporting layer (HTL) and electron-transporting layer (ETL), respectively. However, compositional modification strongly perturbs frontier energy levels and results in energetic mismatch at interfaces.[1] This imposes severe limitation on device characteristics (high $V_{oc,loss}$, *J-V* hysteresis and instability under operating conditions) which are deleterious for tandem application and thus selecting appropriate interlayer is crucial.

With optimized processing conditions and additive formulation, a phase pure $MAPb_{0.5}Sn_{0.5}I_3$ film was obtained with homogenous coverage and excellent crystallinity with a E_g

of ~1.22 eV (**Figure 5.4**). There is a significant mismatch between conduction band minimum (CBM) of $MAPb_{0.5}Sn_{0.5}I_3$ and the lowest unoccupied molecular orbital (LUMO) of C_{60}.[1] The difference in energy levels can be reduced by using an alternate fullerene variant, Indene-C_{60} bis-adduct ($IC_{60}BA$) as ETL (**Figure 5.5a**). To access its impact on device characteristics, p-i-n PVKSCs using PEDOT:PSS as HTL and C_{60} or $IC_{60}BA$ as ETL were fabricated.

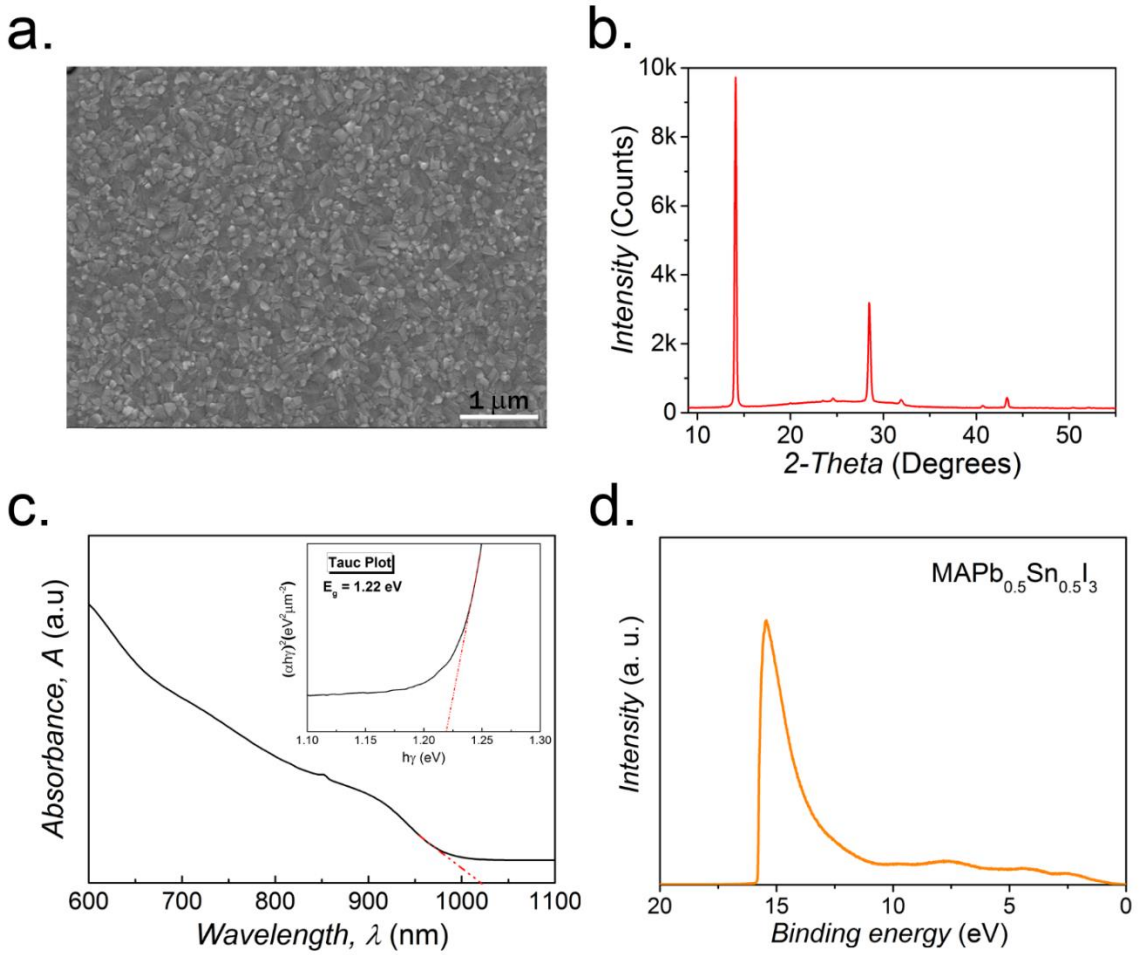

Figure 5.4. $MAPb_{0.5}Sn_{0.5}I_3$ based small bandgap perovskites. a-d, UV-vis absorption spectra with Tauc plot in figure inset (a), scanning electron microscope (SEM) image (b), x-ray diffraction (XRD) pattern (c), and UPS spectra (d) illustrating thin film characteristics of $MAPb_{0.5}Sn_{0.}5I_3$ based small bandgap perovskites.

Choice of ETL strongly perturbed *J-V* characteristics of resultant devices (**Figure 5.5b**). Despite marginal gain in J_{sc} due to higher electron mobility of C_{60},[124] devices with C_{60} showed lower V_{oc} (0.6-0.7 V) and PCE (~10%) with apparent inverted hysteresis (higher V_{oc}, *FF* in forward scan

compared to reverse scan). Conversely, much higher V_{oc} (~0.84 V) and PCE (~15%) with negligible hysteresis could be achieved using $IC_{60}BA$. Contrast in *J-V* characteristics was persistent at different scan rates ranging from 0.01 to 1 V/s. The difference was also evident in the stabilized maximum power output (**Figure 5.5c**), where device with C_{60} shows a significant decay compared to $IC_{60}BA$ which does not show any decay even after 1000 s.

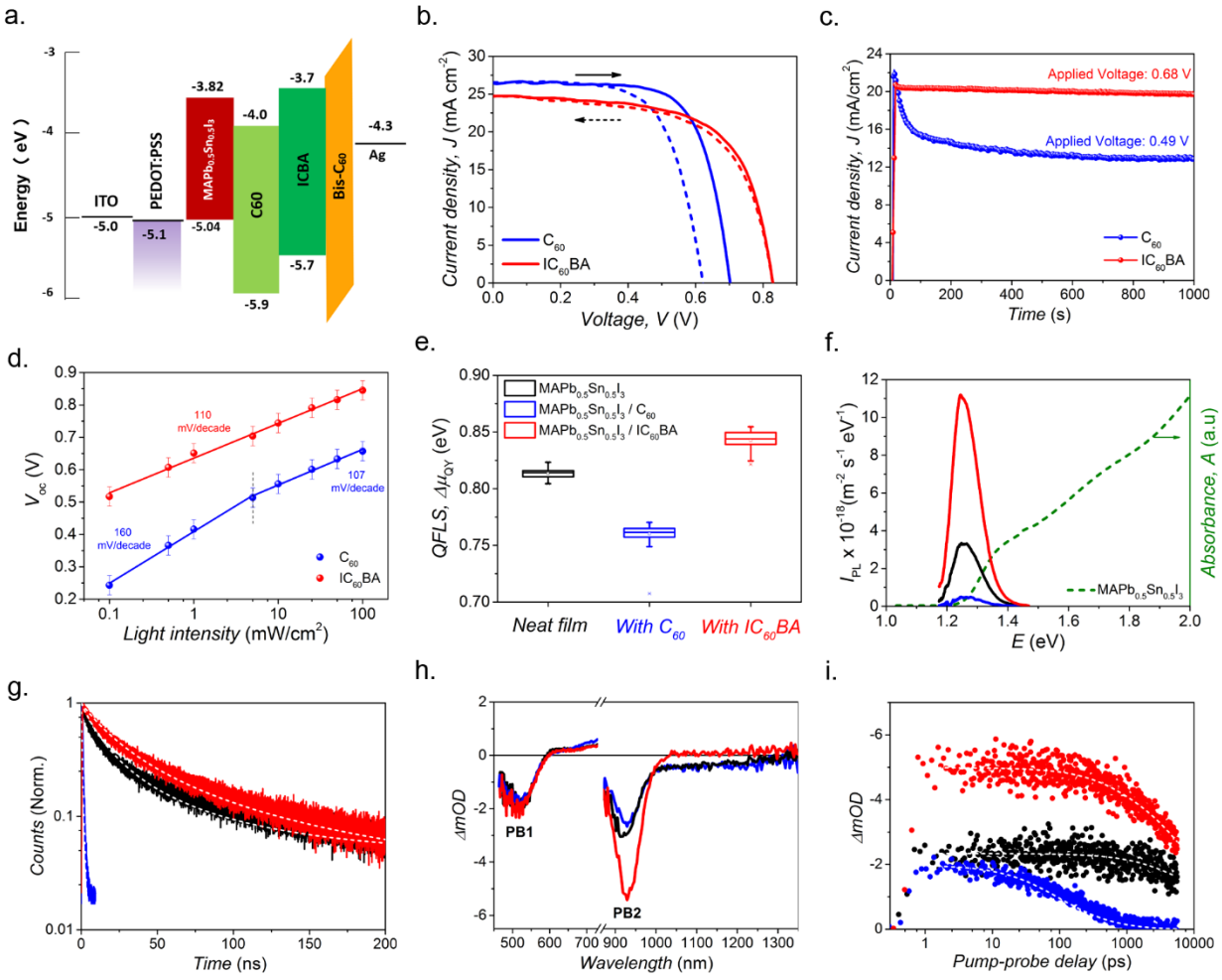

Figure 5.5. Photovoltaic and optoelectronic characteristics of small bandgap (~1.2 eV) perovskites. a-d, Energy level diagram (a), Typical J-V characteristics (b), steady-state current under AM1.5 illumination at an applied voltage corresponding to MPP (c), and light intensity dependence of V_{oc} with corresponding slopes obtained by linear fits (d) for $MAPb_{0.5}Sn_{0.5}I_3$ PVKSCs with C_{60} and $IC_{60}BA$ ETLs. e-g, Quasi-fermi level splitting values (e), photoluminescence spectra (f), transient photoluminescence (g), transient absorption spectra showing two major photo-bleaching signals (PB1 and PB2) at pump-probe delay of 2 ps (h), and kinetics of band edge photo-bleaching (i) for neat $MAPb_{0.5}Sn_{0.5}I_3$, $MAPb_{0.5}Sn_{0.5}I_3$ / C_{60} and $MAPb_{0.5}Sn_{0.5}I_3$ / $IC_{60}BA$ films. Box and whisker plots in (e) show spatial average statistics where boxes are 25-75%, whiskers correspond to 1.5 interquartile range and inner line is median.

The observed behavior is closely tied to the electronic nature of $MAPb_{0.5}Sn_{0.5}I_3$/ETL interface rather than any processing artifact in devices with C_{60}, demonstrated by similarity between devices with solution processed and thermally evaporated C_{60} (**Figure 5.6a**). Demonstration of inverted hysteresis and lower V_{oc} in devices with C_{60}:$IC_{60}BA$ (1:3) blend ETL (**Figure 5.6b**) further reinforces this claim. These results unambiguously demonstrate the superiority of $IC_{60}BA$ compared to C_{60} as ETL in small E_g PVKSCs and establish an intimate link between interfacial properties and device characteristics. The contrast in characteristics of devices with C_{60} ETL compared to previous works[1,387,401] is related to the difference in composition and frontier energy levels of the employed Pb/Sn binary perovskite alloys.

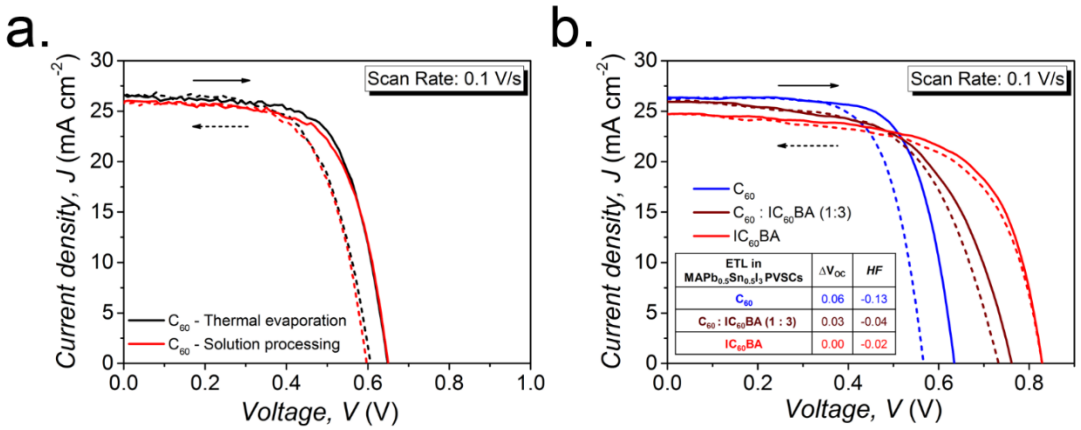

Figure 5.6. Understanding characteristics of *J-V* hysteresis with C_{60} ETL. (a) *J-V* hysteresis of $MAPb_{0.5}Sn_{0.5}I_3$ PVKSCs with solution processed and thermal evaporated C_{60} as ETLs. (b) *J-V* hysteresis of $MAPb_{0.5}Sn_{0.5}I_3$ PVKSCs with different ratios of C_{60} and $IC_{60}BA$ mixture as ETL; table in figure inset compares corresponding change in V_{oc} difference between forward and reverse scan ($\Delta V_{oc} = V_{oc,f} - V_{oc,r}$) and hysteresis factor $\left(HF = \frac{Area_{J_{sc}\rightarrow V_{oc}}}{Area_{V_{oc}\rightarrow J_{sc}}}\right)$.

The light intensity dependence of V_{oc} in devices was investigated to understand the factors influenced by the choice of ETL that determine hysteresis behavior and V_{oc} (**Figure 5.5d**). Devices with C_{60} show two distinct regions (transition from higher to lower slope as the light intensity increases), whereas devices with $IC_{60}BA$ show only a constant slope in the entire range of intensities. Observed slopes are close to previously reported values for Sn-based perovskites[386] and a similar transition of slopes has been previously observed in PVKSCs with defective

TiO_2/$MAPbI_3$ interface.[316] Differences in V_{oc} dependence on light intensity[388] clearly manifests that more pervasive trap-assisted recombination exists in devices with C_{60} compared to devices with $IC_{60}BA$ and is apparently an indication of defective $MAPb_{0.5}Sn_{0.5}I_3/C_{60}$ interface. Sub-bandgap surface defects and interfacial fermi level pinning are likely the origin for such deleterious interface and associated consequences on device performance.[167,301,402–404] This was examined by evaluating the quasi-fermi level splitting (QFLS, $\Delta\mu_{QY}$) in $MAPb_{0.5}Sn_{0.5}I_3$ films with C_{60} and $IC_{60}BA$. QFLS enhanced with $IC_{60}BA$ compared to neat $MAPb_{0.5}Sn_{0.5}I_3$ and films with C_{60} (**Figure 5.5e**), evidently illustrating the significance of rational interlayer selection employed here. Higher QFLS in $MAPb_{0.5}Sn_{0.5}I_3$ (0.84±0.01 eV) realizable with $IC_{60}BA$ correlates well with device V_{oc} (0.84 V) and demonstrates improved quality of interfacial contact.

Additional transient spectroscopic studies were carried out to further pinpoint the impact of interfaces. Recent studies by Petrozza et al.[404] and Ginger et al.[92] clearly illustrate that an optimized contact should have non-quenched PL at open-circuit due to minimized non-radiative interfacial recombination. Accordingly, at open-circuit we observe that PL is dramatically quenched with addition of C_{60} to $MAPb_{0.5}Sn_{0.5}I_3$, whereas an opposite trend is observed with addition of $IC_{60}BA$ (**Figure 5.5f**). In fact, we observe slower PL decay and higher photoluminescence quantum yield (PLQY) with $IC_{60}BA$ compared to that of the neat $MAPb_{0.5}Sn_{0.5}I_3$ films, which highlights the dramatic reduction in non-radiative recombination alike above results (**Figure 5.5g**). Furthermore, femtosecond transient absorption spectroscopy[138,376,377] also revealed distinct beneficial characteristics of interfacial contact with $IC_{60}BA$ (**Figure 5.5h**).

Under same excitation fluence (0.1 $\mu J/cm^2$), both C_{60} and $IC_{60}BA$ exhibited a similar population quenching of photo-bleaching at high energy band (PB1) corresponding to initial

ultrafast charge transfer in vicinity of interfaces along with carrier cooling. However, photo-bleaching at the band edge (PB2) of $MAPb_{0.5}Sn_{0.5}I_3$ films with $IC_{60}BA$ showed drastically higher populations (**Figure 5.5h**) illustrating that both hot and relaxed charge carriers do not suffer from charge transfer losses at the interface during population/repopulation of perovskite films unlike interface with C_{60}. The trend is even clearer in the kinetics of PB2 and PL (**Figure 5.5g, i**). A slow characteristic decay time despite higher band-edge population and strong bimolecular recombination characteristics[92,350] support the formation of intimate contact between $MAPb_{0.5}Sn_{0.5}I_3$ and $IC_{60}BA$ (**Table 5.1**).

Table 5.1. PL metrics extracted from parametric optimization. Initial values for the fitting were given in ratio according to the measured QY values

Sample	n_0 **[10^{16} cm^3]**	k_{em} **[10^9 s^{-1}]**	k_2/n_0 **[10^{-9} cm^3 s^{-1}]**	τ **[ns]**	$\%QY$ **(calc.)**	$\%QY$ **(meas.)**
$MAPb_{0.5}Sn_{0.5}I_3$	3	0.0095	0.0109	101.7	0.031	0.02
$MAPb_{0.5}Sn_{0.5}I_3$ / C_{60}	3	0.3944	0.0034	2.5	0.00026	<0.001
$MAPb_{0.5}Sn_{0.5}I_3$ / $IC_{60}BA$	3	0.0034	0.0210	186.9	0.084	0.05

The intimate contact alleviates non-radiative recombination losses from intrinsic and photo-induced sub-gap defect states[404–406] during charge transfer process across $IC_{60}BA$, in contrast to the mis-matched $MAPb_{0.5}Sn_{0.5}I_3/C_{60}$ interface quenching charge carriers non-radiatively and hindering repopulation process at interfaces. Deleterious interface formation explains the appearance of inverted hysteresis in devices with C_{60}, where pile up charges at the corresponding interface would beneficially impact electron extraction as recently demonstrated by Tress et al.[167] The observations agree well with previously determined analogous correlations between interfacial trap sites, device hysteresis and V_{oc}.[301,379,402] Striking difference in hysteresis behavior between devices with C_{60} and $IC_{60}BA$ is therefore itself an elegant demonstration of

interfaces role in $MAPb_{0.5}Sn_{0.5}I_3$ and signifies importance of $IC_{60}BA$ to realize stable devices with minimized photovoltage loss (**Figure 5.5b-c**).

Relatively small PLQY, faster PL decay along with population and decay behavior of PB2 illustrate dominance of non-radiative losses over beneficial impact of high C_{60} electron mobility on charge transfer at the $MAPb_{0.5}Sn_{0.5}I_3/C_{60}$ interface, which ultimately constrained device performance. With $IC_{60}BA$ we not only mitigate hysteresis related instability but also realize a remarkably high V_{oc} (0.84 V) which is ~88% of the SQ limit. Stable devices with small $V_{oc,loss}$ (~0.38 V) realized here is the lowest among reported small E_g PVKSCs (**Figure 5.2**) and is comparable to the state-of-the-art inorganic photovoltaic technologies.[34] This provides a platform to realize high V_{oc} in 2-T tandem PVKSCs.

5.3.2 Large Bandgap (~1.8 eV) PVKSCs

Development of large E_g perovskites with bandgap between 1.70 to 1.75 eV (by halide mixing) has been driven by the motivation for coupling with silicon solar cell in tandem configuration.[13,355] A challenging issue in the development of large E_g perovskites is material's vulnerability to light-induced phase segregation, which tends to result in high $V_{oc,loss}$ and instability under operating conditions.[369,407] Several approaches like enhancing grain size, mixing of FA and Cs cations, substituting Pb with Sn have been successfully utilized to alleviate adverse impact of phase segregation and realize efficient PVKSCs with E_g ~1.73 eV.[13,355,370] However, the lowest E_g (~1.2 eV) perovskite requires complementary E_g of ~1.80-1.85 eV for current matching in 2-T tandem PVKSCs (**Figure 5.1**). To realize photo-stable, efficient PVKSCs based on ~1.8 eV E_g is an arduous task because phase segregation is sensitive to film composition, morphology, and processing conditions.[369,407,408] Even the state-of-the-art PVKSCs based on photo-stable perovskite with ~1.8 eV E_g still suffer from huge $V_{oc,loss}$ (**Figure 5.2**).[387]

Methylammonium based large E_g perovskites was chosen to avoid the potential formation of deleterious non-perovskite phases and maintain processing temperatures ≤ 100°C. A E_g of ~1.8 eV was realized using $MAPb(I_{0.6}Br_{0.4})_3$ and phase segregation in this composition has been alleviated previously by engineering internal bonding environment through partial substitution of lead by tin, but suffered from low V_{oc} due to poor PLQY.[13] To overcome photo instability without compromising optoelectronic quality, we chose to engineer the lattice in an analogous manner, via partial replacement of MA by Cs.

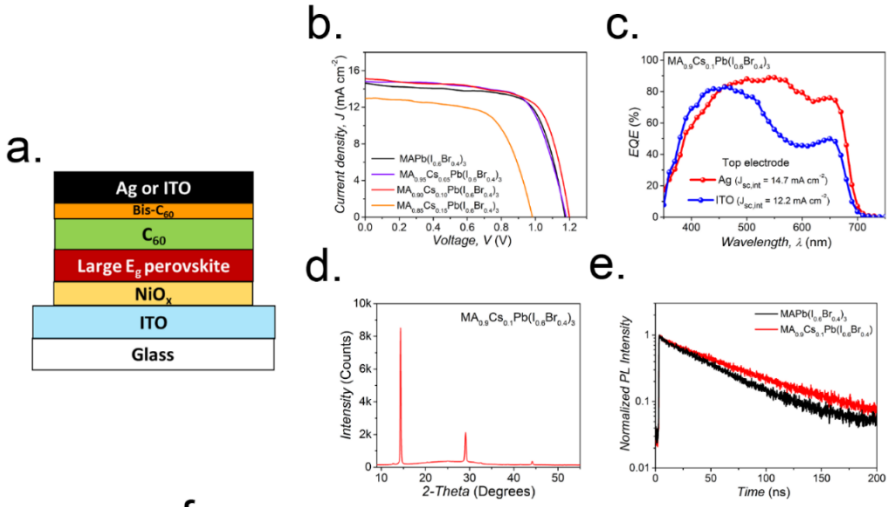

f.

	V_{oc} (V)	J_{sc} (mA/cm²)	FF	PCE (%)
$MA_{0.95}Pb(I_{0.6}Br_{0.4})_3$	1.17	14.7	0.70	12.0
$MA_{0.95}Cs_{0.05}Pb(I_{0.6}Br_{0.4})_3$	1.18	14.9	0.69	12.1
$MA_{0.9}Cs_{0.10}Pb(I_{0.6}Br_{0.4})_3$	1.20	15.1	0.69	12.5
$MA_{0.85}Cs_{0.15}Pb(I_{0.6}Br_{0.4})_3$	0.98	12.9	0.64	8.1

Figure 5.7. Large bandgap perovskites. (a) Device structure for single junction large bandgap PVKSCs. (b) Typical *J-V* characteristics of $MA_{1-x}Cs_xPb(I_{0.6}Br_{0.4})_3$ PVKSCs with different amounts of Cs incorporation. (c) EQE spectra for $MA_{0.9}Cs_{0.1}Pb(I_{0.6}Br_{0.4})_3$ PVKSCs with ITO and Ag top electrode. (d) X-ray diffraction (XRD) pattern for $MA_{0.9}Cs_{0.1}Pb(I_{0.6}Br_{0.4})_3$. € Comparison of PL decay for $MAPb(I_{0.6}Br_{0.4})_3$ and $MA_{0.9}Cs_{0.1}Pb(I_{0.6}Br_{0.4})_3$ films on glass. (f) Performance metrics for $MA_{1-x}Cs_xPb(I_{0.6}Br_{0.4})_3$ PVKSCs with different amounts of Cs incorporation.

A series of single junction PVKSCs (device structure in **Figure 5.7a**) were fabricated to optimize the amount of Cs incorporated in $MAPb(I_{0.6}Br_{0.4})_3$. The device with 10% Cs showed the best device performance (**Figures 5.7b-c, f**) with high V_{oc} of 1.2 V and a PCE of 12.5% with negligible *J-V* hysteresis (**Figure 5.8a**). $MA_{0.9}Cs_{0.1}Pb(I_{0.6}Br_{0.4})_3$ films were phase pure (**Figure**

5.7d) and exhibited relatively longer lifetime (**Figure 5.7e**) due to improved crystallinity with Cs incorporation.[408] Moreover, striking differences were observed in photo-stability of $MAPb(I_{0.6}Br_{0.4})_3$ and $MA_{0.9}Cs_{0.1}Pb(I_{0.6}Br_{0.4})_3$ based PVKSCs. With Cs incorporation, devices were photo-stable and current density at the maximum power point (MPP) was constant under continuous illumination (1 h), whereas devices without Cs showed significant decay in less than 10 min of illumination (**Figure 5.8b**). This stability under operating conditions is critical for 2-T tandem, where any change in subcell behavior will impact current matching and significantly degrade tandem performance.

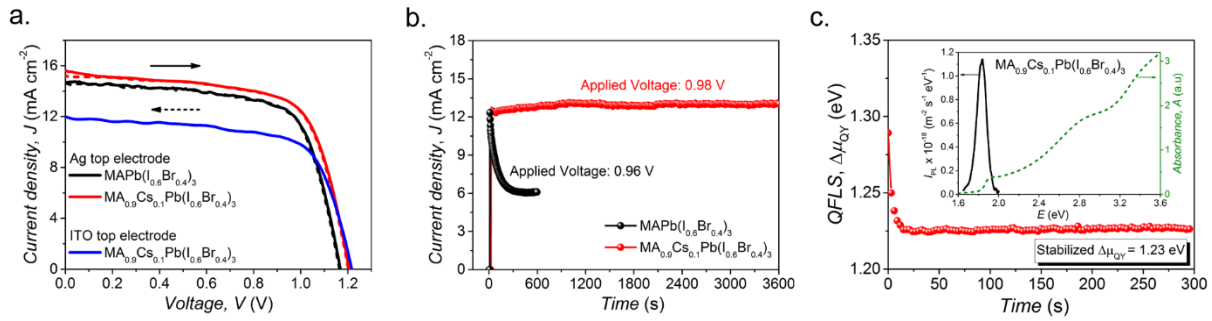

Figure 5.8. Photovoltaic and optoelectronic characteristics of large bandgap (~1.8 eV) perovskites. a-b, Typical J-V characteristics (a) and steady-state current under AM1.5 illumination at an applied voltage corresponding to MPP (b) of $MAPb(I_{0.6}Br_{0.4})_3$ and $MA_{0.9}Cs_{0.1}Pb(I_{0.6}Br_{0.4})_3$ PVKSCs. (c) Stabilized Quasi-fermi level splitting of $MA_{0.9}Cs_{0.1}Pb(I_{0.6}Br_{0.4})_3$ with initial PL spectra and absorbance shown in figure inset.

Optoelectronic quality and photovoltage losses in $MA_{0.9}Cs_{0.1}Pb(I_{0.6}Br_{0.4})_3$ were evaluated using time-resolved photoluminescence (TRPL) spectroscopy. Absolute PL intensity spectra and absorbance are shown in the inset of **Figure 5.8c** and the E_g is ~1.82 eV. A relatively stable QFLS ~1.23 eV was observed which correlates well with the device V_{oc} (**Figure 5.8c**). Though the V_{oc} of large E_g devices obtained here is better than that obtained from previous work[387] (**Figure 5.2**), a $V_{oc,loss}$ of ~0.3 V compared to SQ limit still exists. Deleterious non-radiative recombination due to material quality (PLQY <0.01%) along with mismatched energy levels (~0.35 eV) at the $NiO_x/MA_{0.9}Cs_{0.1}Pb(I_{0.6}Br_{0.4})_3$ interface limited V_{oc} and could be improved in the future by defect passivation and development of appropriate interlayers.

To enable monolithic tandem, the top Ag electrode was replaced with sputtered ITO which transmits unabsorbed light efficiently and provides robustness for subsequent solution processing. The resultant devices performed well and showed a V_{oc} of ~1.22 V, a J_{sc} of ~12.1 mA/cm^2, a *FF* of ~0.69 and a PCE of ~10.1% (**Figure 5.8a**), analogous to Ag electrode devices discussed above. The drop in J_{sc} is reasonable considering an increased transmittance of long wavelength light through top ITO and correlates well with corresponding EQE spectra (**Figure 5.7c**). The device stack is unaffected during sputtering and the superior performance of semitransparent devices without compromising in V_{oc} ensures high optoelectronic quality of sputtered ITO.

5.3.3 2-Terminal Monolithic Tandem PVKSCs

Selection of appropriate ICL and realization of current matching between subcells are keys for achieving effective coupling of above developed small and large E_g PVKSCs to realize successful 2-T tandem cells. Accordingly, the tandem device structure (**Figure 5.9a**) was designed to have sputtered ITO sandwiched between C_{60}/Bis-C_{60} and PEDOT:PSS as ICL. The energetics of ITO relative to adjoining interlayers (**Figure 5.9b**) along with its superior electrical conductivity ensure effective transfer of charge carriers and efficient recombination to reduce electrical losses. To assess current generation in subcells and optical losses limiting J_{sc}, transfer matrix model based optical simulations were performed. Refractive indices of perovskite absorbers and all other layers used in optical simulations are presented in **Figure 5.9c** and **5.10**.

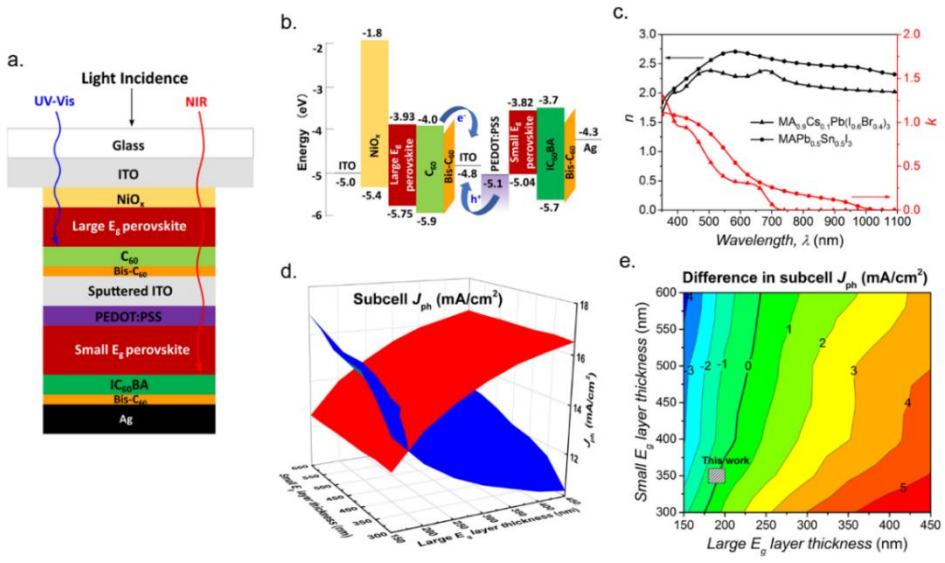

Figure 5.9. Energy level diagram and optical simulation of perovskite-perovskite tandem solar cells. a-b, Device structure (a), and energy level diagram (b) of 2-T tandem solar cell developed here. (c) Refractive indices of small and large bandgap perovskite absorbers. (d) Variation of front (red) and back (blue) subcell photocurrents (J_{ph}) as a function of large E_g and small E_g layer thicknesses. (e) Corresponding difference in subcell photocurrent ($J_{ph,f}$ - $J_{ph,b}$), where contour line representing $J_{ph,f}$ - $J_{ph,b}$ = 0 (ideal current matching) is highlighted and region corresponding to thickness combination used in this work (190±10 nm and 350±10 nm) is marked.

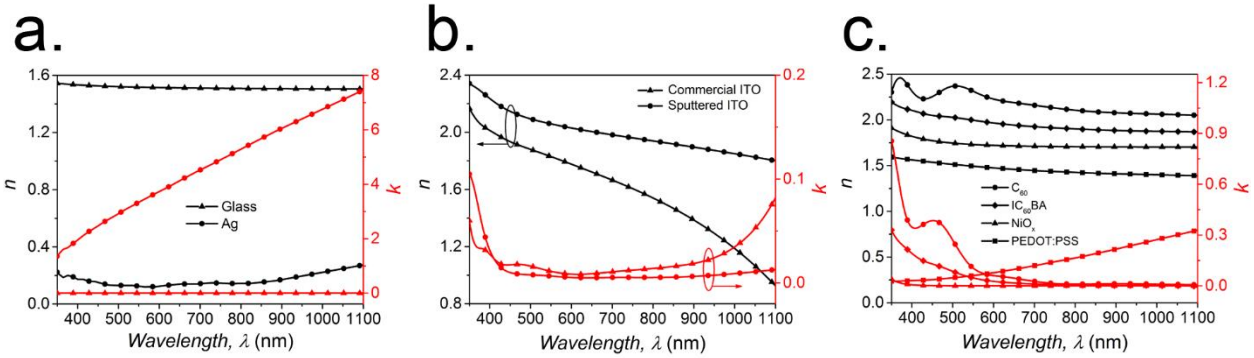

Figure 5.10. Refractive indices. a-c, Real (n) and imaginary part (k) of refractive index for glass substrate and Ag electrode (a), commercial and sputtered ITO (b), and interlayers (c) used in 2-terminal tandem PVKSCs.

Figure 5.9d shows the variation of subcell photocurrents (J_{ph}) as a function of large E_g and small E_g layer thickness ranging from 150-450 nm and 300-600 nm, respectively. As the thickness of large E_g layer increases, the front subcell photocurrent ($J_{ph,f}$) continually increases at the expense of back subcell photocurrent ($J_{ph,b}$). A proportional increase in thickness of small E_g layer can minimize mismatch in J_{ph} arising due to this compromise. The profile of $J_{ph,f}$ and $J_{ph,b}$ intersects at a certain line of thickness corresponding to the current-matched conditions among subcells in

tandem configuration (**Figure 5.9d**). The line of current-matching along with difference in subcell photocurrents for entire range of thicknesses are portrayed via a 2D-contour plot in **Figure 5.9e**. The point of intersection for thickness combination used here was observed to lie right on the line corresponding to the current-matched condition. Further, the ICL ITO thickness has negligible impact on subcell photocurrent and does not significantly diverge from current matching. A 100 nm ICL ITO was chosen and it has small parasitic absorption due to lower extinction coefficient (**Figure 5.10b**).

The fabrication scheme for tandem solar cells was tailored specifically to facilitate contact of ITO ICL and thus enables the possibility for examining each subcell individually (**Figure 5.3**). **Figure 5.11a** shows the cross-section SEM image of a typical tandem cell where clear demarcation between layers are observed. The corresponding layer thicknesses and simulated optical field intensity distribution within device stack are portrayed in **Figure 5.11b**. With our optimized layer thicknesses, wavelength less than and greater than 700 nm are concentrated in large E_g and small E_g layers, respectively, which ensures maximized current generation in subcells.

Table 5.2. Performance metrics for single junction and 2-T perovskite-perovskite tandem solar cells.

	E_g [eV]	$\Delta\mu_{QY,Max}$ [a)] [eV]	V_{oc} [V]	J_{sc} [mA/cm^2]	*FF*	PCE [b)] [%]	S-PCE [c)] [%]	V_{oc}/V_{oc}^{SQ}
Small bandgap single junction	1.22	0.85	0.84	25.5	0.67	14.4	13.9	0.88
Large bandgap single junction	1.82	1.23	1.20	15.1	0.69	12.5	12.8	0.80
2-T monolithic tandem			**1.98**	**12.7**	**0.73**	**18.4**	**18.5**	**0.80** [d)]

[a)]Corresponds to stabilized maximum value; [b)]PCE obtained from forward *J-V* scan; [c)]PCE obtained from steady-state current response of the device maintained at voltage corresponding to maximum power point under AM1.5 illumination; [d)]V_{oc}^{SQ} for tandem obtained by adding SQ limit of subcells.

J-V characteristics of the best performing 2-T tandem (**Figure 5.11c**) shows an exceptional V_{oc} of 1.98 V, a J_{sc} of 12.7 mA/cm^2, and a FF of 0.73 resulting in a remarkable PCE of 18.4%. No obvious *J-V* hysteresis was observed. The EQE of subcells (**Figure 5.11d**) showed excellent current matching as predicted by optical simulations and integrated currents agree well with the J_{sc} obtained from *J-V* characteristics. The reliability of PCE was further confirmed by measuring the steady-state current output at MPP (~1.55 V) which provided a stabilized efficiency of ~18.5% (**Figure 5.11e**). An absolute PCE improvement of ~4% is realized compared to single-junction device (**Figure 5.11c** and **Table 5.2**).

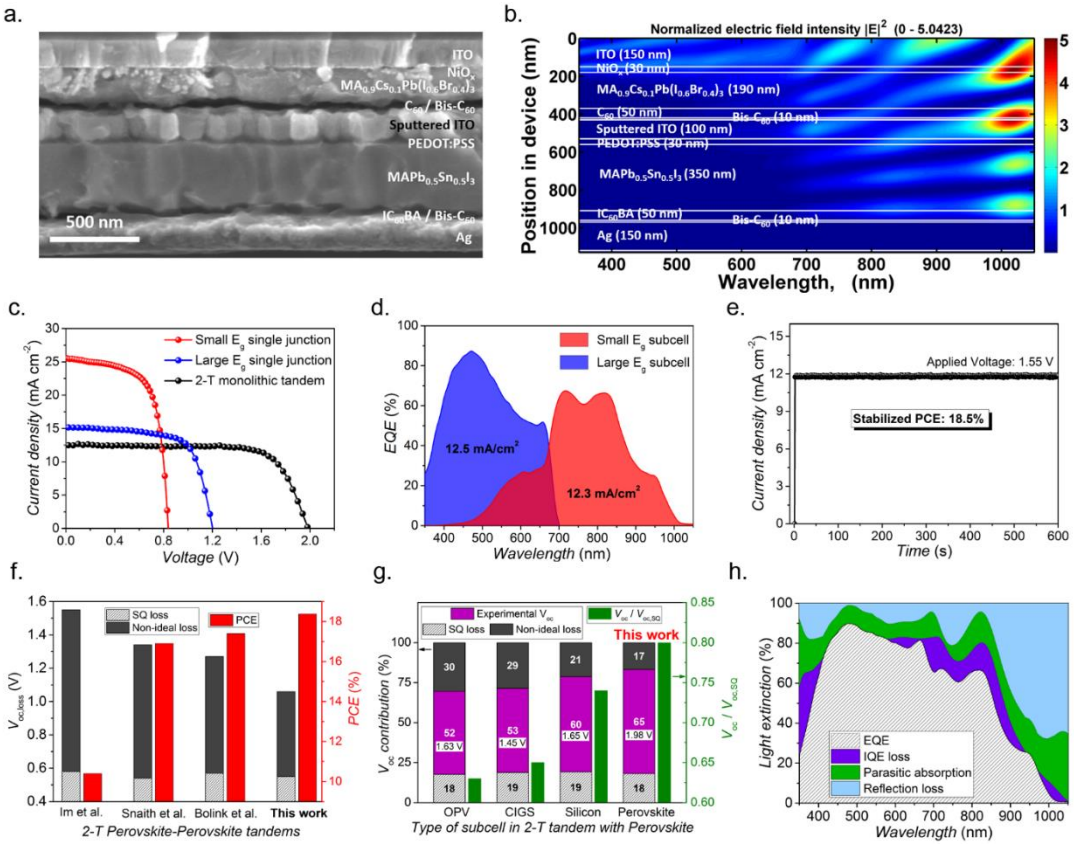

Figure 5.11. Photovoltaic characteristics and analysis of 2-terminal perovskite tandem solar cells. (a) Cross-section SEM of a characteristic device. (b) Simulated electric field intensity distribution within a tandem stack. (c) Typical *J-V* characteristics of 2-terminal tandem solar cell along with that of the small and large bandgap single junction solar cells with Ag electrode. (d) EQE spectra of individual subcells in 2-terminal monolithic tandem. (e) Steady-state current under AM1.5 illumination at an applied voltage corresponding to MPP of tandem solar cells. (f) Comparison of $V_{oc,loss}$ and PCE of perovskite-perovskite tandem developed here in perspective to literature.[13,14,20] (g) Fractional contribution of V_{oc} and associated losses with respect to bandgap for different state-of-art tandem solar cells, where perovskite is monolithically integrated with other photovoltaic technologies.[21,49,50] (h) Contribution of different factors (EQE, IQE loss, parasitic absorption, reflection) for light extinction in tandem solar cell developed here.

When the constituent subcells were combined individually in a 4-terminal configuration, the PCE drops to 16.7% (**Figure 5.12**) due to increased parasitic absorption.

a.

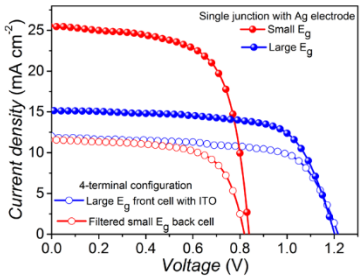

b.

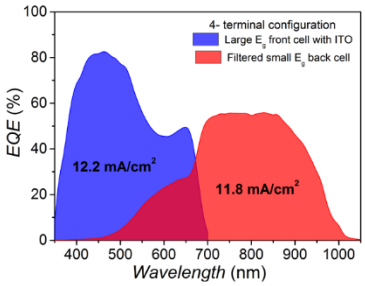

c.

	V_{oc} (V)	J_{sc} (mA/cm^2)	FF	PCE (%)
Single junction cells with Ag electrode				
Small E_g	0.84	25.5	0.67	14.4
Large E_g	1.20	15.1	0.69	12.5
4-terminal configuration				
Large E_g front cell with ITO	1.22	12.1	0.69	10.1
Filtered small E_g back cell	0.82	11.6	0.69	6.6
4-terminal tandem				16.7
2-terminal configuration				
2-terminal monolithic tandem	1.98	12.7	0.73	18.37

Figure 5.12. Photovoltaic characteristics of 4-terminal perovskite-perovskite tandem solar cells. (a) *J-V* characteristics of small and large bandgap single junction solar cells with Ag electrode and corresponding subcells used in 4-terminal configuration; for 4-terminal configuration, a small bandgap single junction solar cell with Ag electrode (back cell) is mechanically stacked on a semitransparent large bandgap single junction solar cell with ITO electrode (front cell). (b) EQE spectra of individual subcells used for 4-terminal configuration. (c) Performance metrics of single junction, 4-terminal tandem and 2-terminal tandem perovskite solar cells. Semitransparent large bandgap cell used in 4-terminal configuration constitutes a 400 nm thick sputtered ITO as electrode, as opposed to 100 nm sputtered ITO used in 2-terminal configuration.

Statistics of performance metrics for all devices studied in this work are summarized in **Figure 5.13**. To the best of our knowledge, 18.5% PCE obtained here is the highest performance for monolithic 2-T tandem PVKSCs reported till date (**Figure 5.11f**).[381,383,387] Further, if an electrolyzer is coupled in series with the 2-T tandem developed here and operated at conditions close to the maximum power point (~1.55 V and 11.8 mA/cm^2), water splitting with remarkably high solar-to-hydrogen (STH) efficiencies ~15% would be realizable (details in supporting information), which is a significant improvement compared to the previous demonstration with series-connected perovskite solar cells.[397]

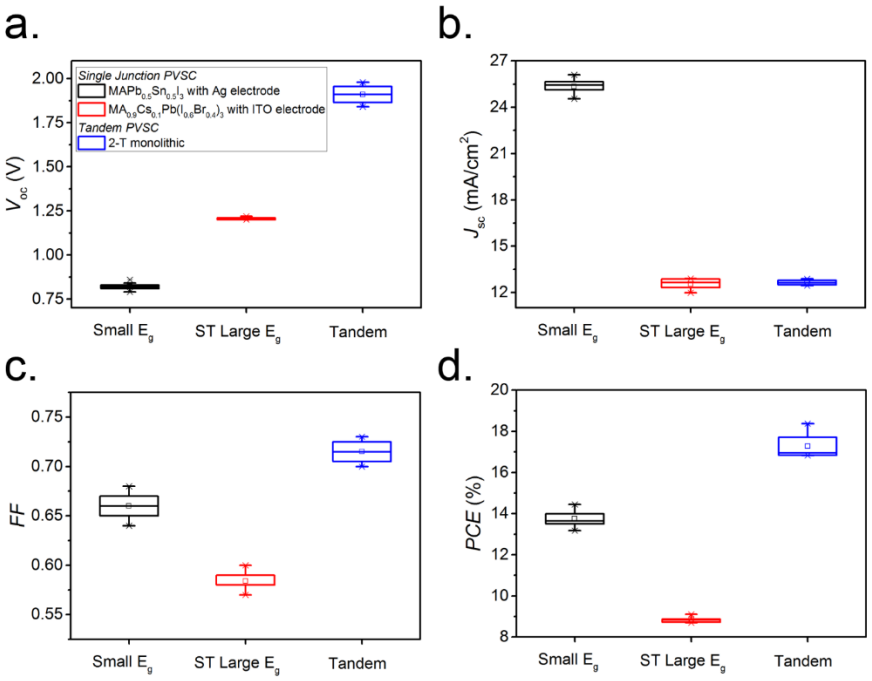

Figure 5.13. Device performance statistics. a-d, Box-and-whisker plots showing statistical variation of open circuit voltage (V_{oc}) (a), short-circuit current density (J_{sc}), fill factor (*FF*) (c), and power conversion efficiency (*PCE*) (d) of different device configurations (single junction and tandem) developed in this work; boxes are 25-75%, whiskers correspond to 1.5 interquartile range, inner line is median and inner small box (□). Reported statistics are obtained by combining 2 to 3 batches of devices for accounting both in-batch and batch-batch variability (minimum of 12 devices).

A large V_{oc} (~1.98 V) close to the sum of subcell *V*oc's realized for tandem cell manifests the effectiveness of rational design in our work. This is a significant improvement compared to previously reported V_{oc} (1.66 V) for similar bandgap-matched 2-T perovskite tandem.[387] Relationships between experimental V_{oc} and the various upper bounds of V_{oc} are summarized in **Figure 5.14**. Overall $V_{oc,loss}$ ($E_{g1}/q + E_{g2}/q - V_{oc}$) for the resultant 2-T tandem is substantially reduced and the non-ideal $V_{oc,loss}$ (related to interfacial energetics and absorber optoelectronic quality) is ~0.5 V which is much smaller than the previously reported non-ideal V_{oc} loss (0.7-0.8 V).[14,20] A comparison of $V_{oc,loss}$ and PCE of 2-T tandem PVKSCs reported so far clearly shows that this work outperforms earlier works (**Figure 5.11f**).[381,383,387]

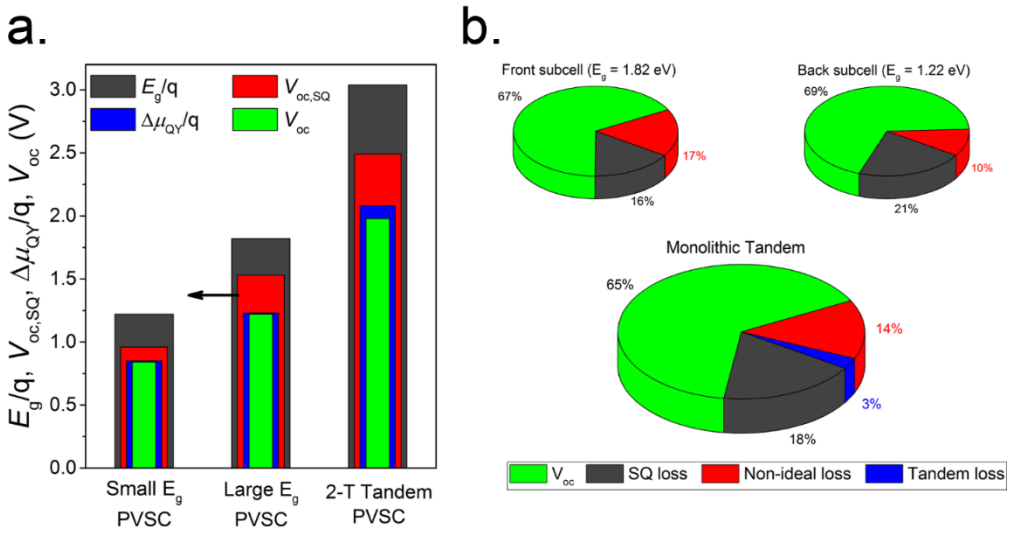

Figure 5.14. Analysis of V_{oc} and associated losses in single junction and 2-T tandem solar cells. (a) Comparison of experimental V_{oc} in perspective to associated bounds like bandgap potential (E_g/q), SQ-limit V_{oc} ($V_{oc,SQ}$) and quasi-fermi level splitting potential ($\Delta\mu_{QY}$/q). (b) Fractional contribution of V_{oc} and associated losses with respect to bandgap potential for devices developed in this work; bandgap potential and SQ loss for tandem solar cell are obtained by adding corresponding subcell values.

To provide broader outlook, the 2-T perovskite tandem developed here was also compared with other state-of-the-art series connected tandem cells (**Figure 5.11g**), where PVKSC is seamlessly coupled with another PV technology (OPV, CIGS and Silicon).[226,409,410] The key difference to note is the non-ideal loss, ~30% of E_g/q in case of tandems with OPV and CIGS, which ultimately limits V_{oc}. However, employment of well-established silicon PV has reduced the non-ideal loss fraction to ~21% in silicon-perovskite tandem and a record PCE of ~23.6% was achieved.[226] The 2-T perovskite tandem developed here has a non-ideal loss fraction (~17%) lower than the record silicon-perovskite tandem and the realized V_{oc} (~1.98 V) corresponds to an impressive ~80% of the theoretical limit (**Figure 5.11g**). It is important to note that there are several other perovskite-silicon tandems reported with different non-ideal loss fractions[411–413] and only the work with highest power conversion efficiency[226] is compared here to maintain simplicity and consistency.

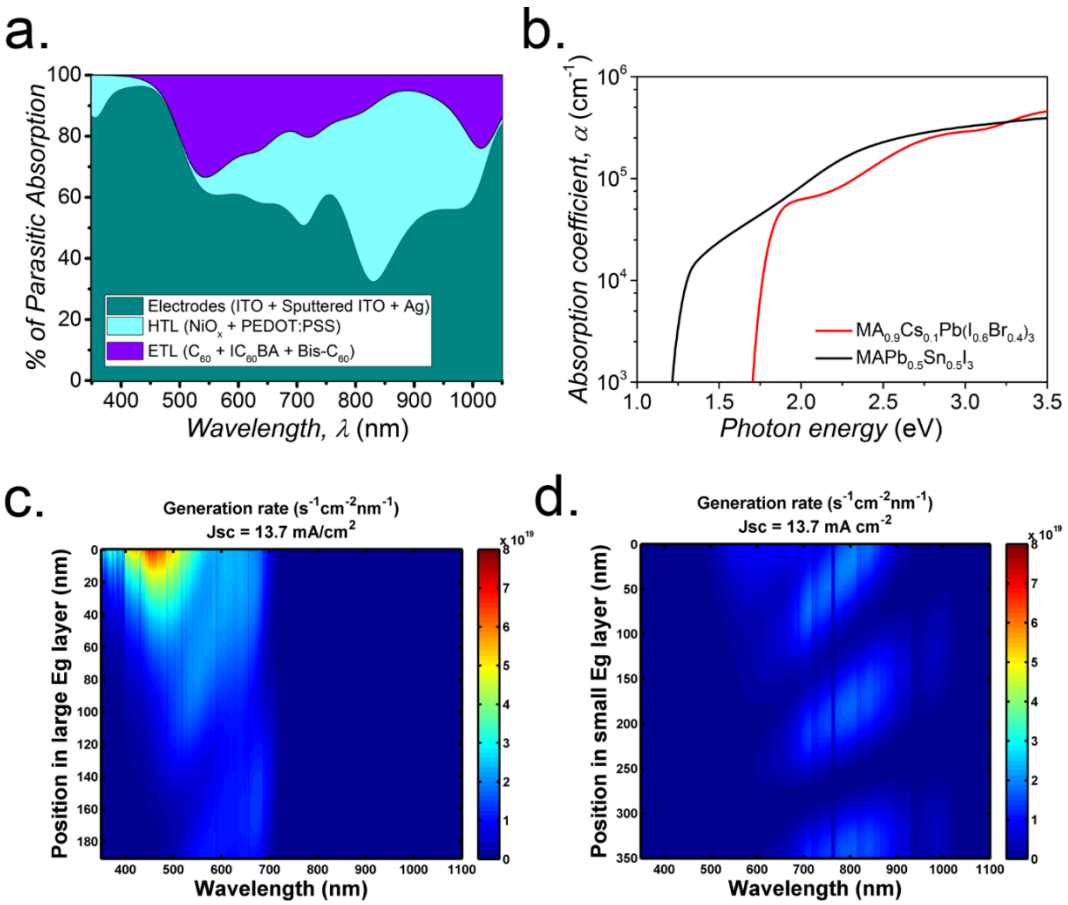

Figure 5.15. Analysis of optical losses and current generation in 2-T tandem solar cells. (a) Fractional contribution of parasitic absorption losses arising from different components in tandem architecture. (b) Absorption coefficient of perovskite absorbers used in tandem architecture. (c-d) Exciton generation profile in large bandgap (a) and small bandgap (b) layer of 2-T tandem solar cell obtained via optical simulation. Weak absorption of $MAPb_{0.5}Sn_{0.5}I_3$ around band edges result in feebler current generation and makes small bandgap subcell the current limiting factor.

With the realization of high V_{oc} and FF, the PCE of tandems are currently limited by relatively moderate J_{sc} (~13 mA/cm^2). The analysis of different aspects in light extinction and current generation in 2-T tandem cells (**Figure 5.11h** and **5.15**) shows that small E_g subcell is the current-limiting factor. An increase in thickness of perovskite layers will substantially improve the J_{sc} and a PCE of ~20-24% is certainly realizable in the near future. Further improvement in optoelectronic quality of perovskite absorbers, minimization of parasitic losses, development of appropriate interlayer and molecular strategies to dope $IC_{60}BA$ may ultimately push the J_{sc} and PCE of 2-T tandem PVKSCs to even higher values.

5.4 Conclusion

In summary, we have successfully realized highly efficient bandgap-matched 2-T perovskite tandem solar cells by applying an integrated process, compositional, interfacial, optical, and device engineering. $IC_{60}BA$ was employed to achieve optimized interfacial contact with a small E_g (~1.2 eV) perovskite ($MAPb_{0.5}Sn_{0.5}I_3$). It shows perfect "non-quenching" at open-circuit due to reduced non-radiative recombination losses. This enables devices with negligible hysteresis and high V_{oc} (0.84 V). Devices based on the large E_g (~1.8 eV) perovskite ($MA_{0.9}Cs_{0.1}Pb(I_{0.6}Br_{0.4})_3$) with sputtered ITO as top electrode showed a high photo-stabilized V_{oc} of 1.22 V. Optical simulations were also used to ensure current matching and the resultant 2-T tandem device exhibited a very high V_{oc} (1.98 V) and PCE (18.5%). The reduced photovoltage loss (V_{oc} approaching 80% of the theoretical limit) is the lowest among all the perovskite based tandem solar cells reported so far, which demonstrates the strong potential of perovskite-perovskite tandems. With further increase in absorber thicknesses and improvement in perovskite optoelectronic quality, even higher PCEs of ~20-24% should be reachable with 2-T tandem PVKSCs.

PART C: PROGRESSION TOWARDS NEXT GENERATION PEROVSKITE TANDEM SOLAR CELLS

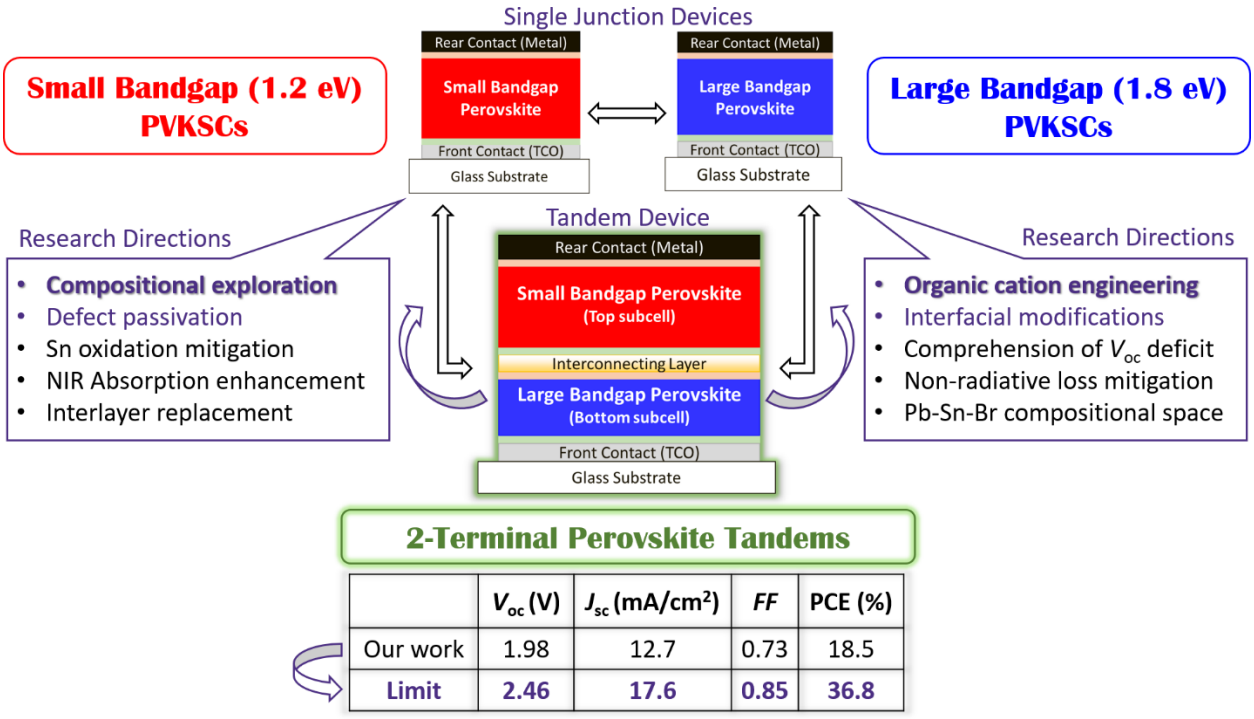

	V_{oc} (V)	J_{sc} (mA/cm^2)	*FF*	PCE (%)
Our work	1.98	12.7	0.73	18.5
Limit	**2.46**	**17.6**	**0.85**	**36.8**

Perspective of research directions for advancement of small and large bandgap subcells necessary to fuel the progression towards next generation perovskite tandem solar cells; theoretical limit for V_{oc} and *FF* obtained using Shockley-Queisser calculations, theoretical limit for J_{sc} calculated assuming a 90% external quantum efficiency.

Chapter 6. OVERCOMING THE PHOTOVOLTAGE PLATEAU IN LARGE BANDGAP PEROVSKITE SOLAR CELLS

6.1 Introduction

Organic-inorganic hybrid perovskites are structurally and functionally versatile materials, brought to prominence because of their exceptional optoelectronic attributes for enabling next generation photovoltaics (PVs).[30,44,52] A rapidly advancing research community has led to an unprecedented growth of hybrid perovskites-based PVs, achieving a power conversion efficiency (PCE) record of 22.7%.[34,58] Progression in PCE for perovskite solar cells (PVKSCs) so far have transpired because of advancements on multiple fronts such as formulation of perovskite composition and processing approaches, design of interfaces, and fabrication of single junction device stacks, all primarily based on 1.6 eV bandgap (E_g) perovskites.[6,27,32] To improve the PCE of PVKSCs past the single-junction Shockley-Queisser (SQ) limit, it is of increasing importance to develop perovskite device stacks with bandgaps tailored for construction of multi-junction (tandem) solar cells.[22,212]

The two-terminal (2-T) PVK-PVK tandem configuration particularly stands out among different choices because of their potential for having the least-energy intensive processing and the lowest energy payback time.[414] The lowest E_g currently achieved with perovskites is ~1.2 eV and it ideally needs to be paired with ~1.8 eV large E_g perovskite to minimize the current matching loss and maximize the potential of 2-T PVK-PVK tandems.[22,212] Succeeding the initial work by Eperon *et al.*,[387] we recently advanced the PCE record to 18.5% for 2-T tandem using 1.2 eV and 1.8 eV E_g perovskite absorbers.[20] This PCE significantly lags the 23.6% record achieved for 2-T Si-PVK tandems[226] and is far below the practically realizable valuation ~35%. Analyses of

optoelectronic losses in 2-T PVK-PVK tandems reveal that the low open-circuit voltage (V_{oc}) in 1.8 eV E_g perovskite subcell is currently the major performance constraint.[20,22,212]

Large bandgaps are commonly realized using mixed-halide (I/Br) perovskite alloys, represented by a general formula $APb(I_{1-y}Br_y)_3$; $0<y<1$, where A = methylammonium (MA), formamidinium (FA), or cesium (Cs). The E_g is continually tunable from 1.5 eV to 2.4 eV by increasing the amount of Br incorporation.[50] Small amount of Br ($y<0.15$) is beneficial for improving the perovskite quality and incorporated in the state-of-the-art ~1.6 eV E_g PVKSCs.[415,416] However, for $y>0.2$, mixed-halide perovskites become inherently vulnerable to reversible phase segregation under high excess carrier concentration, such as exists under illumination or current injection.[3,417] This becomes sharply problematic because mixed-halide perovskites segregate into iodine- and bromine-rich phases under photoexcitation, which deteriorates the transport of charge carriers and absorber optoelectronic quality.[369,418] These consequences become more severe as the E_g increases, which can be explained by either increased driving force for phase segregation or deeper defect levels.[419,420] The material-level issues are reflected in the device-level also, where the functionality of mixed-halide large E_g PVKSCs are limited by the performance decay under continuous illumination and a very high photovoltage loss ($V_{oc,loss} = V_{oc,SQ} - V_{oc}$, where $V_{oc,SQ}$ is the theoretical limit).[13,20,50,417]

A wide-range of approaches have been explored to tackle challenges in mixed-halide large E_g PVKSCs, focused on the 1.65-1.75 eV E_g range required for Si-PVK tandems and applied to the higher E_g ranges. A-site compositional engineering is the most widely employed approach. Since the first demonstration of using double-cation (FA/Cs) at the A-site for alleviating phase segregation,[355] several works have extended this concept to the utilization of triple-cation (FA/MA/Cs)[421] and quadruple-cation (FA/MA/Cs/Rb).[422] Alternate to A-site modifications, we

have demonstrated B-site modification (Pb/Sn binary alloys) also mitigates phase segregation.[13] Besides composition, precursor stoichiometry and film crystallinity have demonstrated some success in controlling the phase segregation behavior.[417] Incorporation of additives ($Pb(SCN)_2$,[423] formamide,[424] potassium[416]) and perovskite surface treatments (with quaternary ammonium halides,[425] benzylamine[426]) have reduced trap states (by modulating perovskite crystallization or passivating defects) and improved the V_{oc} of 1.65-1.75 eV E_g PVKSCs up to 1.24 V. Recently, butylammonium incorporation has been found beneficial to improve the photo- and ambient-stability of mixed-halide perovskites.[427,428] Details regarding perovskite composition, device architecture, and performance metrics for reported works are summarized in **Table 6.1**.

Table 6.1a. Perovskite composition, device architecture, and photovoltaic performance metrics for ~ 1.6 eV E_g mixed-halide hybrid PVKSCs.

Ref.	Perovskite	Interlayers[a]	E_g [eV]	V_{oc} [V]	$V_{oc,loss}$[b] [V]	V_{oc}/V_{oc}^{SQ}	PCE [%]	s-PCE[c] [%]
5	$FA_xMA_{1-x}PbBr_yI_{1-y}$	ETL: m-TiO_2 HTL: Spiro	1.63	1.10	0.25	0.81	17.4	-
			1.64	1.14	0.22	0.84	20.7	
			1.61	1.04	0.29	0.78	12.9	
			1.63	1.04	0.31	0.77	16	
			1.66	1.10	0.28	0.80	13.2	
			1.68	1.18	0.22	0.84	14.7	
			1.68	1.15	0.25	0.82	18.5	
			1.75	1.10	0.36	0.75	15.3	
			1.76	1.17	0.30	0.79	17.5	
			1.76	1.12	0.35	0.76	12.2	
			1.87	1.15	0.43	0.73	11.4	
			1.85	1.11	0.45	0.71	11.7	
			1.85	1.09	0.47	0.70	11.9	
			1.85	1.13	0.43	0.73	10.7	
			1.87	1.12	0.46	0.71	8.6	
6	$(FA,MA,Cs,Rb)Pb(I,Br)_3$	ETL: m-TiO_2 HTL: Spiro	1.63	1.24	0.11	0.92	21.8	21.6

[a] ETL = Electron Transporting Layer, HTL = Hole Transporting Layer; [b] $V_{oc,loss} = V_{oc,SQ} - V_{oc}$; [c] s-PCE = Stabilized PCE at maximum power point. *References indicated in red color represent works that utilize n-i-p (conventional) device architecture, whereas other works utilize p-i-n (inverted) device architecture.

Table 6.1b. Perovskite composition, device architecture, and photovoltaic performance metrics for 1.65 eV < $E_g \leq$ 1.75 eV mixed-halide hybrid PVKSCs.

Ref.	Perovskite	Interlayers[a]	E_g [eV]	V_{oc} [V]	$V_{oc,loss}$[b] [V]	V_{oc}/V_{oc}^{SQ}	PCE [%]	s-PCE[c] [%]
1	$MAPb(I_{0.8}Br_{0.2})_3$	HTL: PEDOT:PSS ETL: PCBM/C_{60}	1.72	1.02	0.42	0.71	12.0	-
2	$MAPb(I_{0.83}Br_{0.17})_3$	HTL: PTAA ETL: PCBM/C_{60}	1.69	1.16	0.25	0.82	16.6	16.3
	$MAPb(I_{0.64}Br_{0.26})_3$		1.75	1.21	0.25	0.83	14.9	14.9
4	$FA_{0.83}Cs_{0.17}Pb(I_{0.6}Br_{0.4})_3$	ETL: SnO_2/PCBM HTL: Spiro	1.74	1.20	0.25	0.82	17.1	16.0
7	$MAPb_{0.75}Sn_{0.25}(I_{0.4}Br_{0.6})_3$	HTL: PEDOT:PSS ETL: PCBM	1.73	1.04	0.41	0.72	12.6	-
9	$(FA_{0.83}MA_{0.17})_{0.95}Cs_{0.05}$ $Pb(I_{0.6}Br_{0.4})_3$	HTL: PTAA ETL: ICBA/C_{60}	1.71	1.20	0.23	0.84	18.3	18.2
10	$FA_{0.8}Cs_{0.2}Pb(I_{0.7}Br_{0.3})_3$ w/ $Pb(SCN)_2$ additive	ETL: SnO_2 HTL: Spiro	1.75	1.23	0.23	0.84	17.7	17.2
12	$FA_{0.75}MA_{0.15}Cs_{0.1}Rb_{0.05}$ $Pb(I_{0.67}Br_{0.33})_3$	ETL: m-TiO_2 HTL: PTAA	1.73	1.13	0.32	0.78	17.3	17.4
13	$FA_{0.83}MA_{0.17}Pb(I_{0.6}Br_{0.4})_3$ w/ QAH passivation	HTL: PTAA ETL: C_{60}	1.72	1.15	0.29	0.80	17.2	-
14	$FA_{0.83}Cs_{0.17}Pb(I_{0.67}Br_{0.34})_3$ w/ TOPO passivation	HTL: Cu:NiO_x ETL: PCBM	1.75	1.12	0.34	0.77	12.0	-
15	$FA_{0.15}Cs_{0.85}Pb(I_{0.73}Br_{0.27})_3$ w/ BA treatment	ETL: TiO_2 HTL: Spiro	1.72	1.24	0.20	0.86	18.1	17.1
16	$BA_{0.09}(FA_{0.83}Cs_{0.17})_{0.91}$ $Pb(I_{0.6}Br_{0.4})_3$	ETL: SnO_2/PCBM HTL: Spiro	1.72	1.18	0.26	0.82	17.2	17.3
19	$MAPb(I_{0.8}Br_{0.2})_3$	ETL: C_{60} HTL: TaTm	1.72	1.12	0.32	0.78	15.9	14.6
20	$FA_{0.6}Cs_{0.4}Pb(I_{0.7}Br_{0.3})_3$	HTL: PTAA ETL: C_{60}	1.68	1.10	0.30	0.79	17.4	-
	$FA_{0.75}Cs_{0.25}Pb(I_{0.8}Br_{0.2})_3$		1.75	1.17	0.29	0.80	16.3	-
21	$FA_{0.8}Cs_{0.2}Pb(I_{0.6}Br_{0.4})_3$ w/ formamide additive	ETL: Cl-TiO_2 HTL: Spiro	1.75	1.23	0.23	0.84	17.8	17.2
23	$CsPbI_3$ QD film	ETL: TiO_2 HTL: Spiro	1.73	1.23	0.50	0.85	10.8	7.9
24	$CsPbI_3$ QD film w/ FAI treatment	ETL: TiO_2 HTL: Spiro	1.72	1.20	0.52	0.84	13.4	13.4

[a] ETL = Electron Transporting Layer, HTL = Hole Transporting Layer; [b] $V_{oc,loss} = V_{oc,SQ} - V_{oc}$; [c] s-PCE = Stabilized PCE at maximum power point. *References indicated in red color represent works that utilize n-i-p (conventional) device architecture, whereas other works utilize p-i-n (inverted) device architecture.

Table 6.1c. Perovskite composition, device architecture, and photovoltaic performance metrics for 1.75 eV < E_g < 1.90 eV mixed-halide hybrid PVKSCs.

Ref.	Perovskite	Interlayers[a]	E_g [eV]	V_{oc} [V]	$V_{oc,loss}$[b] [V]	V_{oc}/V_{oc}^{SQ}	PCE [%]	s-PCE[c] [%]
3	$MAPb(I_{0.67}Br_{0.33})_3$	ETL: TiO_2 HTL: Spiro	1.77	1.08	0.40	0.73	10.7	10.1
7	$MAPb_{0.75}Sn_{0.25}(I_{0.3}Br_{0.7})_3$	HTL: PEDOT:PSS ETL: PCBM	1.80	1.05	0.46	0.70	6.3	-
8	$FA_{0.83}Cs_{0.17}Pb(I_{0.5}Br_{0.5})_3$	HTL: NiO_x ETL: PCBM	1.80	1.12	0.39	0.74	9.8	9.5
11	$MA_{0.90}Cs_{0.10}Pb(I_{0.6}Br_{0.4})_3$	HTL: NiO_x ETL: C_{60}	1.82	1.22	0.31	0.80	12.5	12.8
17	$BAI_{0.8}Br_{0.2}$-$Cs_{0.6}MA_{0.4}$ $Pb(I_{0.8}Br_{0.2})_3$	HTL: poly-TPD ETL: PCBM/C_{60}	1.79	1.04	0.46	0.69	-	-
18	$MA_{0.6}FA_{0.4}Pb(I_{0.6}Br_{0.4})_3$	HTL: PTAA ETL: PCBM	1.76	1.17	0.30	0.79	14.7	-
	$Cs_{0.6}FA_{0.4}Pb(I_{0.6}Br_{0.4})_3$		1.78	1.12	0.37	0.75	12.1	-
	$Cs_{0.6}MA_{0.4}Pb(I_{0.6}Br_{0.4})_3$		1.81	1.17	0.35	0.77	11.1	-
19	$MAPb(I_{0.5}Br_{0.5})_3$	ETL: C_{60} HTL: TaTm	1.87	1.21	0.37	0.77	10.6	-
22	$Cs_{0.06}FA_{0.79}MA_{0.15}Pb$ $(I_{0.4}Br_{0.6})_3$ w/ KI	ETL: m-TiO_2 HTL: Spiro	1.78	1.23	0.27	0.82	17.5	17.1
This work	**$MAPb(I_{0.6}Br_{0.4})_3$ w/ PEA incorporation**	**HTL: NiO_x ETL: ICBA**	**1.82**	**1.30**	**0.23**	**0.85**	**11.9**	**12.2**

[a] ETL = Electron Transporting Layer, HTL = Hole Transporting Layer; [b] $V_{oc,loss} = V_{oc,SQ} - V_{oc}$; [c] s-PCE = Stabilized PCE at maximum power point. *References indicated in red color represent works that utilize n-i-p (conventional) device architecture, whereas other works utilize p-i-n (inverted) device architecture.

Table 6.1d. Citations for points #1 - #22 in **Figure 6.1**.

#	Citation	#	Citation
1	*Adv. Energy Mater.* **2015**, *5*, 1401616	12	*Adv. Energy Mater.* **2017**, *7*, 1700228
2	*Adv. Sci.* **2016**, *3*, 1500301	13	*Nat. Energy* **2017**, *2*, 17102
3	*ACS Appl. Mater. Interfaces* **2016**, *8*, 2232–2237	14	*J. Phys. Chem. Lett.* **2017**, *8*, 3289–3298
4	*Science.* **2016**, *351*, 151–155	15	*Adv. Energy Mater.* **2017**, *7*, 1701048
5	*Energy Environ. Sci.* **2016**, *9*, 1706–1724	16	*Nat. Energy* **2017**, *2*, 17135
6	*Science.* **2016**, *354*, 206–209	17	*Nano Lett.* **2017**, *17*, 6863–6869
7	*Nano Lett.* **2016**, *16*, 7739–7747	18	*Adv. Energy Mater.* **2018**, *8*, 1701543
8	*Science.* **2016**, *354*, 861–865	19	*ACS Energy Lett.* **2018**, *3*, 214–219
9	*Adv. Mater.* **2017**, *29*, 1700607	20	*ACS Energy Lett.* **2018**, *3*, 428–435
10	*ACS Energy Lett.* **2017**, *2*, 1177–1182	21	*Adv. Mater.* **2018**, *30*, 1706275
11	*Adv. Mater.* **2017**, *29*, 1702140	22	*Nature* **2018**, *555*, 497–501

We use V_{oc} to compare the effectiveness of different approaches, since it not only reflects the quality of perovskite absorber and interfaces in PV device stack, but also an important metric for tandem development. **Figure 6.1a** shows V_{oc} as a function of E_g for all reported large E_g PVKSCs based on mixed-halide hybrid perovskites. V_{oc} does not proportionally increase with E_g and the highest V_{oc} achieved so far in the 1.65-1.90 eV E_g range is only 1.24 V, which is same as the record value achieved using ~1.6 eV E_g PVKSCs[429]. **Figure 6.1b** shows the corresponding $V_{oc}/V_{oc,SQ}$ values to provide a straightforward comparison of V_{oc} achieved using different E_g absorbers. It is evident that $V_{oc}/V_{oc,SQ}$ rapidly decreases with increasing E_g and is very low in the E_g range of interest for PVK-PVK tandems. The best $V_{oc}/V_{oc,SQ}$ value currently achieved for the 1.80-1.85 eV E_g range is ~0.80, which is significantly lower than the values of 0.85-0.92 achieved for the 1.60-1.75 eV E_g PVKSCs (**Figure 6.1b**) and 0.92 achieved in our recent work on 1.22 eV E_g PVKSCs[4].

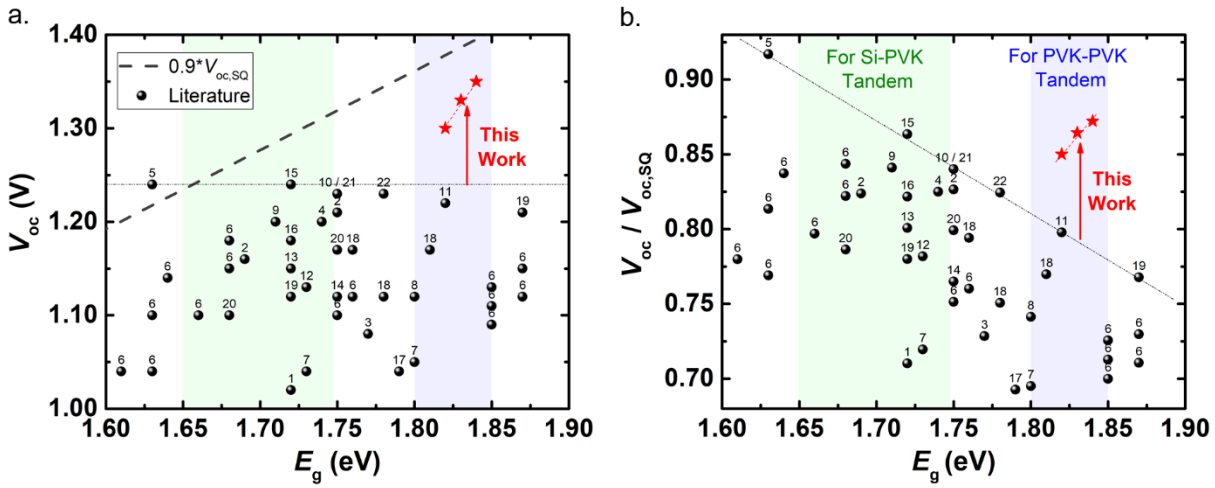

Figure 6.1. Comparison of the figure-of-merit (open-circuit voltage, V_{oc}) for mixed-halide hybrid PVKSCs reported in literature in perspective to this work. (a) V_{oc} and (b) corresponding $V_{oc}/V_{oc,SQ}$ as function of bandgap (E_g) for works in the 1.6-1.9 eV E_g range. Red stars correspond to values obtained in this work. Citations for points 1-22 are provided in **Table 6.1d**.

Since majority of works related to PVKSCs are based on 1.60-1.65 eV E_g perovskites, we choose to show only the record value obtained in this range (#6) in **Figure 6.1**. For 1.65-1.90 eV E_g range, we have included all works based on mixed-halide hybrid perovskites reported till date.

Additionally, we have also included all relevant data points from the compositional screening ($FA_xMA_{1-x}PbBr_yI_{1-y}$) work by Jacobsson et al. (#6) PV performance metrics for all works (#1 - #22) are listed in **Table 6.1a-c**, divided based on the E_g range. Since this study is focused on mixed-halide hybrid perovskites, we have not included data points corresponding to $CsPbI_3$ quantum dots based 1.73 eV E_g PVKSCs in **Figure 6.1**. However, considering the increasing interest in all inorganic PVKSCs, we have included their performance metrics at the end (#23 and #24) of **Table 6.1b** to provide context regarding their potential for application as a large E_g absorber in tandem solar cells.[430,431] All inorganic $CsPbI_2Br$ (E_g ~1.9 eV) is another composition that has been investigated for large E_g PVKSCs, but devices have shown huge disparity in the PCE calculated from *J-V* and stabilized power output at maximum power point.[432] This is indicative of unsolved phase instability issues and therefore we have excluded from the comparison presented here.

Above observations illustrate shortcomings of current approaches and complexity in the development of 1.8 eV E_g mixed-halide PVKSCs. A focused effort is thus vital to surpass the existing limitation of $V_{oc}/V_{oc,SQ}$ ~0.80, hereafter referred to as the photovoltage plateau. Our previous investigation revealed that the primary origin for high $V_{oc,loss}$ is poor absorber optoelectronic quality, where severe non-radiative recombination in $MA_{0.9}Cs_{0.1}Pb(I_{0.6}Br_{0.4})_3$ resulted in low PLQY (<0.01%) and limited the quasi-Fermi level splitting (QFLS) of films to 1.23 eV and V_{oc} of the corresponding devices to 1.22 V ($V_{oc}/V_{oc,SQ}$ ~0.80).[20] The objective of this study is thus to improve the intrinsic material quality for achieving a higher QFLS and overcoming the photovoltage plateau in 1.8 eV E_g perovskites.

Here, we demonstrate the effectiveness of phenylethylammonium (PEA) incorporation for solving the inherent material challenges and minimizing the $V_{oc,loss}$ in 1.8 eV E_g mixed-halide

hybrid PVKSCs. PEA incorporation in $MAPb(I_{0.6}Br_{0.4})_3$ led to enhancements in photo-stability as well as optoelectronic quality and improved the QFLS up to 1.35 eV. Detailed structural and spectroscopic analysis unveiled the origin of improvements and were pivotal in rationalization of the observed trends with different amounts of PEA incorporation. Subsequently with interface optimization, PVKSCs based on PEA-incorporated 1.80-1.85 eV E_g absorbers yielded significantly improved V_{oc} values of 1.30-1.35 V and were stable under illumination. The achieved $V_{oc}/V_{oc,SQ}$ values of 0.85-0.87 surpass the photovoltage plateau in 1.8 eV E_g PVKSCs. Insights obtained from this work are translatable to a wider E_g range of mixed-halide perovskites and crucial for the advancement of perovskite tandems.

6.2 Experimental Methods

Materials: ITO glass (substrate: soda lime float glass with SiO_2, <15 Ω sq^{-1}) was purchased from Colorado Concept Coatings LLC. Nickel (II) acetate tetrahydrate, PbI_2, $PbBr_2$ and all solvents used in this work were purchased from Sigma-Aldrich. $IC_{60}BA$ and C_{60} were purchased from American Dye Source, Inc. Procedures for synthesis of MAI and Bis-C_{60} were same as our previous works. PEAI was synthesized using a previously reported method.[433]

Solution Preparation (Perovskites): Precursor solution for perovskites with PEA incorporation were obtained by mixing PEA0 with either PEA20 or PEA100 and the wt.% of all initial solutions were maintained constant. Quantity of precursors were calculated according to the composition and are listed in **Table 6.2a**. Precursors were dissolved in DMSO and stirred at 60 °C for 2 h. To get solutions with different PEA fractions, the initial solutions were mixed as shown in **Table 6.2b** (calculated based on the 'n' equivalent for a given PEA fraction). All solutions were at room temperature and filtered with 0.22 μm PVDF filters before spin coating.

Table 6.2a. Quantity of precursors used for making initial solution of different compositions.

Composition		MAI (mg)	PEAI (mg)	PbI_2 (mg)	$PbBr_2$ (mg)	DMSO (ml)	wt.%
PEA0 [3D]	$MAPbI_{0.6}Br_{0.4}$	159.0	-	184.4	220.2	1.00	0.34
PEA20 [n = 9]	$PEA_2MA_8Pb_9(I_{0.6}Br_{0.4})_{28}$	132.8	52.0	163.7	214.7	1.00	0.34
PEA100 [2D]	$PEA_2Pb(I_{0.6}Br_{0.4})_4$	-	318.8	59.0	187.9	1.00	0.34

Table 6.2b. Quantity of initial solutions mixed to get precursor solution for a given PEA fraction (calculated based on the corresponding 'n' equivalent). Table on the left shows quantities for using PEA0 and PEA20 initial solutions; table on the right shows quantities for using PEA0 and PEA100 initial solutions.

for 100 µl	PEA0 solution (µl)	PEA20 solution (µl)
PEA0	100	0
PEA5	75	25
PEA10	50	50
PEA20	0	100

for 100 µl	PEA0 solution (µl)	PEA100 solution (µl)
PEA0	100.00	0.00
PEA5	96.05	3.95
PEA10	92.01	7.99
PEA20	83.66	16.34
PEA40	65.75	34.25
PEA100	0.00	100.00

Solution Preparation (Interlayers): For NiO_x, precursor solution was prepared by dissolving Nickel (II) acetate tetrahydrate (124.4 mg) in ethanol (5 mL) and ethanolamine (30 µL) was added to it; the mixture was stirred at 60 °C for 2 h. For C_{60} solution, C_{60} (15 mg/mL) was dissolved in dichlorobenzene and stirred at 80 °C for 2 h. For doped-Indene-C_{60} bis-adduct ($IC_{60}BA$) solution, $IC_{60}BA$ (15 mg/mL) and MAI (10mg/mL) were respectively dissolved in dichlorobenzene and isopropanol alcohol and stirred at 80 °C for 2 h, then mix the $IC_{60}BA$ and MAI solution in a volume ratio of 9:1. For fullerene surfactant, Bis-C_{60} (2 mg/mL) in isopropyl alcohol was dissolved using sonication (typically 1 h). NiO_x solution was filtered with 0.45 µm Nylon filter and other solutions were filtered with 0.22 µm PVDF filters before spin coating.

Device fabrication: ITO glass substrates were cleaned using sequential steps of ultrasonication for 15 min in detergent, deionized water, acetone, and isopropanol alcohol. Cleaned

ITO glass substrates were subjected to UV ozone treatment (10 min) before start of device fabrication. NiO_x precursor was spin coated onto the clean ITO glass at 3000 rpm for 60 s and annealed at 400 ^oC for 1 h in air. After this step, substrates were transferred into N_2-filled gloveboxes. Perovskite precursor solution was spin coated onto the substrate using 2-step spin program (1000 rpm for 5 s and 5000 rpm for 60 s); during the last 20-10 s of the second spin-coating step, toluene (0.7 ml) was dropped onto the spinning substrate and the substrates were annealed at 100 ^oC for 15 min using a hot plate. Subsequently, d-$IC_{60}BA$ or C_{60} solution was spin coated using 1500 rpm for 55 s and 4000 rpm for 5 s followed by annealing at 70 °C for 5 min. Then, Bis-C_{60} surfactant solution was spin coated on top at 3000 rpm for 30 s. Finally, a 150 nm thick silver (Ag) electrode was evaporated under high vacuum ($<1\times10^{-6}$ Torr) through a shadow mask (10 mm^2) to define the device area.

Photovoltaic characterization: Solar cell devices were tested using Class A solar simulator (Solar light 16S-300) inside glovebox. A calibrated reference silicon photodiode was used to measure light intensities. *J-V* scans were measured using Keithley 2400 Source Meter at different scan rates, by varying delay times at constant step size (0.01 V); delay times of 10, 50, 100, 500 and 1000 ms correspond to scan rates 1, 0.2, 0.1, 0.02 and 0.01 V/s respectively. Typical forward *J-V* scans (short circuit, SC → open circuit, OC) measured at 1 V/s were used to calculate solar cell performance metrics, unless specified. Hysteresis characteristics were measured using an uninterrupted sequence of forward and reverse scans (SC→OC→SC). Stabilized PCE were determined using steady-state current measurements at an applied voltage corresponding to maximum power point without encapsulation. For all measurements under illumination, the shutter was opened just before measurement and no intentional light or electrical bias soaking was used. EQE measurements were performed using a setup consisting of xenon lamp (Oriel, 450W) as light

source, monochromator (Newport Cornerstone 130), optical chopper, lock-in amplifier (Stanford Research Corp SR830), and a NIST-certified Si-photodiode (Thorlabs FDS 100-CAL) for calibration. The fluctuation of xenon arc lamp source was within 5% during the entire period of measurements. EQE spectra were integrated over AM 1.5G photon-flux to attain photocurrent density. All EQE measurements were carried out in ambient without any device encapsulation.

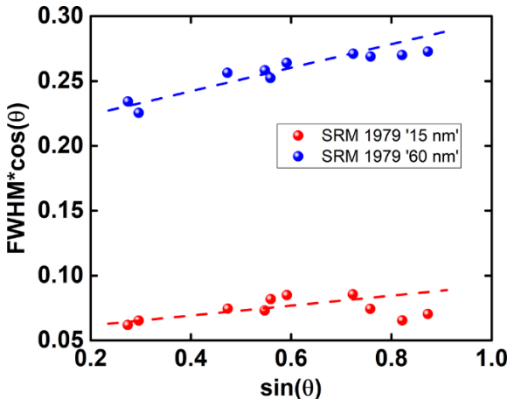

Figure 6.2. Williamson-Hall plot of NIST line shape standards SRM 1979, which contains two differently sized ZnO nanoparticles. For clarity, we omit the XRD peaks where growth or deformation faults effect line broadening in the Williamson-Hall fit (following the work of Cline *et al.*[434]). Comparison of this result with the Williamson-Hall plot of Cline *et al.* helps inform the merits and limitations of the Williamson-Hall technique. We extract size of 38.3 and 148 nm for the two differently sized nanoparticles, compared to 25.6 and 92.2 nm reported by Cline *et. al*, showing that our sizes are consistently about 50% greater. For calculated strain, we measure 0.047% and 0.017% for the smaller and larger particles respectively. Cline *et. al* do not report calculated strain directly, but their slopes are very similar to ours, where the larger particle has very little strain and the smaller particle has slightly larger, identical to our observation. Measuring the NIST line shape and comparing our Williamson-Hall plot an identical plot prepared by the standard developers[434] confirms that while the quantitative results are not precise, the measured trends can be appropriately applied to evaluate relative size and strain in our dataset.

Thin-film characterization, microscopy, and X-ray diffraction: Absorption measurements were carried out using Varian Cary 5000 UV-Vis-NIR spectrometer. Film thicknesses were measured using Bruker DektakXT stylus profiler. An FEI Sirion scanning electron microscope was used for all SEM characterization with 5 kV used for imaging. A Bruker D8 Discover Microfocus XRD with a Cu Kα source (with 1D or 2D detector) was used for XRD measurements. Gamma *vs.* intensity plots were obtained using 2θ-integration (across (100) diffraction ring) of 2D XRD scans, with identical integration parameters. We use the Williamson-Hall method to determine the size and strain components to the XRD peak broadening. To ensure that we have

correctly accounted for instrumental broadening, we first measured our instrumental broadening function using a large-domain low-strain LaB_6 XRD calibration sample. Next, we obtained NIST standard SRM 1979 for domain size and strain calibration, measured the samples on our lab instrument, applied the Williamson-Hall analysis to the data, and compared with that reported by NIST. The W-H plot of the NIST standard samples collected from our diffractometer are shown in **Figure 6.2**.

Absolute Intensity Photoluminescence (AIPL) Measurements: AIPL measurements were conducted as described previously.[369] PL spectra were measured with a Horiba LabRAM HR-800 with 532nm laser excitation, 10x objective, with confocal hole was set to 800 μm using a 150 gr/mm Czerny-Turner monochromater blazed at 500 nm. An Oriel optical power meter and beam profiler was used to calibrate photon flux, which was held constant at the AM1.5 FT solar spectrum integrated above 1.8 eV. The photon detection rate was calibrated using a blackbody source (IR-301, Infrared Systems Development) at 1050 ˚C with 10 μm pinhole. All confocal PL experiments were conducted in N_2 filled container sealed with O-ring and vacuum grease with a quartz window.

Description and discussion of $d\langle E_{PL}\rangle/dt$ calculation: Mixed-halide perovskites that exhibit phase segregation differ in the relative halide content of the segregated phases, the rate of formation of segregated phases, and the mass fraction of segregated phases. The stabilization of PL emission at a lower energy (<1.7 eV, which corresponds with emission from a phase with <20% Br) for PEA0 compared PEA5, PEA10 and PEA20 indicates that the miscibility gap for photo-stabilized phases for the pure 3D film (PEA0) is much greater than films containing PEA. The mean PL emission energy, $\langle E_{PL}\rangle$ is also an excellent metric to observe phase segregation dynamics since it is sensitive to growth of a low energy shoulder even with a constant PL peak position. Thus, study of the first derivative of $\langle E_{PL}\rangle$ *vs.* time is a direct metric to compare the rate of phase

segregation. **Figure 6.8d** presents the numerical derivative of the AIPL results presented in **Figure 6.8b**. We see for each of the compositions, most of the halide redistribution occurs in the first 10-20 s, after which $d\langle E_{PL}\rangle/dt$ is much lower. Further, $d\langle E_{PL}\rangle/dt$ for the pure 3D case (PEA0) is about double that of PEA5 and almost 10 times higher than PEA10 and PEA20. This indicates that the pure 3D film has much faster phase segregation rates in addition to having a greater miscibility gap. We note that the mass fraction of segregated phases cannot be determined from PL results. Other works have studied the mass fraction of I-rich phase formation through observing changes in optical absorbance and XRD pre- and post-illumination with incredibly varied results.[13,368,435] We note that the evolution of quasi-Fermi level splitting with time in these films will depend on the equilibrium populations of carriers in each phase and thus is sensitive to both the bandgap and mass fraction of the I-rich and Br-rich domains.

Photoconductivity measurements: For photoconductivity measurements, 80nm of Au were evaporated at 2 Å/s in a geometry to produce 1mm channel width and 3 mm channel length. Samples were excited with a blue LED from Lumencor SpectraX light source with a 29-nm wide bandpass excitation filter centered at 438 nm. Excitation photon flux was calibrated to 1 Sun with a Newport 91150V Si reference diode. IV sweeps were conducted using a Keithley 2400 SourceMeter, measured between -20 V and +20 V with sweep rate for ~3 V/s. Note that the electric field at 20 V for 3 mm channel length is 3 orders of magnitude lower than electric field present in a device. All IV sweeps produced a linear "ohmic" response, which was fit to calculate conductivity using the channel geometry and film thickness. We note that we would prefer to conduct measurements in 4-point geometry so we can neglect the influence of contact resistance on measurement, yet the photoconductivity signal was not high enough for PEA containing films for precise 4-point measurement. We suspect contact resistance has a minor contribution to our

photoconductivity results. For PEA-containing films, the dark conductivity had the same order of magnitude as the photoconductivity, and for each measurement we calculated photoconductivity as the difference in conductivity in the light and dark. Photoconductivity measurements were conducted in a closed, N_2-filled stage (Linkam Scientific LTSE420-P) with continuous N_2 purge at 70% of maximum flow, with the stage temperature regulated to 20 ˚C.

Discussion of photoconductivity results: As shown previously,[418] a simple photoconductivity measurement can be used to determine mean carrier diffusion length, L_D, which correlates well with device J_{SC} for pure 3D perovskite active layers. **Table 6.3** presents photoconductivity measurements with 2-point geometry for five films with various PEA content. We first notice that the pure 3D perovskite film (PEA0) has photoconductivity about 2 orders of magnitude higher than the next highest (PEA5) film, which corresponds to an L_D value about an order of magnitude higher (L_D has a square root dependence on photoconductivity). Thus, calculated L_D values for each of the perovskite films containing PEA are <20nm, which in the context of our previous findings would suggest devices with these films would have very little photocurrent. In contrast, we observe decent J_{SC} for the films containing PEA, up to ~13 mA/cm^2 for PEA5 case. We therefore conclude that these layered perovskites have strongly anisotropic transport which limits the ability for a device-relevant mean carrier diffusion length to be determined from a lateral photoconductivity measurement. We observe that these perovskite films have much more efficient carrier transport through the depth of the film than laterally. However, the relative trends observed for the PEA containing films still precisely follow the observed device J_{SC}'s, with photoconductivity and J_{SC} both decreasing with increasing PEA content. These findings suggest that the J_{SC} trends observed are due to changes in carrier collection from limited transport in the perovskite layers, and that moderate PEA content will give the best balance between quasi-

Fermi level splitting, transport, and phase stability. The lower J_{SC} for pure 3D device (than PEA5) despite the highest photoconductivity for that film is likely due to phase segregation and higher trap density impacting collected current for that material even in the short timescale of a single *J-V* sweep.

Transient absorption spectroscopy (TAS) and Transient photoluminescence (TRPL) measurements: All spectra were taken by using the Helios laser system with Libra seed laser, with 50 fs FWHM at 80MHz repetition rate and 800 nm fundamental wavelength (Ultrafast Systems). The fundamental beam was split into two beamlines by an 80/20 beam-splitter. The pump wavelength of 365 nm was generated by an optical parametric amplifier (Coherent, Inc.) after splitting the fundamental beam. The pump fluence was modulated by 2 consecutive neutral density filters. The diameter of spot size is 0.85 mm. All samples for TAS and TRPL were prepared on glass and encapsulated to avoid quenching at the air interfaces. For TAS, the white continuum light was generated as the probe through Ti:Sapphire crystal. For TRPL, the same laser set-up was utilized to pump the samples, which were prepared by the same method. The emission was measured through collection optics, spectrometer, and streak camera (Hamamatsu model C-10627). Streak camera and laser source were synchronized through synchronous delay generator (C-10647) and jitters were regulated by delay unit (C1097-05).

Mechanistic analysis of carrier recombination kinetics: We assumed band structure was dominated by the invariant metal halide framework in perovskite alloys, in which direct bandgap facilitates radiative bimolecular recombination: $\frac{\mathrm{d}\bar{n}}{\mathrm{d}t} = -\mathrm{k}_1\bar{n} - \bar{\mathrm{k}}_2\bar{n}^2$, $\bar{n} = \frac{n}{n_0}$ and $\bar{\mathrm{k}}_2 = \mathrm{k}_2 n_0$; where k_1 is the total monomolecular decay rate and n_0 is the initial carrier density which was calculated by Beer-Lambert's law. The differential equation was numerically solved with parametric optimizations to fit the decay data. The initial conditions for the fitting were given by

experimental PL quantum yield (PLQY), which has the following relationship to the decay constants: $\mathrm{PLQY} = \frac{k_2 n_0}{k_1 + k_2 n_0}$. The equation is given by solving differential equation assuming that the PL is dominated by bimolecular recombination. k_2 is dependent on the diffusion length of charge carriers as well as the crystal domain size, which then decide Langevin and non-Langevin characteristics of the recombination.

6.3 Results and Discussion

6.3.1 Phenylethylammonium (PEA) Incorporation in Large Bandgap Perovskites

Phenylethylammonium is a large aromatic ammonium cation, which was initially incorporated into $MAPbI_3$ (3-dimensional framework) to form reduced-dimensionality layered perovskites with improved moisture stability.[433] Subsequent incorporation of PEA into a wide-range of 3D perovskites have unveiled other benefits such as suppression of defect formation,[436] passivation of defects,[437] reduction of recombination losses,[438] and stabilization of metastable perovskite polymorphs.[439,440] Addition of large cations (PEA) to the precursor solution with small cations (MA) typically result in perovskite films which are complex multicomponent multilayered quasi-2D (2D-3D) material, where pure 2D or 3D lead-halide frameworks no longer exist.[433,441] The ratio of large and small cation is the primary controlling variable that determines the composite nature of the resultant quasi-3D perovskites and controls the film characteristics (morphology, preferential orientation, charge carrier dynamics) crucial for PV application.[433,441,442] We thus start this study with the material-level investigation of 1.8 eV E_g mixed-halide perovskites with different amounts of PEA incorporation.

We used $MAPb(I_{0.6}Br_{0.4})_3$ as the baseline composition to realize ~1.8 eV E_g as in our previous studies;[3,13,20] material characteristics and phase segregation behavior for this

composition are well-established.[417] We systematically tuned the composition by mixing $MAPb(I_{0.6}Br_{0.4})_3$ and $(PEA)_2Pb(I_{0.6}Br_{0.4})_4$ precursor solutions in different ratios to get the desired PEA fraction ([moles of PEA] / [moles of MA + moles of PEA]). Films were fabricated using optimized solvent wash method to get homogenous coverage for compositions of interest (**Figure 6.3**). Considering the complex nature of PEA-incorporated films, we simply use precursor solution PEA fraction for referring to films.

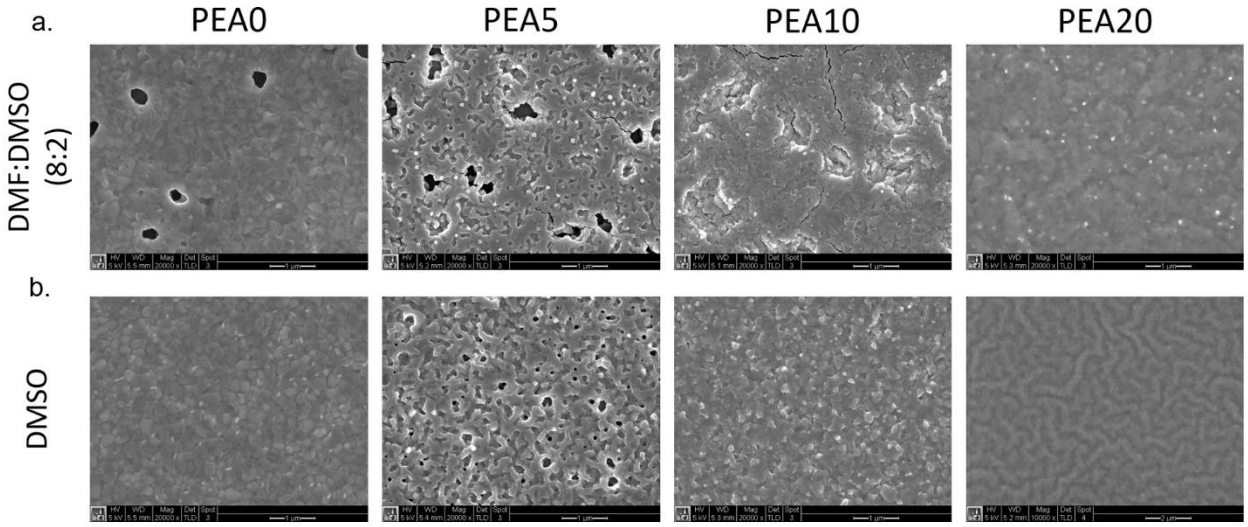

Figure 6.3. Scanning electron microscope (SEM) images of PEA0-PEA20 films processed *via* anti-solvent wash method using (a) 8:2 DMF:DMSO co-solvent system and (b) pure DMSO solvent system; toluene was used as anti-solvent for both cases. Films processed from DMSO (b) show better substrate coverage and were used in this study.

Figure 6.4a shows the photograph of films with PEA fraction from 0 to 100%. The corresponding notation and associated 'n' equivalent for different compositions are listed in **Figure 6.4b**. As PEA fraction increases from PEA0 to PEA20, E_g increases subtly from 1.82 eV to 1.84 eV. With further increase in PEA fraction, E_g increases more significantly and reaches 2.56 eV (PEA100). Additionally, absorbance decreases continually from PEA0 to PEA100 (**Figures 6.4a-c**). Profilometry measurements revealed that all films (PEA0-PEA100) were of comparable thickness (170±10 nm) and eliminated any potential contribution from film thickness on the observed differences in absorption. The E_g increase and absorbance decrease can accordingly be

rationalized because of the stronger dielectric confinement and lower optical frequency dielectric constant in reduced-dimensional perovskites,[443] which are formed increasingly as the PEA fraction increases. Detailed discussion regarding the evolution of optical properties and impact of confinement effects in quasi-2D perovskites can be found elsewhere.[443,444]

a.

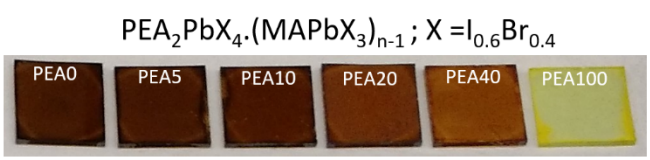

b.

PEA fraction (%)	Notation	'n' equivalent	Br/(I+Br)	Bandgap, E_g (eV)
0	PEA0 [3D]	∞ [$MAPb(I_{0.6}Br_{0.4})_3$]	0.40	1.82
5	PEA5	39	0.40	1.82
10	PEA10	19	0.40	1.83
20	PEA20	9	0.40	1.84
40	PEA40	4	0.40	1.89
100	PEA100 [2D]	1 [$(PEA)_2Pb(I_{0.6}Br_{0.4})_4$]	0.40	2.56

c.

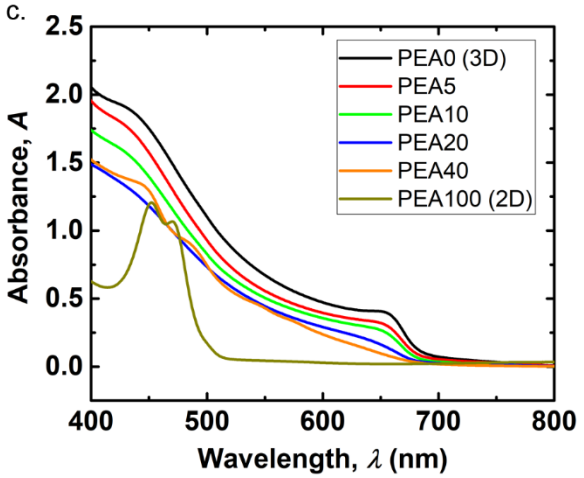

Figure 6.4. Phenylethylammonium (PEA) incorporation in $MAPb(I_{0.6}Br_{0.4})_3$ perovskite. (a) Photographs of films with 0 to 100% PEA fraction ([moles of PEA] / [moles of PEA + moles of MA]). (b) Definition of notations used to represent different compositions and their associated E_g values. 'n' equivalent corresponds to the number of metal-halide sheets sandwiched between PEA cations, if a pure 2D perovskite can be formed; 5-40% PEA fractions here form quasi 2D perovskite, which is a mixture of 3D and 2D perovskite phases with different 'n' values. (c) UV-vis absorption spectra of PEA0-PEA100 thin films.

We confirm the material nature using two-dimensional X-Ray Diffraction (2D XRD) measurements of thin films (**Figure 6.5a-b**). Diffraction patterns for PEA0 and PEA100 correspond to the phase pure 3D (cubic) and 2D (n = 1, with the c-axis perpendicular to the substrate) perovskite structures, respectively. For all the intermediate compositions, diffraction patterns reveal the presence of both 3D and 2D phases (2D-3D composites) and formation of reduced-dimensional phases become more prominent at higher PEA fractions. The absorption and XRD results clearly demonstrate PEA incorporation in mixed-halide perovskites and observations

corroborate with previous studies in pure-iodide perovskites.[433,441] In the context of this work, we choose PEA0-PEA20 (1.80-1.85 eV E_g range) for continued evaluation.

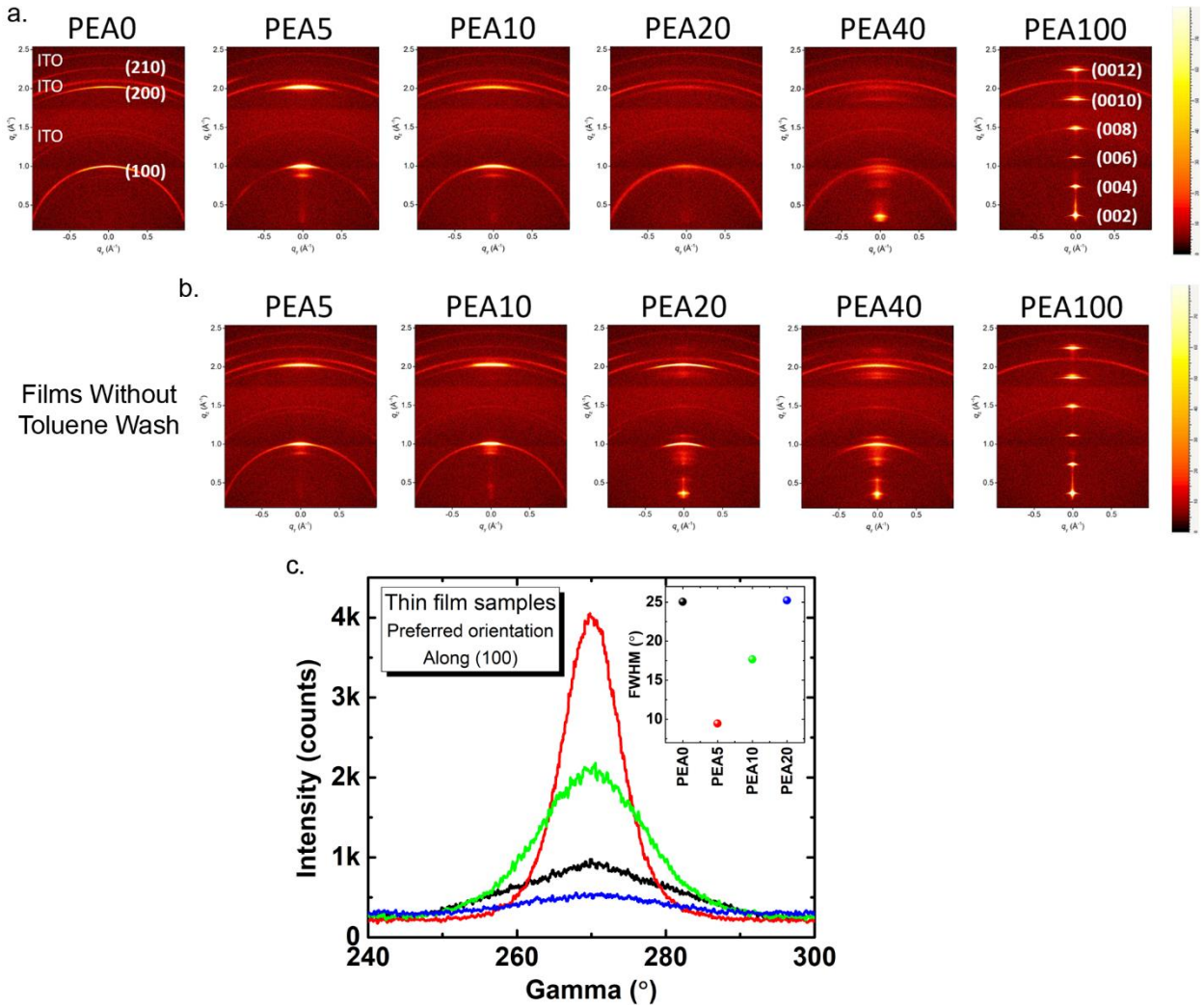

Figure 6.5. (a) 2D X-ray diffraction (XRD) images of PEA0-PEA100 films processed using DMSO solvent system with toluene wash. PEA0 and PEA100 indexing agree with phase pure 3D and 2D perovskite structures, respectively. For all the intermediate compositions, the increase in diffraction signal at smaller angles (below the (100) ring corresponding to the 3D phase) correspond to an increasing amount of reduced-dimensionality phases.[433,441,442,445,446] (b) 2D XRD images of PEA5-PEA100 films processed using DMSO solvent system without toluene wash; it is apparent that with and without toluene wash, the preferential orientation is significantly different for PEA20-PEA40 films, whereas it is relatively unchanged for other compositions. This demonstrates strong dependence of structural characteristics on PEA fraction and indicates different regimes of film formation. Our hypothesis is that the driving force for formation of 3D perovskite is dominant at low PEA fractions (PEA0-PEA10) and the driving force for formation of 2D perovskite is dominant at high PEA fractions (PEA100); for intermediate compositions (PEA20-PEA40), the competition between driving force for crystallization from self-assembly of 2D perovskites and solvent wash results in the destruction of structural order. Additional experiments are required to confirm the hypothesis and however does not affect conclusions drawn in this work. Films with toluene wash were unanimously used in all measurements and devices. (c) Gamma *vs* Intensity plots shown in **Figure 6.6** along with the corresponding FWHM values shown in inset; narrowing of FWHM coupled with increase in peak intensity corresponds to a stronger preferential orientation.

1D XRD measurements were performed for PEA0-PEA20 to obtain detailed structural insights regarding lattice size, crystallite orientation, size, and strain (**Figures 6.6a-b**). The constant peak positions for PEA0-PEA20 (**Figures 6.6a-c**) illustrate that the lattice size is unchanged, and the composition of 3D phases are unaltered with PEA incorporation. Further, this also indicate that the increase in heterogeneity of perovskites with PEA incorporation does not introduce any observable macrostrain in the resultant films. Since film thickness and measurement parameters are constant, significant differences in the XRD peak intensity (**Figures 6.6a** and **6.6c**) indicate that the PEA fraction strongly influences the preferential orientation in thin films ((100) plane of the 3D perovskite crystallites parallel to the substrate). This is also apparent from differences in the 2D XRD images (**Figure 6.5a**), which are correspondingly shown using the gamma *vs* intensity plots in **Figure 6.6d** (gamma represents the direction of diffracted beam on the diffraction cone).

The preferential orientation initially increases for PEA5 and then subsequently decreases with further PEA incorporation up to PEA20. This behavior and associated trend (**Figure 6.5c**) resemble the recent observations in butylammonium based 2D-3D perovskites.[427] It has been illustrated that as the larger cation fraction is increased, the changing balance between the dominance of 3D and 2D phases in perovskite composites changes the energetically favorable orientation for the 2D-3D heterostructures and the overall crystallization behavior. Focused morphological studies required for further understanding the complex growth behavior in quasi-2D perovskites are beyond the scope of this study.

Figures 6.6a-c show that FWHM of {h00} peaks are continually increasing with PEA incorporation. Factors contributing to the increase in FWHM can be reasonably narrowed down to crystallite size and microstrain in this context.

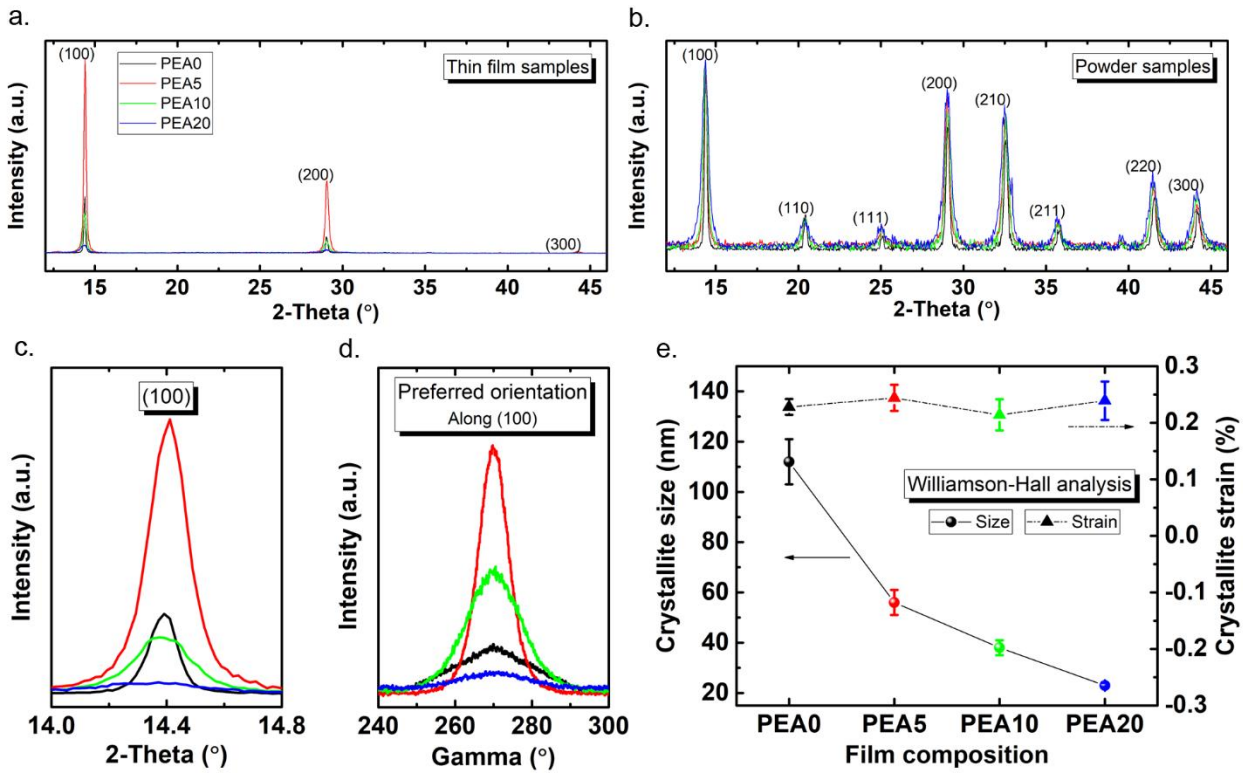

Figure 6.6. X-ray diffraction (XRD) measurements of PEA0-PEA20. Standard θ/2θ XRD scans with a 1D detector for (a) thin film samples and (b) powder samples obtained by scrapping thin films. (c) Zoomed in region of thin film XRD illustrating changes in (100) peak. (d) Gamma *vs* Intensity plots demonstrating extent of preferred orientation along (100); narrowing of peak width coupled with an increase in peak intensity corresponds to a stronger preferential orientation. (e) Crystallite size and strain values obtained using Williamson-Hall analysis of peak broadening in powder samples.

We measured the standard θ/2θ XRD scans with a 1D detector for powder samples of PEA0-PEA20 (**Figure 6.6b**) to achieve a higher resolution and accurately determine broadening parameters. Better sampling distribution in powder samples resulted in diffraction from several additional planes and the characteristics of {h00} peaks were unchanged compared to thin films (**Figures 6.6a-b**). We use Williamson-Hall approach to isolate size and strain contributions in peak broadening (methodology verified using measurement of NIST line shape standards SRM 1979, as described in **Figure 6.2**). It is evident that the FWHM increases due to continuous decrease in crystallite size from 112±9 nm (PEA0) to 23±1 nm (PEA20), and the contribution from strain is almost constant for PEA0-PEA20 (**Figure 6.6e** and **6.7**). The decrease in crystallite size can be attributed to the impeded growth by PEA-induced surface functionalization of perovskite

crystallites, where the large ammonium cations cannot be incorporated into the 3D lattice and act as surface capping ligands.[428,439] Therefore, as the PEA fraction is increased, a decrease in the crystallite size of 3D perovskite coupled with an increase in the formation of layered perovskites are expected. Reduction in crystallite size up to ~10 nm has been previously observed for butylammonium incorporation in 3D perovskites.[428]

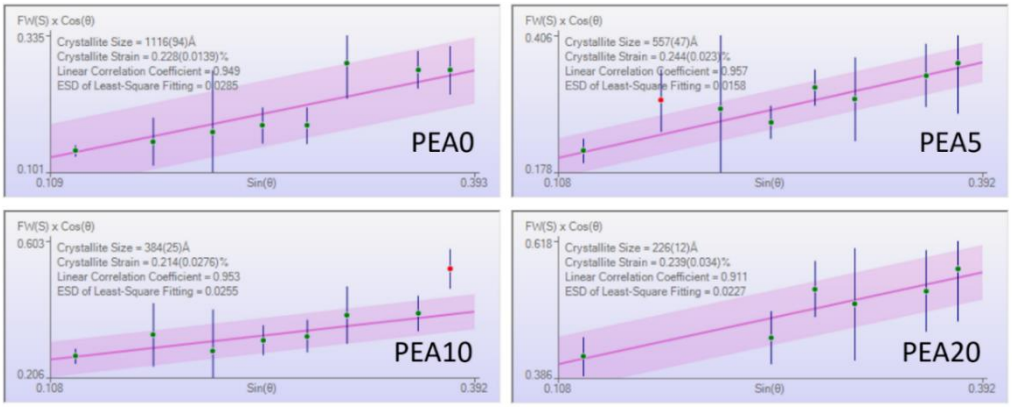

Figure 6.7. Williamson-Hall plots (raw output) generated using XRD pattern processing software (MDI JADE), which uses a LaB_6 pattern for instrument profile function, peak profile fitting to remove contribution of $K\alpha_2$ peak to broadening, and σ^2 weighing in Williamson-Hall linear fit. The ESD indicates the estimated standard deviation (compiled using JADE software) accounts for error in the instrument response function, peak full width half max determination, and Williamson-Hall fit. XRD measurements (1D detector) of powder samples were used for this analysis.

6.3.2 Spectroscopic Characterization of PEA-incorporated Perovskite Thin Films

We use quantitative photoluminescence (PL) techniques to assess the impact of structural and morphological modifications by PEA incorporation on the material quality and phase segregation behavior of the resultant large E_g perovskites. Calibrated absolute intensity photoluminescence (AIPL) measurements give insight on the relative balance of radiative and non-radiative recombination and can be used to measure QFLS. [369,447] **Figure 6.8a** shows the AIPL spectra for PEA0-PEA20 films. The photoluminescence quantum yield (PLQY), obtained by integrating the AIPL spectrum and dividing the incident flux, continually increases with PEA incorporation (**Figure 6.9**) and correspondingly the QFLS increases up to 1.35 eV (PEA20)

(**Figure 6.8a**). The QFLS is calculated using the external PLQY as described previously.[369,448] To account for the E_g change and compare the improvement in material quality, we define a material quality parameter, χ = QFLS/q$V_{oc,SQ}$. As shown in **Figure 6.8c**, χ is ~80% for PEA0 comparable to our previous study[20] and increases significantly to 85-87% for PEA5-PEA20. This demonstrates that we have successfully improved the material quality of ~1.8 eV E_g perovskites by PEA incorporation and the corresponding QFLS results imply that a V_{oc} of 1.30-1.35 V is attainable in devices, provided there is no additional interfacial recombination losses.

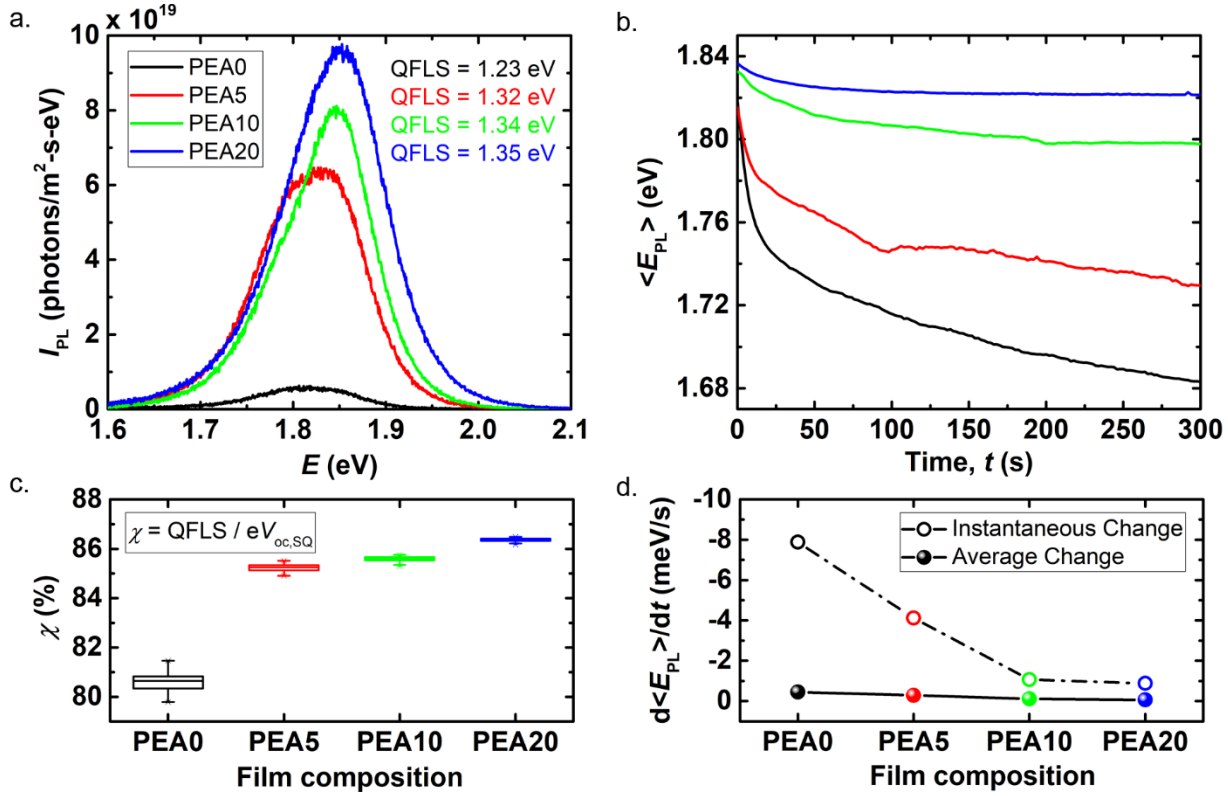

Figure 6.8. Absolute intensity photoluminescence (AIPL) measurements of PEA0-PEA20. (a) AIPL spectra and corresponding quasi-Fermi level splitting (QFLS) values (spectra with median PLQY for each film shown). (b) Mean PL energy (<E_{PL}>) as a function of time under continuous illumination. (c) Material quality parameter (χ) denoting optoelectronic quality (statistics from 121 PL spectra). (d) First derivative of <E_{PL}> *vs.* time (d<E_{PL}>/dt) providing an estimate for the rate of phase segregation under illumination. The "instantaneous change" is the first derivative immediately after illumination (first 2 seconds), while "average change" is the average rate of change over 300 s.

PEA incorporation also considerably reduces the extent of phase segregation and is demonstrated by the slower decay in mean PL energy (<E_{PL}>) over time under continuous illumination (**Figure 6.8b**). The corresponding decay rates (d<E_{PL}>/dt) shown in **Figure 6.8d**

demonstrate that the rate of phase segregation decreases with increase in PEA amount. Details regarding the calculation of d<E_{PL}>/dt are provided in the associated discussion in **Section 6.2**. The mean carrier diffusion length (L_d) in PEA0-PEA20 films estimated using photoconductivity measurements (following previous work[418] and described in **Section 6.2**) reveal that L_d decreases sharply with PEA incorporation (**Table 6.3**) and is intimately linked with the above discussed decrease in crystallite size (**Figure 6.6e**).

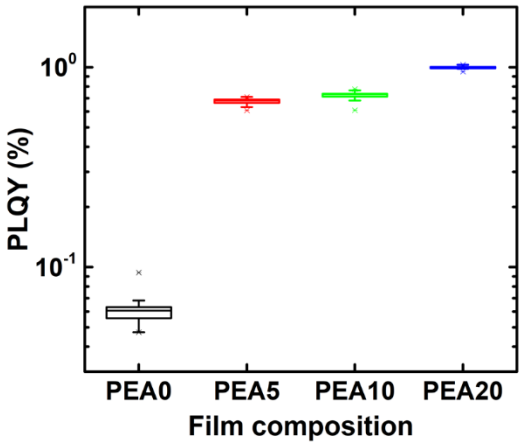

Figure 6.9. Photoluminescence quantum yield (PLQY) of PEA0-PEA20 films calculated using AIPL measurements.

Table 6.3. 2-point photoconductivity and mean carrier diffusion length values for PEA0-PEA20.

	Photoconductivity [S/m]		**Diffusion Length [nm]**	
	Mean	SD	Mean	SD
PEA0	1.16E-03	2.02E-04	133	12
PEA5	2.33E-05	5.49E-06	19	2
PEA10	3.56E-06	4.66E-07	7	1
PEA20	2.31E-06	1.41E-06	6	2

The correlation between the rate of phase segregation and L_d is in accordance to the model proposed by Draguta *et al.*[419] Further, spatially resolved microscopic and spectroscopic studies by Tang *et al.* reveal the crucial role of grain boundaries and illustrate that the phase segregation characteristics are reliant on film topography.[449] Based on these insights, we infer that a combination of the decrease in crystallite size and L_d along with the modification of grain

boundaries by PEA ligands (anchoring on perovskite surfaces) contribute to mitigation of phase segregation in PEA5-PEA20. Our results provide an important validation for the emerging mechanistic picture and the current understanding of phase segregation in mixed-halide perovskites.

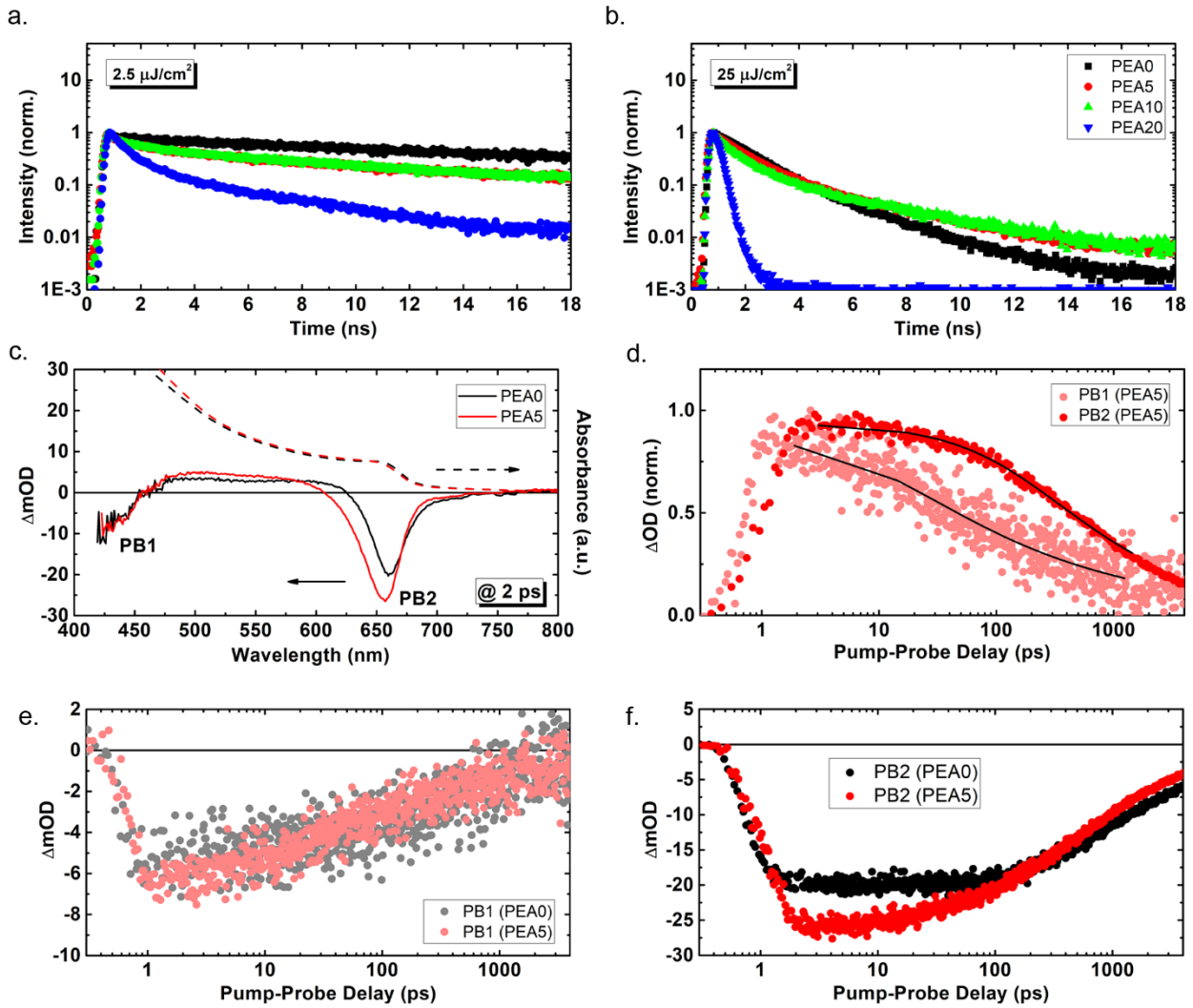

Figure 6.10. Transient spectroscopic measurements. Normalized transient PL decay of PEA0-PEA20 at (a) 2.5 μJ/cm^2 and (b) 25 μJ/cm^2 incident fluence. (c) Photoinduced absorption spectra at pump-probe delay of 2 ps for PEA0-PEA5. Kinetic traces of photobleaching (PB) signals in transient absorption spectra of (d) PB1 and PB2 in PEA5, and their comparison between PEA0 and PEA5 for (e) PB1 and (f) PB2.

We perform additional transient spectroscopic studies to understand recombination dynamics as well as the origin of PL and improved QFLS. Typically, the photoemission from perovskite comes from either excitonic (monomolecular) or non-geminate (bimolecular)

recombination of charge carriers. Previous studies showed that the excitonic behavior is dominant only for higher PEA fractions (>40%),[442] and therefore excitonic emission mediated enhancement of PL can be excluded for PEA0-PEA20 studied here. For non-excitonic perovskite films, the monomolecular decay through trap states is an additional non-emissive decay pathway which alters the PL decay from a single pure exponential or reciprocal dependence on time and appears as a decay rate that is dependent on the initial charge carrier density.[350] The fluence-dependent PL decay therefore reflects the nature of excited states in relation to the quality of perovskite films. Transient PL (TRPL) curves in **Figures 6.10a-b** and **6.11** show that PEA5 and PEA10 exhibit softer dependence on fluence compared to PEA0. This result together with higher PLQY (**Figure 6.9**) indicate either reduced monomolecular recombination rate (k_1) or enhanced effective bimolecular recombination rate (k_2n_0, where n_0 = initial charge carrier density at the band-edge) with PEA incorporation.

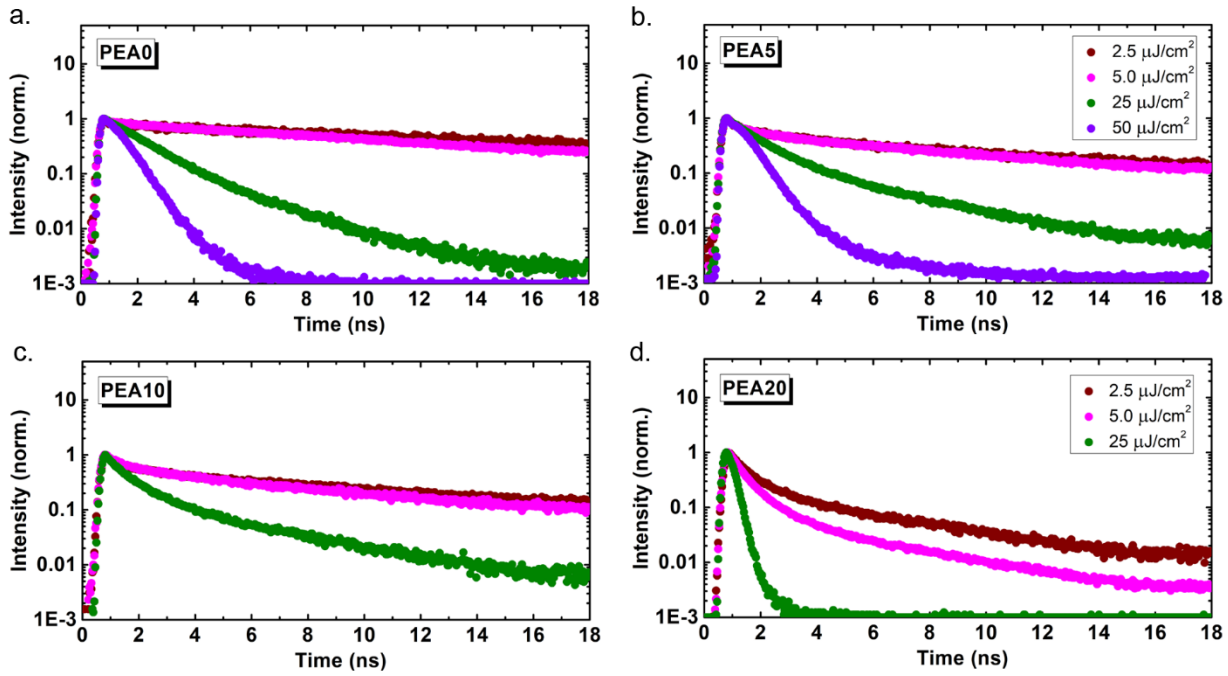

Figure 6.11. Normalized fluence-dependent transient PL decay for (a) PEA0, (b) PEA5, (c) PEA10, and (d) PEA20.

We use femto-second transient absorption spectroscopy (TAS) to assess the initial kinetics of photo-generation of charge carriers. **Figure 6.10c** shows photo-induced absorption spectra at the pump-probe delay of 2ps. Although the origin of high energy photobleaching ~430 nm (PB1) is still under debate, it is clear that the initial excitation firstly populates the hot energetic bands and then cools down to the band-edge (PB2) along with band-edge and dielectric reorganization within 2ps.[376,450] The kinetic trace of PB2 later than 2 ps exhibits reciprocal decay which is characteristic of complex bimolecular recombination behavior, whereas PB1 shows mono-exponential decay which reflects monomolecular process involving transition to PB2 (**Figure 6.10d**). Accordingly, even though PB1 of PEA0 and PEA5 exhibited similar kinetic traces (**Figure 6.10e**), PB2 demonstrated higher initial occupation of band-edge states in PEA5 (**Figure 6.10f**), as we speculated from the PL and TRPL results. Considering that UV-Vis spectra did not show discernable difference in their actual density of states at the band-edge, these results indicate loss of initial hot excited states through monomolecular decay pathway in PEA0 and such a behavior was previously attributed to the strong effect of trap-mediated recombination. This corroborates with demonstrations regarding the effectiveness of PEA in reducing traps and defect formation.[436]

Table 6.4. Recombination rates extracted from fitting for PEA0-PEA20.

	PLQY [%]	**k_1 [10^7 s^{-1}]**	**k_2n_0[#] [10^9 s^{-1}]**	**n_0 [10^{17} cm^3]**	**k_2 [$10^{-9}$$cm^3$$s^{-1}$]**
PEA0	0.061	7.21	0.70	0.79	0.88
PEA5	0.661	1.64	2.34	1.07	2.18
PEA10	0.741	3.00	2.67	0.59	4.48
PEA20	1.005	4.31	3.48	0.39	8.75

[#]Fitted parameter was extracted from kinetic traces of transient absorption spectra. Fitting was conducted using following simple reaction kinetics: $\frac{d\bar{n}}{dt} = -k_1\bar{n} - \bar{k}_2\bar{n}^2$, where $\bar{n} = \frac{n}{n_0}$ and $\bar{k}_2 = k_2 n_0$.

Therefore, we conclude that the superior luminescent behavior of PEA5 compared to PEA0 dominantly stems from the effectively lowered trap density, also validated by recombination rates extracted from the fitting of kinetic traces (**Table 6.4**).

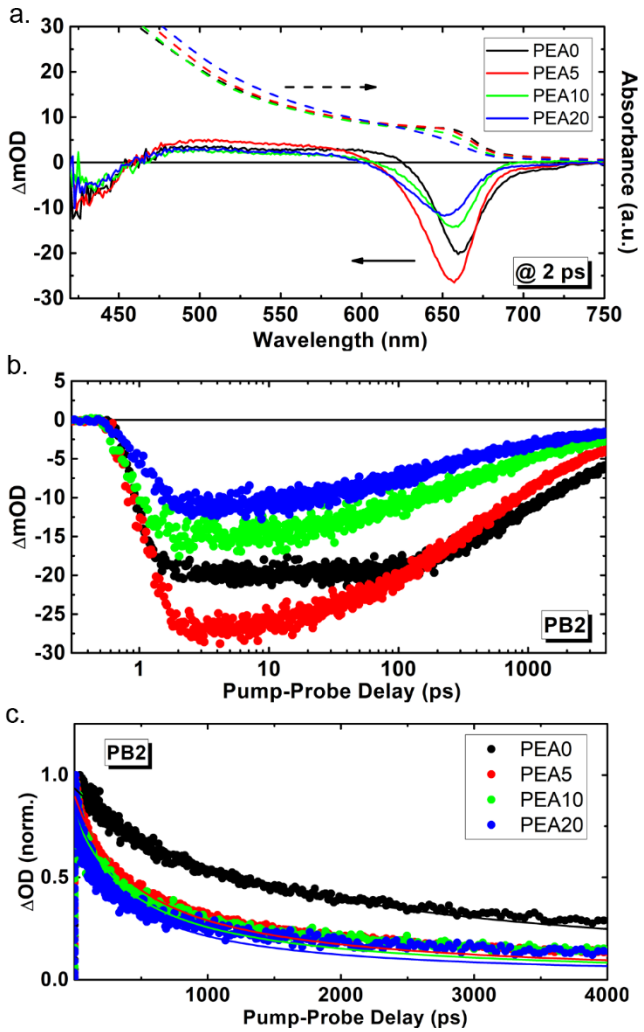

Figure 6.12. (a) Photoinduced absorption spectra at pump-probe delay of 2 ps for PEA0-PEA20. (b) Kinetic traces of photobleaching signals in transient absorption spectra of PB2 for PEA0-PEA20. (c) Fitting of kinetic traces used for extracting recombination rates.

Higher PEA composition films (PEA10 and PEA20) were also analyzed based on their TAS spectra (**Figures 6.12** and **Table 6.4**. It is important to note that, along with the lowered k_1, the k_2 is also significantly increased with PEA incorporation. For PEA5-PEA20, it is more reasonable to relate this behavior to the observed crystalline quality. Hybrid perovskites are characterized as highly crystalline materials which exhibits non-Langevin recombination behavior, due to the high mobility of charge carriers.[136] The smaller crystallite size physically limits the mobility (and L_d) of charge carriers[451] and leads to higher k_2 and PLQY as the PEA incorporation increases (**Table 6.4**). The trend in rate of monomolecular recombination through trap states (k_1)

empirically correlates with the crystalline orientation, where PEA5 with the strongest preferential orientation (**Figure 6.6d**) has the lowest k_1 (**Table 6.4**).[89] However, for PEA fractions >40%, quantum confinement effects will dominate the recombination behavior and the induced additional radiative monomolecular (excitonic) recombination pathway contributes to a higher PLQY.[442] The stronger quantum confinement is also reflected in the steady-state optical characteristics with arising of sharp excitonic absorption for PEA40-PEA100 (**Figure 6.1c**).

6.3.3 Photovoltaic Characteristics of PEA-incorporated Large Bandgap Devices

To assess the impact of structural and optoelectronic characteristics of PEA-incorporated large E_g perovskites on performance, we fabricate PV devices using a p-i-n device configuration (preferred for PVK-PVK tandems) with NiO_x hole-transport layer (HTL) and fullerene electron-transport layer (ETL) (**Figure 6.13a**).

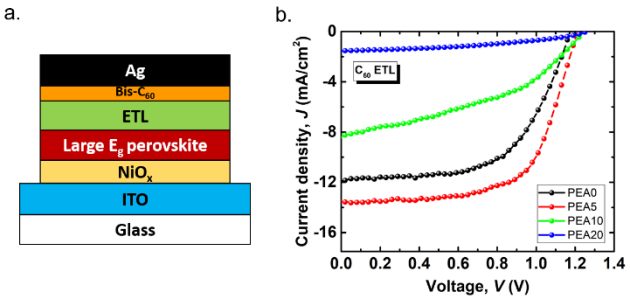

c.

C_{60} ETL	V_{oc} (V)	J_{sc} (mA/cm^2)	FF	PCE (%)
PEA0	1.17	11.9	0.59	8.3
PEA5	1.21	13.5	0.64	10.5
PEA10	1.25	8.3	0.41	4.2
PEA20	1.26	1.5	0.4	0.8

Figure 6.13. (a) PV device architecture used in this study. (b) Forward *J-V* characteristics and (c) corresponding PV performance metrics of PEA0-PEA20 devices with C_{60} ETL.

To assess the impact of structural and optoelectronic characteristics of PEA-incorporated large E_g perovskites on performance, we fabricate PV devices using a p-i-n device configuration (preferred for PVK-PVK tandems) with NiO_x hole-transport layer (HTL) and fullerene electron-

transport layer (ETL) (**Figure 6.13a**). Initially, based on our previous work, we use C_{60} for ETL.[20] The corresponding current-voltage (*J*-*V*) characteristics and PV performance metrics for PEA0-PEA20 devices are shown in **Figures 6.13b-c**. The increase in V_{oc} from 1.17 V (PEA0) to 1.26 V (PEA20) shows the positive effect of improvement in material quality. Even though the increasing trend in V_{oc} follows QFLS results, V_{oc} values are considerably lower than their corresponding QFLS values (**Figure 6.8a**). The added $V_{oc,loss}$ in devices indicate that with improvement in absorber optoelectronic quality, additional limitations on V_{oc} imposed by the non-optimized interfacial contacts are apparent.

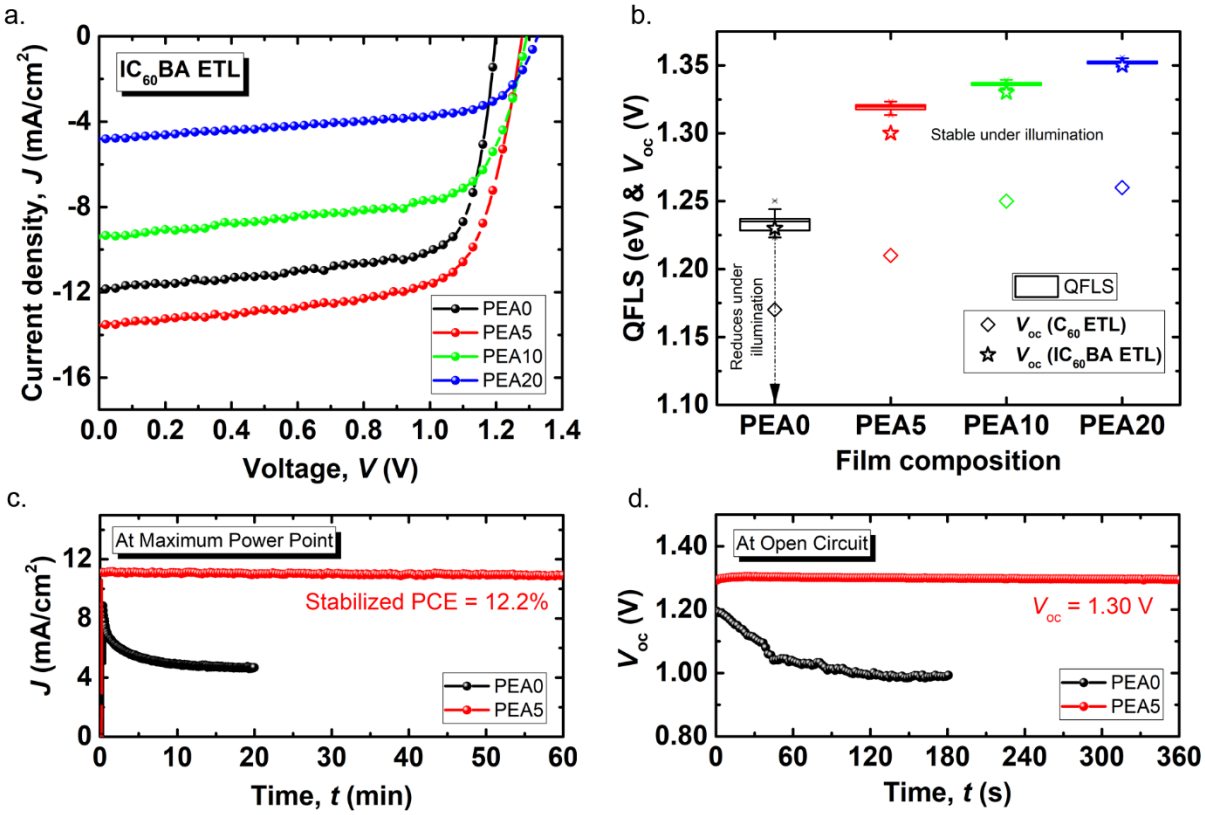

Figure 6.14. Photovoltaic characteristics of PEA0-PEA20 devices with $IC_{60}BA$ ETL. (a) Forward *J*-*V* characteristics of devices with median PCE measured under AM1.5 illumination. (b) Comparison of quasi-Fermi level splitting (QFLS) and V_{oc} values. (c) Steady-state current density (*J*) under AM1.5 illumination at an applied voltage corresponding to maximum power point (1 V for PEA0 and 1.10 V for PEA5). (d) V_{oc} output as a function of time under AM1.5 illumination.

We subsequently fabricate another series of devices with an alternate fullerene variant doped-Indene-C_{60} bis-adduct ($IC_{60}BA$) as ETL, which has been found beneficial for improving the

quality of perovskite/ETL interface.[4,5,20,421] The *J-V* characteristics and associated PV performance metrics for PEA0-PEA20 devices with $IC_{60}BA$ ETL are shown in **Figures 6.14a** and **6.15a-b**, respectively. Strikingly, V_{oc} values are significantly improved compared to their C_{60} ETL counterparts. The highest V_{oc} (1.23-1.35 V) for each of the composition (PEA0-PEA20) precisely agree with the corresponding QFLS values (**Figure 6.14b**) and distinctly overcome the photovoltage plateau in large E_g perovskites (**Figure 6.1**). This shows the importance of synergetic development of perovskite absorber and coupled interfaces to mitigate V_{oc} deficit and will become more crucial as absorber optoelectronic quality is further improved.

a.

$IC_{60}BA$ ETL	V_{oc} (V)	$V_{oc,\ highest}$ (V)	J_{sc} (mA/cm^2)	$J_{sc,EQE}$ (mA/cm^2)	FF	PCE (%)	$V_{oc}/V_{oc,SQ}$
PEA0	1.20 ± 0.02	1.23	11.4 ± 1.0	12.4	0.66 ± 0.03	9.3 ± 0.8	0.80
PEA5	1.28 ± 0.01	1.30	12.9 ± 1.1	12.9	0.65 ± 0.02	11.6 ±0.6	0.85
PEA10	1.30 ± 0.02	1.33	9.2 ± 1.0	10.7	0.63 ± 0.03	7.5 ± 0.8	0.86
PEA20	1.32 ± 0.01	1.35	5.1 ± 1.0	7.8	0.57 ± 0.04	3.3 ± 0.3	0.87

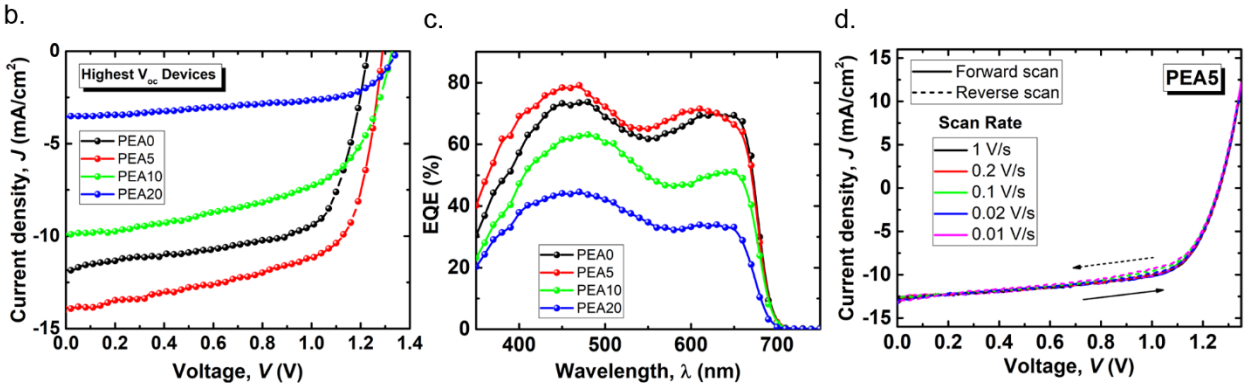

Figure 6.15. (a) PV performance metrics of PEA0-PEA20 devices with $IC_{60}BA$ ETL. (b) Forward *J-V* characteristics of PEA0-PEA20 devices with the highest V_{oc}. (c) External quantum efficiency (EQE) characteristics of PEA0-PEA20 devices with $IC_{60}BA$ ETL. (d) Scan-rate dependent *J-V* characteristics for a PEA5 device with $IC_{60}BA$ ETL.

Another observation in these series of devices (**Figures 6.13, 6.14a** and **6.15**) is that there is an increasing compromise in J_{sc} for PEA10-PEA20, also apparent from the external quantum efficiency curves (**Figure 6.15c**). This trend can be attributed to the decrease in charge collection

efficiency, limited by the carrier transport in perovskite layers (additional discussion of photoconductivity results in **Section 6.2**). PEA5 provides an optimum balance between QFLS, transport, as well as phase stability and yields the best PCE in the series (**Figure 6.15a**). We suspect the J_{sc} is lower in PEA0 (despite higher L_d) than PEA5 because phase segregation is causing limitations in current collection even in the brief timescale of a *J-V* sweep. For PEA10 and PEA20, utilization of a mesoporous device architecture will relieve the transport limitations and improve the PCE further.

We test the photostability of our best performing PEA5 devices in comparison to the reference PEA0 devices (**Figures 6.14c-d**). As expected, for PEA0 devices, both current density at maximum power point and V_{oc} significantly decay under illumination. On the other hand, PEA5 devices exhibit tremendous photostability and show a stabilized PCE and V_{oc} of 12.2% and 1.30 V respectively (~99% of the initial values). We also perform *J-V* measurements at different scan rates (0.01-1 V/s) and confirm that PEA5 devices do not exhibit significant hysteresis (**Figure 6.15d**). We highlight the interesting phenomena where for PEA5 we see a stable V_{oc} with time despite observing some extent of phase segregation in films (indicated by slow PL peak red shift in **Figure 6.8b**). This behavior is similar to what we observed previously in the (MA,Cs)Pb(I,Br)$_3$ system.[3,20] However, this behavior contrasts recent work where Bush *et al.* see the opposite - certain of their (FA,Cs)Pb(I,Br)$_3$ materials show stable PL emission with time (even up to 10 Suns), yet device V_{oc} decrease with time under illumination.[452] Collectively, these results indicate that the impact of phase segregation on device parameters (especially V_{oc}) are not yet fully understood, and remain a topic for future exploration. For the present study, we show PEA5 devices to have stable device parameters with time, which is the most important metric for development of high efficiency perovskite tandems stable under operation[3]. Thus, all the above

results clearly establish that PEA-incorporated mixed-halide perovskites successfully overcome both photovoltage plateau and device-level instabilities under illumination that have been plaguing large E_g PVKSCs till date and provide an important breakthrough.

6.4 Conclusion

In summary, we have demonstrated the structural and optoelectronic merits of PEA incorporation in mixed-halide perovskites to solve the inherent material-level and device-level issues in 1.8 eV E_g PVKSCs. Material insights obtained from detailed investigation regarding the influence of PEA on crystallite size, orientation, optoelectronic quality, and carrier recombination dynamics are valuable beyond the scope of this work. Incorporation of PEA considerably improved the QFLS and slowed down the rate of phase segregation in 1.8 eV E_g perovskites. With judiciously chosen PEA fractions and interfaces, the improved material characteristics were effectively translated to devices. In perspective to literature, V_{oc} values of 1.30-1.35 V achieved in this work overcome the photovoltage plateau in 1.80-1.85 eV E_g range and represent the highest V_{oc} achieved thus far for mixed-halide hybrid PVKSCs (**Figure 6.1a**). The corresponding $V_{oc}/V_{oc,SQ}$ values of 0.85-0.87 are comparable to the best value of 0.86 realized in the more pervasively explored 1.65-1.75 eV E_g range (**Figure 6.1b**). This minimizes the disparity in $V_{oc}/V_{oc,SQ}$ values when compared to the lower E_g variants and is a significant step forward for 1.80-1.85 E_g PVKSCs. Results in this work clearly establish that synergetic development of perovskite absorber with improved optoelectronic quality and coupled interfaces are pivotal for mitigating $V_{oc,loss}$ in large E_g PVKSCs. Future research efforts to explore defect passivation approaches and alternate device architectures will further unleash the potential of large E_g PVKSC platform developed here for next generation perovskite tandems.

Chapter 7. IMPACT OF COMPOSITIONAL MODIFICATION ON BANDGAP BOWING AND OPTOELECTRONIC QUALITY IN SMALL BANDGAP PEROVSKITE ALLOYS

7.1 Introduction

Organic-inorganic hybrid perovskite (OIHP) semiconductors are making an unprecedented mark in the photovoltaic industry because of their exceptional structure-property-processing-performance attributes.[6,32,57,453–455] Efficiency limits for single- and multi-junction perovskite solar cells (PVKSCs) are predominantly dependent on the bandgap (E_g) and optoelectronic quality of OIHP absorber(s).[354,456] Bandgap of a typical OIHP with 3-dimensional (AMX_3) perovskite crystal structure can be tuned extensively by engineering the chemical composition.[457] Atomic orbitals of divalent metal cations (*M*-s and *M*-*p*) and halide anions (*X*-*p*) dominate electronic character of band edges and primarily determine the bandgap. *A*-site monovalent cations (organic or inorganic) influence tilting of $[MX_6]^{4-}$ octahedra and strength of hydrogen bonding in the 3-dimensional framework and indirectly affect the bandgap. Choices of *A*, *M* and *X* sites also alter structural aspects such as lattice size, octahedral distortion, tilting or rotation, and *M*-cation displacement, all of which have profound impact on the bandgap.[56,57,457] Composition also influences the nature of defect energy levels, phase stability, and homogeneity at nanoscale, all of which have profound impact on the optoelectronic quality.[355,458,459] Researching perovskite compositional space thus has immense potential for modulating the bandgap as well as improving the optoelectronic quality of OIHPs.

Methylammonium lead iodide ($MAPbI_3$), a representative OIHP composition has a bandgap ~1.6 eV. Through alloying at one or more sites without breaking the AMX_3 structure, E_g

of OIHPs have been tuned from 1.2 to 3.2 eV.[457] Common choices for alloying include formamidinium (FA), guanidinium (GA), cesium (Cs) at *A*-site, tin (Sn) at *M*-site, and bromine (Br) and chlorine (Cl) at *X*-site. Bandgaps for three widely employed binary OIHP alloys [(MA,FA)PbI_3, MA(Pb,Sn)I_3 and MAPb(I,Br)$_3$] over the entire composition range are shown in **Figure 7.1a**. It is evident that bandgaps for alloys deviate from simple linear interpolation between end members and show parabolic dependence on the composition. Alloy ($I_{1-x}II_x$) bandgaps can be well defined with a quadratic fit: $E_g(I_{1-x}II_x) = (1-x).E_g(I) + (x).E_g(II) - b.(x).(1-x)$, where b is a parameter that incorporates the non-linearity component and represents the extent of bandgap bowing. Deviation of E_g values from the linear behavior (bandgap bowing) is substantial for MA(Pb,Sn)I_3 alloys, much reduced for MAPb(I,Br)$_3$ alloys, and almost negligible for (MA,FA)PbI_3 alloys (**Figure 7.1b**). In MA(Pb,Sn)I_3 alloys, strong bandgap bowing is coupled with observance of lower bandgaps at intermediate alloy compositions relative to end members and is uncharacteristic when compared with other OIHP alloys. Lower bandgap Pb-Sn OIHP alloys are of great interest for application in single-junction (ideal E_g ~1.3 – 1.5 eV) and multi-junction (~1.0 – 1.2 eV for small-E_g subcell) PVKSCs.

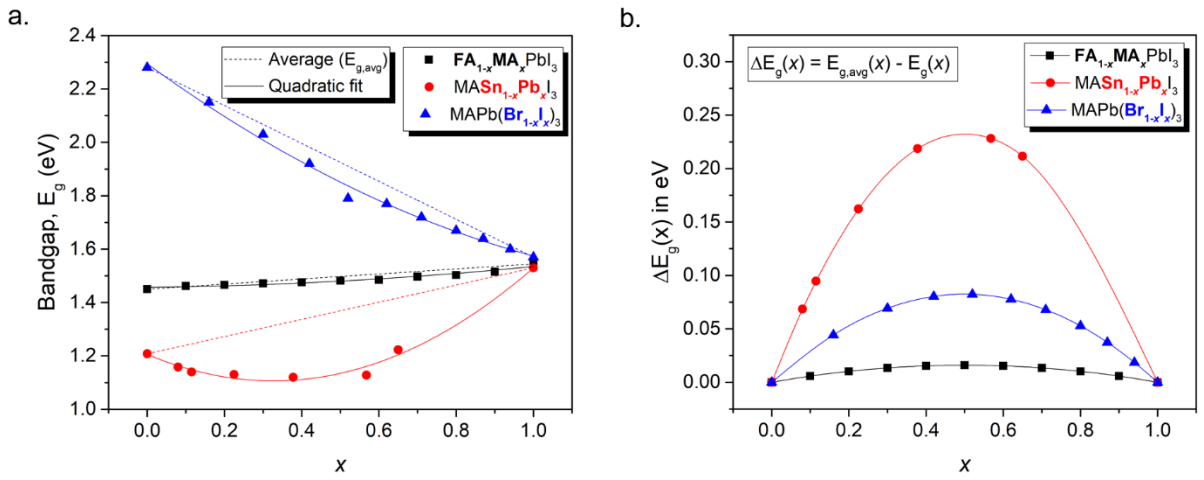

Figure 7.1. Bandgap variation in widely employed binary organic-inorganic hybrid perovskite (OIHP) alloys. (a) Bandgap (E_g) values for (MA,FA)PbI_3, MA(Pb,Sn)I_3 and MAPb(I,Br)$_3$ obtained from literature.[362,399,460] (b) Calculated differences in bandgap values (ΔE_g) between simple linear interpolation of end members ($E_{g,avg}$) and quadratic fit of the experimental data (E_g) shown in (a).

First-principles electronic structure calculations thus far provide conflicting explanations for pronounced bandgap bowing behavior in Pb-Sn OIHP alloys. Im et al.[399] relate the bandgap lowering to composition induced changes in spin-orbit coupling and structural distortion, whereas Eperon et al.[387] relate it to the short-range ordering of Pb and Sn atoms in mixed compositions. In contrary, a recent theoretical study by Goyal et al.[461] show that the composition induced changes in spin-orbit coupling, structural distortion, and short-range ordering all have negligible impact on the bandgap non-linearity and identify chemical effects (mismatch in energy for atomic orbitals of Pb and Sn atoms that constitute band edges in alloys) as the major contributor for bandgap bowing in OIHP alloys. Experimental results from the study by Parrott et al.[458] using temperature-dependent optical absorption and photoluminescence measurements illustrate that bandgap bowing in mixed Pb-Sn OIHP alloys strongly depends on the structural phase, and the characteristic parabolic-nature of bowing can be explained by composition dependent local changes in bond-angle for mixed alloys. Further experimental investigations on systematic compositional modification in Pb-Sn OIHP alloys are valuable to shed more light on the mechanistic origin and modulation of bandgap bowing in the relevant alloys.

Compositional modifications also influence the material quality of Pb-Sn OIHP alloys. In our earlier studies in 2016, we have demonstrated that binary *A*-site compositions such as (MA,FA)[1] and (FA,Cs) or (MA,Cs)[2] are beneficial to improve the performance of $A(Pb,Sn)I_3$ PVKSCs. Later in 2017, we also demonstrated that *X*-site modification *via* Br-incorporation [$MA(Pb,Sn)(I,Br)_3$] significantly improved the absorber optoelectronic quality and yielded PVKSCs with improved photovoltage (V_{oc} = 0.89 V) and efficiency (η = 17.6%).[5] Over the years, other groups also have found improvement of Pb-Sn PVKSCs using a diverse range of *A*-site and *X*-site modifications, often ascribed to improved morphology and processability,[387] alteration of

defect chemistry,[458] defect passivation,[462] larger grain size,[463] and higher stability (phase, air, thermal)[387,464]. Optoelectronic properties also change as function of Pb-Sn content, where ~50-75% Sn containing compositions possess the best properties among mixed compositions for a given APb$_{1-x}$Sn$_x$$X_3$ alloy series.[5,458] The current best performing small-E_g PVKSC (E_g = 1.27 eV, V_{oc} = 0.89 V, η = 19%) employs an optimized composition of (FA$_{0.60}$MA$_{0.40}$)(Pb$_{0.40}$Sn$_{0.60}$)(I$_{0.94}$Br$_{0.06}$)$_3$.[462] Expanding the *A*-site composition to ternary formulations [(FA,MA,Cs), (FA,Cs,Rb)] have been effective to improve the performance and reproducibility of 1.5-1.6 eV E_g Pb-based PVKSCs;[32,465] ternary *A*-site combinations [(FA,MA,Cs), (FA,GA,Cs)] have also been pivotal to alleviate the halide phase segregation and improve the optoelectronic quality in 1.7-1.9 eV E_g mixed-halide PVKSCs[8,466]. Utilization of ternary *A*-site composition is relatively unexplored in small-E_g PVKSCs and has potential to improve the intrinsic quality of Pb-Sn OIHP alloys.

In this work, we experimentally investigate how *A*-site composition modification influences the bandgap bowing and optoelectronic quality in Pb-Sn OIHP alloys. In the first part, we fabricate several series of APb$_{1-x}$Sn$_x$I$_3$ alloys using different single and binary *A*-site formulations and determine the associated bandgap bowing using optical absorption measurements. With additional structural measurements, we find that *A*-site modification affects the lattice strain (chemical pressure on the octahedral frameworks), and the bandgap bowing in APb$_{1-x}$Sn$_x$$X_3$ alloys increase proportionally with the microstrain in Pb-end members. Integrating our experimental results with insights from literature, we comprehensively rationalize the origin and modulation of bandgap bowing in OIHP alloys. In the second part, we utilize high-throughput compositional exploration *via* spray coating and quantitative steady-state photoluminescence analysis to study the impact of ternary *A*-site formulations on the optoelectronic quality (χ =

$\Delta E_F/V_{OC,SQ}$, where ΔE_F is the quasi-fermi level splitting and $V_{OC,SQ}$ is the theoretical limit for photovoltage) of APb$_{1-x}$Sn$_x$I$_3$ alloys. We find that within the (MA,FA,Cs)Pb$_{1-x}$Sn$_x$I$_3$ compositional space, certain ternary *A*-site combinations improve χ up to 86% and are better than single and binary *A*-site combinations. Based on these investigations, we identify (MA$_{0.24}$FA$_{0.61}$Cs$_{0.15}$)(Pb$_{0.35}$Sn$_{0.65}$)I$_3$ as the optimal composition with low-E_g and high optoelectronic quality, and has remarkable potential to improve the performance of perovskite multi-junction solar cells.

7.2 Experimental Methods

Materials: Soda lime glass substrate was purchased from Colorado Concept Coatings LLC. CsI, PbI_2, $PbBr_2$, SnI_2 (99.999% trace metal basis), SnF_2 (99%) and all anhydrous solvents (DMF, DMSO, Toluene) used in this work were purchased from Sigma-Aldrich. $SnBr_2$ (Alfa Aesar, 99.4%) was purchased from Fisher Scientific. Organic salts (MAI, MABr, FAI, GAI) were purchased from Greatcell Solar.

Perovskite solution preparation: AMX_3 perovskite precursor solutions were prepared by adding 1 M 1:1 AX:MX_2 salts in 0.5 ml of 7:3 DMF:DMSO co-solvent system; additionally 10 mol% SnF_2 was included in ASnX_3 solutions (**Table 7.1a**). Precursors were dissolved by stirring the solutions at 70 °C for 2 h. All solutions were stored at room temperature overnight before use. Solutions for perovskite compositions with multiple *A*-site and *B-site* cations were obtained by mixing the end member AMX_3 solutions (maintained at room temperature) in appropriate ratios according to the stoichiometry (**Tables 7.1b-c**). All solutions were mixed well, left at room temperature and used without further filtering before spin coating.

Table 7.1a. Quantity of precursors for making solutions of end member (AMX_3) compositions.

***AMX*$_3$ Composition**	***AX* salt**	***MX*$_2$ salt**	**Additive**	**Solvent**	
$MAPbI_3$	MAI (mg)	PbI_2 (mg)		DMF (µl)	DMSO (µl)
	79.5	230.5		350	150
$MASnI_3$	MAI (mg)	SnI_2 (mg)	SnF_2 (mg)	DMF (µl)	DMSO (µl)
	79.5	186.3	7.8	350	150
$FAPbI_3$	FAI (mg)	PbI_2 (mg)		DMF (µl)	DMSO (µl)
	86.0	230.5		350	150
$FASnI_3$	FAI (mg)	SnI_2 (mg)	SnF_2 (mg)	DMF (µl)	DMSO (µl)
	86.0	186.3	7.8	350	150
$CsPbI_3$	CsI (mg)	PbI_2 (mg)		DMF (µl)	DMSO (µl)
	129.9	230.5		350	150
$CsSnI_3$	CsI (mg)	SnI_2 (mg)	SnF_2 (mg)	DMF (µl)	DMSO (µl)
	129.9	186.3	7.8	350	150
$GAPbI_3$	GAI (mg)	PbI_2 (mg)		DMF (µl)	DMSO (µl)
	93.5	230.5		350	150
$GASnI_3$	GAI (mg)	SnI_2 (mg)	SnF_2 (mg)	DMF (µl)	DMSO (µl)
	93.5	186.3	7.8	350	150
$MAPbBr_3$	MABr (mg)	$PbBr_2$ (mg)		DMF (µl)	DMSO (µl)
	56.0	183.5		350	150
$MASnBr_3$	MABr (mg)	$SnBr_2$ (mg)	SnF_2 (mg)	DMF (µl)	DMSO (µl)
	56.0	139.3	7.8	350	150

Table 7.1b. Quantity of end member solutions mixed to get precursor solutions for compositions with mixed *A*-site.

***AM*I$_3$ solutions, *M* = Pb or Sn (for 100 µl)**					
Notation	***A*-site**	MA***M*I$_3$ (µl)	FA***M*I$_3$ (µl)	Cs***M*I$_3$ (µl)	GA***M*I$_3$ (µl)
MACs	$MA_{0.8}Cs_{0.2}$	80	-	20	-
MAGA	$MA_{0.8}GA_{0.2}$	80	-	-	20
FACs	$FA_{0.8}Cs_{0.2}$	-	80	20	-
MAFA	$MA_{0.5}FA_{0.5}$	50	50	-	-
MAFACs	$MA_{0.24}FA_{0.61}Cs_{0.15}$	24	61	15	-
FAGACs	$FA_{0.42}GA_{0.12}Cs_{0.46}$	-	42	46	12

Table 7.1c. Quantity of end member solutions mixed to get $APb_{1-x}Sn_xX_3$ precursor solutions.

$\boldsymbol{APb_{1-x}Sn_xX_3}$ **solutions (for 100 µl)**			
Notation	x	$\boldsymbol{APbX_3}$ (µl)	$\boldsymbol{ASnX_3}$ (µl)
Pb	0.00	100	0
25Sn	0.25	75	25
50Sn	0.50	50	50
75Sn	0.75	25	75
Sn	1.00	0	100

Perovskite film fabrication: Glass substrates were cleaned using sequential steps of ultrasonication for 10 min in detergent, deionized water, acetone, and isopropanol alcohol. Cleaned glass substrates were subjected to UV ozone treatment (10 min) before film fabrication. Perovskite precursor solution was spin coated onto the substrate using 2-step spin program (1000 rpm for 5 s , 5000 rpm for 30 s); during the last 20-15 s of the second spin-coating step, toluene (0.7 ml) was dropped onto the spinning substrate. Substrates were then annealed for 15 min at 100 ^oC (for films with MA, MACs and MAGA as *A*-site), 160 ^oC (for films with FA, FACs and MAFA as *A*-site) and 350 ^oC (for films with pure Cs as *A*-site) using a hot plate. Solution handing and film fabrication were carried out inside a glovebox (H_2O and O_2 levels ~ 0.1 – 10 ppm).

Bandgap measurement and analysis: Thin film absorption measurements were carried out using Varian Cary 5000 UV-Vis-NIR spectrometer. Bandgap values were estimated from the absorption spectrum onset extracted using the 'steepest gradient' method, in accordance to the recommendation by Parrott et al.[458] In their work, they find that 'Steepest gradient' method is more reliable than 'Tauc Plot method' for comparison of absorption onsets in Pb-Sn perovskite alloys. 'Steepest Gradient' method cannot be used to accurately determine the true band-gap, but rather provides more meaningful results for quantitatively comparing the absorption onsets because of its less sensitivity to problems commonly encountered with 'Tauc Plot' method. It is

important to note that bandgap values obtained using 'Steepest Gradient' method is slightly larger than values from 'Tauc Plot' method. We use this internally consistent method to compare bandgap values for different compositions and use them in the bandgap bowing analysis (**Figures 7.3**, **7.7**, **7.9**, and **7.11**). We use 'Tauc Plot' method when we need an accurate estimation of the bandgap value and to compare them in perspective with values reported in literature.

Bandgap bowing parameter (*b*) is obtained using quadratic fit of the bandgap data as a function of composition for a given series of Pb-Sn or I-Br alloy:

$$y(x) = E_g(I_{1-x}II_x) = (1-x).E_g(I) + (x).E_g(II) - b.(x).(1-x) \quad \text{or} \quad y(x) = E_g(I_{1-x}II_x) = ax + bx^2 + c$$

where, $a = [(E_g(II) - E_g(I) - b]$ and $c = E_g(I)$.

Adjusted R^2 values estimate the goodness of the fits (**Tables S3**, **S8** and **S9**). Bowing analysis is sensitive to the bandgap values and hence the choice of method used for bandgap determination must be taken into consideration for comparison with values in literature. With same analysis method, bandgap values and bowing parameter for $FAPb_{1-x}Sn_xI_3$ in our work match well with that reported by Parrott et al.[458]

X-ray diffraction and strain analysis: A Bruker D8 Discover Microfocus XRD with a Cu Kα source and 1D detector was used for XRD measurements to achieve a higher resolution and accurately determine broadening parameters. Similar to our previous works,[7,8] we use powder samples (scrapped from thin film samples) for attaining better sampling distribution and get diffraction signal from additional planes compared to thin films which often show signal from limited set of planes because of preferential orientation; peak positions were unchanged in powder and thin film samples. All XRD peaks were indexed manually and used for determining the lattice parameters. The evolutionary algorithm in the Solver package of Excel was used to minimize the

sum of residuals squared produced between measured and calculated plane spacings to arrive at lattice parameters providing the best fit for the data assuming either tetragonal or cubic Bravais lattice.[19] Tetragonal system lattice parameters (a and c) were converted to pseudo-cubic lattice parameters based on the geometric relationship between them: $a^* = \frac{\sqrt{2a^2}}{2}$; $c^* = \frac{c}{2}$ and the average of a^* and c^* was used to determine a single pseudo-cubic lattice parameter.[363]

Broadening values for XRD peaks (Δd_{hkl}) and instrumental broadening (Δd_{ins}) were determined using MDI JADE (an XRD pattern processing software); Pearson-VII peak shape function provided the best fit for all samples in this work. Microstrain (ε) values were obtained using a modified Williamson-Hall (W-H) analysis method:[467] $\Delta d_{hkl}^2 - \Delta d_{ins}^2 = \Delta d_{size}^2 + \varepsilon^2 d^2$. Accordingly, $(\Delta d_{hkl}^2 - \Delta d_{ins}^2)^{0.5}$ was plotted versus d and the slope of the linear fit gives ε (**Figures 7.6** and **7.10**). We found this method of analysis is more suited for samples with anisotropic strain and has also been applied in previous perovskite works.[368,468] We used only {hk0} peaks for linear fits in samples with tetragonal crystal structure,[469] whereas all {hkl} peaks were used for linear fits in samples with cubic crystal structure. Adjusted R^2 values in **Figures 7.6b** and **7.10b** estimate the goodness of the fits.

Composition exploration via spray coating: Spray coated experiments were conducted with a similar methodology as described previously.[8] In this study, we employed an anti-solvent bath approach to control perovskite crystallization in order to attain the most relevant comparison with spin coated films. Stoichiometric perovskite inks were prepared at 0.25 M concentration in 80/20 vol/vol DMF/DMSO and stirred. 10 mol% SnF_2 relative to Sn content was also included in each ink. Perovskite ink was deposited in a N_2-filled glovebox via an ultrasonic spray nozzle, which translated above the substrate, delivering ink at a constant rate of 100 µL/min while

translating along the 75mm x 25mm glass substrate at a rate of 1 mm/s. A composition gradient was achieved by mixing streams delivered by two pumps with linearly changing flow rates, one ramping up and one ramping down such that 100 µL/min total flow rate was maintained. After ink deposition, the substrate was left to dry for 1 minute (at room temperature), then submerged in a diethyl ether bath for 1 minute or until the color stopped changing. Then the substrate was annealed at 160 ˚C for 10 minutes.

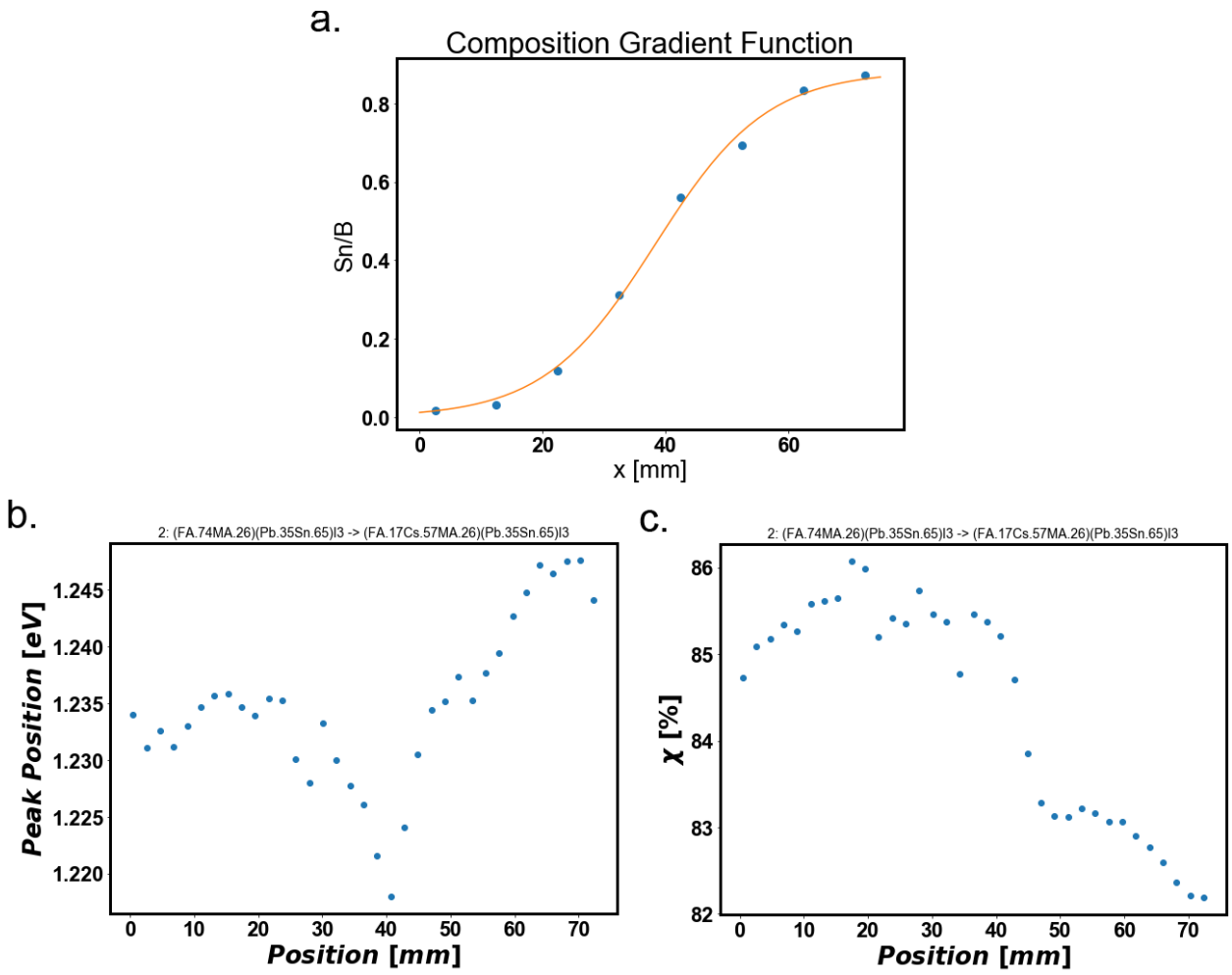

Figure 7.2. (a) EDS data demonstrating the changing composition as a function of distance along the 75 mm substrate. For this validation gradient, we used a pure Pb to a pure Sn composition, $(FA_{0.75}Cs_{0.25})PbI_3$ to $(FA_{0.75}Cs_{0.25})SnI_3$, since Pb and Sn are easy to differentiate with EDS. (b) example PL peak position and (c) example optoelectronic quality χ ($\chi \equiv \Delta E_F/V_{OC,SQ}$) for a single composition gradient, where the composition changes from $(FA_{0.74}MA_{0.26})(Pb_{0.35}Sn_{0.65})I_3$ at 0 mm to $(FA_{0.17}Cs_{.57}MA_{0.26})(Pb_{0.35}Sn_{0.65})I_3$ at 75mm according to the gradient function shown in (a).

Although the syringe pumps are ramped in a linearly from the two end member solutions, the gradient on the substrate will not be precisely linear due to mixing effects. Since it is difficult to measure changes in organic cation ratios, we fabricated a pure Pb to pure Sn gradient to validate our process, and quantified the Pb-Sn ratio with Energy Dispersive Spectroscopy (EDS), as shown in **Figure 7.2a**. This "Composition Gradient Function" was used to infer composition for other gradients.

Photoluminescence (PL) measurements: Confocal absolute intensity PL was performed as reported previously.[369] Samples were excited with a 532nm laser and calibrated to above bandgap photon flux (1 Sun, 10 Suns, or 100 Suns) (for a 1.2eV bandgap material based on AM1.5GT spectrum) using an Oriel optical power meter and beam profiler. Photoluminescence spectra were collected with a Horiba LabRAM HR-800 with 10x objective using a monochromator blazed at 1200mm with 150 gr/mm with confocal hole set to 800 µm. Calibration of the photon detection rate was performed with a blackbody source (IR-301, Infrared Systems Development) at 1050 ˚C with a pinhole size of 10 µm to determine a calibration factor for photons per count for this system.

For spin coated films, PL measurements were collected at 1 Sun, 10 Suns, and 100 Suns with both a Si and InGaAs detector (as emission of ~1.2 eV lies in a non-ideal range for either detector). We found minimal dependence of PLQY on illumination intensity, and the 100 Suns measurements gave best signal-to-noise for all samples. PL Peak position was determined by taking the PL peak maximum after conversion to absolute intensity units. Quasi-Fermi Level splitting was determined using the PLQY method, first proposed by Ross:[448]

$$\Delta E_F = \Delta E_{F,max} + kT \ln PLQY_{Ext}$$

In this work, we used the 1 Sun Shockley-Queisser limit (assuming the bandgap equals the PL peak position) for $\Delta E_{F,max}$, we assumed T = 300K, and we used PLQY determined from 100 Sun measurement (see **Figure 7.3** for 1 Sun and 100 Sun comparison).

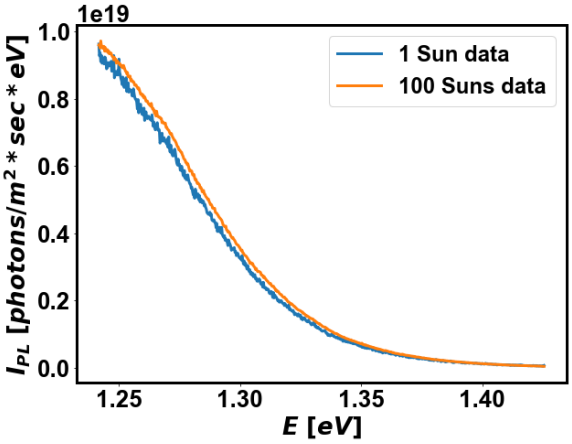

Figure 7.3. Comparison of PL emission of a typical MAFACs spin coated film measured at 1 Suns and measured at 100 Suns with 1 Sun correction. The 100 Suns data was corrected to 1 Sun by multiplying by dividing the spectrum by N-Suns, where N-Suns is the precise ratio of incident laser photon flux divided by 1 Sun above bandgap photon flux at AM 1.5. Since 1 Sun data and 100 Sun corrected data give the same emission flux, we conclude that PLQY is similar at 1 Sun and 100 Suns and can appropriately use 100 Sun data in our 1 Sun quasi-Fermi Level splitting corrections. The data above was collected with Si detector, which has low responsivity below 1.25eV, while the InGaAs detector has high background. Thus using 100 Sun data collected with InGaAs detector is the most appropriate method to quality AIPL data in this study.

Statistics for spin coated films were collected by taking 25 measurements spatially distributed across the substrate with illumination times of 1-5 s each. Statistics for spray coated films were collected in a grid of 10 measurements along the width and 36 measurements along the length of the gradient. The statistics of each set of 10 lateral measurements were averaged to create a series of 36 data points describing the characteristics along the length of the gradient (**Figures 7.2b-c** show one example gradient). The response surfaces shown in ternary plots were created by fitting a polynomial model to interpolate within all the spray coating data.

The above "PLQY method" for quasi-Fermi level splitting determination does not account for deviations in the peak position from true bandgap nor does it consider losses due to sub-bandgap

absorptivity. We employed the "full peak fit" method first derived by Katahara and Hillhouse,[470] where the photoluminescence is fit to a modified Lasher-Stern-Wuerfel equation given by:

$$I_{PL}(E) = \frac{2\pi E^2}{h^3 c^2} \cdot \frac{a(E, \Delta E_F, T)}{\exp\left(\frac{E - \Delta E_F}{kT}\right) - 1}$$

Details about the absorption model used can be found in the publication by Katahara and Hillhouse.[470] The data in **Figure 7.15f** was measured at ~100 Suns then corrected to 1 Suns using an Oriel optical power to quantify excitation intensity. **Figure 7.3** demonstrates the validity of this approach.

7.3 Results and Discussion

7.3.1 Optical and Structural Characteristics of MA(Pb,Sn)I_3 alloys

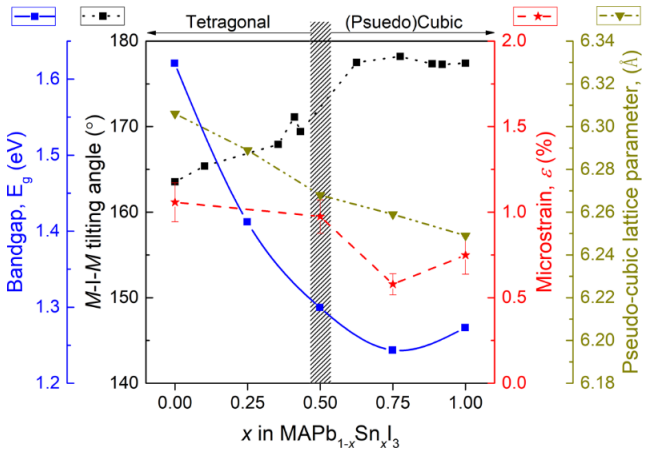

Figure 7.4. Structural and optical characteristics of $MAPb_{1-x}Sn_xI_3$ alloys. Bandgaps were determined from the onset of absorption spectra using the 'steepest gradient' method and solid line represents the quadratic fit of the data (details in **Section 7.2**). *M*-I-*M* tilting angles were taken from literature.[399] Microstrain and pseudo-cubic lattice parameters were obtained from XRD measurements of powder samples using 1D detector.

Pb and Sn have similar outer-shell electronic configuration (ns^2 np^2), octahedral coordination geometry, ionic radius (Sn^{2+} smaller than Pb^{2+} by <10%) and facilitate formation of binary metal substitutional alloys ($APb_{1-x}Sn_xX_3$) with complete solid solubility and small lattice distortions. To contextualize the evolution of bandgap in Pb-Sn OIHP alloys, we start with the investigation of $MAPb_{1-x}Sn_xI_3$ ($0 \leq x \leq 1$). $MAPb_{1-x}Sn_xI_3$ alloys have a bandgap bowing (*b*) of 0.61

± 0.03 eV with the E_g minimum located ~ x = 0.75 (**Figure 7.4**). Lower E_g at intermediate compositions can be explained by the staggered (Type II) nature of band offsets between end members ($MAPbI_3$ and $MASnI_3$), which cause Sn-*s* / I-*p* and Pb-*p* / I-*p* orbitals to dominate characteristics of valence band maximum (VBM) and conduction band minimum (CBM) respectively, and result in the observed behavior for Pb-Sn OIHP alloys (**Figure 7.5**).[461] In contrast, the straddled (Type I) nature of band offsets between end members in MA-FA and I-Br OIHP alloys constrain E_g values in alloy compositions to be in between that of the end member bandgaps (**Figures 7.1** and **7.5**).[362,471] Coupled with this chemical effect, effects due to volume deformation potential and local structural relaxations / distortions are additional contributors to bandgap bowing in OIHP and inorganic compound alloys.[461,472,473]

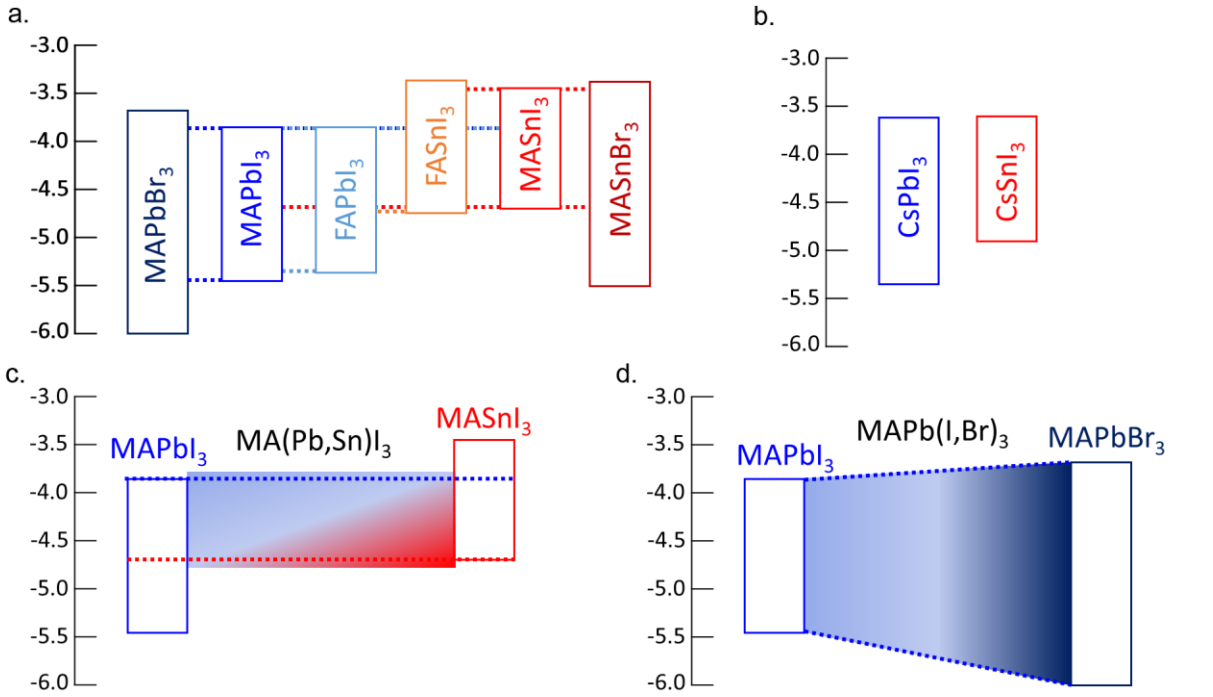

Figure 7.5. Frontier energy level variation as a function of composition in OIHPs. (a, b) Positions of valence band maximum (VBM) and conduction band minimum (CBM) for different Pb- and Sn-based OIHP compositions. VBM data for $MAPbI_3$,[1] $MASnI_3$,[1] $FAPbI_3$,[474] $FASnI_3$,[475] $MAPbBr_3$,[476] $MASnBr_3$,[477] $CsPbI_3$,[478] and $CsSnI_3$[479] were obtained from the associated references in literature; corresponding positions of CBM were calculated using the bandgap. (c, d) Schematic illustration for dependence of VBM and CBM characteristics on the nature of band offsets between end members in OIHP alloys; staggered (Type II) nature of band offset between $MAPbI_3$ and $MASnI_3$ results in the lowest bandgap at an intermediate alloy composition (c), whereas straddled (Type I) nature of band offset between $MAPbI_3$ and $MAPbBr_3$ results in the lowest bandgap at an end member composition (d).[461]

At room temperature, $MAPbI_3$ and $MASnI_3$ crystallize in the tetragonal *I*4*cm* (β-phase) and (pseudo)cubic *P*4*mm* (α-phase) space groups, respectively.[364] As x increases, the lattice size decreases and a tetragonal to (pseudo)cubic structural transition is observed ~ x = 0.50 (**Figures 7.4** and **7.6**, **Table 7.2**).

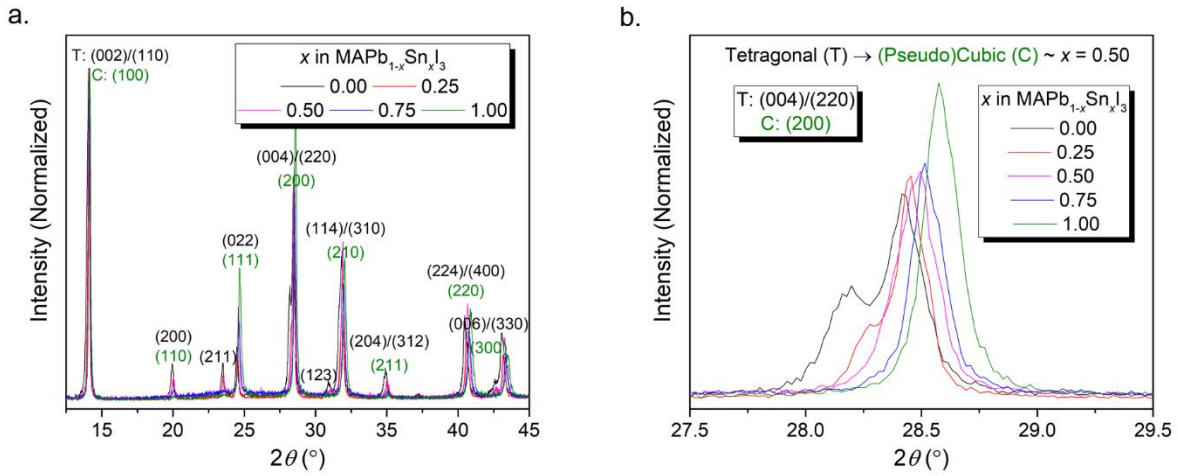

Figure 7.6. X-ray diffraction (XRD) measurements for powder samples of $MAPb_{1-x}Sn_xI_3$ alloys using a 1D detector. (a) XRD data with indexed peaks; indices in black color are for samples (x < 0.50) with tetragonal (T) structure and indices in green color are for samples ($x \geq 0.50$) with cubic (C) structure. (b) Zoomed-in T: (004)/(220) / C: (200) peak region from (a) to illustrate changes in peak position and transition from tetragonal to (pseudo)cubic structure ~ x = 0.50.

Table 7.2. Crystal structure and lattice parameters for $MAPb_{1-x}Sn_xI_3$ ($0 \leq x \leq 1$) alloys.

Composition	**Crystal Structure**	**Lattice Parameters**		
		Tetragonal		**Pseudo-cubic**
		a = b (Å)	c (Å)	(Å)
$MAPbI_3$	Tetragonal	8.88	12.67	6.306
$MAPb_{0.75}Sn_{0.25}I_3$	Tetragonal	8.87	12.61	6.289
$MAPb_{0.50}Sn_{0.50}I_3$	(Pseudo)Cubic	-	-	6.268
$MAPb_{0.25}Sn_{0.75}I_3$	(Pseudo)Cubic	-	-	6.259
$MASnI_3$	(Pseudo)Cubic	-	-	6.249

The phase transition is induced by reduction in out-of-phase tilting of $[MX_6]^{4-}$ octahedra as x increases and is corroborated by the increase in *M*-I-*M* tilting angle from ~163.55° (for $MAPbI_3$) to ~177.43° (for $MASnI_3$) (**Figure 7.4**); this demonstrates less deviation from linearity for *M*-I-*M*

bonds in Sn-rich alloys.[364,399] Additionally, as *x* increases, octahedral distortion because of the stereochemically active lone pair on Sn increases and become prominent in the Sn-end member.[399,480,481] Overall mircrostrain in the lattice decreases with increase in *x* and a minimum is observed ~ *x* = 0.75 (**Figures 7.4** and **7.7**). This can be rationalized by opposing trends of decrease in octahedral tilting and increase in octahedral distortion as *x* increases, which are expected to have a competing influence on the lattice strain of $MAPb_{1-x}Sn_xI_3$ alloys.[482] Correlation of bandgap and mircrostrain with minimum values attained similarly ~ x = 0.75 point out to the pivotal contributions of local structural relaxations / deformations on the bandgap for Pb-Sn OIHP alloys,[483–487] and corroborate with the postulation for bandgap bowing provided by Parrott et al.[458]

a.

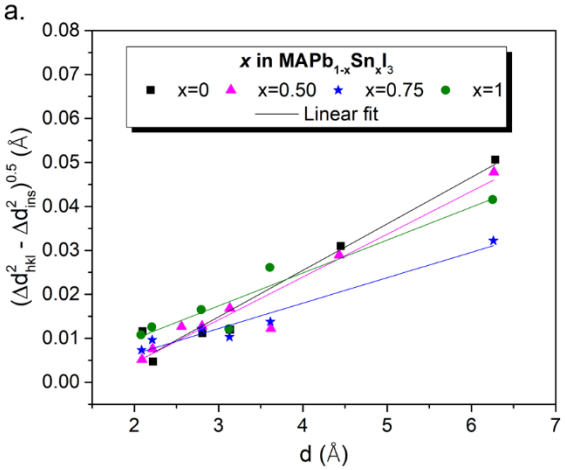

b.

x	Slope, ε	Standard Error	Adjusted R^2
0.00	0.0106	0.0011	0.945
0.50	0.0098	0.0010	0.933
0.75	0.0058	0.0006	0.947
1.00	0.0075	0.0011	0.900

Figure 7.7. Modified Williamson-Hall (W-H) plots for $MAPb_{1-x}Sn_xI_3$ alloys. (a) Plots of $(\Delta d^2_{hkl} - \Delta d^2_{ins})^{0.5}$ versus d along with linear fits of the data. (b) Linear fit parameters for fits in (a); slope represents microstrain (ε). Analysis method is described in **Section 7.2**.

7.3.2 Modulation of Bandgap Bowing in *A*(Pb,Sn)I_3 Alloys via *A*-site Modification

Modification of *A*-site composition alters chemical pressure on the octahedral framework and affects lattice strain by influencing the octahedral tilt angle and distortion.[487–489] To assess its impact on bandgap bowing, we fabricated series of $APb_{1-x}Sn_xI_3$ films with various combinations of *A*-site cations and determined their bandgap from the onset of optical absorption (details in

Section 7.2). Bandgaps for different $APb_{1-x}Sn_xI_3$ alloys [A = Cs, MA, FA, $FA_{0.8}Cs_{0.2}$ (FACs), $MA_{0.8}Cs_{0.2}$ (MACs), $MA_{0.5}FA_{0.5}$ (MAFA), $MA_{0.8}GA_{0.2}$ (MAGA)] are shown in **Figure 7.8a**. It is evident that for every series of $APb_{1-x}Sn_xI_3$ alloys, variation in E_g as a function of composition (x) can be well-defined by a quadratic fit (**Figure 7.8a** and **Table 7.3**).

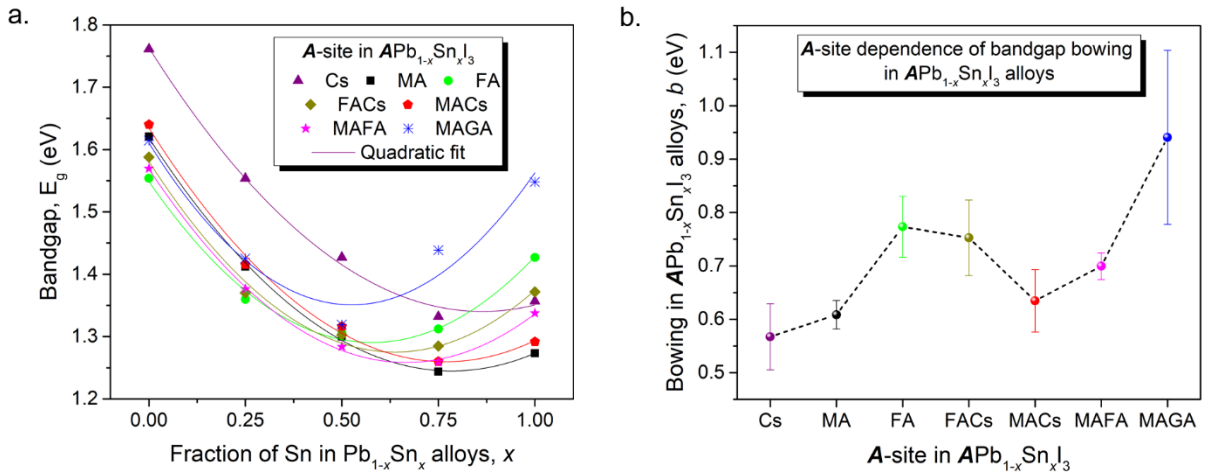

Figure 7.8. (a) Bandgap variation in $APb_{1-x}Sn_xI_3$ alloy compositions ($0 \leq x \leq 1$); bandgap values were determined from the onset of absorption spectra using the 'steepest gradient' method and solid lines represent the quadratic fit of the data (details in the **Section 7.2**). (b) *A*-site dependence of bandgap bowing (b) in $APb_{1-x}Sn_xI_3$ alloys; dashed lines are provided as a visual aid for observance of changes in b.

Table 7.3. Quadratic fit parameters for composition dependence of bandgap in $APb_{1-x}Sn_xX_3$ alloys.

Bowing (b) in $APb_{1-x}Sn_xX_3$ alloys obtained from quadratic fit of E_g data: $y = E_g(x) = ax + bx^2 + c$						
A-site	*X*-site	a ($E_{Sn} - E_{Pb} - b$)	**b, eV**	c (E_{pb})	Adjusted R^2	Location of $E_{g,\,min}$ (x_{min})
Cs	I	-0.98	**0.57 ± 0.06**	1.76	0.993	0.86
MA	I	-0.95	**0.61 ± 0.03**	1.62	0.998	0.78
FA	I	-0.89	**0.77 ± 0.06**	1.55	0.983	0.58
$FA_{0.8}Cs_{0.2}$	I	-0.96	**0.75 ± 0.07**	1.58	0.981	0.64
$MA_{0.8}Cs_{0.2}$	I	-0.98	**0.63 ± 0.06**	1.63	0.992	0.77
$MA_{0.8}FA_{0.2}$	I	-0.93	**0.70 ± 0.02**	1.57	0.998	0.66
$MA_{0.8}GA_{0.2}$	I	-0.99	**0.94 ± 0.16**	1.61	0.890	0.53
MA	Br	-0.68	**0.49 ± 0.13**	2.35	0.877	0.70

The bandgap bowing is dependent on the choice of *A*-site and varies considerably, ranging from 0.57 ± 0.06 eV (for $CsPb_{1-x}Sn_xI_3$) to 0.94 ± 0.16 eV (for $MA_{0.8}GA_{0.2}Pb_{1-x}Sn_xI_3$) as shown in **Figure 7.8b**. The location of minimum E_g (x_{min}) also changes and appears to vary inversely with bowing (**Figure 7.9**). Integrating this observation together with the earlier discussion on the influence of band offsets imply that by increasing the bandgap bowing and / or staggered nature of band offsets between end members, we can shift the x_{min} towards lower Sn fractions. These results offer essential guidelines for realization of lower bandgaps with smaller levels of Sn incorporation, which is desired from stability perspective.[490]

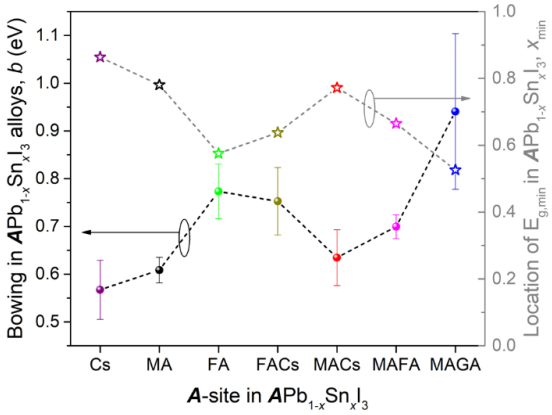

Figure 7.9. *A*-site dependence of bandgap bowing (*b*) and location of minimum bandgap (x_{min}) in $APb_{1-x}Sn_xI_3$ alloys.

A-site modification affects the bandgap of Sn-end members, $ASnI_3$ ($x = 1$) immensely compared to Pb-end members, $APbI_3$ ($x = 0$) (**Figure 7.8a**). This is due to structural dissimilarities between $[PbI_6]^{4-}$ and $[SnI_6]^{4-}$ octahedral framework arising from inherent differences in the chemical nature of Pb and Sn. In $APbX_3$, second order Jahn-Teller steric effect (tilts stabilize orbital hybridizations) along with hydrogen bonding between organic *A*-cation and halide framework facilitate octahedral tilting.[487,489] Whereas in $ASnX_3$, the weakened inert pair effect and increased stereochemically activity of lone pair on Sn[480,481,491] reduces the propensity for octahedral tilting and orbital hybridizations are stabilized by Jahn-Teller octahedral distortion.[489,492,493] These effects explain the above discussed structural deformation trends in $MAPb_{1-x}Sn_xI_3$, where

octahedral tilting and octahedral distortion is maximum for $MAPbI_3$ and $MASnI_3$ respectively (**Figure 7.4**).[364,399] Altogether, for changes in chemical pressure (*A*-site modification), the resultant bandgap is modulated by variations in octahedral tilting (changes in linearity of *M-X-M* bonds) for Pb-perovskites and volumetric effects (changes in lattice size and strain) for Sn-perovskites. Bandgaps of intermediate alloy compositions in $APb_{1-x}Sn_xI_3$ accordingly change based on how a given *A*-site impacts structural deformation of end members. The interplay between steric effects and strength of hydrogen bonding, which governs the resultant octahedral tilting in intermediate alloy compositions, changes significantly with *A*-site modification[487,489,494] and hence the strong dependence of bandgap bowing on *A*-site for Pb-Sn OIHP alloys.

For further understanding and obtaining a more comprehensive picture encompassing both *A*-site and *X*-site modifications influence on bandgap bowing, we additionally analyze the bandgaps of $MAPb_{1-x}Sn_xBr_3$ alloys. They have a relatively smaller bandgap bowing (*b*) of 0.49 ± 0.13 eV with the E_g minimum located ~ x = 0.70 (**Figure 7.10a** and **Table 7.3**). The significant increase in bandgaps for $MAPb_{1-x}Sn_xBr_3$ alloys compared to $MAPb_{1-x}SnI_3$ alloys can be attributed to the increase in electronegativity of the halide ligand; more strongly bound Br-*p* atomic orbitals lead to upshift of CBM and downshift of VBM in bromine containing compositions relative to their iodine counterparts and hence contain larger bandgaps (**Figure 7.5**).[471,495] We subsequently performed structural characterization of Pb-end members to get additional insight regarding the bandgap bowing trend in series of $APb_{1-x}Sn_xX_3$ alloys; $FAPbI_3$ and $CsPbI_3$ were omitted due to the difficulty in data acquisition because of the associated phase instabilities.[496] One-dimensional X-ray diffraction (XRD) measurements (standard $\theta/2\theta$ XRD scans with a 1D detector) of powder samples were performed to determine crystal structure, lattice parameters and mircrostrain of Pb-end members (details in **Section 7.2**).

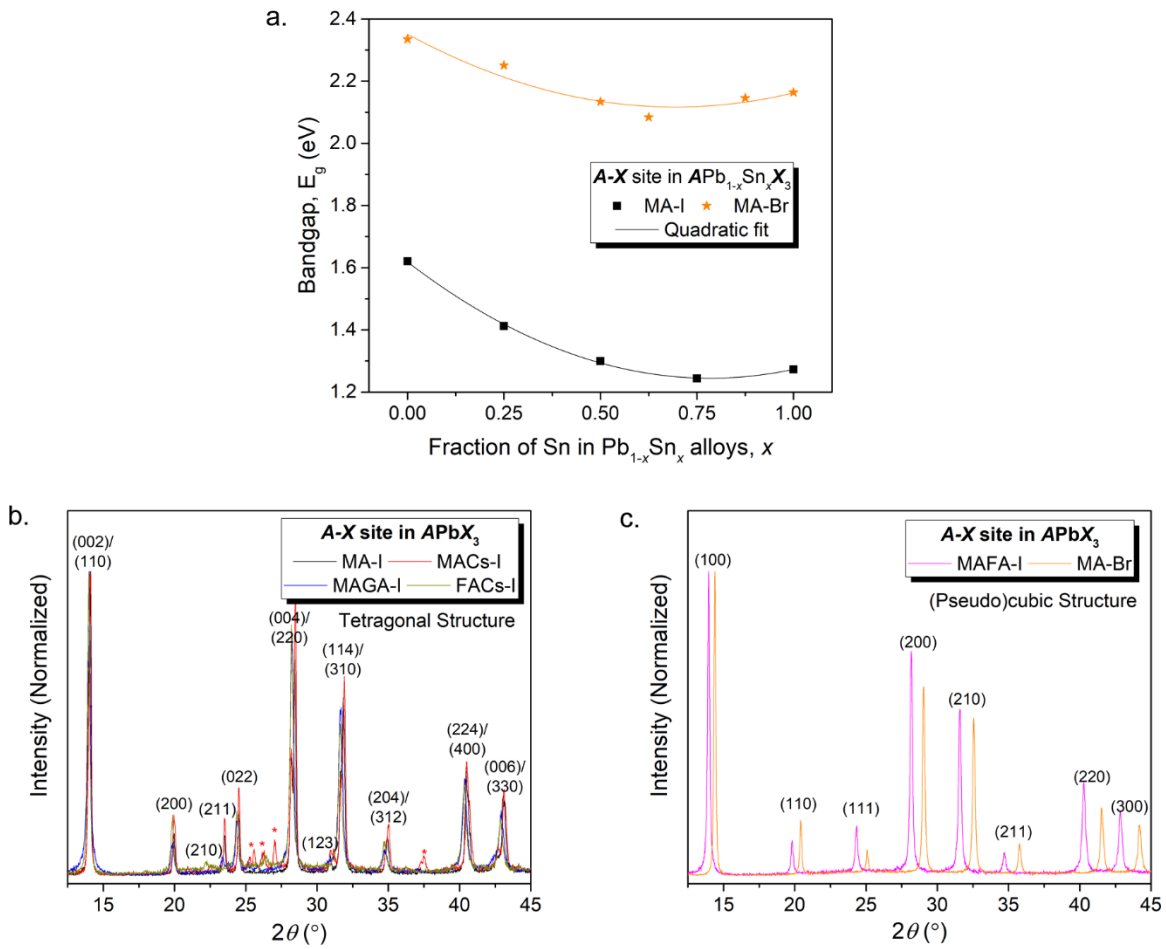

Figure 7.10. (a) Bandgap variation in $MAPb_{1-x}Sn_xBr_3$ alloys in comparison to $MAPb_{1-x}Sn_xI_3$ alloys. (b, c) XRD data (measurements for powder samples using a 1D detector) with indexed peaks for different $APbX_3$ end member compositions; secondary impurity phases were observed only in MACs-I and are indicated by red asterisks.

Table 7.4. Crystal structure and lattice parameters for different $APbX_3$ end members.

***AMX*$_3$ composition**	**Crystal Structure**	**Lattice Parameters**		
		Tetragonal		**Pseudo-cubic**
		a = b (Å)	c (Å)	(Å)
$MAPbI_3$	Tetragonal	8.88	12.67	6.306
$MA_{0.8}Cs_{0.2}PbI_3$	Tetragonal	8.86	12.65	6.296
$MA_{0.8}GA_{0.2}PbI_3$	Tetragonal	8.95	12.95	6.400
$MA_{0.5}FA_{0.5}PbI_3$	(Pseudo)Cubic	-	-	6.338
$FA_{0.8}Cs_{0.2}PbI_3$	Tetragonal	8.95	12.71	6.340
$MAPbBr_3$	(Pseudo)Cubic	-	-	5.933

Figures 7.10b-c show XRD scans for all samples and the associated crystal structure and lattice parameters are listed in **Table 7.4**. The higher symmetry ((pseudo)cubic crystal structure)

in $MAPbBr_3$ and $MA_{0.5}FA_{0.5}PbI_3$ can be rationalized by steric considerations (relative ionic sizes that decrease tilting of octahedra).[362,460] Lattice parameters obtained conform the trend in lattice size predicted from relative sizes of *A*- and *X*-site ions: $MAPbBr_3$ < $MA_{0.8}Cs_{0.2}PbI_3$ < $MAPbI_3$ < $MA_{0.5}FA_{0.5}PbI_3$ < $FA_{0.8}Cs_{0.2}PbI_3$ < $MA_{0.8}GA_{0.2}PbI_3$. Analysis of microstrain and corresponding values are summarized in **Figure 7.11**.

a.

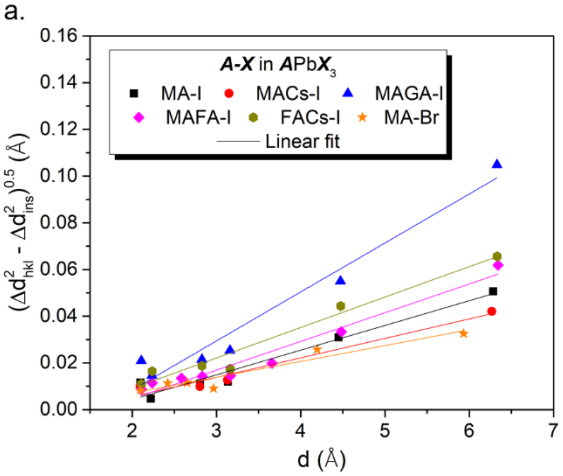

b.

A-X in $APbX_3$	Slope, ε	Standard Error	Adjusted R^2
MA-I	0.0106	0.0011	0.945
MACs-I	0.0083	0.0011	0.950
MAGA-I	0.0210	0.0021	0.950
MAFA-I	0.0123	0.0010	0.952
FACs-I	0.0130	0.0012	0.959
MA-Br	0.0068	0.0011	0.906

Figure 7.11. Modified Williamson-Hall (W-H) plots for $APbX_3$ end members. (a) Plots of $(\Delta d^2_{hkl} - \Delta d^2_{ins})^{0.5}$ versus d along with linear fits of the data. (b) Linear fit parameters for fits in (a); slope represents microstrain (ε). Analysis method is described in **Section 7.2**.

$MAPbBr_3$ has the lowest microstrain and the amount of microstrain increases with increase in effective size of the *A*-site for $APbI_3$. This trend clearly reflects the impact of increasing chemical pressure *via* compositional modification. The above results reveal that the bowing (*b*) in $APb_{1-x}Sn_xX_3$ alloys are directly correlated with the extent of microstrain (ε) in the $APbX_3$ end members. A plot of *b* versus ε shows linear correlation with Pearson's $r \sim 0.87$ (**Figure 7.12**). Mechanistically this implies that as the strain in Pb-end member increases, local lattice relaxations relieve structural deformations to a greater extent with increase in Sn fraction (*x*) and causes a larger deviation in alloy bandgaps from linear interpolation, which transpires as larger bandgap bowing (*b*) for the Pb-Sn alloy series under consideration.

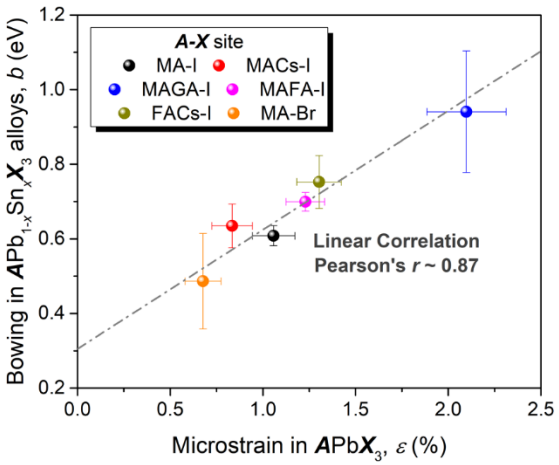

Figure 7.12. Plot of bandgap bowing (b) in APb$_{1-x}$Sn$_x$$X_3$ alloys versus microstrain in their respective APbX_3 end members; a linear correlation with Pearson's r ~ 0.87 is observed.

Figure 7.12 also shows that in the extreme case of zero microstrain, the bandgap bowing intercept in APb$_{1-x}$Sn$x$$X_3$ alloys is non-zero (~0.3 eV). This indicates the existence of a secondary factor which is independent of A-site composition but influences the bowing in APb$_{1-x}$Sn$x$$X_3$ alloys with a preset contribution. Combining this observation with results from literature,[461] it is evident that the mismatch in energy for atomic orbitals of Pb and Sn atoms that constitute band edges in alloys (chemical effect) is the secondary factor providing added contribution to bowing in in APb$_{1-x}$Sn$x$$X_3$ alloys. Thus, local structural relaxations and chemical effect collectively mediate the bandgap evolution and resultant bowing characteristics in APb$_{1-x}$Sn$x$$X_3$ alloys.

To evaluate the applicability of this concept for other binary OHIP alloys, we considered bandgap bowing in I-Br alloys. Bandgap values for series of MAM(I$_{1-y}$Br$_y$)$_3$ alloys (M = Pb, Pb$_{0.75}$Sn$_{0.25}$, Sn and $0 \leq y \leq 1$) were obtained from literature (**Figure 7.13a**).[13,362,497] Decrease in bandgap bowing from 0.26 ± 0.03 for MAPb(I$_{1-y}$Br$_y$)$_3$ to 0.11 ± 0.05 for MASn(I$_{1-y}$Br$_y$)$_3$ correlates well with the decrease in strain from MAPbI$_3$ to MASnI$_3$ end members; a plot of bowing in MAM(I$_{1-y}$Br$_y$)$_3$ alloys versus microstrain in MAMI$_3$ end members show linear correlation with Pearson's r ~ 0.99 (**Table 7.5** and **Figure 7.13b**). The reduced bandgap bowing intercept in **Figure**

7.13b indicates less profound contribution from chemical effect on bandgap bowing in MA*M*($I_{1-y}Br_y$)$_3$ alloys, as rationalized in the discussion above (**Figure 7.5**).

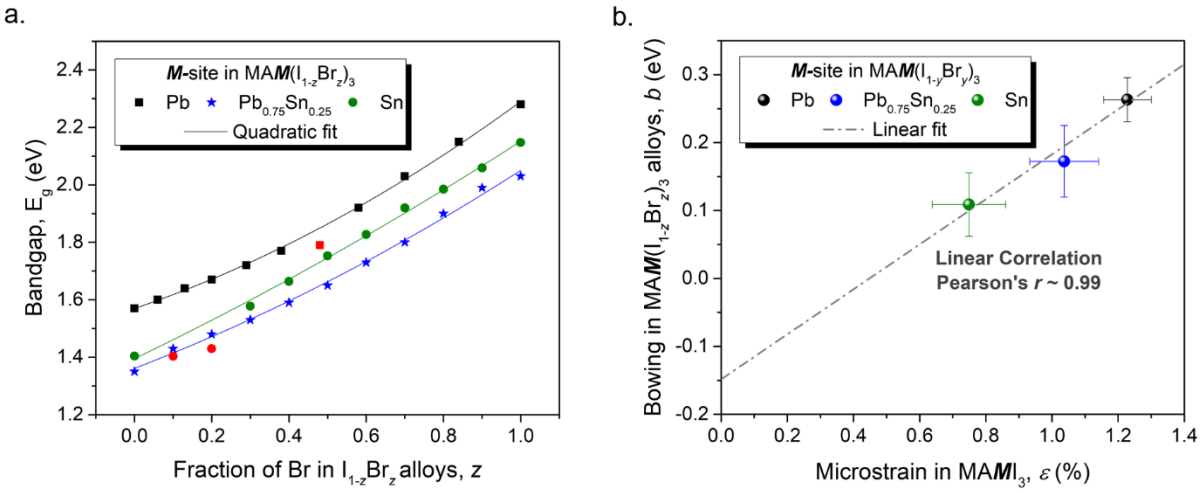

Figure 7.13. Bandgap variation in mixed halide (I-Br) OIHP alloys. (a) Bandgap data for different MA*M*($I_{1-z}Br_z$)$_3$ alloy compositions along with quadratic fits; absorption onset data for MAPb($I_{1-z}Br_z$)$_3$,[362] MAPb$_{0.75}$Sn$_{0.25}$($I_{1-z}Br_z$)$_3$,[13] and MASn($I_{1-z}Br_z$)$_3$[497] were taken from the associated references in literature. Data points indicated in red color were considered as outliers and excluded from fitting. (b) Plot of bandgap bowing (*b*) in MA*M*($I_{1-z}Br_z$)$_3$ alloys versus microstrain (ε) in their respective MA*M*I$_3$ end members; a linear correlation with Pearson's *r* ~ 0.99 is observed.

Table 7.5. Quadratic fit parameters for composition dependence of bandgap in MA*M*($I_{1-z}Br_z$)$_3$ alloys.

Bowing (*b*) in MA*M*($I_{1-z}Br_z$)$_3$ alloys obtained from quadratic fit of E_g data: $y = E_g(z) = az + bz^2 + c$					
A-site	*M*-site	a (E_{Br} - E_I - *b*)	***b*, eV**	c (E_I)	Adjusted R^2
MA	Pb	0.46	**0.26 ± 0.03**	1.57	0.999
MA	$Pb_{0.75}Sn_{0.25}$	0.52	**0.17 ± 0.05**	1.36	0.996
MA	Sn	0.65	**0.11 ± 0.05**	1.39	0.997

We also considered bandgap bowing in reduced-dimensionality (2D) Pb-Sn OIHP alloys. Bandgap values for three different 2D Pb-Sn alloy series and the associated structural characteristics of end members were obtained from literature (**Tables 7.6a-b** and **Figure 7.14a**).[498,499] Bandgap bowing increases with increase in octahedral tilting (deviation from linearity for Sn-I-Sn bonds) (**Table 7.6c** and **Figure 7.14b**).

Table 7.6a. Molecular structure of different organic cations employed for synthesis of 2-dimensional (2D) mixed Pb-Sn perovskite alloys in literature.[498,499]

Organic Cation	Notation	Structure	Ref.
Benzylammonium	$(BZA)^+$	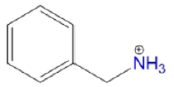	[498]
Benzimidazolium	$(Bn)^+$	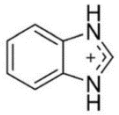	[499]
Histammonium	$(HA)^{2+}$	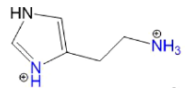	[498]

Table 7.6b. Structural and optical characteristics of 2D perovskite Sn-end members with organic cations employed for synthesis of mixed Pb-Sn perovskite alloys in literature.[498,499]

Composition	Sn-I-Sn tilting angle (°)	E_g (eV)	Ref.
$(BZA)_2SnI_4$	160.6	1.89	[498]
$(Bn)_2SnI_4$	173.9	1.81	[499]
$(HA)SnI_4$	160.0/178.5	1.67	[498]

Table 7.6c. Quadratic fit parameters for composition dependence of bandgap in 2D mixed Pb-Sn perovskite alloys.

Bowing (*b*) in $APb_{1-x}Sn_xI_4$ (2D) alloys obtained from quadratic fit of E_g data: $y = E_g(x) = ax + bx^2 + c$				
A-site	a (E_{Sn} - E_{Pb} - *b*)	***b*, eV**	c (E_{Pb})	Adjusted R^2
$(BZA)_2$	-1.14	**0.89 ± 0.25**	2.15	0.851
$(Bn)_2$	-0.86	**0.60 ± 0.15**	2.08	0.882
(HA)	-0.78	**0.46 ± 0.30**	2.02	0.775

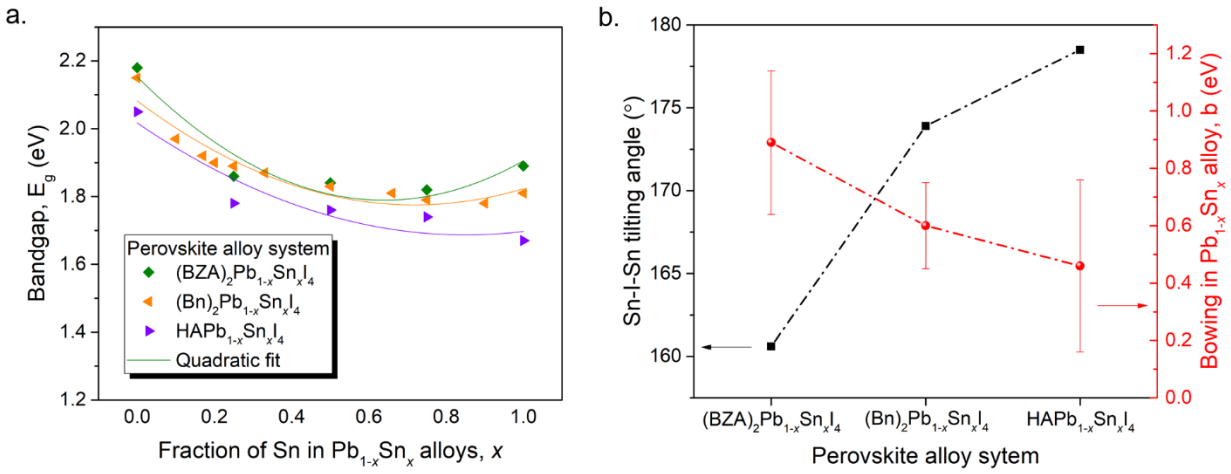

Figure 7.14. (a) Bandgap data for various mixed Pb-Sn 2D perovskite alloy systems with different fractions of Sn; data for $(BZA)_2Pb_{1-x}Sn_xI_4$,[498] $(Bn)_2Pb_{1-x}Sn_xI_4$,[499] and $HAPb_{1-x}Sn_xI_4$[498] were taken from the associated references in literature. (b) Variations in bandgap bowing for different mixed Pb-Sn 2D perovskite alloy systems and Sn-I-Sn tilting angle in their respective Sn-end members.

These examples further merit the pivotal role of local structural relaxations on bandgap evolution and generality of their implications in terms of modulating bandgap bowing behavior in OIHP alloys. Detailed study of the local structure in OIHP alloys using Pair Distribution Function (PDF) analysis, nanoscale imaging, and computational modelling will be worthwhile, but are beyond the scope of this study.

7.3.3 Compositional Exploration for High Optoelectronic Quality

In pursuit of high efficiency all perovskite tandem solar cells, lowering the bottom cell bandgap will increase the attainable (detailed-balance limit theoretical maximum) two-terminal efficiency. However, the actual efficiency will also depend strongly on the bottom cell optoelectronic quality. Thus, compositional screening of small-E_g OIHP candidates must include metrics for both bandgap and optoelectronic quality. Here, we employed absolute intensity photoluminescence (AIPL) to quantify the balance between radiative and non-radiative recombination processes in OIHP films and assess optoelectronic quality. We define an optoelectronic quality parameter χ, where χ is the quasi-Fermi level splitting as a percent of the Shockley-Queisser limit ($\Delta E_F / V_{oc,SQ}$); see **Section 7.2** for discussion of quasi-Fermi level splitting calculations. Further, we employ combinatorial spray coating to prepare composition gradients with a validated dependence of composition on distance along the substrate (see **Figure 7.2a** and discussion in **Section 7.2**). Finally, using our compositional screening we chose select compositions to further study with spin coated films, which have the same processing as device fabrication[20]. This compositional screening processes is similar to our prior work exploring (FA,GA,Cs) alloys for high bandgap perovskites.[8]

Eight spray coated composition gradients were selected to fully explore the (MA,FA,Cs) composition space, limiting our exploration compositions with Goldschmidt tolerance factor

between 0.92 and 1.00. The specific gradients are shown in **Figure 7.15a** (note that pure $Cs(Pb_{0.35}Sn_{0.65})I_3$ and pure $FA(Pb_{0.35}Sn_{0.65})I_3$ are excluded since their tolerance factor lies outside of desired range). 360 PL spectra were collected along each composition gradient, creating a total dataset of ~3000 spectra each indexed by composition. Example data for a single gradient are presented in **Figure 7.2b-c**.

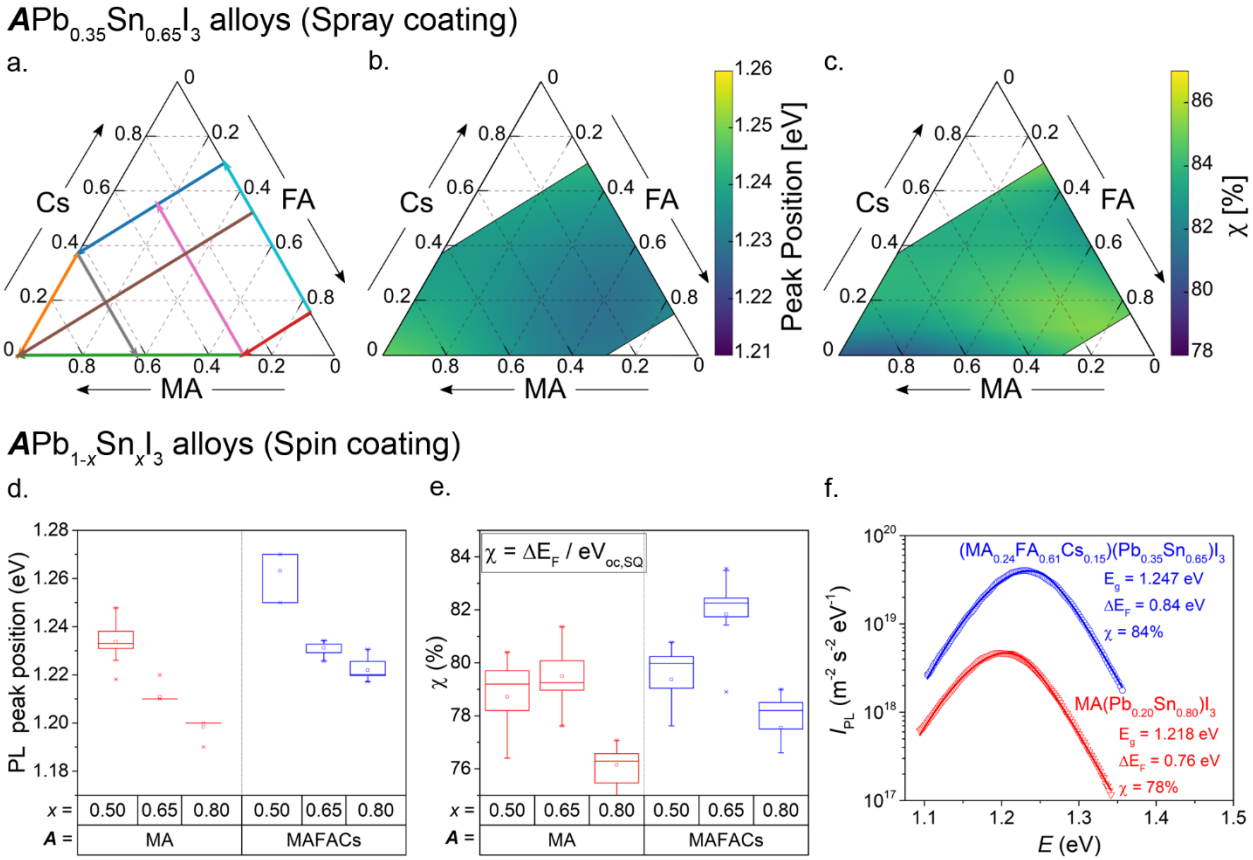

Figure 7.15. Optoelectronic properties determined from photoluminescence (PL) measurements on spray coated (a-c) and spin coated (d-f) films. (a) Ternary plot demonstrating the eight gradients included in the (MA,FA,Cs) compositional exploration (each color represents one gradient). The triangle vertices correspond to pure *A* alloys, the edges correspond to two-component alloys, and interior represents ternary (MA,FA,Cs) alloys (65% Sn for all spray coated compositions) (b) PL peak position and (c) optoelectronic quality χ, where χ is the quasi-Fermi level splitting as a percent of the Shockley-Queisser limit, calculated with the PLQY method. (d) PL peak position and (e) optoelectronic quality χ for select spin coated films (statistics from 25 PL spectra collected throughout the film), calculated with the PLQY method. (f) Absolute Intensity PL spectra for $[(MA_{0.24}FA_{0.61}Cs_{0.15})(Pb_{0.35}Sn_{0.65})I_3]$ - the spin coated film with the highest optoelectronic quality and $[(MA)(Pb_{0.20}Sn_{0.30})I_3]$ - the spin coated film with the lowest peak position compared with fit to a full peak photoluminescence model.[470] The full peak fit gives the most realistic quasi-Fermi level splitting value since this method accounts for bandgap differences from PL peak and losses from sub-bandgap absorption. Details on the full peak fit and PLQY methods are discussed in **Section 7.2**. Bandgap values from full peak fit method is blue-shifted compared to values obtained from Tauc plot analysis of absorption spectra (**Figure 7.18b**).

Response surfaces to interpolate PL peak position and optoelectronic quality χ within this dataset are presented in **Figures 7.15b** and **7.15c** respectively. The peak position remains relatively constant across the entire dataset; all spectra have peak position between 1.22 and 1.25 eV. Note that the Sn content at the bandgap minimum varies with *A*-site composition (**Figures 7.8** and **7.9**) and we only explore 65% Sn in spray coating studies, thus this does not represent the lowest attainable peak position for a particular *A*-site. The optoelectronic results demonstrate the importance of a small Cs content in attaining high optoelectronic quality, with (MA,Cs) and (FA,Cs) both demonstrating higher quality than (MA,FA) alloys. The ternary (MA,FA,Cs) alloys give the highest overall optoelectronic quality, with the maximum occurring at A = $MA_{0.24}FA_{0.61}Cs_{0.15}$, which demonstrates χ = 86% and peak position = 1.23 eV.

We also note that stability is an important consideration when choosing compositions. Substantial evidence suggests that any compositions containing MA are less stable than the MA-free alternatives,[464,500] although it is still unclear if device innovations and encapsulation strategies can overcome these issues. Thus we also explored MA-free (FA,GA,Cs) compositions, and identified certain (FA,GA,Cs) alloys with higher optoelectronic quality than the (FA,Cs) binary alternatives (**Figure 7.16**); incorporation of GA also slightly blue shifts the PL peak position and maximum χ occurrs at A = $FA_{0.42}Cs_{0.45}GA_{0.12}$. We note comparable A = (FA,Cs) binary compositions in **Figure 7.16** have slightly lower χ than the same compositions in the (FA,MA,Cs) dataset in **Figure 7.15**, which likely arises due to differences in quantities of Sn^{2+} oxidation.

Collectively, our compositional screening results highlight the potential of ternary *A*-site formulations with Cs to realize small-E_g Pb-Sn OIHPs with intrinsically higher optoelectronic quality. In the light of recent results from mechanistic studies on understanding impact of composition in OIHPs (using transmission electron microscopy,[501] nano-x-ray fluorescence,[459]

and Kelvin probe force microscopy[502]), we attribute the observed finding to improved homogeneity of composition and electrical response at nanoscale with Cs incorporation. Furthermore, other recent studies have shown that (MA,FA,Cs) *A*-site formulation in Pb-based mixed-halide compositions [(MA,FA,Cs)(Pb)(I,Br)] is beneficial for increasing the defect tolerance,[466] and the single-crystal alloys remain stable during at least 10,000 h water-oxygen and 1000 h light stability tests[503].

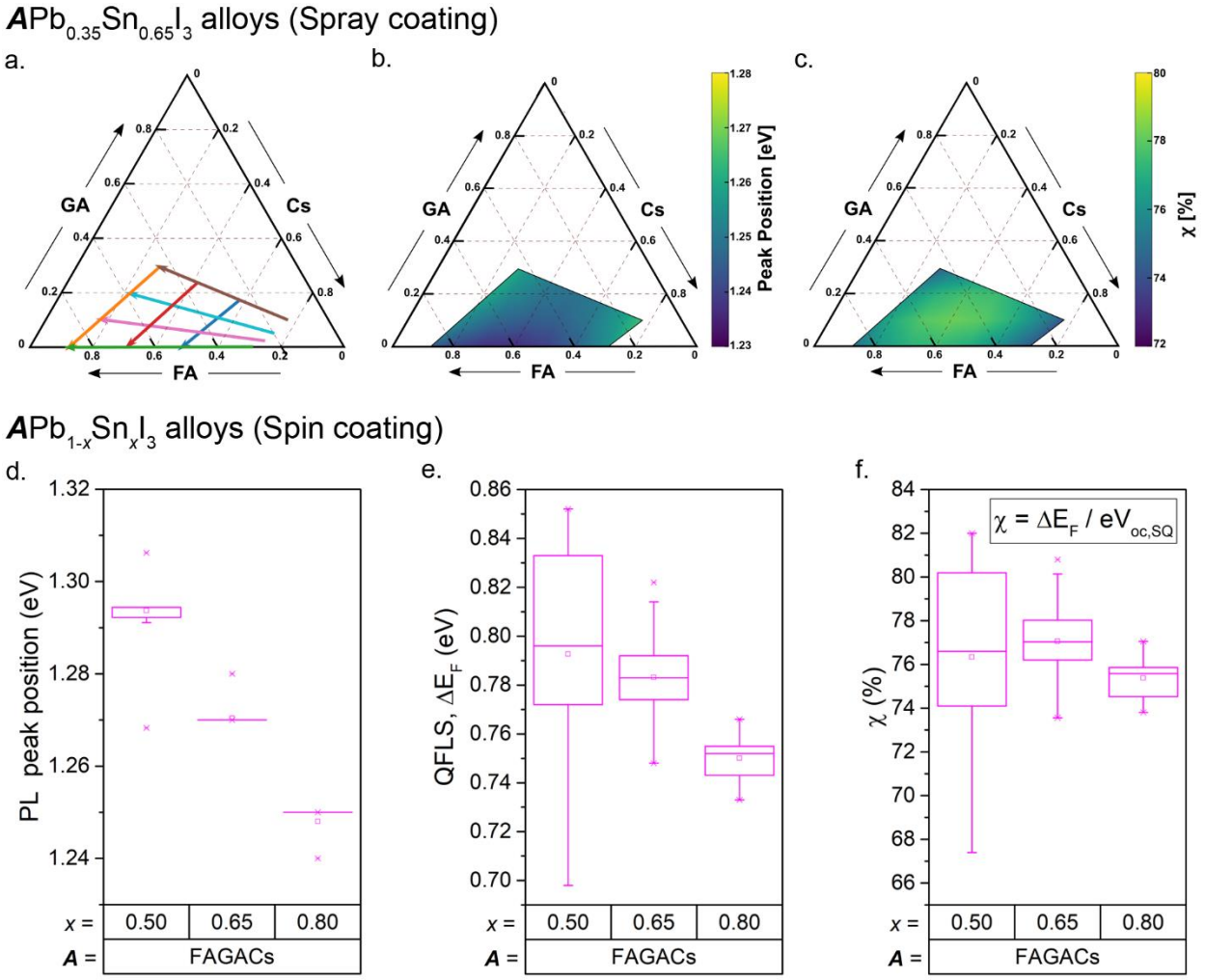

Figure 7.16. (a-c) Spray coating results for FAGACs films. (a) The seven gradients used to explore the FAGACs composition space (each color represents one gradient). Compositions were chosen to keep effective tolerance factor between 0.92 and 1.00. (b) PL peak position for (FA,GA,Cs) dataset. (c) Optoelectronic quality χ ($\chi \equiv \Delta E_F / V_{OC,SQ}$) for the (FA,GA,Cs) dataset. (d-f) PL results on FAGACs spin coated films, where A = $FA_{0.42}Cs_{0.45}GA_{0.12}$ and x = Sn/Pb+Sn = 0.50, 0.65, or 0.80.

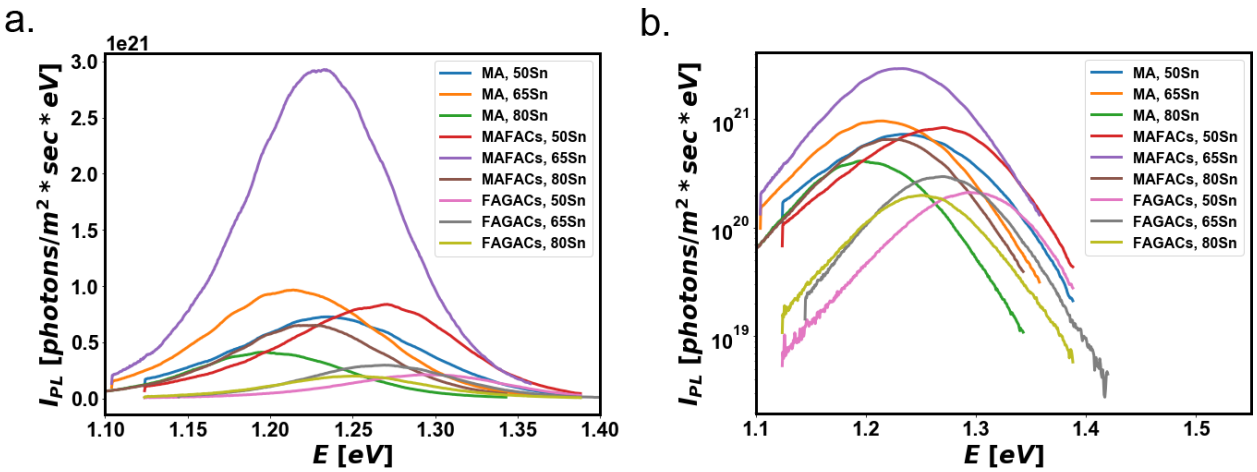

Figure 7.17. Absolute intensity Photoluminescence spectra for spin coated films with three different *A*-site and *B*-site compositions, plot on a linear (a) and log (b) axis. MAFACs represent $A = MA_{0.24}FA_{0.61}Cs_{0.15}$, and FAGACs represents $A = FA_{0.42}Cs_{0.45}GA_{0.12}$. 50Sn, 65Sn, and 80Sn correspond to *B*-site composition of x = Sn/Pb+Sn = 0.50, 0.65, and 0.80, respectively.

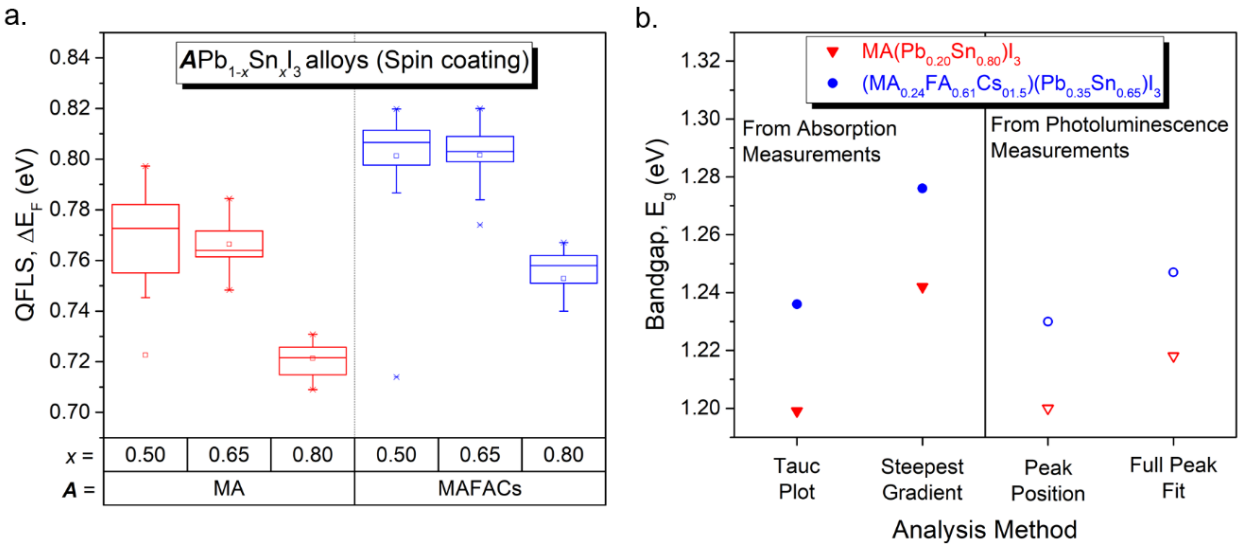

Figure 7.18. (a) Quasi-Fermi Level splitting of MA and MAFACs spin coated films with x = Sn/Pb+Sn = 0.50, 0.65, and 0.80. MAFACs represent $A = MA_{0.24}FA_{0.61}Cs_{0.15}$. (b) Bandgap of $[(MA)(Pb_{0.20}Sn_{0.30})I_3]$ and $[(MA_{0.24}FA_{0.61}Cs_{0.15})(Pb_{0.35}Sn_{0.65})I_3]$ determined using different analysis methods: Tauc plot and steepest gradient methods were used to obtain bandgap from absorption (UV-vis) measurements; Peak position and full peak fit of the PL spectra were used to obtain bandgap from photoluminescence (AIPL) measurements. Details of different analysis methods are provided in **Section 7.2**.

PL results of spin coated films (**Figures 7.15d-f**, **7.17**, and **7.18a**) confirm the finding that the (MA,FA,Cs) alloys have higher optoelectronic quality than pure MA. Further, we see that 65% Sn yield the highest optoelectronic quality (for both *A* = MA and *A* = (MA,FA,Cs)). A comparison of the AIPL spectra for the film with the highest optoelectronic quality and the lowest peak position in $(MA,FA,Cs)(Pb,Sn)I_3$ compositional space are shown in **Figure 7.15f**. They demonstrate that

to lower the bandgap by 30 meV with the chosen choice of composition, the ΔE_F decreases from 0.84 to 0.76 eV. Typical PL spectra for all spin coated films studied are shown in **Figure 7.17**. Note that the processing changes between the spray coated and spin coated films result in slightly different PL metrics (e.g. χ maximum is 86% for spray coated films and 84% for spin coated films). This suggests that processing also has a strong impact on optoelectronic properties, and that χ of at least 86% should be attainable for spin coated (MA,FA,Cs) films with process optimization, and can be further improved by adapting bulk and interfacial defect passivation approaches from our previous demonstrations of small-E_g Pb-Sn PVKSCs[4,20].

7.4 Conclusion

In summary, we have investigated the influence of *A*-site modification in $A Pb_{1-x}Sn_xI_3$ alloys for understanding the bandgap bowing behavior in OIHP alloys and identifying the optimal composition with low-E_g and high optoelectronic quality for small-E_g PVKSCs. Bandgap bowing in $APb_{1-x}Sn_xI_3$ alloys is strongly dependent on the *A*-site composition. Systematic optical and structural measurements showed that the extent of bandgap bowing in alloy systems are directly correlated with the microstrain in end-members and demonstrated the significant role of local structural relaxations / deformations on the bandgap evolution in OIHP alloys. Subsequently, we utilized high-throughput combinatorial spray coating and AIPL measurements to screen the *A*-site compositional space for $A(Pb_{0.35}Sn_{0.65})I_3$ alloys. Results revealed that the ternary *A*-site formulations [(FA,MA,Cs) and (FA,GA,Cs)] have superior optoelectronic quality with respect to their single and binary counterparts. We have found $(MA_{0.24}FA_{0.61}Cs_{0.15})(Pb_{0.35}Sn_{0.65}I_3)I_3$ to be the optimal composition that has low-E_g (1.23 eV) and high optoelectronic quality (χ = 86%). The enhanced intrinsic optoelectronic quality for the identified small-E_g composition provides a promising platform for the development of next-generation OIHP multi-junction solar cells.

Chapter 8. CONCLUSION

8.1 Summary of Results

In **Chapter 2**, I investigated reverse bias (RB) induced abnormal hysteresis in perovskite solar cells (PVKSCs) with nickel oxide (NiO_x)/methylammonium lead iodide ($CH_3NH_3PbI_3$) interfaces (**Figure 8.1**). Through comprehensive I-V characterization and bias dependent external quantum efficiency (EQE) measurements, it is demonstrated that this phenomenon is caused by the interfacial ion accumulation intrinsic to $CH_3NH_3PbI_3$. Subsequently, via systematic analysis it was discovered that the abnormal I-V behavior is remarkably similar to tunnel diode I-V characteristics and is due to the formation of a transient tunnel junction at NiO_x/$CH_3NH_3PbI_3$ interfaces under RB. The detailed analysis navigating the complexities of I-V behavior in $CH_3NH_3PbI_3$ based solar cells provided here ultimately illuminates possibilities in modulating ion motion and RB induced operational instability *via* interfacial engineering in PVKSCs. Further, this work shows that RB can alter how $CH_3NH_3PbI_3$ contributes to the functional nature of devices and provides the first steps towards approaching functional perovskite interfaces in new ways for metrology and analysis of complex transient processes.

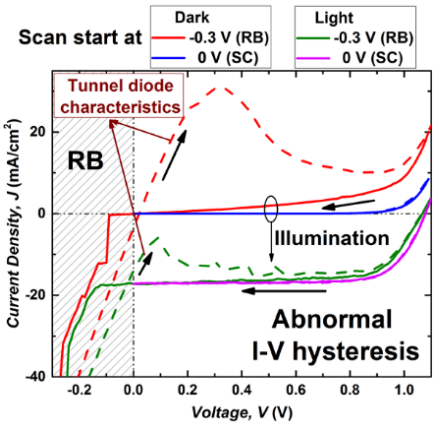

Figure 8.1. Abnormal current–voltage (I-V) hysteresis induced by reverse bias in organic–inorganic hybrid perovskite photovoltaics with NiO_x HTL. Adapted with permission from the associated publication.[16] Copyright 2016, American Chemical Society.

In **Chapter 3**, I studied how a set of closely related transition metals (Mn, Fe, Co, and Ni) modify $CH_3NH_3PbI_3$ functionality and properties by first identifying primary and secondary controlling variables that determine the nature of material growth and resulting morphology. Leveraging this understanding to minimize the impact of morphological phenomena on performance, I analyzed the compositional impact of these transition metals on optoelectronic quality using $CH_3NH_3Pb(Fe)_yI_3$ as a model system showing that transition metal inclusion of this type leads to trap-assisted recombination within the perovskite bulk that both sharply limits *Jsc* and causes significant hysteresis. By comparing device performance of Mn, Fe, Co, and Ni based systems, it is shown that Mn relieves this sharp limitation on *Jsc* and almost eliminates hysteresis (**Figure 8.2**). $CH_3NH_3Pb(Mn)_yI_3$ thus allows the implementation of direct perovskite nucleation while minimizing the deleterious impact of transition metal inclusion. PL analysis shows that this material is also more emissive than $CH_3NH_3PbI_3$, making it ideal for light production as well.

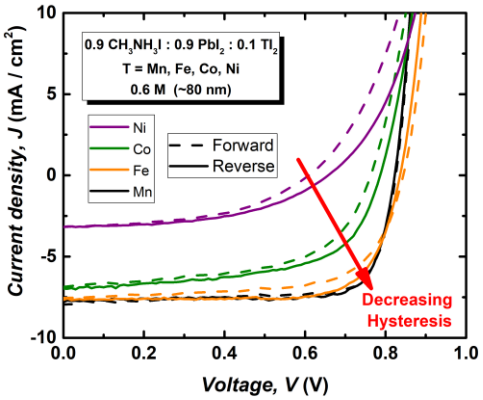

Figure 8.2. I–V hysteresis characteristics of $CH_3NH_3Pb(T)_{0.1}I_3$ solar cell devices demonstrating the influence of different transition metal inclusion (T = Mn, Fe, Co, Ni). Adapted with permission from the associated publication.[19] Copyright 2017, The Royal Society of Chemistry.

In **Chapter 4**, I investigated the unstable photovoltaic performance in wide bandgap $MAPb(I_{1-y}Br_y)_3$ perovskites caused by phase segregation under illumination. Stabilization of the I/Br phase by partially replacing Pb^{2+} with Sn^{2+} is successfully demonstrated and verified with X-ray diffractometry and transient absorption spectroscopy. The resulting $MAPb_{0.75}Sn_{0.25}(I_{1-y}Br_y)_3$

perovskite solar cells show stable photovoltaic performance under continuous illumination (**Figure 8.3**). Among these cells, the one based on $MAPb_{0.75}Sn_{0.25}(I_{0.4}Br_{0.6})_3$ perovskite shows the highest efficiency of 12.59% with a band-gap of 1.73 eV, making it a promising wide bandgap candidate for application in tandem solar cells. The engineering of internal bonding environment by partial Sn substitution is speculated to be the main reason for making $MAPb_{0.75}Sn_{0.25}(I_{1-y}Br_y)_3$ perovskite less vulnerable to phase segregation during the photostriction under illumination. This study establishes composition engineering of the metal site as a promising strategy to impart phase stability in hybrid perovskites under illumination.

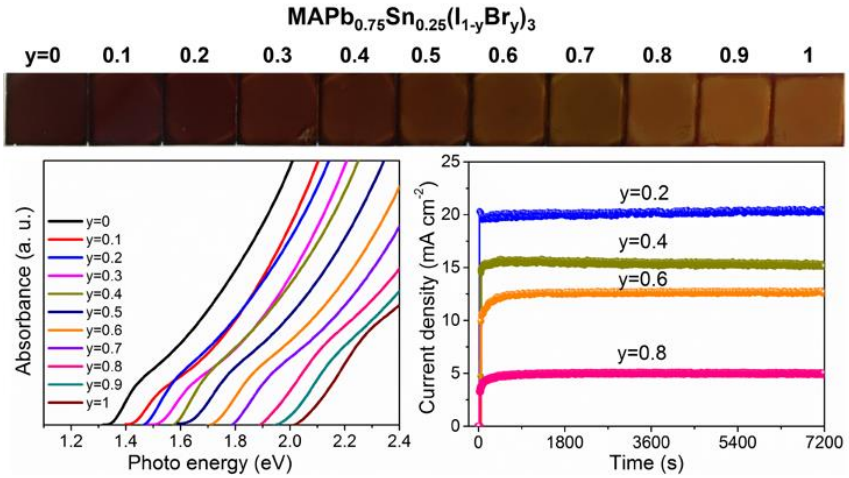

Figure 8.3. Stabilized wide bandgap perovskite solar cells by tin substitution. Adapted with permission from the associated publication.[13] Copyright 2016, American Chemical Society.

In **Chapter 5**, I utilized an integrated approach to improve V_{oc} of subcells with optimized bandgaps and fabricated perovskite-perovskite tandem solar cells with small $V_{oc,loss}$. A fullerene variant, Indene-C_{60} bis-adduct is used to achieve optimized interfacial contact in small bandgap (~1.2 eV) subcell that facilitates higher quasi-fermi level splitting, reduces non-radiative recombination, alleviates hysteresis instabilities, and improves V_{oc} to 0.84 V. Compositional engineering of large bandgap (~1.8 eV) perovskite is employed to realize a subcell with transparent top electrode and photo-stabilized V_{oc} of 1.22 V. The resultant monolithic perovskite-perovskite

tandem solar cell shows a high V_{oc} of 1.98 V (approaching 80% of the theoretical limit) and a stabilized PCE of 18.5% (**Figure 8.4**). The significantly minimized non-ideal $V_{oc,loss}$ is better than the state-of-the-art silicon-perovskite tandem solar cells, which highlights prospects of using perovskite-perovskite tandems for solar energy generation. It also unlocks opportunities for water splitting using hybrid perovskites with solar-to-hydrogen (STH) efficiencies beyond 15%.

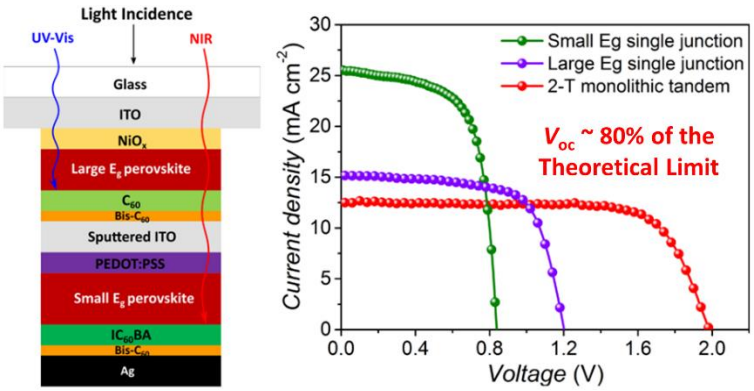

Figure 8.4. Highly efficient perovskite-perovskite tandem solar cells reaching 80% of the theoretical limit in photovoltage (V_{oc}). Adapted with permission from the associated publication.[20] Copyright 2017, Wiley-VCH.

In **Chapter 6**, I focused on the development of large bandgap (1.80-1.85 eV E_g) perovskite that is crucial for perovskite-perovskite tandem solar cells. It is observed that the photovoltage (V_{oc}) does not proportionally increase with E_g due to lower optoelectronic quality of conventional (MA,FA,Cs)Pb(I,Br)$_3$ and results in a photovoltage plateau (V_{oc} limited to 80% of the theoretical limit for ~1.8 eV E_g). I incorporated phenylethylammonium (PEA) in a mixed-halide perovskite composition to solve the inherent material-level challenges in 1.80-1.85 eV E_g perovskites. The amount of PEA incorporation governs the topography and optoelectronic properties of resultant films. The origin of improved material quality with higher luminescence was rationalized with detailed structural and spectroscopic characterization. With careful interface optimization, the improved material characteristics were translated to devices and V_{oc} values of 1.30-1.35 V were achieved, which correspond to 85-87% of the theoretical limit (**Figure 8.5**). Using an optimal amount of PEA incorporation to balance the increase in V_{oc} and the decrease in charge collection,

a highest power conversion efficiency of 12.2% was realized. Results here clearly overcome the photovoltage plateau in the 1.80-1.85 eV E_g range and represent the highest V_{oc} achieved for mixed-halide PVKSCs. This study provides widely translatable insights, an important breakthrough, and a promising platform for next-generation perovskite tandems.

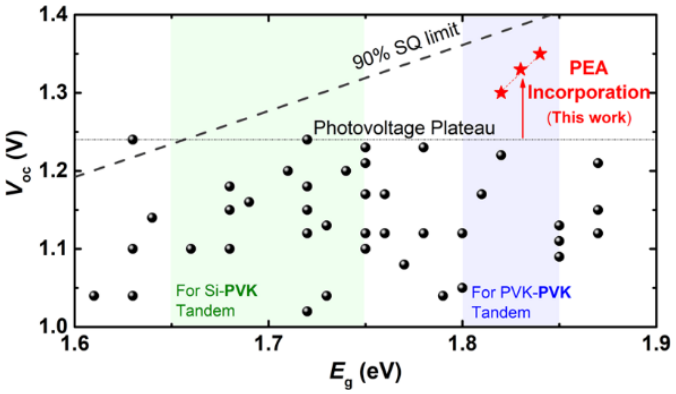

Figure 8.5. Overcoming the photovoltage plateau in large bandgap perovskite photovoltaics using phenylethylammonium (PEA) incorporation. Adapted with permission from the associated publication.[7] Copyright 2018, American Chemical Society.

In **Chapter 7**, I systematically explored a wide-range of *A*-site compositions to understand the modulation of bandgap bowing and identify the optimal Pb-Sn alloy composition (**Figure 8.6**). Bandgap of intermediate compositions in $APb_{1-x}Sn_xI_3$ ($0 < x < 1$) alloys significantly deviate from the linear interpolation between end-member bandgaps and the non-linearity is defined as bandgap bowing. The choice of *A*-site (monoatomic cation) in $APb_{1-x}Sn_xI_3$ influences the evolution of bandgap and optoelectronic quality for alloys. Optical and structural investigations of different $APb_{1-x}Sn_xI_3$ alloys revealed that the bandgap bowing is correlated to the extent of microstrain in their respective Pb-end members and demonstrated the predominant role of local structural relaxations on bandgap evolution in OIHP alloys. Subsequently, using high-throughput combinational spray coating and photoluminescence analysis, it was found that ternary combinations of methylammonium (MA), formamidinium (FA), and cesium (Cs) are beneficial to improve the optoelectronic quality of $APb_{1-x}Sn_xI_3$ alloys. The optimal composition,

$(MA_{0.24}FA_{0.61}Cs_{0.15})(Pb_{0.35}Sn_{0.65}I_3)I_3$ has the desired low bandgap (1.23 eV) and high intrinsic optoelectronic quality (86% detailed balance limit quasi-Fermi level splitting). This study provides valuable insights regarding bandgap evolution in OIHP alloys and the optimal small-bandgap absorber composition desired for next-generation OIHP tandems.

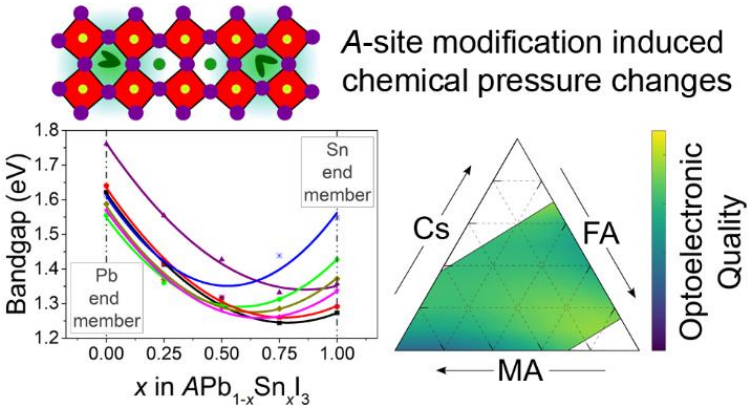

Figure 8.6. Impact of Compositional Modification on Bandgap Bowing and Optoelectronic Quality in Pb-Sn Hybrid Perovskite Alloys.

8.2 Extensions through Collaborative Work

Knowledge in hybrid perovskite material chemistry and film processing, photovoltaic device fabrication and analysis, semiconductor device physics, optical modeling, and structural material characterization techniques accrued over the years through works presented in this dissertation coupled with the interdisciplinary nature of Jen Group research have facilitated my active participation in several projects with collaborators. Successful projects span across a wide-range of topics such as, engineering composition and additive formulations for low bandgap Pb-Sn binary perovskites,[1,2,4,5,17] understanding current-induced phase segregation in mixed-halide perovskites,[3] enhancing defect tolerance and phase stability of high bandgap perovskites *via* guanidinium alloying,[8] developing chalcopyrite-perovskite 2-terminal tandem solar cells,[3,11] modulating carrier concentrations in hybrid perovskites *via* Ag incorporation,[18] passivating surface defects in hybrid perovskites by diammonium iodide post treatment,[14] controlling

orientation in bromide perovskites *via* ion exchange for ultrahigh color purity green light emission,[10] and assessing open-circuit voltage and carrier transport in hybrid perovskites with photoluminescence and photoconductivity measurements.[9] Among the above-mentioned collaborative efforts, the following are notable developments that employ concepts / methodologies developed in the course of works part of this dissertation, and are direct extensions that have contributed towards further progress in the corresponding research topics.

8.2.1 Realization of Four-Terminal All-Perovskite Tandem Solar Cells

In this work, we employed a combined compositional, process, and interfacial engineering to develop highly efficient and stable Pb–Sn binary perovskite solar cells to realize a high-performance four-terminal all-perovskite tandem solar cell. By adopting solvent-washing methodology, homogeneous and densely crystalline $MA_{1-y}FA_yPb_{1-x}Sn_xI_3$ films could be attained. The energy levels of these resultant binary perovskites were carefully investigated to facilitate the selection of appropriate charge transport layers (CTLs) for minimizing recombination losses and maximizing charge transfer efficiency of the derived devices. Due to the improved morphology of low-E_g $MAPb_{0.75}Sn_{0.25}I_3$ and carefully chosen CTLs, the derived PVKSC showed an impressive PCE of 14.35%. More importantly, the tendency of easy Sn^{2+} oxidation could be alleviated by incorporating FA cations to form a low-E_g (1.33 eV) mixed-cation Sn-based perovskite, $MA_{0.5}FA_{0.5}Pb_{0.75}Sn_{0.25}I_3$. As a result, a PVKSC with a stabilized PCE of 14.19% can be achieved. Moreover, 80% and 94% of initial PCE can be retained after 12 and 30 d storage in ambient (30–40% RH) and inert atmospheres, respectively. Ultimately, this low-Eg PVKSC was coupled with a semitransparent $MAPbI_3$ PVKSC to demonstrate a highly efficient four-terminal all-perovskite tandem solar cell with a PCE of 19.08% (**Figure 8.7**). This work revealed the key challenges in developing high performance low-E_g PVKSCs and provided effective ways to solve those

challenges. Further, the performances of low-E_g PVKSC and four-terminal all-perovskite tandem solar cell achieved here were record values when the work was published in 2016.[1]

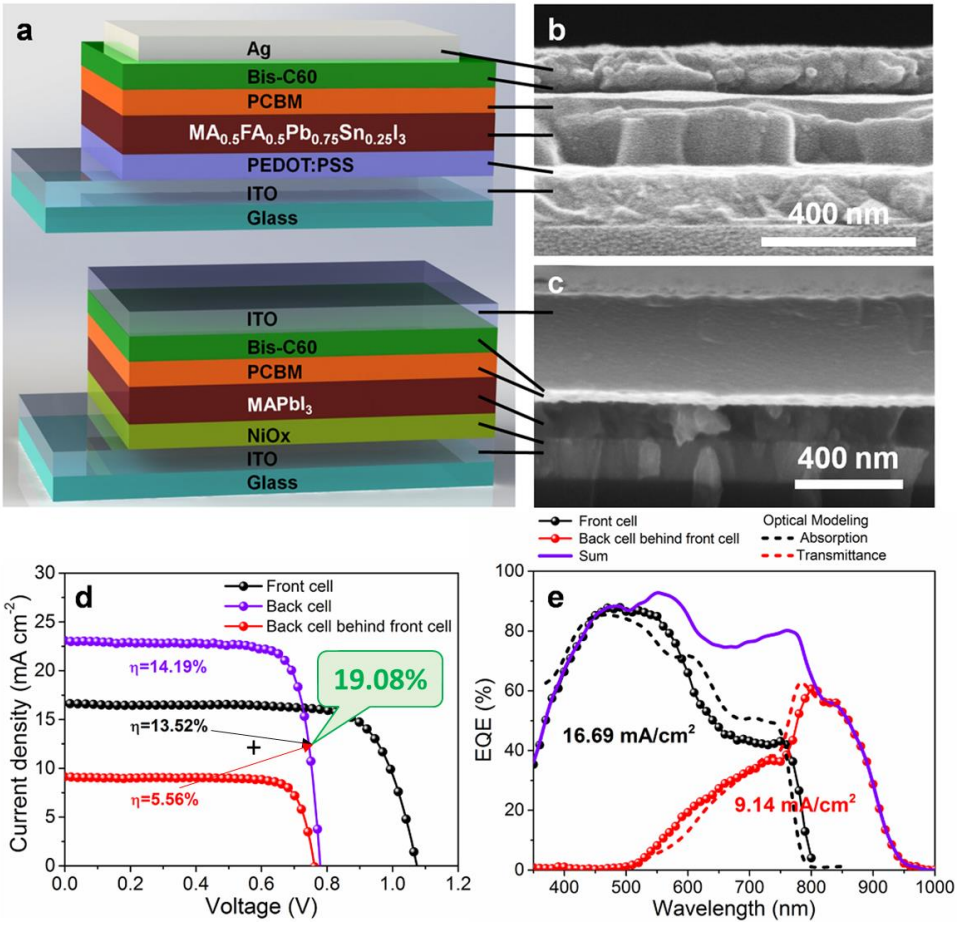

Figure 8.7. (a-c) Schematic illustration and SEM images of the structure of four-terminal perovskite–perovskite tandem solar cells. (d) J-V characteristics (measured under AM 1.5 illumination) of the tandem solar cells based on top $MA_{0.5}FA_{0.5}Pb_{0.75}Sn_{0.25}I_3$ and bottom semitransparent $MAPbI_3$ PVKSCs. (e) EQE spectra and optical modeling of individual sub-cells in the tandem solar cells. Adapted with permission from the associated publication.[1] Copyright 2016, Wiley-VCH.

8.2.2 Improvement of Low Bandgap Pb-Sn Binary PVKSCs by Defect Passivation

Significant advancements have been made in the performance of low-bandgap Pb−Sn binary alloys in our prior works, which were pivotal in realizing high-performance perovskite tandem solar cells (**Chapter 5**).[1,2,17,20] Defect passivation in this class of perovskite alloys has immense potential to further reduce the photovoltage deficit but is relatively unexplored. In this work, we incorporated fluoroalkyl-substituted fullerene (DF-C_{60}), in low-bandgap binary Pb−Sn

perovskites to form a graded heterojunction (GHJ) structure. A graded distribution of DF-C_{60} in $MAPb_{0.5}Sn_{0.5}I_3$ contributed to beneficial defect passivation and a lower Urbach energy in resultant films, a reduced number of trap sites, dominant bimolecular recombination, and higher resistance to surface/bulk recombination. The improved optoelectronic quality of films with a GHJ structure has resulted in improved performance for corresponding photovoltaic devices. With additional interlayer and process optimization, devices with a GHJ perovskite structure showed a high PCE of 15.61% and a remarkably high V_{oc} of 0.89 V (**Figure 8.8**). A V_{oc} ~92% of the Shockley–Queisser (SQ) limit is comparable to those from the state-of-the-art inorganic counterparts and is the best among PVKSCs reported to date.[4] Additionally, we found that the application of DF-C_{60} in GHJ devices can slow down moisture penetration, and the oxidative susceptibility of Sn in binary perovskites is what constraints overall stability.

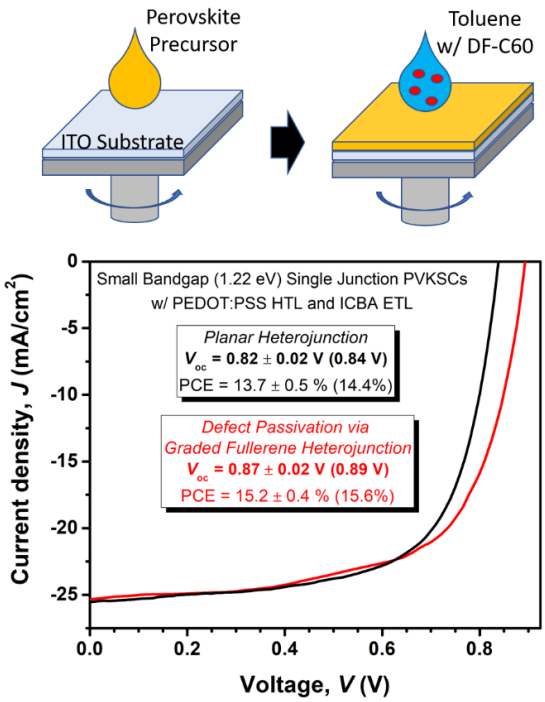

Figure 8.8. Defect passivation *via* a graded fullerene heterojunction in low-bandgap Pb–Sn binary perovskite photovoltaics. Adapted with permission from the associated publication.[4] Copyright 2017, American Chemical Society. Data for planar heterojunction is reproduced here from **Chapter 5** to elucidate the impact of defect passivation on solar cell performance metrics. V_{oc} and PCE in parentheses correspond to the highest values obtained.

8.2.3 Advancement of Ideal Bandgap Single-Junction Perovskite Solar Cells

Development of ideal bandgap (1.3-1.4 eV) absorbers is pivotal for single junction perovskite solar cells (PVKSCs) because of better balance between absorption loss of sub-bandgap photons and thermalization loss of above-bandgap photons, as demonstrated by Shockley-Queisser detailed balanced calculation. Ideal bandgap PVKSCs are hindered by poor optoelectronic quality of perovskite absorbers and their PCEs have stagnated at <15%. In this work, we identified and developed a new ideal bandgap (E_g = 1.35 eV) perovskite composition ($MAPb_{0.5}Sn_{0.5}(I_{0.8}Br_{0.2})_3$) with superior optoelectronic properties through material insights attained via an integrated photoluminescence and photovoltaic analysis. Improved material properties of ($MAPb_{0.5}Sn_{0.5}(I_{0.8}Br_{0.2})_3$) (lower nonradiative recombination states, band edge disorder, Urbach energy, and higher absorption coefficient) reduced the $V_{oc,loss}$ (0.45 V) and improved solar cell performance (V_{oc} = 0.90 V, J_{sc} = 25.9 mA/cm^2, PCE = 17.6%.) (**Figure 8.9**).

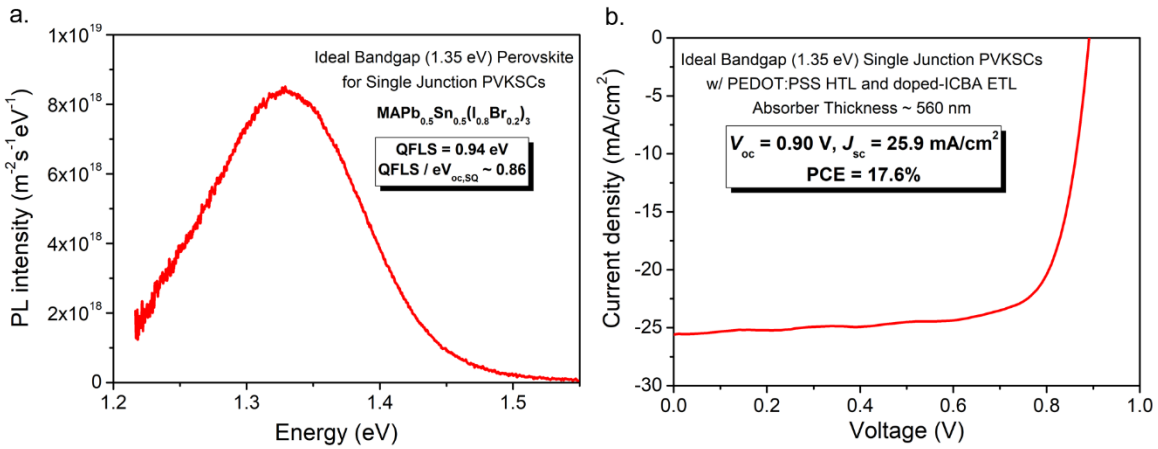

Figure 8.9. (a) Absolute intensity photoluminescence (PL) spectra for newly developed ideal bandgap perovskite composition ($MAPb_{0.5}Sn_{0.5}(I_{0.8}Br_{0.2})_3$). (b) J-V characteristics (measured under AM 1.5 illumination) for the best performing ideal bandgap single junction PVKSC. Adapted with permission from the associated publication.[5] Copyright 2017, Wiley-VCH.

This represented the highest performance for ideal bandgap PVKSCs realized when the work was published in 2017,[5] and was a significant improvement compared to the previous state-of-the-art result based on $MAPb_{0.25}Sn_{0.75}I_3$ (E_g = 1.35 eV, $V_{oc,loss}$ = 0.55 V, PCE = 15.21%). This work

provides a promising platform for unleashing the complete potential of ideal bandgap PVKSCs and prospects for further improvement are provided in the associated publication.[5]

8.2.4 Demonstration of Monolithic Chalcopyrite-Perovskite Tandem Solar Cells

The combination of PVKSCs with existing commercial PV technologies, such as pc-Si or CIGS solar modules, in a tandem device could pose the biggest impact for the hybrid perovskite (HP) technology and ultimately facilitate the commercialization of PVKSCs. In this work, we employed solution-process CIS devices (E_g = 1.0 eV) as bottom cells in monolithic tandem devices with perovskite top cells. Stabilized PCEs up to 8.55% were obtained with V_{oc}s up to 1.40 V which resembles near perfect voltage addition between top and bottom cells (**Figure 8.10**).

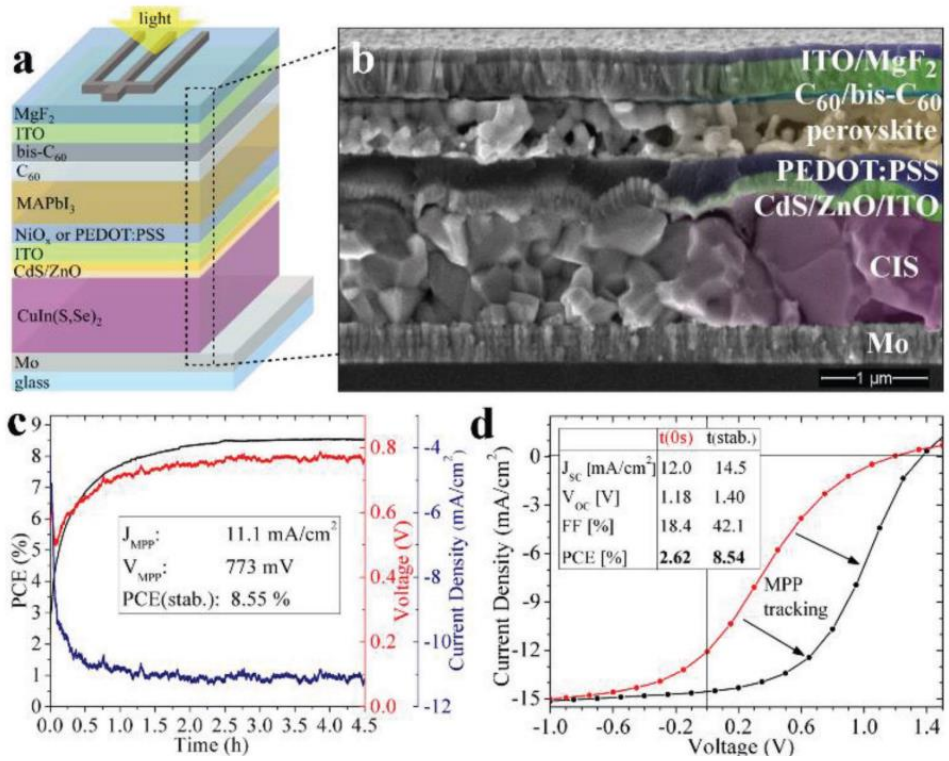

Figure 8.10. (a) Schematic of monolithic HP-CIS tandem solar cell. (b) SEM cross section of tandem solar cell. (c-d) Maximum power point tracking shows improving and stabilizing active area PCE from initial 2.6% up to 8.6% after 4 h. Adapted with permission from the associated publication.[11] Copyright 2018, Wiley-VCH.

Tandem PCEs were found to be limited mainly by low FF values which were seen to dramatically improve with light soaking under MPP. This problem was related to the performance of our

semitransparent PSCs which suffered from poor morphologies when deposited on relatively rougher CIS substrates (compared to glass) and experienced dramatic FF losses when operated in substrate configuration with illumination through the ETL, suggesting a carrier extraction problem in the top cell. Increased tandem PCEs can therefore be expected from tandem devices with thinner HP absorbers and improved carrier diffusion length and morphology. Nevertheless, results in this work highlight the potential of solution-processing methods for high efficiency thin film single junction and monolithic tandem solar cells based on CIS and HP absorbers as means to dramatically reduce the cost of clean and renewable electricity from the sun.[11]

8.3 Intellectual Merits, Research Impact and Products of Lasting Value

Perovskite solar cells (PVKSCs) have undergone a rapid progress that is unmatched by any other PV technologies till date[353] and were listed as one of the "Top 10 Emerging Technologies of 2016" by the World Economic Forum[504]. The technological advancement is being fueled by a dynamic and fiercely competitive research community, which has seen a huge surge in the number of researchers since its initial stages in 2012. I have been part of this research community from 2014 and worked on a diverse set of topics in the last 5 years. As the field evolves, certain results could become obsolete quickly and is therefore vital to extract key value from research studies and adapt accordingly for effectively progressing forward. Here, I have identified intellectual merits, research impact and products of lasting value from my doctoral research.

Navigating Complexities of Perovskite Film Processing and Compositional Modification

Although DMSO is ideal in the solution state, we found that it causes CH_3NH_3I-PbI_2-DMSO formation which leads to the rod-like thin film morphology that a great deal of work in the perovskite field endeavors to circumvent *via* creative processing techniques like 2-step deposition and solvent washing. We found that transition metal inclusion allows direct perovskite nucleation

to strongly compete with CH_3NH_3I-PbI_2-DMSO formation. While we found that solution concentration, atmospheric composition, and annealing profile all impact the route through which transformation proceeds, CH_3NH_3I stoichiometry and magnetic field have unique optoelectronic consequences that should be considered when studying this class of perovskite alloy. Methodology and insights developed herein[19] provide a general approach for navigating complexities of perovskite film processing and compositional modification.

State-of-the-art Photovoltages for Single- and Multi-Junction Perovskite Solar Cells

Systematic and comprehensive research efforts in our work toward solving inherent material- and device-level challenges in small bandgap Pb-Sn binary PVKSCs and large bandgap I-Br mixed halide PVKCSs have consistently improved their performances. Significance and pioneering nature of our work is evident from **Figure 8.11** (comparison of the figure-of-merit, $V_{oc}/V_{oc,SQ}$), which demonstrates that we have realized state-of-the-art photovoltages in several bandgap ranges of interest.

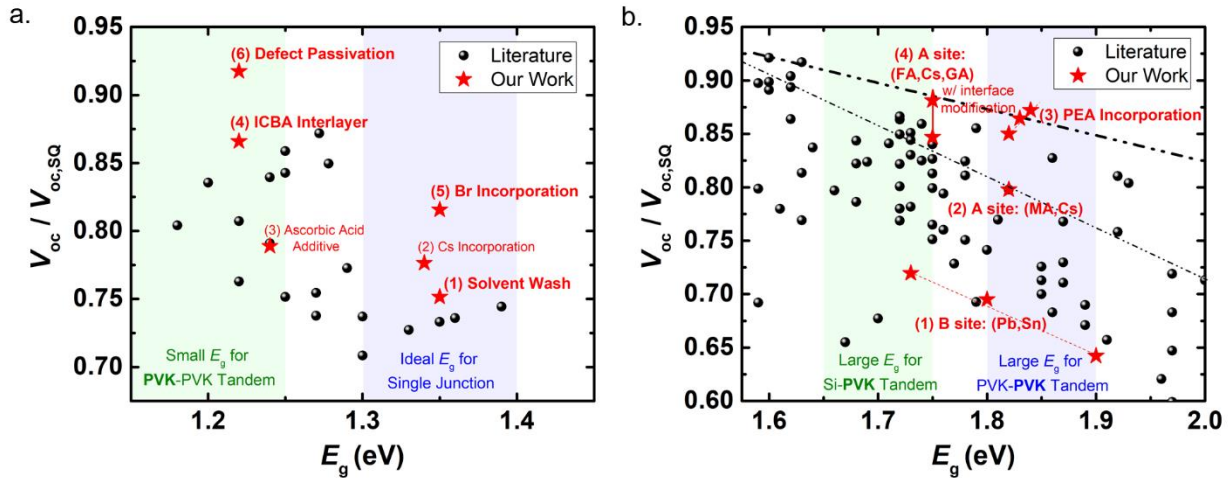

Figure 8.11. Comparison of the figure-of-merit (open-circuit voltage, V_{oc}) for PVKSCs reported in literature in perspective to our works. ($V_{oc}/V_{oc,SQ}$) as a function of bandgap (E_g) for works in the (a) 1.2−1.4 eV (small) E_g range and (a) 1.6−2.0 eV (large) E_g range. Red stars correspond to values obtained in our works.[1,2,4,5,7,8,13,17,20] Black dotted line in (b) shows the current state-of-the art $V_{oc}/V_{oc,SQ}$ values as a function of E_g, which are significantly improved compared to the prior values (grey dotted line).

Successful implementation of small and large bandgap subcells developed in this work led to the realization of monolithic (2T) perovskite-perovskite tandem with high V_{oc} (1.98 V) and PCE (18.5%), both of which were record values for 2T all-perovskite tandem architecture at the time of publication (June 2017).[20] With the evolution of the field, the PCE record for 2T all-perovskite tandem has been pushed to 19.1% by McGehee et al.[464] (in August 2018) and 21.0% by Yan et al.[463] (in November 2018). Our work still represents the highest photovoltage ($V_{oc}/V_{oc,SQ}$ ~ 0.80) realized for 2T all-perovskite tandem, which is a testimony to the value of contribution here (**Figure 8.12**).

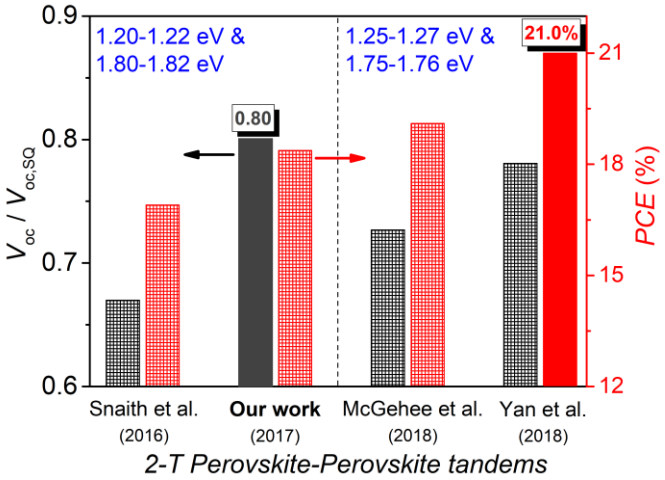

Figure 8.12. Comparison of $V_{oc}/V_{oc,SQ}$ and PCE of state-of-the art perovskite–perovskite tandems at different points in their evolution, demonstrating merits of our work[20] in perspective to literature[387,463,464]; V_{oc} / $V_{oc,SQ}$ of 0.80 obtained in our work and PCE of 21.0% obtained in the work by Yan et al. represent current record values in the respective categories (highlighted by solid color fill).

The record V_{oc}'s of 0.89 V ($V_{oc}/V_{oc,SQ}$ = 0.92) and 1.30 V ($V_{oc}/V_{oc,SQ}$ = 0.85) achieved for small and large Eg PVKSCs in our work[4,7] provide a promising platform for next-generation perovskite tandems, where PCEs beyond single junction solar cells are realizable. When the small and large bandgap PVKSCs developed here are integrated in a tandem configuration, without any substantial optimization we can obtain a high PCE estimate ~25% (projected based on our single junction demonstrations, using V_{oc} ~ 2.21 along with *FF* ~0.75 and J_{sc} ~15 mA/cm^2 attainable using thicker absorbers). A step-by-step efficiency estimation is provided in **Figure 8.13**.

a.

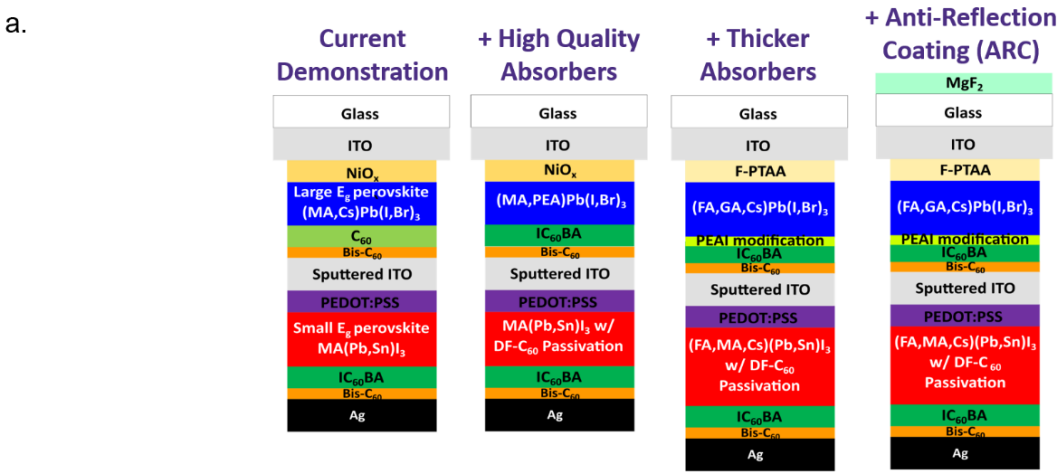

	Current Demonstration	+ High Quality Absorbers	+ Thicker Absorbers	+ Anti-Reflection Coating (ARC)
V_{oc} (V)	1.98	**2.12**	2.12	2.12
J_{sc} (mA/cm^2)	12.7	12.7	**14.8**	**15.4**
FF	0.73	0.75	0.75	0.75
PCE (%)	**18.4**	**20.2**	**23.5**	**24.5**

b.

High Quality Absorbers Developed Here			
Small E_g (1.20-1.22 eV) Perovskites		**Large E_g (1.80-1.82 eV) Perovskites**	
Approach	*ΔE_f of film (eV) / V_{oc} of device (V)*	*Approach*	*ΔE_f of film (eV) / V_{oc} of device (V)*
$MA(Pb_{0.5}Sn_{0.5})I_3$	ΔE_f = 0.81 eV	$MA(Pb_{0.75}Sn_{0.25})(I_{0.3}Br_{0.7})_3$	V_{oc} = 1.01 V
+ $IC_{60}BA$ ETL	ΔE_f = 0.84 eV / V_{oc} = 0.84 V	$(MA_{0.9}Cs_{0.1})Pb(I_{0.6}Br_{0.4})_3$	ΔE_f = 1.28 eV / V_{oc} = 1.22 V
+ DF-C_{60} Passivation in Thicker Absorber	V_{oc} = 0.89 V	$(MA,PEA)Pb(I_{0.6}Br_{0.4})_3$	ΔE_f = 1.32 eV / V_{oc} = 1.30 V
$(MA_{0.24}FA_{0.61}Cs_{0.15})(Pb_{0.35}Sn_{0.65})I_3$	ΔE_f = 0.84 eV	Thicker $(FA,GA,Cs)Pb(I,Br)_3$ + PEAI modification + F-PTAA HTL + $IC_{60}BA$ ETL	V_{oc} = 1.29 V

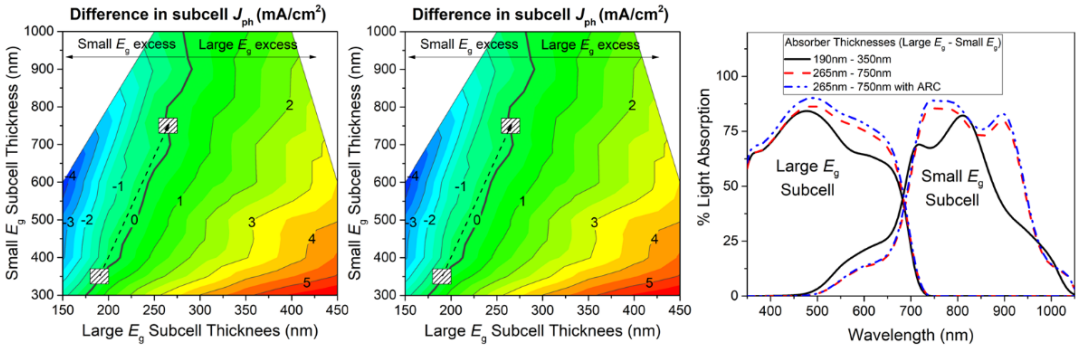

Figure 8.13. (a) Device architecture and associated estimation of photovoltaic metrics for next-generation 2T all-perovskite tandems, in perspective to our current demonstration. (b) Relevant data and calculations utilized to estimate efficiency for next generation tandem architectures in (a); based on results discussed in **Chapters 4-8**. Anti-Reflection Coating (ARC) refers to 100 nm MgF_2.

Perspective and Review Articles

- **Current Challenges and Prospective Research for Upscaling Hybrid PVKSCs:**[15] This article offers a perspective on the practical market potential of PVKSCs, the nature of fundamental PVKSC challenges at scale, and an outline of prospective solutions for achieving module scale PVKSC production tailored to intrinsic advantages of hybrid perovskites. Although integrating PVKSCs into the energy grid is complicated by hybrid perovskite degradation, the ability of PVKSCs to contribute to consumer electronics and other niche markets like those organic photovoltaics have sought footing in rests primarily upon the technology's price point. Thus, slot die, roll-to-roll processing has the greatest potential to enable PVKSC scale-up, and herein, we present a perspective on the research necessary to realize fully printable PVKSCs at scale (**Figure 8.14**). A perspective video presenting a short conversation between me and my colleague going through highlights of our manuscript can be found in association with the manuscript.

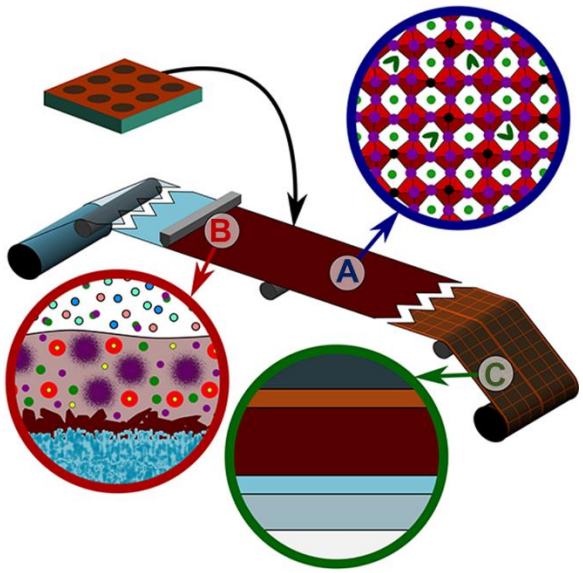

Figure 8.14. Prospective research directions necessary to fuel PVKSC technological translation *via* slot die R2R coating. (a) Material engineering can address intrinsic ion diffusivity and degradation of $CH3NH_3PbI_3$, (b) optimization of perovskite growth under R2R conditions is necessary to reach performance requirements, and (c) device engineering is required to extend device life and expand the material toolbox for PVSKC design. Adapted with permission from the associated publication.[15] Copyright 2016, American Chemical Society.

- **Toward PVKSC Commercialization – A Perspective and Research Roadmap Based on Interfacial Engineering:**[6] This review offers a unique outlook on the paths toward commercialization of PVKSCs from the interfacial engineering perspective, relevant to both specialists and non-specialists in the field through a brief introduction of the background of the field, current state-of-the-art evolution, and future research prospects. The multifaceted role of interfaces in facilitating PVKSC development is explained (**Figure 8.15**). Beneficial impacts of diverse charge-transporting materials and interfacial modifications are summarized. In addition, the role of interfaces in improving efficiency and stability for all emerging areas of PVKSC design are also evaluated. Finally, future research opportunities for interfacial material development and applications along with scalability–durability–sustainability considerations pivotal for facilitating laboratory to industry translation are presented. This article was part of the *Advanced Materials* Hall of Fame virtual issue.

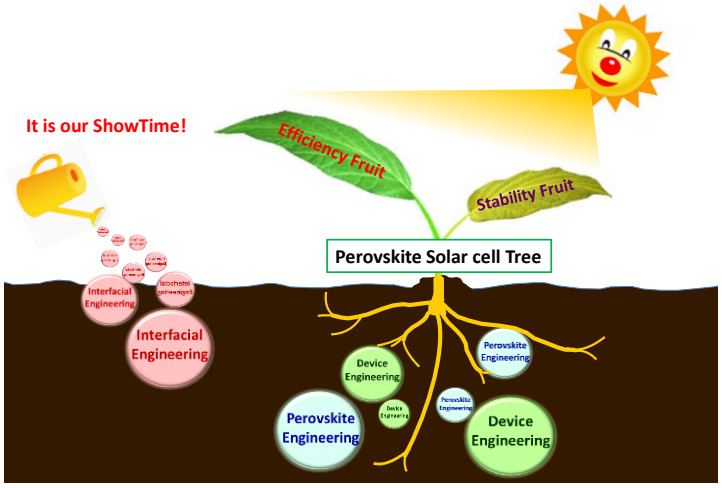

Figure 8.15. Review on the paths toward commercialization of PVKSCs from the interfacial engineering perspective. Interfacial engineering will continue to propel the efficiency and stability of PVKSCs through four different facets: (i) Perovskite Film Formation – interfacial materials modulate the crystallization and material quality of perovskite thin films; (ii) Perovskite Defect Passivation – interfacial materials facilitate the passivation of surface and bulk defects; (iii) Interfacial Charge Dynamics – interfacial contacts control the charge extraction, accumulation, and recombination processes governing functionality of a PVKSC; (iv) Device Stability and Durability – interfacial contacts sandwiching perovskite absorber act as a first line of defense to mitigate intrinsic and extrinsic degradation pathways. Adapted with permission from the associated publication.[6] Copyright 2018, Wiley-VCH.

8.4 Perspectives for Continued Development of Perovskite Tandem Solar Cells

Combining multiple p-n junctions with complementary absorbers in a tandem (multi-junction) configuration is promising to further improve the PCE by mitigating absorption loss of low energy below E_g photons and thermalization loss of high energy above E_g photons. Exceptional charge generation and transport capabilities, high photovoltages and facile bandgap tunability enabled by versatility of hybrid perovskites make them ideal candidates for building tandem devices. Improvement of the individual subcell performance will directly lead to higher 4-terminal (4T) tandem efficiencies (mechanically stacked subcells), whereas added electrical considerations (subcell current matching) exist for successful design of 2-terminal (2T) tandems (monolithically integrated subcells). The general device configuration for 2T and 4T tandems are shown in **Figure 8.16a**. Perovskite based 2T tandems are economically viable and can be designed by integrating large bandgap (1.6-1.8 eV) PVKSCs with other small bandgap (1-1.2 eV) PV technologies or PVKSCs itself (**Figure 8.16b**). Currently no 4-terminal tandem PV module has been commercially installed because of prohibitively high capital requirements.

Unique merits exist for different combination of perovskite tandems. Perovskite-Silicon (PVK-Si) tandems provide an opportunity to build upon an established platform for enhancing performance of Si PV and help market penetration for PVKSCs;[505,506] Perovskite-Chalcogenide (PVK-CIS or CIGS or CZTS) tandems are attractive from both performance (smaller bandgaps ~ 1eV realizable) and application (processible on flexible substrates) perspective;[22,507] Perovskite-organic PV (PVK-OPV) tandems are interesting because of potential to achieve high IR absorption through novel design of organic molecules;[507,508] Perovskite-Perovskite (PVK-PVK) tandems retain intrinsic low temperature processability and superior optoelectronic property merits of PVKSCs with high efficiency potential.[22,212] Recent environmental analysis show that among

different tandem configurations, 2-terminal PVK-PVK tandem is more environmental friendly with least-energy intensive processing and has the lowest energy payback time.[414] There are several recent reviews that provide detailed summary of perovskite tandem development.[22,212,506–511] Here, I provide a complementary discussion on the roadmap for further progress, with specific emphasis on the importance of interfacial engineering in the path forward. The discussion is categorized into three parts: tandem perspective, large bandgap subcell perspective, and small bandgap subcell perspective. Implementation of perspectives provided below in the above-discussed state-of-the-art tandem platform (**Figure 8.13**) will faciltate realization of next-generation perovskite tandems with efficiencies beyond 30%.

A. Tandem Perspective

The foundational building block for tandem construction is a ST-PVKSC that facilitates passage of light to the complementary subcell. Transparency of interlayers and electrodes are key for ST-PVKSC development. Large bandgap, transparent inorganic materials are ideal interlayer candidates.[512] Several different materials like thin metal film, transparent conducting oxide (TCO), silver nanowire (Ag-NW), PEDOT:PSS, carbon nanotube (CNT), and graphene have been successfully employed as transparent electrodes in ST-PVKSCs.[211] Successful application of such transparent electrodes on the top of perovskite absorber requires incorporation of functional interfacial or buffer layers and are critical from multiple perspectives (processing, performance and stability). Typical functions of interfacial layers include modulation of the electrode work function, growth, adhesion and compatibility with the perovskite layer, protection of the perovskite from processing induced damages, and enhancement of device stability. From the processing perspective, PEDOT:PSS buffer layer improves adhesion between perovskite and graphene electrode during the lamination process,[513] metal oxide buffer layer prevents damage of the

perovskite during deposition of top electrodes via sputtering or atomic layer deposition,[226,384,514–516] and Cu seed layer (1 nm) enables formation of a continuous ultrathin Au film (7 nm) with superior transparency and conductivity.[517] From the performance perspective, electrode modifications play a crucial role in maximizing V_{oc} and *FF* for ST-PVKSCs.[518] From the stability perspective, barrier oxide layer shields perovskite from the metal electrode induced degradation and detrimental moisture attack.[516,519]

A large bandgap ST-PVKSC in a substrate configuration is required for integrating with the inorganic PVs, whereas a superstrate configuration is desired for integrating with the organic or PVK subcell. Discussion of the ST-PVKSC development above is pertinent to tandems with an added consideration for efficient interconnecting layer (ICL) to couple subcells. Diversity of ICLs used in different representative 2T tandem solar cells are outlined in **Figure 8.15c**. It is apparent that majority of solution processed perovskite tandems employ ITO for ICL, which functions as an efficient recombination layer and also enables orthogonal processability.[20,226,410] Optical analysis of 23.6% PVK-Si tandem (McGehee & Snaith *et al.*)[226] and our 18.5% PVK-PVK tandem[20] reveal that a significant fraction of current loss is incurred by the parasitic absorption in interlayers (charge selective contacts, ICL) and the reflection loss at the light incident surface. Loss-inducing interlayers should be replaced with thinner and less-absorbing alternatives without compromise in the electrical requirements (conductivity and band alignment). Rational interlayer material and thickness optimization is important to maximize the current matching and stability. Employment of an anti-reflection coating (ARC) at the incident surface and light management strategies (texturing and plasmonics) can further enhance the current generation. Recently proposed alternate device designs like graded bandgap PVKSCs[520] and 3-terminal (3T) tandem configuration using nanoscale back-contact top cells[521] are worth exploring.

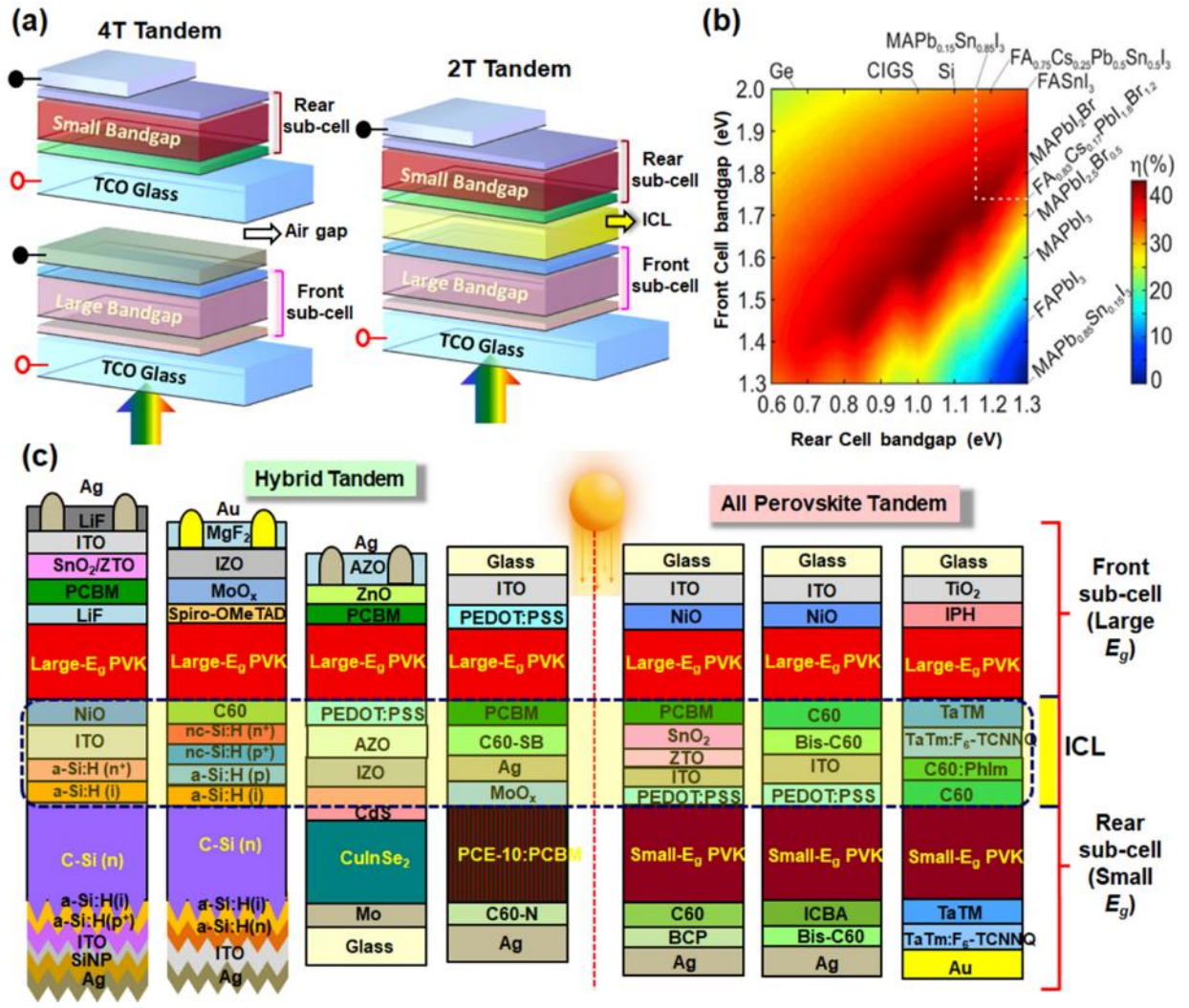

Figure 8.16. Design of perovskite tandem solar cells. a) Device configuration for two-terminal (2T) and four-terminal (4T) tandem solar cells. b) Calculated theoretical power conversion efficiency (PCE, η) for 2T tandem solar cells with different bandgap (E_g) combinations of front and rear sub-cell absorbers. c) Comparison of device stacks for different representative 2T tandem solar cells, with interconnecting layers (ICLs) highlighted.[20,226,383,387,409,522,523] Adapted with permission from the associated publication.[6] Copyright 2018, Wiley-VCH.

B. Large Bandgap Subcell Perspective

Large bandgap perovskites are achieved using mixed halide (I/Br) alloys and the E_g choice is dependent on the subcell combination (Figure 15b). Mixed halide alloys suffer from photo-instability (phase segregation to I- and Br-rich alloys) and poor optoelectronic quality (non-radiative recombination in the bulk). Morphological optimization,[370,423,426] additive incorporation,[416,424,524] and compositional modifications like A-site alloying (FA/Cs,[355] MA/Cs,[20] FA/MA/Cs,[466] FA/MA/Cs/Rb,[422] FA/GA/Cs[8]), B-site alloying (Pb/Sn[13]) or large

organic cation alloying (MA/PEA,[7] MA/Cs/BA[428]) have shown varying degrees of success in mitigating phase segregation. Despite such improvements, the large E_g (1.7-1.8 eV) PVKSCs suffer from characteristically large in-loss potential (~0.5 V) that severely limits the subcell V_{oc} (<1.35 V). As a result, the highest reported photovoltage for any perovskite based tandem solar cells is only ~85-87% of the theoretical limit.[7] Though the exact origin and mechanism of phase segregation is still shaping up,[3,407,408,417,435,525,526] it is apparent that the phase segregation and dominant crystalline defects in bulk are adversely impacting J_{sc} and $V_{oc.}$[369,527] Additional limitations on V_{oc} are imposed by interfacial contacts, which will become more apparent as the material quality is further improved. Therefore, synergistic improvements of the bulk material quality of large bandgap perovskites (via defect passivation) and optimization of interfacial contacts (via band alignment) are key to reach values beyond 1.3-1.4 V.

C. Small Bandgap Subcell Perspective

Small bandgap perovskites are realized using Pb/Sn alloys and the inherent bandgap bowing behavior results in a E_g ~1.2 eV using alloys with 50-75% Sn.[364] Overcoming the processing challenges for Pb/Sn alloys *via* an integrated device engineering in our work led to one of the earlier demonstrations of low bandgap PVKSCs with PCEs ~15% and their application in 4-T PVK-PVK tandem.[1] Since then, impressive material and device level progress by several groups have improved the PCE to 17.6% for Pb/Sn based small E_g perovskites,[401,492] and have led to the successful fabrication of 2-T PVK-PVK tandem with optimized bandgaps.[20,387] Recently, an impressive V_{oc} of 0.89 V (~92% of SQ limit, highest value reported for PVKSC) has been realized in our work for small E_g PVKSCs *via* defect passivation.[4] At this juncture, current generation in the small E_g subcell is the limiting factor and is apparent in all PVK-PVK tandem demonstrations.[20,387,401,463,464] Development of thicker (~1 μm) absorbers with superior charge

transporting properties, compositional exploration for the discovery of perovskites with E_g <1.2 eV, and implementation of absorbers with improved optoelectronic quality are all important to relieve the limitation imposed by small E_g PVKSCs. Besides, all small E_g PVKSCs to date universally employ PEDOT:PSS and fullerene as the HTL and ETL, respectively. Understanding the nature of interfaces and finding alternate interlayer replacements with better band alignment will further advance the performance of Pb/Sn based small E_g perovskites. The acquired knowledge is also directly translatable for progress of the ideal bandgap single junction PVKSCs.[5] Material engineering to overcome instabilities associated with Sn incorporation is highly important. Specific attention to the interfacial reactivity is critical when new metal substituents are employed for lowering the bandgap and realizing Pb-free perovskites.

BIBLIOGRAPHY

Publications of Adharsh Rajagopal (References [1-20] listed in chronological order)

*Lead authored works are highlighted in purple color

AR-1: **Rajagopal, A.**; Williams, S. T.; Chueh, C.-C.; Jen, A. K.-Y. Abnormal Current–Voltage Hysteresis Induced by Reverse Bias in Organic–Inorganic Hybrid Perovskite Photovoltaics. *J. Phys. Chem. Lett.* **2016**, *7*, 995.

AR-2: Yang, Z.; **Rajagopal, A.**; Chueh, C.; Jo, S. B.; Liu, B.; Zhao, T.; Jen, A. K.-Y. Stable Low-Bandgap Pb-Sn Binary Perovskites for Tandem Solar Cells. *Adv. Mater.* **2016**, *28*, 8990.

AR-3: Williams, S. T.; **Rajagopal, A.**; Chueh, C.-C.; Jen, A. K.-Y. Current Challenges and Prospective Research for Upscaling Hybrid Perovskite Photovoltaics. *J. Phys. Chem. Lett.* **2016**, *7*, 811.

AR-4: Zhao, T.; Chueh, C.-C.; Chen, Q.; **Rajagopal, A.**; Jen, A. K.-Y. Defect Passivation of Organic–Inorganic Hybrid Perovskites by Diammonium Iodide toward High-Performance Photovoltaic Devices. *ACS Energy Lett.* **2016**, *1*, 757.

AR-5: Yang, Z.; **Rajagopal, A.**; Jo, S. B.; Chueh, C.-C.; Williams, S.; Huang, C.-C.; Katahara, J. K.; Hillhouse, H. W.; Jen, A. K.-Y. Stabilized Wide Bandgap Perovskite Solar Cells by Tin Substitution. *Nano Lett.* **2016**, *16*, 7739.

AR-6: Liu, X.; Yang, Z.; Chueh, C.-C.; **Rajagopal, A.**; Williams, S. T.; Sun, Y.; Jen, A. K.-Y. Improved Efficiency and Stability of Pb–Sn Binary Perovskite Solar Cells by Cs Substitution. *J. Mater. Chem. A* **2016**, *4*, 17939.

AR-7: Williams, S. T.; **Rajagopal, A.**; Jo, S. B.; Chueh, C.-C.; Tang, T. F. L.; Kraeger, A.; Jen, A. K.-Y. Realizing a New Class of Hybrid Organic–inorganic Multifunctional Perovskite. *J. Mater. Chem. A* **2017**, *5*, 10640.

AR-8: **Rajagopal, A.**; Yang, Z.; Jo, S. B.; Braly, I. L.; Liang, P.-W.; Hillhouse, H. W.; Jen, A. K.-Y. Highly Efficient Perovskite-Perovskite Tandem Solar Cells Reaching 80% of the Theoretical Limit in Photovoltage. *Adv. Mater.* **2017**, *29*, 1702140.

AR-9: Xu, X.; Chueh, C.-C.; Yang, Z.; **Rajagopal, A.**; Xu, J.; Jo, S. B.; Jen, A. K.-Y. Ascorbic Acid as an Effective Antioxidant Additive to Enhance the Efficiency and Stability of Pb/Sn-Based Binary Perovskite Solar Cells. *Nano Energy* **2017**, *34*, 392.

AR-10: Chen, Q.; Chen, L.; Ye, F.; Zhao, T.; Tang, F.; **Rajagopal, A.**; Jiang, Z.; Jiang, S.; Jen, A. K.-Y.; Xie, Y.; et al. Ag-Incorporated Organic–Inorganic Perovskite Films and Planar Heterojunction Solar Cells. *Nano Lett.* **2017**, *17*, 3231.

AR-11: Braly, I. L.; Stoddard, R. J.; **Rajagopal, A.**; Uhl, A. R.; Katahara, J. K.; Jen, A. K.; Hillhouse, H. W. Current-Induced Phase Segregation in Mixed Halide Hybrid Perovskites and Its Impact on Two-Terminal Tandem Solar Cell Design. *ACS Energy Lett.* **2017**, *2*, 1841.

AR-12: **Rajagopal, A.**; Liang, P.-W.; Chueh, C.-C.; Yang, Z.; Jen, A. K.-Y. Defect Passivation via a Graded Fullerene Heterojunction in Low-Bandgap Pb–Sn Binary Perovskite Photovoltaics. *ACS Energy Lett.* **2017**, *2*, 2531.

AR-13: Yang, Z.; **Rajagopal, A.**; Jen, A. K.-Y. Ideal Bandgap Organic-Inorganic Hybrid Perovskite Solar Cells. *Adv. Mater.* **2017**, *29*, 1704418.

AR-14: **Rajagopal, A.**; Yao, K.; Jen, A. K.-Y. Towards Perovskite Solar Cell Commercialization: A Perspective and Research Roadmap Based on Interfacial Engineering. *Adv. Mater.* **2018**, *30*, 1800455.

AR-15: **Rajagopal, A.**; Stoddard, R. J.; Jo, S. B.; Hillhouse, H. W.; Jen, A. K.-Y. Overcoming Photovoltage Bottleneck in Large Bandgap Perovskite Photovoltaics. *Nano Lett.* **2018**, *18*, 3985.

AR-16: Stoddard, R. J.; **Rajagopal, A.**; Palmer, R. L.; Braly, I. L.; Jen, A. K.-Y.; Hillhouse, H. W. Enhancing Defect Tolerance and Phase Stability of High-Bandgap Perovskites via Guanidinium Alloying. *ACS Energy Lett.* **2018**, *3*, 1261.

AR-17: Braly, I. L.; Stoddard, R. J.; **Rajagopal, A.**; Jen, A. K.-Y.; Hillhouse, H. W. Photoluminescence and Photoconductivity to Assess Maximum Open-Circuit Voltage and Carrier Transport in Hybrid Perovskites and Other Photovoltaic Materials. *J. Phys. Chem. Lett.* **2018**, *9*, 3779.

AR-18: Zhao, T.; Liu, H.; Ziffer, M. E.; **Rajagopal, A.**; Zuo, L.; Ginger, D. S.; Li, X; Jen, A. K.-Y. Realization of Highly Oriented $MAPbBr_3$ Thin Film *via* Ion Exchange for Ultrahigh Color Purity Green Light Emission. *ACS Energy Lett.* **2018**, *3*, 1662.

AR-19: Uhl, A. R.; **Rajagopal, A.**; Clark, J. A.; Murray, A.; Feurer, T.; Jen, A. K.-Y.; Hillhouse, H. W. Solution-Processed Low-Bandgap $CuIn(S,Se)_2$ Absorbers for High Efficiency Single Junction and Monolithic Chalcopyrite-Perovskite Tandem Solar Cells. *Adv. Energy Mater.* **2018**, *8*, 1801254.

AR-20: **Rajagopal, A.**; Stoddard, R. J.; Hillhouse, H. W.; Jen, A. K.-Y. Impact of Compositional Modification on Bandgap Bowing and Optoelectronic Quality in Pb-Sn Hybrid Perovskite Alloys. *In Preparation*. **2019**.

Presentations of Adharsh Rajagopal (Listed in chronological order)

1) **Adharsh Rajagopal** and Alex K.-Y. Jen. (June 2016). Current-Voltage Hysteresis Instability in Organic-Inorganic Hybrid Perovskite Photovoltaics. *Gordon Research Conference on Hybrid Electronic & Photonic Materials*, Hong Kong, China. (Poster)
2) **Adharsh Rajagopal**, Zhibin Yang, and Alex K.-Y. Jen. (August 2016). Functional Role of Tin Substitution in Perovskite Solar Cells. *Office of Naval Research Workshop on Perovskite Solar Cell Stability*, Seattle, USA. (Poster)
3) Spencer Williams, **Adharsh Rajagopal**, Sae Byeok Jo, Chu-Chen Chueh, Tiffany F.L. Tang, and Alex K.-Y. Jen. (October 2016). Bringing Perovskite Photovoltaics to Scale through Material Engineering. *University of Washington MSE Industry Day*, Seattle, USA. (Oral)
4) **Adharsh Rajagopal**, Zhibin Yang, and Alex K.-Y. Jen. (October 2016). Functional Role of Tin Substitution in Perovskite Solar Cells. *University of Washington MSE Industry Day*, Seattle, USA. (Poster)
5) Spencer Williams, **Adharsh Rajagopal**, and Alex K.-Y. Jen. (April 2017). Controlling Growth Thermodynamics and Phase Stability through Rational Engineering of the Interstitial Site in Hybrid Organic-Inorganic Perovskites. *Materials Research Society Spring Meeting*, Phoenix, USA. (Oral)
6) **Adharsh Rajagopal**, Zhibin Yang, and Alex K.-Y. Jen. (October 2017). Highly Efficient Perovskite-Perovskite Tandem Solar Cells. *University of Washington MSE Industry Day*, Seattle, USA. (Oral)
7) **Adharsh Rajagopal**, Zhibin Yang, and Alex K.-Y. Jen. (November 2017). Development of Highly Efficient Perovskite-Perovskite Tandem Solar Cells. *Materials Research Society Fall Meeting*, Boston, USA. (Poster)
8) **Adharsh Rajagopal** and Alex K.-Y. Jen. (April 2018). Breakthrough in Photovoltages of Small and Large Bandgap Perovskite Solar Cells Tailored for Tandem Applications. *Materials Research Society Spring Meeting*, Phoenix, USA. (Oral – Won "Best Presentation Award for Young Researchers")

REFERENCES

[1] Z. Yang, A. Rajagopal, C. Chueh, S. B. Jo, B. Liu, T. Zhao, A. K.-Y. Jen, *Adv. Mater.* **2016**, *28*, 8990.
[2] X. Liu, Z. Yang, C.-C. Chueh, A. Rajagopal, S. T. Williams, Y. Sun, A. K.-Y. Jen, *J. Mater. Chem. A* **2016**, *4*, 17939.
[3] I. L. Braly, R. J. Stoddard, A. Rajagopal, A. R. Uhl, J. K. Katahara, A. K. Jen, H. W. Hillhouse, *ACS Energy Lett.* **2017**, *2*, 1841.
[4] A. Rajagopal, P.-W. Liang, C.-C. Chueh, Z. Yang, A. K.-Y. Jen, *ACS Energy Lett.* **2017**, *2*, 2531.
[5] Z. Yang, A. Rajagopal, A. K.-Y. Jen, *Adv. Mater.* **2017**, *29*, 1704418.
[6] A. Rajagopal, K. Yao, A. K.-Y. Jen, *Adv. Mater.* **2018**, *30*, 1800455.
[7] A. Rajagopal, R. J. Stoddard, S. B. Jo, H. W. Hillhouse, A. K.-Y. Jen, *Nano Lett.* **2018**, *18*, 3985.
[8] R. J. Stoddard, A. Rajagopal, R. L. Palmer, I. L. Braly, A. K.-Y. Jen, H. W. Hillhouse, *ACS Energy Lett.* **2018**, *3*, 1261.
[9] I. L. Braly, R. J. Stoddard, A. Rajagopal, A. K.-Y. Jen, H. W. Hillhouse, *J. Phys. Chem. Lett.* **2018**, *9*, 3779.
[10] T. Zhao, H. Liu, M. E. Ziffer, A. Rajagopal, L. Zuo, D. S. Ginger, X. Li, A. K. Y. Jen, *ACS Energy Lett.* **2018**, *3*, 1662.
[11] A. R. Uhl, A. Rajagopal, J. A. Clark, A. Murray, T. Feurer, S. Buecheler, A. K.-Y. Jen, H. W. Hillhouse, *Adv. Energy Mater.* **2018**, *8*, 1801254.
[12] A. Rajagopal, R. J. Stoddard, H. W. Hillhouse, A. K. -Y. Jen, *In Preparation.* **2019**.
[13] Z. Yang, A. Rajagopal, S. B. Jo, C.-C. Chueh, S. Williams, C.-C. Huang, J. K. Katahara, H. W. Hillhouse, A. K.-Y. Jen, *Nano Lett.* **2016**, *16*, 7739.
[14] T. Zhao, C.-C. Chueh, Q. Chen, A. Rajagopal, A. K.-Y. Jen, *ACS Energy Lett.* **2016**, *1*, 757.
[15] S. T. Williams, A. Rajagopal, C.-C. Chueh, A. K.-Y. Jen, *J. Phys. Chem. Lett.* **2016**, *7*, 811.
[16] A. Rajagopal, S. T. Williams, C.-C. Chueh, A. K.-Y. Jen, *J. Phys. Chem. Lett.* **2016**, *7*, 995.
[17] X. Xu, C.-C. Chueh, Z. Yang, A. Rajagopal, J. Xu, S. B. Jo, A. K.-Y. Jen, *Nano Energy* **2017**, *34*, 392.
[18] Q. Chen, L. Chen, F. Ye, T. Zhao, F. Tang, A. Rajagopal, Z. Jiang, S. Jiang, A. K.-Y. Jen, Y. Xie, J. Cai, L. Chen, *Nano Lett.* **2017**, *17*, 3231.
[19] S. T. Williams, A. Rajagopal, S. B. Jo, C.-C. Chueh, T. F. L. Tang, A. Kraeger, A. K.-Y. Jen, *J. Mater. Chem. A* **2017**, *5*, 10640.
[20] A. Rajagopal, Z. Yang, S. B. Jo, I. L. Braly, P.-W. Liang, H. W. Hillhouse, A. K.-Y. Jen, *Adv. Mater.* **2017**, *29*, 1702140.

[21] S. P. Group, "International Technology Roadmap for Photovoltaic—," can be found under http://www.itrpv.net/Reports/Downloads/, **2017**.
[22] M. Anaya, G. Lozano, M. E. Calvo, H. Míguez, *Joule* **2017**, *1*, 769.
[23] J. Jean, P. R. Brown, R. L. Jaffe, T. Buonassisi, V. Bulović, *Energy Environ. Sci.* **2015**, *8*, 1200.
[24] S. Samadi, *Renew. Sustain. Energy Rev.* **2018**, *82*, 2346.
[25] G. F. Nemet, *Energy Policy* **2006**, *34*, 3218.
[26] L. Qiu, L. K. Ono, Y. Qi, *Mater. Today Energy* **2017**, DOI 10.1016/j.mtener.2017.09.008.
[27] M. L. Petrus, J. Schlipf, C. Li, T. P. Gujar, N. Giesbrecht, P. Müller-Buschbaum, M. Thelakkat, T. Bein, S. Hüttner, P. Docampo, *Adv. Energy Mater.* **2017**, *7*, 1700264.
[28] J.-P. Correa-Baena, A. Abate, M. Saliba, W. Tress, T. Jesper Jacobsson, M. Grätzel, A. Hagfeldt, *Energy Environ. Sci.* **2017**, *10*, 710.
[29] C. C. Stoumpos, M. G. Kanatzidis, *Adv. Mater.* **2016**, *28*, 5778.
[30] J. S. Manser, J. A. Christians, P. V. Kamat, *Chem. Rev.* **2016**, *116*, 12956.
[31] M. A. Green, A. Ho-Baillie, *ACS Energy Lett.* **2017**, *2*, 822.
[32] J.-P. Correa-Baena, M. Saliba, T. Buonassisi, M. Grätzel, A. Abate, W. Tress, A. Hagfeldt, *Science.* **2017**, *358*, 739.
[33] Y. Zhao, K. Zhu, *Chem. Soc. Rev.* **2016**, *45*, 655.
[34] A. Polman, M. Knight, E. C. Garnett, B. Ehrler, W. C. Sinke, *Science.* **2016**, *352*, aad4424.
[35] Z. Song, C. L. McElvany, A. B. Phillips, I. Celik, P. W. Krantz, S. C. Watthage, G. K. Liyanage, D. Apul, M. J. Heben, *Energy Environ. Sci.* **2017**, *10*, 1297.
[36] T. Ibn-Mohammed, S. C. L. Koh, I. M. Reaney, A. Acquaye, G. Schileo, K. B. Mustapha, R. Greenough, *Renew. Sustain. Energy Rev.* **2017**, *80*, 1321.
[37] J. Gong, S. B. Darling, F. You, *Energy Environ. Sci.* **2015**, *8*, 1953.
[38] S. De Wolf, J. Holovsky, S. J. Moon, P. Löper, B. Niesen, M. Ledinsky, F. J. Haug, J. H. Yum, C. Ballif, *J. Phys. Chem. Lett.* **2014**, *5*, 1035.
[39] M. Kaltenbrunner, G. Adam, E. D. Głowacki, M. Drack, R. Schwödiauer, L. Leonat, D. H. Apaydin, H. Groiss, M. C. Scharber, M. S. White, N. S. Sariciftci, S. Bauer, *Nat. Mater.* **2015**, *14*, 1032.
[40] I. Celik, Z. Song, A. J. Cimaroli, Y. Yan, M. J. Heben, D. Apul, *Sol. Energy Mater. Sol. Cells* **2016**, *156*, 157.
[41] M. Sessolo, H. J. Bolink, *Science.* **2015**, *350*, 917.
[42] P. D. Matthews, D. J. Lewis, P. O'Brien, *J. Mater. Chem. A* **2017**, *5*, 17135.
[43] T. Leijtens, K. Bush, R. Cheacharoen, R. Beal, A. Bowring, M. D. McGehee, W. Tress, K. Schenk, J. Teuscher, J.-E. Moser, H. Rensmo, A. Hagfeldt, M. A. Alam, G. Gupta, J. Lou, P. M. Ajayan, M. J. Bedzyk, M. G. Kanatzidis, A. D. Mohite, *J. Mater. Chem. A* **2017**, *5*, 11483.
[44] B. Saparov, D. B. Mitzi, *Chem. Rev.* **2016**, *116*, 4558.
[45] W. Li, Z. Wang, F. Deschler, S. Gao, R. H. Friend, A. K. Cheetham, *Nat. Rev. Mater.* **2017**, *2*, 16099.
[46] C. Li, X. Lu, W. Ding, L. Feng, Y. Gao, Z. Guo, *Acta Crystallogr. Sect. B Struct. Sci.* **2008**, *64*, 702.
[47] C. C. Stoumpos, C. D. Malliakas, M. G. Kanatzidis, *Inorg. Chem.* **2013**, *52*, 9019.
[48] J.-W. Xiao, L. Liu, D. Zhang, N. De Marco, J.-W. Lee, O. Lin, Q. Chen, Y. Yang, *Adv. Energy Mater.* **2017**, *7*, 1700491.
[49] L. K. Ono, E. J. Juarez-Perez, Y. Qi, *ACS Appl. Mater. Interfaces* **2017**, *9*, 30197.
[50] E. L. Unger, L. Kegelmann, K. Suchan, D. Sörell, L. Korte, S. Albrecht, *J. Mater. Chem. A* **2017**, *5*, 11401.
[51] Z. Shi, J. Guo, Y. Chen, Q. Li, Y. Pan, H. Zhang, Y. Xia, W. Huang, *Adv. Mater.* **2017**, *29*, 1605005.
[52] J. Huang, Y. Yuan, Y. Shao, Y. Yan, *Nat. Rev. Mater.* **2017**, *2*, 17042.
[53] B. R. Sutherland, E. H. Sargent, *Nat. Photonics* **2016**, *10*, 295.
[54] J. M. Ball, A. Petrozza, *Nat. Energy* **2016**, *1*, 16149.
[55] W. Tress, *Adv. Energy Mater.* **2017**, *7*, 1602358.
[56] T. M. Brenner, D. A. Egger, L. Kronik, G. Hodes, D. Cahen, *Nat. Rev. Mater.* **2016**, *1*, 15007.
[57] Z. Xiao, Y. Yan, *Adv. Energy Mater.* **2017**, *7*, 1701136.
[58] M. A. Green, Y. Hishikawa, E. D. Dunlop, D. H. Levi, J. Hohl-Ebinger, A. W. Y. Ho-Baillie, *Prog. Photovoltaics Res. Appl.* **2018**, *26*, 3.
[59] J. S. Manser, M. I. Saidaminov, J. A. Christians, O. M. Bakr, P. V Kamat, *Acc. Chem. Res.* **2016**, *49*, 330.
[60] D. T. Moore, H. Sai, K. W. Tan, D.-M. Smilgies, W. Zhang, H. J. Snaith, U. Wiesner, L. a. Estroff, *J. Am. Chem. Soc.* **2015**, *137*, 2350.
[61] B. Conings, J. Drijkoningen, N. Gauquelin, A. Babayigit, J. D'Haen, L. D'Olieslaeger, A. Ethirajan, J. Verbeeck, J. Manca, E. Mosconi, F. De Angelis, H. Boyen, *Adv. Energy Mater.* **2015**, *5*, 1500477.
[62] Y. Zhao, K. Zhu, *J. Phys. Chem. Lett.* **2014**, *5*, 4175.

[63] W. Zhang, G. E. Eperon, H. J. Snaith, *Nat. Energy* **2016**, *1*, 16048.
[64] L. K. Ono, M. R. Leyden, S. Wang, Y. Qi, *J. Mater. Chem. A* **2016**, *4*, 6693.
[65] A. Sharenko, M. F. Toney, *J. Am. Chem. Soc.* **2016**, *138*, 463.
[66] Z. Xiao, Y. Yuan, Q. Wang, Y. Shao, Y. Bai, Y. Deng, Q. Dong, M. Hu, C. Bi, J. Huang, *Mater. Sci. Eng. R Reports* **2016**, *101*, 1.
[67] Q. Chen, N. De Marco, Y. (Michael) Yang, T.-B. Song, C.-C. Chen, H. Zhao, Z. Hong, H. Zhou, Y. Yang, *Nano Today* **2015**, *10*, 355.
[68] N.-G. Park, *CrystEngComm* **2016**, *18*, 5977.
[69] Y. Zhou, N. P. Padture, *ACS Energy Lett.* **2017**, *2*, 2166.
[70] N.-G. Park, *Inorg. Chem.* **2017**, *56*, 3.
[71] X. Peng, J. Yuan, S. Shen, M. Gao, A. S. R. Chesman, H. Yin, J. Cheng, Q. Zhang, D. Angmo, *Adv. Funct. Mater.* **2017**, *27*, 1703704.
[72] M. Remeika, Y. Qi, *J. Energy Chem.* **2017**, DOI 10.1016/j.jechem.2017.10.005.
[73] S. A. Veldhuis, P. P. Boix, N. Yantara, M. Li, T. C. Sum, N. Mathews, S. G. Mhaisalkar, *Adv. Mater.* **2016**, *28*, 6804.
[74] Y. Kim, H. Cho, T. Lee, *Proc. Natl. Acad. Sci.* **2016**, *113*, 11694.
[75] F. P. García de Arquer, A. Armin, P. Meredith, E. H. Sargent, *Nat. Rev. Mater.* **2017**, *2*, 16100.
[76] Y. M. You, W. Q. Liao, D. Zhao, H. Y. Ye, Y. Zhang, Q. Zhou, X. Niu, J. Wang, P. F. Li, D. W. Fu, Z. Wang, S. Gao, K. Yang, J. M. Liu, J. Li, Y. Yan, R. G. Xiong, *Science.* **2017**, *357*, 306.
[77] K. Du, Q. Tu, X. Zhang, Q. Han, J. Liu, S. Zauscher, D. B. Mitzi, *Inorg. Chem.* **2017**, *56*, 9291.
[78] S. D. Stranks, *ACS Energy Lett.* **2017**, *2*, 1515.
[79] N.-G. Park, M. Grätzel, T. Miyasaka, K. Zhu, K. Emery, *Nat. Energy* **2016**, *1*, 16152.
[80] Y. Yuan, J. Huang, *Acc. Chem. Res.* **2016**, *49*, 286.
[81] B. Chen, M. Yang, S. Priya, K. Zhu, *J. Phys. Chem. Lett.* **2016**, *7*, 905.
[82] J. M. Azpiroz, E. Mosconi, J. Bisquert, F. De Angelis, *Energy Environ. Sci.* **2015**, *8*, 2118.
[83] J. Yang, T. L. Kelly, *Inorg. Chem.* **2017**, *56*, 92.
[84] T. A. Berhe, W. Su, C.-H. Chen, C.-J. Pan, J.-H. Cheng, H.-M. Chen, M.-C. Tsai, L.-Y. Chen, A. A. Dubale, B.-J. Hwang, *Energy Environ. Sci.* **2015**, *9*, 323.
[85] Q. Wang, B. Chen, Y. Liu, Y. Deng, Y. Bai, Q. Dong, J. Huang, *Energy Environ. Sci.* **2017**, *10*, 516.
[86] J.-P. Correa-Baena, M. Anaya, G. Lozano, W. Tress, K. Domanski, M. Saliba, T. Matsui, T. J. Jacobsson, M. E. Calvo, A. Abate, M. Grätzel, H. Míguez, A. Hagfeldt, *Adv. Mater.* **2016**, *28*, 5031.
[87] H. Do Kim, H. Ohkita, H. Benten, S. Ito, *Adv. Mater.* **2016**, *28*, 917.
[88] C. Bi, Q. Wang, Y. Shao, Y. Yuan, Z. Xiao, J. Huang, *Nat. Commun.* **2015**, *6*, 7747.
[89] S. Y. Leblebici, L. Leppert, Y. Li, S. E. Reyes-Lillo, S. Wickenburg, E. Wong, J. Lee, M. Melli, D. Ziegler, D. K. Angell, D. F. Ogletree, P. D. Ashby, F. M. Toma, J. B. Neaton, I. D. Sharp, A. Weber-Bargioni, *Nat. Energy* **2016**, *1*, 16093.
[90] S. Draguta, S. Thakur, Y. V. Morozov, Y. Wang, J. S. Manser, P. V. Kamat, M. Kuno, *J. Phys. Chem. Lett.* **2016**, *7*, 715.
[91] Y. Kutes, Y. Zhou, J. L. Bosse, J. Steffes, N. P. Padture, B. D. Huey, *Nano Lett.* **2016**, *16*, 3434.
[92] G. E. Eperon, D. Moerman, D. S. Ginger, *ACS Nano* **2016**, *10*, 10258.
[93] Q. Xue, G. Chen, M. Liu, J. Xiao, Z. Chen, Z. Hu, X.-F. Jiang, B. Zhang, F. Huang, W. Yang, H.-L. Yip, Y. Cao, *Adv. Energy Mater.* **2016**, *6*, 1502021.
[94] Q. Lin, D. M. Stoltzfus, A. Armin, P. L. Burn, P. Meredith, *Adv. Mater. Interfaces* **2016**, *3*, 1500420.
[95] A. Giuri, S. Masi, S. Colella, A. Kovtun, S. Dell'Elce, E. Treossi, A. Liscio, C. Esposito Corcione, A. Rizzo, A. Listorti, *Adv. Funct. Mater.* **2016**, *26*, 6985.
[96] C. Momblona, L. Gil-Escrig, E. Bandiello, E. M. Hutter, M. Sessolo, K. Lederer, J. Blochwitz-Nimoth, H. J. Bolink, *Energy Environ. Sci.* **2016**, *9*, 3456.
[97] Z. Zhou, X. Li, M. Cai, F. Xie, Y. Wu, Z. Lan, X. Yang, Y. Qiang, A. Islam, L. Han, *Adv. Energy Mater.* **2017**, *7*, 1700763.
[98] Y. Bai, H. Chen, S. Xiao, Q. Xue, T. Zhang, Z. Zhu, Q. Li, C. Hu, Y. Yang, Z. Hu, F. Huang, K. S. Wong, H.-L. Yip, S. Yang, *Adv. Funct. Mater.* **2016**, *26*, 2950.
[99] Q. Wang, C.-C. Chueh, T. Zhao, J. Cheng, M. Eslamian, W. C. H. Choy, A. K.-Y. Jen, *ChemSusChem* **2017**, *10*, 3794.
[100] A. Mei, X. Li, L. Liu, Z. Ku, T. Liu, Y. Rong, M. Xu, M. Hu, J. Chen, Y. Yang, M. Grätzel, H. Han, *Science.* **2014**, *345*, 295.
[101] B. Li, Y. Chen, Z. Liang, D. Gao, W. Huang, *RSC Adv.* **2015**, *5*, 94290.

[102] L. Zuo, Z. Gu, T. Ye, W. Fu, G. Wu, H. Li, H. Chen, *J. Am. Chem. Soc.* **2015**, *137*, 2674.
[103] Y. Ogomi, A. Morita, S. Tsukamoto, T. Saitho, Q. Shen, T. Toyoda, K. Yoshino, S. S. Pandey, T. Ma, S. Hayase, *J. Phys. Chem. C* **2014**, *118*, 16651.
[104] J.-S. Yeo, R. Kang, S. Lee, Y.-J. Jeon, N. Myoung, C.-L. Lee, D.-Y. Kim, J.-M. Yun, Y.-H. Seo, S.-S. Kim, S.-I. Na, *Nano Energy* **2015**, *12*, 96.
[105] J. S. Yeo, C. H. Lee, D. Jang, S. Lee, S. M. Jo, H. I. Joh, D. Y. Kim, *Nano Energy* **2016**, *30*, 667.
[106] Z. K. Wang, X. Gong, M. Li, Y. Hu, J. M. Wang, H. Ma, L. S. Liao, *ACS Nano* **2016**, *10*, 5479.
[107] T. Geske, J. Li, M. Worden, X. Shan, M. Chen, S. G. R. Bade, Z. Yu, *Adv. Funct. Mater.* **2017**, *27*, 1702180.
[108] X. Liu, F. Lin, C.-C. Chueh, Q. Chen, T. Zhao, P.-W. Liang, Z. Zhu, Y. Sun, A. K.-Y. Jen, *Nano Energy* **2016**, *30*, 417.
[109] K. Wang, C. Liu, P. Du, J. Zheng, X. Gong, *Energy Environ. Sci.* **2015**, *8*, 1245.
[110] C. Liu, W. Li, H. Li, C. Zhang, J. Fan, Y. Mai, *Nanoscale* **2017**, *9*, 13967.
[111] M. Li, Y.-H. Chao, T. Kang, Z.-K. Wang, Y. Yang, S. Feng, Y. Hu, X. Gao, L.-S. Liao, C.-S. Hsu, *J. Mater. Chem. A* **2016**, *4*, 15088.
[112] Y. Wang, W.-Y. Rho, H.-Y. Yang, T. Mahmoudi, S. Seo, D.-H. Lee, Y.-B. Hahn, *Nano Energy* **2016**, *27*, 535.
[113] S. Ye, H. Rao, Z. Zhao, L. Zhang, H. Bao, W. Sun, Y. Li, F. Gu, J. Wang, Z. Liu, Z. Bian, C. Huang, *J. Am. Chem. Soc.* **2017**, *139*, 7504.
[114] M. Hadadian, J.-P. Correa-Baena, E. K. Goharshadi, A. Ummadisingu, J.-Y. Seo, J. Luo, S. Gholipour, S. M. Zakeeruddin, M. Saliba, A. Abate, M. Grätzel, A. Hagfeldt, *Adv. Mater.* **2016**, *28*, 8681.
[115] Y. Yang, M. Yang, D. T. Moore, Y. Yan, E. M. Miller, K. Zhu, M. C. Beard, *Nat. Energy* **2017**, *2*, 16207.
[116] B. Murali, E. Yengel, C. Yang, W. Peng, E. Alarousu, O. M. Bakr, O. F. Mohammed, *ACS Energy Lett.* **2017**, *2*, 846.
[117] R. J. Stewart, C. Grieco, A. V Larsen, J. J. Maier, J. B. Asbury, *J. Phys. Chem. Lett.* **2016**, *7*, 1148.
[118] Y. Lin, L. Shen, J. Dai, Y. Deng, Y. Wu, Y. Bai, X. Zheng, J. Wang, Y. Fang, H. Wei, W. Ma, X. C. Zeng, X. Zhan, J. Huang, *Adv. Mater.* **2017**, *29*, 1604545.
[119] X. Bao, J. Wang, Y. Li, D. Zhu, Y. Wu, P. Guo, X. Wang, Y. Zhang, J. Wang, H.-L. Yip, R. Yang, *Adv. Mater. Interfaces* **2017**, *4*, 1600948.
[120] C. Sun, Z. Wu, H. Yip, H. Zhang, X. Jiang, Q. Xue, Z. Hu, Z. Hu, Y. Shen, M. Wang, F. Huang, Y. Cao, *Adv. Energy Mater.* **2016**, *6*, 1501534.
[121] H. Chen, W. Fu, C. Huang, Z. Zhang, S. Li, F. Ding, M. Shi, C.-Z. Li, A. K.-Y. Jen, H. Chen, *Adv. Energy Mater.* **2017**, *7*, 1700012.
[122] N. K. Noel, A. Abate, S. D. Stranks, E. S. Parrott, V. M. Burlakov, A. Goriely, H. J. Snaith, *ACS Nano* **2014**, *8*, 9815.
[123] Y. Shao, Z. Xiao, C. Bi, Y. Yuan, J. Huang, *Nat. Commun.* **2014**, *5*, 5784.
[124] P.-W. Liang, C.-C. Chueh, S. T. Williams, A. K.-Y. Jen, *Adv. Energy Mater.* **2015**, *5*, 1402321.
[125] C. Cui, Y. Li, Y. Li, *Adv. Energy Mater.* **2017**, *7*, 1601251.
[126] Y. Fang, C. Bi, D. Wang, J. Huang, *ACS Energy Lett.* **2017**, *2*, 782.
[127] A. Buin, R. Comin, J. Xu, A. H. Ip, E. H. Sargent, *Chem. Mater.* **2015**, *27*, 4405.
[128] C.-H. Chiang, C.-G. Wu, *Nat. Photonics* **2016**, *10*, 196.
[129] J. Xu, A. Buin, A. H. Ip, W. Li, O. Voznyy, R. Comin, M. Yuan, S. Jeon, Z. Ning, J. J. McDowell, P. Kanjanaboos, J.-P. Sun, X. Lan, L. N. Quan, D. H. Kim, I. G. Hill, P. Maksymovych, E. H. Sargent, *Nat. Commun.* **2015**, *6*, 7081.
[130] Y. Zhao, W. Zhou, W. Ma, S. Meng, H. Li, J. Wei, R. Fu, K. Liu, D. Yu, Q. Zhao, *ACS Energy Lett.* **2016**, *1*, 266.
[131] Y. Wu, X. Yang, W. Chen, Y. Yue, M. Cai, F. Xie, E. Bi, A. Islam, L. Han, *Nat. Energy* **2016**, *1*, 16148.
[132] F. Zhang, W. Shi, J. Luo, N. Pellet, C. Yi, X. Li, X. Zhao, T. J. S. Dennis, X. Li, S. Wang, Y. Xiao, S. M. Zakeeruddin, D. Bi, M. Grätzel, *Adv. Mater.* **2017**, *29*, 1606806.
[133] T. T. Ngo, I. Suarez, G. Antonicelli, D. Cortizo-Lacalle, J. P. Martinez-Pastor, A. Mateo-Alonso, I. Mora-Sero, *Adv. Mater.* **2017**, *29*, 1604056.
[134] A. Marchioro, J. Teuscher, D. Friedrich, M. Kunst, R. van de Krol, T. Moehl, M. Grätzel, J.-E. Moser, *Nat. Photonics* **2014**, *8*, 250.
[135] L. M. Herz, *Annu. Rev. Phys. Chem.* **2016**, *67*, 65.
[136] M. B. Johnston, L. M. Herz, *Acc. Chem. Res.* **2016**, *49*, 146.
[137] C. S. Ponseca, Y. Tian, V. Sundström, I. G. Scheblykin, *Nanotechnology* **2016**, *27*, 082001.
[138] T. C. Sum, N. Mathews, G. Xing, S. S. Lim, W. K. Chong, D. Giovanni, H. A. Dewi, *Acc. Chem. Res.* **2016**, *49*, 294.

[139] J. Peng, Y. Chen, K. Zheng, T. Pullerits, Z. Liang, *Chem. Soc. Rev.* **2017**, *46*, 5714.
[140] A. Todinova, J. Idígoras, M. Salado, S. Kazim, J. a. Anta, *J. Phys. Chem. Lett.* **2015**, *6*, 3923.
[141] T. Handa, D. M. Tex, A. Shimazaki, A. Wakamiya, Y. Kanemitsu, *J. Phys. Chem. Lett.* **2017**, *8*, 954.
[142] R. Ihly, A.-M. Dowgiallo, M. Yang, P. Schulz, N. J. Stanton, O. G. Reid, A. J. Ferguson, K. Zhu, J. J. Berry, J. L. Blackburn, *Energy Environ. Sci.* **2016**, *9*, 1439.
[143] J. Leng, J. Liu, J. Zhang, S. Jin, *J. Phys. Chem. Lett.* **2016**, *7*, 5056.
[144] J. C. Brauer, Y. H. Lee, M. K. Nazeeruddin, N. Banerji, *J. Phys. Chem. Lett.* **2015**, *6*, 3675.
[145] E. M. Hutter, J.-J. Hofman, M. L. Petrus, M. Moes, R. D. Abellón, P. Docampo, T. J. Savenije, *Adv. Energy Mater.* **2017**, *7*, 1602349.
[146] M. Petrović, T. Ye, C. Vijila, S. Ramakrishna, *Adv. Energy Mater.* **2017**, *7*, 1602610.
[147] A. Corani, M. Li, P. Shen, P. Chen, T. Guo, A. El Nahhas, K. Zheng, A. Yartsev, V. Sundström, C. S. Ponseca, *J. Phys. Chem. Lett.* **2016**, *7*, 1096.
[148] W. Tian, R. Cui, J. Leng, J. Liu, Y. Li, C. Zhao, J. Zhang, W. Deng, T. Lian, S. Jin, *Angew. Chemie Int. Ed.* **2016**, *55*, 13067.
[149] W. Tress, N. Marinova, O. Inganäs, M. K. Nazeeruddin, S. M. Zakeeruddin, M. Graetzel, *Adv. Energy Mater.* **2015**, *5*, 1400812.
[150] T. S. Sherkar, C. Momblona, L. Gil-Escrig, H. J. Bolink, L. J. A. Koster, *Adv. Energy Mater.* **2017**, *7*, 1602432.
[151] A. Fakharuddin, L. Schmidt-Mende, G. Garcia-Belmonte, R. Jose, I. Mora-Sero, *Adv. Energy Mater.* **2017**, *7*, 1700623.
[152] Y. Hou, W. Chen, D. Baran, T. Stubhan, N. A. Luechinger, B. Hartmeier, M. Richter, J. Min, S. Chen, C. O. R. Quiroz, N. Li, H. Zhang, T. Heumueller, G. J. Matt, A. Osvet, K. Forberich, Z.-G. Zhang, Y. Li, B. Winter, P. Schweizer, E. Spiecker, C. J. Brabec, *Adv. Mater.* **2016**, *28*, 5112.
[153] S. Wheeler, D. Bryant, J. Troughton, T. Kirchartz, T. Watson, J. Nelson, J. R. Durrant, *J. Phys. Chem. C* **2017**, *121*, 13496.
[154] C. M. Wolff, F. Zu, A. Paulke, L. P. Toro, N. Koch, D. Neher, *Adv. Mater.* **2017**, *29*, 1700159.
[155] N. Ishida, A. Wakamiya, A. Saeki, *ACS Photonics* **2016**, *3*, 1678.
[156] Q. Wang, C.-C. Chueh, M. Eslamian, A. K.-Y. Jen, *ACS Appl. Mater. Interfaces* **2016**, *8*, 32068.
[157] J.-P. Correa-Baena, W. Tress, K. Domanski, E. H. Anaraki, S.-H. Turren-Cruz, B. Roose, P. P. Boix, M. Grätzel, M. Saliba, A. Abate, A. Hagfeldt, *Energy Environ. Sci.* **2017**, *10*, 1207.
[158] J. Peng, Y. Wu, W. Ye, D. A. Jacobs, H. Shen, X. Fu, Y. Wan, T. Duong, N. Wu, C. Barugkin, H. T. Nguyen, D. Zhong, J. Li, T. Lu, Y. Liu, M. N. Lockrey, K. J. Weber, K. R. Catchpole, T. P. White, *Energy Environ. Sci.* **2017**, *10*, 1792.
[159] M. Stolterfoht, C. M. Wolff, Y. Amir, A. Paulke, L. Perdigón-Toro, P. Caprioglio, D. Neher, *Energy Environ. Sci.* **2017**, *10*, 1530.
[160] H. Tan, A. Jain, O. Voznyy, X. Lan, F. P. García de Arquer, J. Z. Fan, R. Quintero-Bermudez, M. Yuan, B. Zhang, Y. Y. Zhao, F. Fan, P. Li, L. N. Quan, Y. Y. Zhao, Z.-H. Lu, Z. Yang, S. Hoogland, E. H. Sargent, *Science.* **2017**, *355*, 722.
[161] R. Gottesman, P. Lopez-Varo, L. Gouda, J. A. Jimenez-Tejada, J. Hu, S. Tirosh, A. Zaban, J. Bisquert, *Chem* **2016**, *1*, 776.
[162] T.-Y. Yang, G. Gregori, N. Pellet, M. Grätzel, J. Maier, *Angew. Chemie Int. Ed.* **2015**, *54*, 7905.
[163] C. Eames, J. M. Frost, P. R. F. Barnes, B. C. O'Regan, A. Walsh, M. S. Islam, *Nat. Commun.* **2015**, *6*, 7497.
[164] O. Almora, I. Zarazua, E. Mas-Marza, I. Mora-Sero, J. Bisquert, G. Garcia-Belmonte, *J. Phys. Chem. Lett.* **2015**, *6*, 1645.
[165] Z. Xiao, Y. Yuan, Y. Shao, Q. Wang, Q. Dong, C. Bi, P. Sharma, A. Gruverman, J. Huang, *Nat. Mater.* **2014**, *14*, 193.
[166] L. A. Frolova, N. N. Dremova, P. A. Troshin, *Chem. Commun.* **2015**, *51*, 14917.
[167] W. Tress, J. P. Correa Baena, M. Saliba, A. Abate, M. Graetzel, *Adv. Energy Mater.* **2016**, *6*, 1600396.
[168] W. Tress, N. Marinova, T. Moehl, S. M. Zakeeruddin, M. K. Nazeeruddin, M. Grätzel, *Energy Environ. Sci.* **2015**, *8*, 995.
[169] A. R. Bowring, L. Bertoluzzi, B. C. O'Regan, M. D. McGehee, *Adv. Energy Mater.* **2018**, *8*, 1702365.
[170] O. Almora, C. Aranda, I. Zarazua, A. Guerrero, G. Garcia-Belmonte, *ACS Energy Lett.* **2016**, *1*, 209.
[171] K. Domanski, B. Roose, T. Matsui, M. Saliba, S.-H. Turren-Cruz, J.-P. Correa-Baena, C. R. Carmona, G. Richardson, J. M. Foster, F. De Angelis, J. M. Ball, A. Petrozza, N. Mine, M. K. Nazeeruddin, W. Tress, M. Grätzel, U. Steiner, A. Hagfeldt, A. Abate, *Energy Environ. Sci.* **2017**, *10*, 604.
[172] N. H. Nickel, F. Lang, V. V. Brus, O. Shargaieva, J. Rappich, *Adv. Electron. Mater.* **2017**, *3*, 1700158.
[173] H.-S. Kim, I.-H. Jang, N. Ahn, M. Choi, A. Guerrero, J. Bisquert, N.-G. Park, *J. Phys. Chem. Lett.* **2015**, *6*,

4633.
[174] M. De Bastiani, G. Dell'Erba, M. Gandini, V. D'Innocenzo, S. Neutzner, A. R. S. Kandada, G. Grancini, M. Binda, M. Prato, J. M. Ball, M. Caironi, A. Petrozza, *Adv. Energy Mater.* **2016**, *6*, 1501453.
[175] C.-Z. Li, C.-C. Chueh, F. Ding, H.-L. Yip, P.-W. Liang, X. Li, A. K.-Y. Jen, *Adv. Mater.* **2013**, *25*, 4425.
[176] L. Deng, S. Xie, F. Gao, *Adv. Electron. Mater.* **2017**, 1700435.
[177] M. Ahmadi, Y.-C. Hsiao, T. Wu, Q. Liu, W. Qin, B. Hu, *Adv. Energy Mater.* **2017**, *7*, 1601575.
[178] Y. Hou, S. Scheiner, X. Tang, N. Gasparini, M. Richter, N. Li, P. Schweizer, S. Chen, H. Chen, C. O. R. Quiroz, X. Du, G. J. Matt, A. Osvet, E. Spiecker, R. H. Fink, A. Hirsch, M. Halik, C. J. Brabec, *Adv. Mater. Interfaces* **2017**, *4*, 1700007.
[179] I. Levine, P. K. Nayak, J. T.-W. Wang, N. Sakai, S. Van Reenen, T. M. Brenner, S. Mukhopadhyay, H. J. Snaith, G. Hodes, D. Cahen, *J. Phys. Chem. C* **2016**, *120*, 16399.
[180] S. Wang, Y. Jiang, E. J. Juarez-Perez, L. K. Ono, Y. Qi, *Nat. Energy* **2016**, *2*, 16195.
[181] A. Leguy, Y. Hu, M. Campoy-Quiles, M. I. Alonso, O. J. Weber, P. Azarhoosh, M. van Schilfgaarde, M. T. Weller, T. Bein, J. Nelson, P. Docampo, P. R. F. Barnes, *Chem. Mater.* **2015**, *27*, 3397.
[182] G. Niu, X. Guo, L. Wang, *J. Mater. Chem. A* **2015**, *3*, 8970.
[183] N. Ahn, K. Kwak, M. S. Jang, H. Yoon, B. Y. Lee, J.-K. Lee, P. V. Pikhitsa, J. Byun, M. Choi, *Nat. Commun.* **2016**, *7*, 13422.
[184] M. Bag, L. A. Renna, R. Y. Adhikari, S. Karak, F. Liu, P. M. Lahti, T. P. Russell, M. T. Tuominen, D. Venkataraman, *J. Am. Chem. Soc.* **2015**, *137*, 13130.
[185] Z. Zhu, V. G. Hadjiev, Y. Rong, R. Guo, B. Cao, Z. Tang, F. Qin, Y. Li, Y. Wang, F. Hao, S. Venkatesan, W. Li, S. Baldelli, A. M. Guloy, H. Fang, Y. Hu, Y. Yao, Z. Wang, J. Bao, *Chem. Mater.* **2016**, *28*, 7385.
[186] E. Tenuta, C. Zheng, O. Rubel, *Sci. Rep.* **2016**, *6*, 37654.
[187] J. M. Frost, K. T. Butler, F. Brivio, C. H. Hendon, M. van Schilfgaarde, A. Walsh, *Nano Lett.* **2014**, *14*, 2584.
[188] J. Yang, B. D. Siempelkamp, D. Liu, T. L. Kelly, *ACS Nano* **2015**, *9*, 1955.
[189] R. L. Milot, G. E. Eperon, H. J. Snaith, M. B. Johnston, L. M. Herz, *Adv. Funct. Mater.* **2015**, *25*, 6218.
[190] W. Deng, X. Liang, P. S. Kubiak, P. J. Cameron, *Adv. Energy Mater.* **2018**, *8*, 1701544.
[191] W. Nie, J.-C. Blancon, A. J. Neukirch, K. Appavoo, H. Tsai, M. Chhowalla, M. A. Alam, M. Y. Sfeir, C. Katan, J. Even, S. Tretiak, J. J. Crochet, G. Gupta, A. D. Mohite, *Nat. Commun.* **2016**, *7*, 11574.
[192] N. Aristidou, I. Sanchez-Molina, T. Chotchuangchutchaval, M. Brown, L. Martinez, T. Rath, S. A. Haque, *Angew. Chemie - Int. Ed.* **2015**, *54*, 8208.
[193] D. Bryant, N. Aristidou, S. Pont, I. Sanchez-Molina, T. Chotchunangatchaval, S. Wheeler, J. R. Durrant, S. A. Haque, *Energy Environ. Sci.* **2016**, *9*, 1655.
[194] A. J. Pearson, G. E. Eperon, P. E. Hopkinson, S. N. Habisreutinger, J. T.-W. Wang, H. J. Snaith, N. C. Greenham, *Adv. Energy Mater.* **2016**, *6*, 1600014.
[195] J. Carrillo, A. Guerrero, S. Rahimnejad, O. Almora, I. Zarazua, E. Mas-Marza, J. Bisquert, G. Garcia-Belmonte, *Adv. Energy Mater.* **2016**, *6*, 1502246.
[196] H. Back, G. Kim, J. Kim, J. Kong, T. K. Kim, H. Kang, H. Kim, J. Lee, S. Lee, K. Lee, *Energy Environ. Sci.* **2016**, *9*, 1258.
[197] L. Zhao, R. A. Kerner, Z. Xiao, Y. L. Lin, K. M. Lee, J. Schwartz, B. P. Rand, *ACS Energy Lett.* **2016**, *1*, 595.
[198] K. Domanski, J. P. Correa-Baena, N. Mine, M. K. Nazeeruddin, A. Abate, M. Saliba, W. Tress, A. Hagfeldt, M. Gr??tzel, *ACS Nano* **2016**, *10*, 6306.
[199] T. Leijtens, G. E. Eperon, S. Pathak, A. Abate, M. M. Lee, H. J. Snaith, *Nat. Commun.* **2013**, *4*, 2885.
[200] S. Ito, S. Tanaka, K. Manabe, H. Nishino, *J. Phys. Chem. C* **2014**, *118*, 16995.
[201] J. Yang, B. D. Siempelkamp, E. Mosconi, F. De Angelis, T. L. Kelly, *Chem. Mater.* **2015**, *27*, 4229.
[202] P. Zhang, J. Wu, T. Zhang, Y. Wang, D. Liu, H. Chen, L. Ji, C. Liu, W. Ahmad, Z. D. Chen, S. Li, *Adv. Mater.* **2018**, *30*, 1703737.
[203] Y. Dkhissi, S. Meyer, D. Chen, H. C. Weerasinghe, L. Spiccia, Y. B. Cheng, R. A. Caruso, *ChemSusChem* **2016**, *9*, 687.
[204] L. Yang, B. Xu, D. Bi, H. Tian, G. Boschloo, L. Sun, A. Hagfeldt, E. M. J. Johansson, *J. Am. Chem. Soc.* **2013**, *135*, 7378.
[205] Z. Hawash, L. K. Ono, S. R. Raga, M. V. Lee, Y. Qi, *Chem. Mater.* **2015**, *27*, 562.
[206] R. L. Z. Hoye, P. Schulz, L. T. Schelhas, A. M. Holder, K. H. Stone, J. D. Perkins, D. Vigil-Fowler, S. Siol, D. O. Scanlon, A. Zakutayev, A. Walsh, I. C. Smith, B. C. Melot, R. C. Kurchin, Y. Wang, J. Shi, F. C. Marques, J. J. Berry, W. Tumas, S. Lany, V. Stevanovi?, M. F. Toney, T. Buonassisi, *Chem. Mater.* **2017**, *29*, 1964.
[207] J. a. Christians, J. S. Manser, P. V Kamat, *J. Phys. Chem. Lett.* **2015**, *6*, 852.

[208] Y. Tian, I. G. Scheblykin, *J. Phys. Chem. Lett.* **2015**, *6*, 3466.
[209] Editorial, *Nat. Mater.* **2015**, *14*, 1073.
[210] F. Di Giacomo, A. Fakharuddin, R. Jose, T. M. Brown, *Energy Environ. Sci.* **2016**, *9*, 3007.
[211] Q. Tai, F. Yan, *Adv. Mater.* **2017**, *29*, 1700192.
[212] G. E. Eperon, M. T. Hörantner, H. J. Snaith, *Nat. Rev. Chem.* **2017**, *1*, 0095.
[213] Q. Tai, P. You, H. Sang, Z. Liu, C. Hu, H. L. W. Chan, F. Yan, *Nat. Commun.* **2016**, *7*, 11105.
[214] M. Yang, Z. Li, M. O. Reese, O. G. Reid, D. H. Kim, S. Siol, T. R. Klein, Y. Yan, J. J. Berry, M. F. A. M. van Hest, K. Zhu, *Nat. Energy* **2017**, *2*, 17038.
[215] G. Grancini, C. Roldán-Carmona, I. Zimmermann, E. Mosconi, X. Lee, D. Martineau, S. Narbey, F. Oswald, F. De Angelis, M. Graetzel, M. K. Nazeeruddin, *Nat. Commun.* **2017**, *8*, 15684.
[216] L. Lucera, F. Machui, P. Kubis, H. D. Schmidt, J. Adams, S. Strohm, T. Ahmad, K. Forberich, H.-J. Egelhaaf, C. J. Brabec, *Energy Environ. Sci.* **2016**, *9*, 89.
[217] H. Chen, F. Ye, W. Tang, J. He, M. Yin, Y. Wang, F. Xie, E. Bi, X. Yang, M. Grätzel, L. Han, *Nature* **2017**, *550*, 92.
[218] X. Zhang, X. Ren, B. Liu, R. Munir, X. Zhu, D. Yang, J. Li, Y. Liu, D.-M. Smilgies, R. Li, Z. Yang, T. Niu, X. Wang, A. Amassian, K. Zhao, S. F. Liu, *Energy Environ. Sci.* **2017**, *10*, 2095.
[219] T. Malinauskas, M. Saliba, T. Matsui, M. Daskeviciene, S. Urnikaite, P. Gratia, R. Send, H. Wonneberger, I. Bruder, M. Graetzel, V. Getautis, M. K. Nazeeruddin, *Energy Environ. Sci.* **2016**, *9*, 1681.
[220] N. L. Chang, A. W. Yi Ho-Baillie, P. A. Basore, T. L. Young, R. Evans, R. J. Egan, *Prog. Photovoltaics Res. Appl.* **2017**, *25*, 390.
[221] "Basic understanding of IEC standard testing for photovoltaic panels," can be found under http://www.tuv-sud.us/services/photovoltaics/ArticleBasicUnderstandingPV.pdf, **2010**.
[222] "IEC 61646:2008," can be found under https://webstore.iec.ch/publication/5697, **2008**.
[223] N. Rolston, A. D. Printz, J. M. Tracy, H. C. Weerasinghe, D. Vak, L. J. Haur, A. Priyadarshi, N. Mathews, D. J. Slotcavage, M. D. McGehee, R. E. Kalan, K. Zielinski, R. L. Grimm, H. Tsai, W. Nie, A. D. Mohite, S. Gholipour, M. Saliba, M. Grätzel, R. H. Dauskardt, *Adv. Energy Mater.* **2017**, 1702116.
[224] N. Rolston, B. L. Watson, C. D. Bailie, M. D. McGehee, J. P. Bastos, R. Gehlhaar, J.-E. Kim, D. Vak, A. T. Mallajosyula, G. Gupta, A. D. Mohite, R. H. Dauskardt, *Extrem. Mech. Lett.* **2016**, *9*, 353.
[225] B. L. Watson, N. J. Rolston, A. D. Printz, R. H. Dauskardt, *Energy Environ. Sci.* **2017**, *10*, 2500.
[226] K. A. Bush, A. F. Palmstrom, Z. (Jason) Yu, M. Boccard, R. Cheacharoen, J. P. Mailoa, D. P. McMeekin, R. L. Z. Hoye, C. D. Bailie, T. Leijtens, I. M. Peters, M. C. Minichetti, N. Rolston, R. Prasanna, S. Sofia, D. Harwood, W. Ma, F. Moghadam, H. J. Snaith, T. Buonassisi, Z. C. Holman, S. F. Bent, M. D. McGehee, *Nat. Energy* **2017**, *2*, 17009.
[227] R. Cheacharoen, N. Rolston, D. Harwood, K. A. Bush, R. H. Dauskardt, M. D. McGehee, *Energy Environ. Sci.* **2018**, *11*, 144.
[228] N. Rolston, A. D. Printz, F. Hilt, M. Q. Hovish, K. Brüning, C. J. Tassone, R. H. Dauskardt, *J. Mater. Chem. A* **2017**, *5*, 22975.
[229] M.-H. Park, J.-Y. Kim, T.-H. Han, T.-S. Kim, H. Kim, T.-W. Lee, *Adv. Mater.* **2015**, *27*, 4308.
[230] A. Babayigit, A. Ethirajan, M. Muller, B. Conings, *Nat. Mater.* **2016**, *15*, 247.
[231] B. Hailegnaw, S. Kirmayer, E. Edri, G. Hodes, D. Cahen, *J. Phys. Chem. Lett.* **2015**, *6*, 1543.
[232] A. Abate, *Joule* **2017**, *1*, 659.
[233] F. Giustino, H. J. Snaith, *ACS Energy Lett.* **2016**, *1*, 1233.
[234] F. P. Byrne, S. Jin, G. Paggiola, T. H. M. Petchey, J. H. Clark, T. J. Farmer, A. J. Hunt, C. Robert McElroy, J. Sherwood, *Sustain. Chem. Process.* **2016**, *4*, 7.
[235] S. J. Yoon, S. Draguta, J. S. Manser, O. Sharia, W. F. Schneider, M. Kuno, P. V. Kamat, *ACS Energy Lett.* **2016**, *1*, 290.
[236] K. Yan, M. Long, T. Zhang, Z. Wei, H. Chen, S. Yang, J. Xu, *J. Am. Chem. Soc.* **2015**, *137*, 4460.
[237] T. Bu, L. Wu, X. Liu, X. Yang, P. Zhou, X. Yu, T. Qin, J. Shi, S. Wang, S. Li, Z. Ku, Y. Peng, F. Huang, Q. Meng, Y.-B. Cheng, J. Zhong, *Adv. Energy Mater.* **2017**, *7*, 1700576.
[238] K. L. Gardner, J. G. Tait, T. Merckx, W. Qiu, U. W. Paetzold, L. Kootstra, M. Jaysankar, R. Gehlhaar, D. Cheyns, P. Heremans, J. Poortmans, *Adv. Energy Mater.* **2016**, *6*, 1600386.
[239] N. K. Noel, S. N. Habisreutinger, B. Wenger, M. T. Klug, M. T. Hörantner, M. B. Johnston, R. J. Nicholas, D. T. Moore, H. J. Snaith, *Energy Environ. Sci.* **2017**, *10*, 145.
[240] J. Stevenson, B. Sorenson, V. H. Subramaniam, J. Raiford, P. P. Khlyabich, Y. L. Loo, P. Clancy, *Chem. Mater.* **2017**, *29*, 2435.
[241] J. M. Kadro, N. Pellet, F. Giordano, A. Ulianov, O. Müntener, J. Maier, M. Grätzel, A. Hagfeldt, *Energy*

Environ. Sci. **2016**, *9*, 3172.
[242] C. G. Poll, G. W. Nelson, D. M. Pickup, A. V. Chadwick, D. J. Riley, D. J. Payne, *Green Chem.* **2016**, *18*, 2946.
[243] L. Serrano-Lujan, N. Espinosa, T. T. Larsen-Olsen, J. Abad, A. Urbina, F. C. Krebs, *Adv. Energy Mater.* **2015**, *5*, 1501119.
[244] M. K. Nazeeruddin, H. Snaith, *MRS Bull.* **2015**, *40*, 641.
[245] A. Kojima, K. Teshima, Y. Shirai, T. Miyasaka, *JACS Commun.* **2009**, *131*, 6050.
[246] M. M. Lee, J. Teuscher, T. Miyasaka, T. N. Murakami, H. J. Snaith, *Science.* **2012**, *338*, 643.
[247] H.-S. Kim, C.-R. Lee, J.-H. Im, K.-B. Lee, T. Moehl, A. Marchioro, S.-J. Moon, R. Humphry-Baker, J.-H. Yum, J. E. Moser, M. Grätzel, N.-G. Park, *Sci. Rep.* **2012**, *2*, 591.
[248] H. J. Snaith, A. Abate, J. M. Ball, G. E. Eperon, T. Leijtens, N. K. Noel, S. D. Stranks, J. T.-W. Wang, K. Wojciechowski, W. Zhang, *J. Phys. Chem. Lett.* **2014**, *5*, 1511.
[249] M. Herman, M. Jankovec, M. Topič, *Int. J. Photoenergy* **2012**, *2012*, 1.
[250] E. L. Unger, E. T. Hoke, C. D. Bailie, W. H. Nguyen, A. R. Bowring, T. Heumüller, M. G. Christoforo, M. D. McGehee, *Energy Environ. Sci.* **2014**, *7*, 3690.
[251] Y. Zhang, M. Liu, G. E. Eperon, T. C. Leijtens, D. McMeekin, M. Saliba, W. Zhang, M. de Bastiani, A. Petrozza, L. M. Herz, M. B. Johnston, H. Lin, H. J. Snaith, *Mater. Horiz.* **2015**, *2*, 315.
[252] A. M. a. Leguy, J. M. Frost, A. P. McMahon, V. G. Sakai, W. Kochelmann, C. Law, X. Li, F. Foglia, A. Walsh, B. C. O'Regan, J. Nelson, J. T. Cabral, P. R. F. Barnes, *Nat. Commun.* **2015**, *6*, 7124.
[253] W. Nie, H. Tsai, R. Asadpour, J.-C. Blancon, A. J. Neukirch, G. Gupta, J. J. Crochet, M. Chhowalla, S. Tretiak, M. A. Alam, H.-L. Wang, A. D. Mohite, *Science.* **2015**, *347*, 522.
[254] W. S. Yang, J. H. Noh, N. J. Jeon, Y. C. Kim, S. Ryu, J. Seo, S. I. Seok, *Science.* **2015**, *348*, 1234.
[255] J. P. Correa Baena, L. Steier, W. Tress, M. Saliba, S. Neutzner, T. Matsui, F. Giordano, T. J. Jacobsson, A. R. Srimath Kandada, S. M. Zakeeruddin, A. Petrozza, A. Abate, M. K. Nazeeruddin, M. Grätzel, A. Hagfeldt, *Energy Environ. Sci.* **2015**, *8*, 2928.
[256] K. Wojciechowski, T. Leijtens, S. Siprova, C. Schlueter, M. T. Hörantner, J. T.-W. Wang, C.-Z. Li, A. K.-Y. Jen, T.-L. Lee, H. J. Snaith, *J. Phys. Chem. Lett.* **2015**, *6*, 2399.
[257] H. Zhang, C. Liang, Y. Zhao, M. Sun, H. Liu, J. Liang, D. Li, F. Zhang, Z. He, *Phys. Chem. Chem. Phys.* **2015**, *17*, 9613.
[258] J. Shi, X. Xu, D. Li, Q. Meng, *Small* **2015**, *11*, 2472.
[259] D. Bryant, S. Wheeler, B. C. O'Regan, T. Watson, P. R. F. Barnes, D. Worsley, J. Durrant, *J. Phys. Chem. Lett.* **2015**, *6*, 3190.
[260] L. K. Ono, S. R. Raga, S. Wang, Y. Kato, Y. Qi, *J. Mater. Chem. A* **2015**, *3*, 9074.
[261] H. Chen, N. Sakai, M. Ikegami, T. Miyasaka, *J. Phys. Chem. Lett.* **2015**, *6*, 164.
[262] K. H. Kim, C. Takahashi, Y. Abe, M. Kawamura, *Optik (Stuttg).* **2014**, *125*, 2899.
[263] S. Liu, R. Liu, Y. Chen, S. Ho, J. H. Kim, F. So, *Chem. Mater.* **2014**, *26*, 4528.
[264] J. H. Kim, P. Liang, S. T. Williams, N. Cho, C. Chueh, M. S. Glaz, D. S. Ginger, A. K.-Y. Jen, *Adv. Mater.* **2015**, *27*, 695.
[265] M.-H. Li, P.-S. Shen, K.-C. Wang, T.-F. Guo, P. Chen, *J. Mater. Chem. A* **2015**, *3*, 9011.
[266] S. F. Völker, S. Collavini, J. L. Delgado, *ChemSusChem* **2015**, *8*, 3012.
[267] C. Wang, Y. Chen, B. Zhang, S. Liu, Q. Chen, Y. Cao, S. Sun, *Dalt. Trans.* **2016**, *45*, 484.
[268] E. J. Yoo, M. Lyu, J.-H. Yun, C. J. Kang, Y. J. Choi, L. Wang, *Adv. Mater.* **2015**, *27*, 6170.
[269] G. Lin, Y. Lin, R. Cui, H. Huang, X. Guo, C. Li, J. Dong, X. Guo, B. Sun, *J. Mater. Chem. C* **2015**, *3*, 10793.
[270] J. C. Scott, L. D. Bozano, *Adv. Mater.* **2007**, *19*, 1452.
[271] F. Pan, S. Gao, C. Chen, C. Song, F. Zeng, *Mater. Sci. Eng. R* **2014**, *83*, 1.
[272] P. Heremans, G. H. Gelinck, R. Müller, K.-J. Baeg, D.-Y. Kim, Y.-Y. Noh, *Chem. Mater.* **2011**, *23*, 341.
[273] S. M. Sze, K. K. Ng, *Physics of Semiconductor Devices*, John Wiley & Sons, New Jersey, **2006**.
[274] L. Solymar, D. Walsh, *Electrical Properties of Materials*, Oxford University Press, Oxford, **2010**.
[275] B. Chen, M. Yang, X. Zheng, C. Wu, W. Li, Y. Yan, J. Bisquert, G. Garcia-Belmonte, K. Zhu, S. Priya, *J. Phys. Chem. Lett.* **2015**, *6*, 4693.
[276] B. C. O'Regan, P. R. F. Barnes, X. Li, C. Law, E. Palomares, J. M. Marin-Beloqui, *J. Am. Chem. Soc.* **2015**, *137*, 5087.
[277] S. S. Hegedus, W. N. Shafarman, *Prog. Photovoltaics Res. Appl.* **2004**, *12*, 155.
[278] C. Zhao, B. Chen, X. Qiao, L. Luan, K. Lu, B. Hu, *Adv. Energy Mater.* **2015**, *5*, 1500279.
[279] L. Esaki, *Phys. Rev.* **1958**, *109*, 603.
[280] T. Leijtens, E. T. Hoke, G. Grancini, D. J. Slotcavage, G. E. Eperon, J. M. Ball, M. De Bastiani, A. R. Bowring,

N. Martino, K. Wojciechowski, M. D. McGehee, H. J. Snaith, A. Petrozza, *Adv. Energy Mater.* **2015**, *5*, 1500962.
[281] Y. Deng, Z. Xiao, J. Huang, *Adv. Energy Mater.* **2015**, *5*, 1500721.
[282] W. Guter, A. W. Bett, *IEEE Trans. Electron Devices* **2006**, *53*, 2216.
[283] M. Hermle, G. Létay, S. P. Philipps, A. W. Bett, *Prog. Photovoltaics Res. Appl.* **2008**, *16*, 409.
[284] J. M. Gordon, E. a. Katz, W. Tassew, D. Feuermann, *Appl. Phys. Lett.* **2005**, *86*, 073508.
[285] T. Moehl, J. H. Im, Y. H. Lee, K. Domanski, F. Giordano, S. M. Zakeeruddin, M. I. Dar, L. Heiniger, M. K. Nazeeruddin, N. Park, M. Grätzel, *J. Phys. Chem. Lett.* **2014**, *5*, 3931.
[286] K. Domanski, W. Tress, T. Moehl, M. Saliba, M. K. Nazeeruddin, M. Grätzel, *Adv. Funct. Mater.* **2015**, *25*, 6936.
[287] Y. Xia, K. Sun, J. Chang, J. Ouyang, *J. Mater. Chem. A* **2015**, *3*, 15897.
[288] V. Roiati, E. Mosconi, A. Listorti, S. Colella, G. Gigli, F. De Angelis, *Nano Lett.* **2014**, *14*, 2168.
[289] H. Back, J. Kim, G. Kim, T. Kyun Kim, H. Kang, J. Kong, S. Ho Lee, K. Lee, *Sol. Energy Mater. Sol. Cells* **2016**, *144*, 309.
[290] O. Almora, A. Guerrero, G. Garcia-Belmonte, *Appl. Phys. Lett.* **2016**, *108*, 043903.
[291] L. Li, F. Wang, X. Wu, H. Yu, S. Zhou, N. Zhao, *J. Phys. Chem. C* **2016**, *120*, 2536.
[292] I. Zarazua, J. Bisquert, G. Garcia-Belmonte, *J. Phys. Chem. Lett.* **2016**, *7*, 525.
[293] J. R. Manders, S.-W. Tsang, M. J. Hartel, T.-H. Lai, S. Chen, C. M. Amb, J. R. Reynolds, F. So, *Adv. Funct. Mater.* **2013**, *23*, 2993.
[294] Q. Wang, Y. Shao, H. Xie, L. Lyu, X. Liu, Y. Gao, J. Huang, *Appl. Phys. Lett.* **2014**, *105*, 163508.
[295] A. Kojima, K. Teshima, Y. Shirai, T. Miyasaka, *J. Am. Chem. Soc.* **2009**, *131*, 6050.
[296] N. J. Jeon, J. H. Noh, W. S. Yang, Y. C. Kim, S. Ryu, J. Seo, S. Il Seok, *Nature* **2015**, *517*, 476.
[297] E. L. Unger, E. T. Hoke, C. D. Bailie, W. H. Nguyen, A. R. Bowring, T. Heumuller, M. G. Christoforo, M. D. McGehee, *Energy Environ. Sci.* **2014**, *7*, 3690.
[298] D. S. Albin, J. A. del Cueto, in *SPIE Sol. Energy + Technol. Int. Soc. Opt. Photonics* (Eds.: N.G. Dhere, J.H. Wohlgemuth, K. Lynn), **2010**, p. 77730N–77730N.
[299] H. J. Snaith, A. Abate, J. M. Ball, G. E. W. Eperon, T. Leijtens, N. K. Noel, S. D. Stranks, J. T. T.-W. W. Wang, K. Wojciechowski, W. Zhang, T. Leigtens, *J. Phys. Chem. Lett.* **2014**, *5*, 1511.
[300] K. Wojciechowski, S. D. Stranks, A. Abate, G. Sadoughi, A. Sadhanala, N. Kopidakis, G. Rumbles, C. Li, R. H. Friend, A. K.-Y. Jen, H. J. Snaith, *ACS Nano* **2014**, *8*, 12701.
[301] S. van Reenen, M. Kemerink, H. J. Snaith, *J. Phys. Chem. Lett.* **2015**, *6*, 3808.
[302] J. Wei, Y. Zhao, H. Li, G. Li, J. Pan, D. Xu, Q. Zhao, D. Yu, *J. Phys. Chem. Lett.* **2014**, *5*, 3937.
[303] H. Chen, N. Sakai, M. Ikegami, T. Miyasaka, *J. Phys. Chem. Lett.* **2015**, *6*, 164.
[304] E. J. Juarez-Perez, R. S. Sanchez, L. Badia, G. Garcia-Belmonte, Y. S. Kang, I. Mora-Sero, J. Bisquert, *J. Phys. Chem. Lett.* **2014**, *5*, 2390.
[305] R. S. Sanchez, V. Gonzalez-Pedro, J.-W. W. Lee, N.-G. G. Park, Y. S. Kang, I. Mora-Sero, J. Bisquert, *J. Phys. Chem. Lett.* **2014**, *5*, 2357.
[306] K. G. Stamplecoskie, J. S. Manser, P. V Kamat, *Energy Environ. Sci.* **2015**, *8*, 208.
[307] R. Gottesman, L. Gouda, B. S. Kalanoor, E. Haltzi, S. Tirosh, E. Rosh-Hodesh, Y. Tischler, A. Zaban, C. Quarti, E. Mosconi, F. De Angelis, *J. Phys. Chem. Lett.* **2015**, 2332.
[308] J. M. Azpiroz, E. Mosconi, J. Bisquert, F. De Angelis, *Energy Environ. Sci.* **2015**, *8*, 2118.
[309] J. Haruyama, K. Sodeyama, L. Han, Y. Tateyama, *J. Am. Chem. Soc.* **2015**, *137*, 10048.
[310] P.-W. Liang, C.-C. Chueh, X.-K. Xin, F. Zuo, S. T. Williams, C.-Y. Liao, A. K.-Y. Jen, *Adv. Energy Mater.* **2015**, *5*, 1400960.
[311] Z. Yang, C.-C. Chueh, P.-W. Liang, M. Crump, F. Lin, Z. Zhu, A. K.-Y. Jen, *Nano Energy* **2016**, *22*, 328.
[312] F. Zuo, S. T. Williams, P.-W. Liang, C.-C. Chueh, C.-Y. Liao, A. K.-Y. Jen, *Adv. Mater.* **2014**, *26*, 6454.
[313] Q. Wang, Y. Shao, Q. Dong, Z. Xiao, Y. Yuan, J. Huang, *Energy Environ. Sci.* **2014**, *7*, 2359.
[314] S. T. Williams, F. Zuo, C.-C. Chueh, C.-Y. Liao, P.-W. Liang, A. K.-Y. K.-Y. Jen, *ACS Nano* **2014**, *8*, 10640.
[315] C.-Z. Li, C.-C. Chueh, H.-L. Yip, K. M. O'Malley, W.-C. Chen, A. K.-Y. Jen, *J. Mater. Chem.* **2012**, *22*, 8574.
[316] L. Gouda, R. Gottesman, A. Ginsburg, D. A. Keller, E. Haltzi, J. Hu, S. Tirosh, A. Y. Anderson, A. Zaban, P. P. Boix, *J. Phys. Chem. Lett.* **2015**, *6*, 4640.
[317] J. Nelson, *The Physics of Solar Cells*, Imperial College Press, **2003**.
[318] V. D. Mihailetchi, J. Wildeman, P. W. M. Blom, *Phys. Rev. Lett.* **2005**, *94*, 126602.
[319] L. J. A. Koster, V. D. Mihailetchi, R. Ramaker, P. W. M. Blom, *Appl. Phys. Lett.* **2005**, *86*, 123509.
[320] L. J. A. Koster, V. D. Mihailetchi, H. Xie, P. W. M. Blom, *Appl. Phys. Lett.* **2005**, *87*, 203502.

[321] S. R. Cowan, A. Roy, A. J. Heeger, *Phys. Rev. B* **2010**, *82*, 245207.
[322] T. Kirchartz, F. Deledalle, P. S. Tuladhar, J. R. Durrant, J. Nelson, *J. Phys. Chem. Lett.* **2013**, *4*, 2371.
[323] A. Pockett, G. E. Eperon, T. Peltola, H. J. Snaith, A. Walker, L. M. Peter, P. J. Cameron, *J. Phys. Chem. C* **2015**, *119*, 3456.
[324] G.-J. A. H. Wetzelaer, M. Scheepers, A. M. Sempere, C. Momblona, J. Ávila, H. J. Bolink, *Adv. Mater.* **2015**, *27*, 1837.
[325] B. Qi, Z.-G. Zhang, J. Wang, *Sci. Rep.* **2015**, *5*, 7803.
[326] X. Xu, Z. Liu, Z. Zuo, M. Zhang, Z. Zhao, Y. Shen, H. Zhou, Q. Chen, Y. Yang, M. Wang, *Nano Lett.* **2015**, *15*, 2402.
[327] I. Mora-Seró, G. Garcia-Belmonte, P. P. Boix, M. a. Vázquez, J. Bisquert, *Energy Environ. Sci.* **2009**, *2*, 678.
[328] J.-W. Lee, D.-H. Kim, H.-S. Kim, S.-W. Seo, S. M. Cho, N.-G. Park, *Adv. Energy Mater.* **2015**, *5*, 1501310.
[329] Y. Shao, Y. Yuan, J. Huang, *Nat. Energy* **2016**, *1*, 15001.
[330] H.-S. Kim, I. Mora-Sero, V. Gonzalez-Pedro, F. Fabregat-Santiago, E. J. Juarez-Perez, N.-G. Park, J. Bisquert, *Nat. Commun.* **2013**, *4*, 2242.
[331] S. T. Williams, C. Chueh, A. K.-Y. Jen, *Small* **2015**, *11*, 3088.
[332] L. I. Katzin, *J. Inorg. Nucl. Chem.* **1957**, *4*, 187.
[333] N. J. Jeon, J. H. Noh, Y. C. Kim, W. S. Yang, S. Ryu, S. Il Seok, *Nat. Mater.* **2014**, *13*, 897.
[334] S. Ito, S. Tanaka, H. Nishino, *J. Phys. Chem. Lett.* **2015**, *6*, 881.
[335] Y. Guo, K. Shoyama, W. Sato, Y. Matsuo, K. Inoue, K. Harano, C. Liu, H. Tanaka, E. Nakamura, *J. Am. Chem. Soc.* **2015**, *137*, 15907.
[336] Y. Zhou, M. Yang, W. Wu, A. L. Vasiliev, K. Zhu, N. P. Padture, *J. Mater. Chem. A* **2015**, *3*, 8178.
[337] Z. Song, S. C. Watthage, A. B. Phillips, B. L. Tompkins, R. J. Ellingson, M. J. Heben, *Chem. Mater.* **2015**, *27*, 4612.
[338] X. Ke, J. Yan, A. Zhang, B. Zhang, Y. Chen, *Appl. Phys. Lett.* **2015**, *107*, 091904.
[339] Q. Lin, A. Armin, R. C. R. Nagiri, P. L. Burn, P. Meredith, *Nat. Photonics* **2014**, *9*, 106.
[340] G. Catalan, A. Lubk, a H. G. Vlooswijk, E. Snoeck, C. Magen, A. Janssens, G. Rispens, G. Rijnders, D. H. a Blank, B. Noheda, *Nat. Mater.* **2011**, *10*, 963.
[341] X. R. Huang, S. S. Jiang, X. B. Hu, W. J. Liu, *J. Phys. Condens. Matter* **1997**, *9*, 4467.
[342] M. U. Rothmann, W. Li, Y. Zhu, U. Bach, L. Spiccia, J. Etheridge, Y.-B. Cheng, *Nat. Commun.* **2017**, *8*, 14547.
[343] T. Zhao, S. T. Williams, C.-C. Chueh, D. W. DeQuilettes, P.-W. Liang, D. S. Ginger, A. K.-Y. Jen, *RSC Adv.* **2016**, *6*, 27475.
[344] W. J. Mir, M. Jagadeeswararao, S. Das, A. Nag, *ACS Energy Lett.* **2017**, *2*, 537.
[345] H. Liu, Z. Wu, J. Shao, D. Yao, H. Gao, Y. Liu, W. Yu, H. Zhang, B. Yang, *ACS Nano* **2017**, *11*, 2239.
[346] A. Dualeh, T. Moehl, N. Tétreault, J. Teuscher, P. Gao, M. K. Nazeeruddin, M. Grätzel, *ACS Nano* **2014**, *8*, 362.
[347] B. Suarez, V. Gonzalez-Pedro, T. S. Ripolles, R. S. Sanchez, L. Otero, I. Mora-sero, *J. Phys. Chem. Lett.* **2014**, *5*, 1628.
[348] M. T. Klug, A. Osherov, A. A. Haghighirad, S. D. Stranks, P. R. Brown, S. Bai, J. T.-W. Wang, X. Dang, V. Bulović, H. J. Snaith, A. M. Belcher, *Energy Environ. Sci.* **2017**, *10*, 236.
[349] Y. Yamada, T. Nakamura, M. Endo, A. Wakamiya, Y. Kanemitsu, *J. Am. Chem. Soc.* **2014**, *136*, 11610.
[350] L. Ma, F. Hao, C. C. Stoumpos, B. T. Phelan, M. R. Wasielewski, M. G. Kanatzidis, *J. Am. Chem. Soc.* **2016**, *138*, 14750.
[351] B. Náfrádi, P. Szirmai, M. Spina, H. Lee, O. V Yazyev, A. Arakcheeva, D. Chernyshov, M. Gibert, L. Forró, E. Horváth, *Nat. Commun.* **2016**, *7*, 13406.
[352] H. Yu, H. Lu, F. Xie, S. Zhou, N. Zhao, *Adv. Funct. Mater.* **2016**, *26*, 1411.
[353] Nrel.gov, "National Renewable Energy Laboratory," can be found under https://www.nrel.gov/pv/assets/images/efficiency-chart.png, **2019**.
[354] W. Shockley, H. J. Queisser, *J. Appl. Phys.* **1961**, *32*, 510.
[355] D. P. McMeekin, G. Sadoughi, W. Rehman, G. E. Eperon, M. Saliba, M. T. Horantner, A. Haghighirad, N. Sakai, L. Korte, B. Rech, M. B. Johnston, L. M. Herz, H. J. Snaith, *Science.* **2016**, *351*, 151.
[356] A. Kojima, K. Teshima, Y. Shirai, T. Miyasaka, *J. Am. Chem. Soc.* **2009**, *131*, 6050.
[357] S. D. Stranks, G. E. Eperon, G. Grancini, C. Menelaou, M. J. P. Alcocer, T. Leijtens, L. M. Herz, A. Petrozza, H. J. Snaith, *Science.* **2013**, *342*, 341.
[358] H. Zhou, Q. Chen, G. Li, S. Luo, T. -b. Song, H.-S. Duan, Z. Hong, J. You, Y. Liu, Y. Yang, *Science.* **2014**, *345*, 542.

[359] Q. Dong, Y. Fang, Y. Shao, P. Mulligan, J. Qiu, L. Cao, J. Huang, *Science.* **2015**, *347*, 967.
[360] T. Jesper Jacobsson, J.-P. Correa-Baena, M. Pazoki, M. Saliba, K. Schenk, M. Grätzel, A. Hagfeldt, *Energy Environ. Sci.* **2016**, *9*, 1706.
[361] D. Bi, W. Tress, M. I. Dar, P. Gao, J. Luo, C. Renevier, K. Schenk, A. Abate, F. Giordano, J.-P. Correa Baena, J.-D. Decoppet, S. M. Zakeeruddin, M. K. Nazeeruddin, M. Gra tzel, A. Hagfeldt, *Sci. Adv.* **2016**, *2*, e1501170.
[362] J. H. Noh, S. H. Im, J. H. Heo, T. N. Mandal, S. Il Seok, *Nano Lett.* **2013**, *13*, 1764.
[363] G. E. Eperon, S. D. Stranks, C. Menelaou, M. B. Johnston, L. M. Herz, H. J. Snaith, *Energy Environ. Sci.* **2014**, *7*, 982.
[364] F. Hao, C. C. Stoumpos, R. P. H. Chang, M. G. Kanatzidis, *J. Am. Chem. Soc.* **2014**, *136*, 8094.
[365] Y. Ogomi, A. Morita, S. Tsukamoto, T. Saitho, N. Fujikawa, Q. Shen, T. Toyoda, K. Yoshino, S. S. Pandey, T. Ma, S. Hayase, *J. Phys. Chem. Lett.* **2014**, *5*, 1004.
[366] Y. Zhao, K. Zhu, *J. Am. Chem. Soc.* **2014**, *136*, 12241.
[367] C. Bi, Y. Yuan, Y. Fang, J. Huang, *Adv. Energy Mater.* **2015**, *5*, 1401616.
[368] E. T. Hoke, D. J. Slotcavage, E. R. Dohner, A. R. Bowring, H. I. Karunadasa, M. D. McGehee, *Chem. Sci.* **2015**, *6*, 613.
[369] I. L. Braly, H. W. Hillhouse, *J. Phys. Chem. C* **2016**, *120*, 893.
[370] M. Hu, C. Bi, Y. Yuan, Y. Bai, J. Huang, *Adv. Sci.* **2016**, *3*, 1500301.
[371] C. Yi, J. Luo, S. Meloni, A. Boziki, N. Ashari-Astani, C. Grätzel, S. M. Zakeeruddin, U. Röthlisberger, M. Grätzel, *Energy Environ. Sci.* **2016**, *9*, 656.
[372] F. Brivio, C. Caetano, A. Walsh, *J. Phys. Chem. Lett.* **2016**, *7*, 1083.
[373] Y. Zhou, L. You, S. Wang, Z. Ku, H. Fan, D. Schmidt, A. Rusydi, L. Chang, L. Wang, P. Ren, L. Chen, G. Yuan, L. Chen, J. Wang, *Nat. Commun.* **2016**, *7*, 11193.
[374] F. Hao, C. C. Stoumpos, P. Guo, N. Zhou, T. J. Marks, R. P. H. Chang, M. G. Kanatzidis, *J. Am. Chem. Soc.* **2015**, *137*, 11445.
[375] M. B. Price, J. Butkus, T. C. Jellicoe, A. Sadhanala, A. Briane, J. E. Halpert, K. Broch, J. M. Hodgkiss, R. H. Friend, F. Deschler, *Nat. Commun.* **2015**, *6*, 8420.
[376] J. S. Manser, P. V Kamat, *Nat. Photonics* **2014**, *8*, 737.
[377] G. Xing, N. Mathews, S. Sun, S. S. Lim, Y. M. Lam, M. Gratzel, S. Mhaisalkar, T. C. Sum, *Science.* **2013**, *342*, 344.
[378] G. . Williamson, W. . Hall, *Acta Metall.* **1953**, *1*, 22.
[379] J. Yao, T. Kirchartz, M. S. Vezie, M. A. Faist, W. Gong, Z. He, H. Wu, J. Troughton, T. Watson, D. Bryant, J. Nelson, *Phys. Rev. Appl.* **2015**, *4*, 014020.
[380] C. D. Bailie, M. D. McGehee, *MRS Bull.* **2015**, *40*, 681.
[381] J. H. Heo, S. H. Im, *Adv. Mater.* **2016**, *28*, 5121.
[382] F. Jiang, T. Liu, B. Luo, J. Tong, F. Qin, S. Xiong, Z. Li, Y. Zhou, *J. Mater. Chem. A* **2016**, *4*, 1208.
[383] D. Forg?cs, L. Gil-Escrig, D. P?rez-Del-Rey, C. Momblona, J. Werner, B. Niesen, C. Ballif, M. Sessolo, H. J. Bolink, *Adv. Energy Mater.* **2017**, *7*, 1602121.
[384] K. A. Bush, C. D. Bailie, Y. Chen, A. R. Bowring, W. Wang, W. Ma, T. Leijtens, F. Moghadam, M. D. McGehee, *Adv. Mater.* **2016**, *28*, 3937.
[385] W. Liao, D. Zhao, Y. Yu, N. Shrestha, K. Ghimire, C. R. Grice, C. Wang, Y. Xiao, A. J. Cimaroli, R. J. Ellingson, N. J. Podraza, K. Zhu, R.-G. Xiong, Y. Yan, *J. Am. Chem. Soc.* **2016**, *138*, 12360.
[386] B. Zhao, M. Abdi-Jalebi, M. Tabachnyk, H. Glass, V. S. Kamboj, W. Nie, A. J. Pearson, Y. Puttisong, K. C. Gödel, H. E. Beere, D. A. Ritchie, A. D. Mohite, S. E. Dutton, R. H. Friend, A. Sadhanala, *Adv. Mater.* **2017**, *29*, 1604744.
[387] G. E. Eperon, T. Leijtens, K. A. Bush, R. Prasanna, T. Green, J. T.-W. Wang, D. P. McMeekin, G. Volonakis, R. L. Milot, R. May, A. Palmstrom, D. J. Slotcavage, R. A. Belisle, J. B. Patel, E. S. Parrott, R. J. Sutton, W. Ma, F. Moghadam, B. Conings, A. Babayigit, H. Boyen, S. Bent, F. Giustino, L. M. Herz, M. B. Johnston, M. D. McGehee, H. J. Snaith, *Science.* **2016**, *354*, 861.
[388] L. Schmidt-Mende, J. Weickert, *Organic and Hybrid Solar Cells: An Introduction*, Walter De Gruyter GmbH, Berlin, Germany, **2016**.
[389] B. Johs, J. S. Hale, *Phys. Status Solidi Appl. Mater. Sci.* **2008**, *205*, 715.
[390] C. C. Katsidis, D. I. Siapkas, *Appl. Opt.* **2002**, *41*, 3978.
[391] M. Sugiyama, K. Fujii, S. Nakamura, *Solar to Chemical Energy Conversion: Theory and Application*, Springer International Publishing, Switzerland, **2016**.
[392] N.-T. Suen, S.-F. Hung, Q. Quan, N. Zhang, Y.-J. Xu, H. M. Chen, *Chem. Soc. Rev.* **2017**, *46*, 337.
[393] I. Roger, M. A. Shipman, M. D. Symes, *Nat. Rev. Chem.* **2017**, *1*, 0003.

[394] B. Zhang, B. Zhang, X. Zheng, O. Voznyy, R. Comin, M. Bajdich, M. García-melchor, L. Han, J. Xu, M. Liu, L. Zheng, F. P. G. De Arquer, C. T. Dinh, F. Fan, M. Yuan, E. Yassitepe, N. Chen, T. Regier, P. Liu, Y. Li, P. De Luna, H. L. Xin, H. Yang, A. Vojvodic, E. H. Sargent, *Science.* **2016**, *352*, 333.
[395] L. C. Seitz, C. F. Dickens, K. Nishio, Y. Hikita, J. Montoya, A. Doyle, C. Kirk, A. Vojvodic, H. Y. Hwang, J. K. Norskov, T. F. Jaramillo, *Science.* **2016**, *353*, 1011.
[396] J. Jia, L. C. Seitz, J. D. Benck, Y. Huo, Y. Chen, J. W. D. Ng, T. Bilir, J. S. Harris, T. F. Jaramillo, *Nat. Commun.* **2016**, *7*, 13237.
[397] J. Luo, J.-H. Im, M. T. Mayer, M. Schreier, M. K. Nazeeruddin, N.-G. Park, S. D. Tilley, H. J. Fan, M. Gratzel, *Science.* **2014**, *345*, 1593.
[398] N. K. Noel, S. D. Stranks, A. Abate, C. Wehrenfennig, S. Guarnera, A. Haghighirad, A. Sadhanala, G. E. Eperon, S. K. Pathak, M. B. Johnston, A. Petrozza, L. M. Herz, H. J. Snaith, *Energy Environ. Sci.* **2014**, *7*, 3061.
[399] J. Im, C. C. Stoumpos, H. Jin, A. J. Freeman, M. G. Kanatzidis, *J. Phys. Chem. Lett.* **2015**, *6*, 3503.
[400] Y. Li, W. Sun, W. Yan, S. Ye, H. Rao, H. Peng, Z. Zhao, Z. Bian, Z. Liu, H. Zhou, C. Huang, *Adv. Energy Mater.* **2016**, *6*, 1601353.
[401] D. Zhao, Y. Yu, C. Wang, W. Liao, N. Shrestha, C. R. Grice, A. J. Cimaroli, L. Guan, R. J. Ellingson, K. Zhu, X. Zhao, R.-G. Xiong, Y. Yan, *Nat. Energy* **2017**, *2*, 17018.
[402] D. W. Miller, G. E. Eperon, E. T. Roe, C. W. Warren, H. J. Snaith, M. C. Lonergan, *Appl. Phys. Lett.* **2016**, *109*, 153902.
[403] S. Chen, Y. Hou, H. Chen, M. Richter, F. Guo, S. Kahmann, X. Tang, T. Stubhan, H. Zhang, N. Li, N. Gasparini, C. O. R. Quiroz, L. S. Khanzada, G. J. Matt, A. Osvet, C. J. Brabec, *Adv. Energy Mater.* **2016**, *6*, 1600132.
[404] T. Leijtens, G. E. Eperon, A. J. Barker, G. Grancini, W. Zhang, J. M. Ball, A. R. S. Kandada, H. J. Snaith, A. Petrozza, *Energy Environ. Sci.* **2016**, *9*, 3472.
[405] E. S. Parrott, R. L. Milot, T. Stergiopoulos, H. J. Snaith, M. B. Johnston, L. M. Herz, *J. Phys. Chem. Lett.* **2016**, *7*, 1321.
[406] S. G. Motti, M. Gandini, A. J. Barker, J. M. Ball, A. R. Srimath Kandada, A. Petrozza, *ACS Energy Lett.* **2016**, *1*, 726.
[407] D. J. Slotcavage, H. I. Karunadasa, M. D. McGehee, *ACS Energy Lett.* **2016**, *1*, 1199.
[408] W. Rehman, D. P. McMeekin, J. B. Patel, R. L. Milot, M. B. Johnston, H. J. Snaith, L. M. Herz, *Energy Environ. Sci.* **2017**, *10*, 361.
[409] Y. Liu, L. A. Renna, M. Bag, Z. A. Page, P. Kim, J. Choi, T. Emrick, D. Venkataraman, T. P. Russell, *ACS Appl. Mater. Interfaces* **2016**, *8*, 7070.
[410] T. Todorov, T. Gershon, O. Gunawan, Y. S. Lee, C. Sturdevant, L.-Y. Chang, S. Guha, *Adv. Energy Mater.* **2015**, *5*, 1500799.
[411] S. Albrecht, M. Saliba, J. P. Correa Baena, F. Lang, L. Kegelmann, M. Mews, L. Steier, A. Abate, J. Rappich, L. Korte, R. Schlatmann, M. K. Nazeeruddin, A. Hagfeldt, M. Grätzel, B. Rech, *Energy Environ. Sci.* **2016**, *9*, 81.
[412] J. Werner, L. Barraud, A. Walter, M. Bräuninger, F. Sahli, D. Sacchetto, N. Tétreault, B. Paviet-Salomon, S.-J. Moon, C. Allebé, M. Despeisse, S. Nicolay, S. De Wolf, B. Niesen, C. Ballif, *ACS Energy Lett.* **2016**, *1*, 474.
[413] J. Werner, C.-H. Weng, A. Walter, L. Fesquet, J. P. Seif, S. De Wolf, B. Niesen, C. Ballif, *J. Phys. Chem. Lett.* **2016**, *7*, 161.
[414] I. Celik, A. B. Phillips, Z. Song, Y. Yan, R. J. Ellingson, M. J. Heben, D. Apul, *Energy Environ. Sci.* **2017**, *10*, 1874.
[415] W. S. Yang, B.-W. Park, E. H. Jung, N. J. Jeon, Y. C. Kim, D. U. Lee, S. S. Shin, J. Seo, E. K. Kim, J. H. Noh, S. Il Seok, *Science.* **2017**, *356*, 1376.
[416] M. Abdi-Jalebi, Z. Andaji-Garmaroudi, S. Cacovich, C. Stavrakas, B. Philippe, J. M. Richter, M. Alsari, E. P. Booker, E. M. Hutter, A. J. Pearson, S. Lilliu, T. J. Savenije, H. Rensmo, G. Divitini, C. Ducati, R. H. Friend, S. D. Stranks, *Nature* **2018**, *555*, 497.
[417] M. C. Brennan, S. Draguta, P. V. Kamat, M. Kuno, *ACS Energy Lett.* **2018**, *3*, 204.
[418] R. J. Stoddard, F. T. Eickemeyer, J. K. Katahara, H. W. Hillhouse, *J. Phys. Chem. Lett.* **2017**, *8*, 3289.
[419] S. Draguta, O. Sharia, S. J. Yoon, M. C. Brennan, Y. V. Morozov, J. S. Manser, P. V. Kamat, W. F. Schneider, M. Kuno, *Nat. Commun.* **2017**, *8*, 200.
[420] C. M. Sutter-Fella, D. W. Miller, Q. P. Ngo, E. T. Roe, F. M. Toma, I. D. Sharp, M. C. Lonergan, A. Javey, *ACS Energy Lett.* **2017**, *2*, 709.

[421] Y. Lin, B. Chen, F. Zhao, X. Zheng, Y. Deng, Y. Shao, Y. Fang, Y. Bai, C. Wang, J. Huang, *Adv. Mater.* **2017**, *29*, 1700607.
[422] T. Duong, Y. Wu, H. Shen, J. Peng, X. Fu, D. Jacobs, E.-C. Wang, T. C. Kho, K. C. Fong, M. Stocks, E. Franklin, A. Blakers, N. Zin, K. McIntosh, W. Li, Y.-B. Cheng, T. P. White, K. Weber, K. Catchpole, *Adv. Energy Mater.* **2017**, *7*, 1700228.
[423] Y. Yu, C. Wang, C. R. Grice, N. Shrestha, D. Zhao, W. Liao, L. Guan, R. A. Awni, W. Meng, A. J. Cimaroli, K. Zhu, R. J. Ellingson, Y. Yan, *ACS Energy Lett.* **2017**, *2*, 1177.
[424] J. Kim, M. I. Saidaminov, H. Tan, Y. Zhao, Y. Kim, J. Choi, J. W. Jo, J. Fan, R. Quintero-Bermudez, Z. Yang, L. N. Quan, M. Wei, O. Voznyy, E. H. Sargent, *Adv. Mater.* **2018**, *30*, 1706275.
[425] X. Zheng, B. Chen, J. Dai, Y. Fang, Y. Bai, Y. Lin, H. Wei, X. Zeng, J. Huang, *Nat. Energy* **2017**, *2*, 17102.
[426] Y. Zhou, F. Wang, Y. Cao, J.-P. Wang, H.-H. Fang, M. A. Loi, N. Zhao, C.-P. Wong, *Adv. Energy Mater.* **2017**, *7*, 1701048.
[427] Z. Wang, Q. Lin, F. P. Chmiel, N. Sakai, L. M. Herz, H. J. Snaith, *Nat. Energy* **2017**, *2*, 17135.
[428] Z. Xiao, L. Zhao, N. L. Tran, Y. L. Lin, S. H. Silver, R. A. Kerner, N. Yao, A. Kahn, G. D. Scholes, B. P. Rand, *Nano Lett.* **2017**, *17*, 6863.
[429] M. Saliba, T. Matsui, K. Domanski, J.-Y. Seo, A. Ummadisingu, S. M. Zakeeruddin, J.-P. Correa-Baena, W. R. Tress, A. Abate, A. Hagfeldt, M. Gratzel, *Science.* **2016**, *354*, 206.
[430] A. Swarnkar, A. R. Marshall, E. M. Sanehira, B. D. Chernomordik, D. T. Moore, J. A. Christians, T. Chakrabarti, J. M. Luther, *Science.* **2016**, *354*, 92.
[431] E. M. Sanehira, A. R. Marshall, J. A. Christians, S. P. Harvey, P. N. Ciesielski, L. M. Wheeler, P. Schulz, L. Y. Lin, M. C. Beard, J. M. Luther, *Sci. Adv.* **2017**, *3*, eaao4204.
[432] Q. Zeng, X. Zhang, X. Feng, S. Lu, Z. Chen, X. Yong, S. A. T. Redfern, H. Wei, H. Wang, H. Shen, W. Zhang, W. Zheng, H. Zhang, J. S. Tse, B. Yang, *Adv. Mater.* **2018**, *30*, 1705393.
[433] L. N. Quan, M. Yuan, R. Comin, O. Voznyy, E. M. Beauregard, S. Hoogland, A. Buin, A. R. Kirmani, K. Zhao, A. Amassian, D. H. Kim, E. H. Sargent, *J. Am. Chem. Soc.* **2016**, *138*, 2649.
[434] J. P. Cline, M. Leoni, D. Black, A. Henins, J. E. Bonevich, P. S. Whitfield, P. Scardi, *Powder Diffr.* **2013**, *28*, S22.
[435] A. J. Barker, A. Sadhanala, F. Deschler, M. Gandini, S. P. Senanayak, P. M. Pearce, E. Mosconi, A. J. Pearson, Y. Wu, A. R. Srimath Kandada, T. Leijtens, F. De Angelis, S. E. Dutton, A. Petrozza, R. H. Friend, *ACS Energy Lett.* **2017**, *2*, 1416.
[436] W. Peng, J. Yin, K. Ho, O. Ouellette, M. De Bastiani, B. Murali, O. El Tall, C. Shen, X. Miao, J. Pan, E. Alarousu, J. He, B. S. Ooi, O. F. Mohammed, E. Sargent, O. M. Bakr, *Nano Lett.* **2017**, *17*, 4759.
[437] D. S. Lee, J. S. Yun, J. Kim, A. M. Soufiani, S. Chen, Y. Cho, X. Deng, J. Seidel, S. Lim, S. Huang, A. W. Y. Ho-Baillie, *ACS Energy Lett.* **2018**, *3*, 647.
[438] Y. Bai, S. Xiao, C. Hu, T. Zhang, X. Meng, H. Lin, Y. Yang, S. Yang, *Adv. Energy Mater.* **2017**, *7*, 1701038.
[439] Y. Fu, T. Wu, J. Wang, J. Zhai, M. J. Shearer, Y. Zhao, R. J. Hamers, E. Kan, K. Deng, X. Y. Zhu, S. Jin, *Nano Lett.* **2017**, *17*, 4405.
[440] N. Li, Z. Zhu, C. Chueh, H. Liu, B. Peng, A. Petrone, X. Li, L. Wang, A. K.-Y. Jen, *Adv. Energy Mater.* **2017**, *7*, 1601307.
[441] M. Yuan, L. N. Quan, R. Comin, G. Walters, R. Sabatini, O. Voznyy, S. Hoogland, Y. Zhao, E. M. Beauregard, P. Kanjanaboos, Z. Lu, D. H. Kim, E. H. Sargent, *Nat. Nanotechnol.* **2016**, *11*, 872.
[442] R. L. Milot, R. J. Sutton, G. E. Eperon, A. A. Haghighirad, J. Martinez Hardigree, L. Miranda, H. J. Snaith, M. B. Johnston, L. M. Herz, *Nano Lett.* **2016**, *16*, 7001.
[443] B. Liu, C. M. M. Soe, C. C. Stoumpos, W. Nie, H. Tsai, K. Lim, A. D. Mohite, M. G. Kanatzidis, T. J. Marks, K. D. Singer, *Sol. RRL* **2017**, *1*, 1700062.
[444] B. Traore, L. Pedesseau, L. Assam, X. Che, J.-C. Blancon, H. Tsai, W. Nie, C. C. Stoumpos, M. G. Kanatzidis, S. Tretiak, A. D. Mohite, J. Even, M. Kepenekian, C. Katan, *ACS Nano* **2018**, *12*, 3321.
[445] I. C. Smith, E. T. Hoke, D. Solis-Ibarra, M. D. McGehee, H. I. Karunadasa, *Angew. Chemie* **2014**, *126*, 11414.
[446] Y. Hu, J. Schlipf, M. Wussler, M. L. Petrus, W. Jaegermann, T. Bein, P. Müller-Buschbaum, P. Docampo, *ACS Nano* **2016**, *10*, 5999.
[447] I. L. Braly, D. W. DeQuilettes, L. M. Pazos-Outón, S. Burke, M. E. Ziffer, D. S. Ginger, H. W. Hillhouse, *Nat. Photonics* **2018**, 1.
[448] R. T. Ross, *J. Chem. Phys.* **1967**, *46*, 4590.
[449] X. Tang, M. van den Berg, E. Gu, A. Horneber, G. J. Matt, A. Osvet, A. J. Meixner, D. Zhang, C. J. Brabec, *Nano Lett.* **2018**, *18*, 2172.
[450] S. Nah, B. Spokoyny, C. Stoumpos, C. M. M. Soe, M. Kanatzidis, E. Harel, *Nat. Photonics* **2017**, *11*, 285.

[451] O. G. Reid, M. Yang, N. Kopidakis, K. Zhu, G. Rumbles, *ACS Energy Lett.* **2016**, *1*, 561.
[452] K. A. Bush, K. Frohna, R. Prasanna, R. E. Beal, T. Leijtens, S. A. Swifter, M. D. McGehee, *ACS Energy Lett.* **2018**, *3*, 428.
[453] M. Jung, S.-G. Ji, G. Kim, S. Il Seok, *Chem. Soc. Rev.* **2019**, DOI 10.1039/C8CS00656C.
[454] Z. Li, T. R. Klein, D. H. Kim, M. Yang, J. J. Berry, M. F. A. M. van Hest, K. Zhu, *Nat. Rev. Mater.* **2018**, *3*, 18017.
[455] M. Chen, M.-G. Ju, M. Hu, Z. Dai, Y. Hu, Y. Rong, H. Han, X. C. Zeng, Y. Zhou, N. P. Padture, *ACS Energy Lett.* **2018**, *4*, 276.
[456] A. De Vos, *J. Phys. D. Appl. Phys.* **1980**, *13*, 839.
[457] Z. Xiao, Y. Zhou, H. Hosono, T. Kamiya, N. P. Padture, *Chem. - A Eur. J.* **2018**, *24*, 2305.
[458] E. S. Parrott, T. Green, R. L. Milot, M. B. Johnston, H. J. Snaith, L. M. Herz, *Adv. Funct. Mater.* **2018**, *28*, 1802803.
[459] J.-P. Correa-Baena, Y. Luo, T. M. Brenner, J. Snaider, S. Sun, X. Li, M. A. Jensen, N. T. P. Hartono, L. Nienhaus, S. Wieghold, J. R. Poindexter, S. Wang, Y. S. Meng, T. Wang, B. Lai, M. V Holt, Z. Cai, M. G. Bawendi, L. Huang, T. Buonassisi, D. P. Fenning, *Science.* **2019**, *363*, 627.
[460] O. J. Weber, B. Charles, M. T. Weller, *J. Mater. Chem. A* **2016**, *4*, 15375.
[461] A. Goyal, S. McKechnie, D. Pashov, W. Tumas, M. Van Schilfgaarde, V. Stevanović, *Chem. Mater.* **2018**, *30*, 3920.
[462] C. Li, Z. Song, D. Zhao, C. Xiao, B. Subedi, N. Shrestha, M. M. Junda, C. Wang, C.-S. Jiang, M. Al-Jassim, R. J. Ellingson, N. J. Podraza, K. Zhu, Y. Yan, *Adv. Energy Mater.* **2019**, *9*, 1803135.
[463] D. Zhao, C. Chen, C. Wang, M. M. Junda, Z. Song, C. R. Grice, Y. Yu, C. Li, B. Subedi, N. J. Podraza, X. Zhao, G. Fang, R. Xiong, K. Zhu, Y. Yan, *Nat. Energy* **2018**, *3*, 1093.
[464] T. Leijtens, R. Prasanna, K. A. Bush, G. E. Eperon, J. A. Raiford, A. Gold-Parker, E. J. Wolf, S. A. Swifter, C. C. Boyd, H.-P. Wang, M. F. Toney, S. F. Bent, M. D. McGehee, *Sustain. Energy Fuels* **2018**, *2*, 2450.
[465] S.-H. Turren-Cruz, A. Hagfeldt, M. Saliba, *Science.* **2018**, *362*, 449.
[466] H. Tan, F. Che, M. Wei, Y. Zhao, M. I. Saidaminov, P. Todorović, D. Broberg, G. Walters, F. Tan, T. Zhuang, B. Sun, Z. Liang, H. Yuan, E. Fron, J. Kim, Z. Yang, O. Voznyy, M. Asta, E. H. Sargent, *Nat. Commun.* **2018**, *9*, 3100.
[467] Y. Zhao, J. Zhang, *J. Appl. Crystallogr.* **2008**, *41*, 1095.
[468] J. T.-W. Wang, Z. Wang, S. Pathak, W. Zhang, D. W. DeQuilettes, F. Wisnivesky-Rocca-Rivarola, J. Huang, P. K. Nayak, J. B. Patel, H. A. Mohd Yusof, Y. Vaynzof, R. Zhu, I. Ramirez, J. Zhang, C. Ducati, C. Grovenor, M. B. Johnston, D. S. Ginger, R. J. Nicholas, H. J. Snaith, *Energy Environ. Sci.* **2016**, *9*, 2892.
[469] D. Kim, J. S. Yun, P. Sharma, D. S. Lee, J. Kim, A. M. Soufiani, S. Huang, M. A. Green, A. W. Y. Ho-Baillie, J. Seidel, *Nat. Commun.* **2019**, *10*, 444.
[470] J. K. Katahara, H. W. Hillhouse, *J. Appl. Phys.* **2014**, *173504*, DOI 10.1063/1.4898346.
[471] K. T. Butler, J. M. Frost, A. Walsh, *Mater. Horiz.* **2015**, *2*, 228.
[472] S. Lee, R. D. Levi, W. Qu, S. C. Lee, C. A. Randall, *J. Appl. Phys.* **2010**, *107*, 023523.
[473] C. S. Schnohr, *Appl. Phys. Rev.* **2015**, *2*, 031304.
[474] J.-W. Lee, D.-J. Seol, A.-N. Cho, N.-G. Park, *Adv. Mater.* **2014**, *26*, 4991.
[475] W. Ke, C. C. Stoumpos, J. L. Logsdon, M. R. Wasielewski, Y. Yan, G. Fang, M. G. Kanatzidis, *J. Am. Chem. Soc.* **2016**, *138*, 14998.
[476] J. Endres, D. A. Egger, M. Kulbak, R. A. Kerner, L. Zhao, S. H. Silver, G. Hodes, B. P. Rand, D. Cahen, L. Kronik, A. Kahn, *J. Phys. Chem. Lett.* **2016**, *7*, 2722.
[477] F. Hao, C. C. Stoumpos, D. H. Cao, R. P. H. Chang, M. G. Kanatzidis, *Nat. Photonics* **2014**, *8*, 489.
[478] B. Li, Y. Zhang, L. Zhang, L. Yin, *Adv. Mater.* **2017**, *29*, 1701221.
[479] N. Wang, Y. Zhou, M.-G. Ju, H. F. Garces, T. Ding, S. Pang, X. C. Zeng, N. P. Padture, X. W. Sun, *Adv. Energy Mater.* **2016**, *6*, 1601130.
[480] K. Korshunova, L. Winterfeld, W. J. D. Beenken, E. Runge, *Phys. status solidi* **2016**, *253*, 1907.
[481] D. H. Fabini, G. Laurita, J. S. Bechtel, C. C. Stoumpos, H. A. Evans, A. G. Kontos, Y. S. Raptis, P. Falaras, A. Van der Ven, M. G. Kanatzidis, R. Seshadri, *J. Am. Chem. Soc.* **2016**, *138*, 11820.
[482] N. W. Thomas, *Acta Crystallogr. Sect. B Struct. Sci.* **1996**, *52*, 954.
[483] C. Grote, R. F. Berger, *J. Phys. Chem. C* **2015**, *119*, 22832.
[484] Y. K. Jung, J. H. Lee, A. Walsh, A. Soon, *Chem. Mater.* **2017**, *29*, 3181.
[485] R. X. Yang, J. M. Skelton, E. L. Da Silva, J. M. Frost, A. Walsh, *J. Phys. Chem. Lett.* **2017**, *8*, 4720.
[486] J. S. Bechtel, A. Van der Ven, *Phys. Rev. Mater.* **2018**, *2*, 025401.
[487] D. Ghosh, A. R. Smith, A. B. Walker, M. S. Islam, *Chem. Mater.* **2018**, *30*, 5194.

[488] M. R. Filip, G. E. Eperon, H. J. Snaith, F. Giustino, *Nat. Commun.* **2014**, *5*, 5757.
[489] J.-H. Lee, N. C. Bristowe, J. H. Lee, S.-H. Lee, P. D. Bristowe, A. K. Cheetham, H. M. Jang, *Chem. Mater.* **2016**, *28*, 4259.
[490] T. Leijtens, R. Prasanna, A. Gold-Parker, M. F. Toney, M. D. McGehee, *ACS Energy Lett.* **2017**, *2*, 2159.
[491] I. Abrahams, D. Z. Demetriou, *J. Solid State Chem.* **2000**, *149*, 28.
[492] R. Prasanna, A. Gold-Parker, T. Leijtens, B. Conings, A. Babayigit, H.-G. Boyen, M. F. Toney, M. D. McGehee, *J. Am. Chem. Soc.* **2017**, *139*, 11117.
[493] R. J. D. Tilley, *Perovskites: Structure–Property Relationships*, John Wiley & Sons, Ltd, Chichester, UK, **2016**.
[494] A. Amat, E. Mosconi, E. Ronca, C. Quarti, P. Umari, M. K. Nazeeruddin, M. Grätzel, F. De Angelis, *Nano Lett.* **2014**, *14*, 3608.
[495] I. E. Castelli, J. M. García-Lastra, K. S. Thygesen, K. W. Jacobsen, *APL Mater.* **2014**, *2*, 081514.
[496] Z. Li, M. Yang, J.-S. Park, S.-H. Wei, J. J. Berry, K. Zhu, *Chem. Mater.* **2016**, *28*, 284.
[497] M. L. Lai, T. Y. S. Tay, A. Sadhanala, S. E. Dutton, G. Li, R. H. Friend, Z.-K. Tan, *J. Phys. Chem. Lett.* **2016**, *7*, 2653.
[498] L. Mao, H. Tsai, W. Nie, L. Ma, J. Im, C. C. Stoumpos, C. D. Malliakas, F. Hao, M. R. Wasielewski, A. D. Mohite, M. G. Kanatzidis, *Chem. Mater.* **2016**, *28*, 7781.
[499] I. Zimmermann, S. Aghazada, M. K. Nazeeruddin, *Angew. Chemie Int. Ed.* **2019**, *58*, 1072.
[500] D. Chi, S. Huang, M. Zhang, S. Mu, Y. Zhao, Y. Chen, J. You, *Adv. Funct. Mater.* **2018**, *28*, 1804603.
[501] Y. Zong, N. Wang, L. Zhang, M.-G. Ju, X. C. Zeng, X. W. Sun, Y. Zhou, N. P. Padture, *Angew. Chemie Int. Ed.* **2017**, *56*, 12658.
[502] E. M. Tennyson, B. Roose, J. L. Garrett, C. Gong, J. N. Munday, A. Abate, M. S. Leite, *ACS Nano* **2019**, acsnano.8b07295.
[503] L. Chen, Y.-Y. Tan, Z.-X. Chen, T. Wang, S. Hu, Z.-A. Nan, L.-Q. Xie, Y. Hui, J.-X. Huang, C. Zhan, S.-H. Wang, J.-Z. Zhou, J.-W. Yan, B.-W. Mao, Z. Tian, *J. Am. Chem. Soc.* **2019**, *141*, 1665.
[504] World Economic Forum's Meta-Council on Emerging Technologies, *Top 10 Emerging Technologies of 2016*, Switzerland, **2016**.
[505] Z. (Jason) Yu, M. Leilaeioun, Z. Holman, *Nat. Energy* **2016**, *1*, 16137.
[506] J. Werner, B. Niesen, C. Ballif, *Adv. Mater. Interfaces* **2018**, *5*, 1700731.
[507] J.-W. Lee, Y.-T. Hsieh, N. De Marco, S.-H. Bae, Q. Han, Y. Yang, *J. Phys. Chem. Lett.* **2017**, *8*, 1999.
[508] G. Li, W.-H. Chang, Y. Yang, *Nat. Rev. Mater.* **2017**, *2*, 17043.
[509] B. Chen, X. Zheng, Y. Bai, N. P. Padture, J. Huang, *Adv. Energy Mater.* **2017**, *7*, 1602400.
[510] N. N. Lal, Y. Dkhissi, W. Li, Q. Hou, Y.-B. Cheng, U. Bach, *Adv. Energy Mater.* **2017**, *7*, 1602761.
[511] J. Hu, Q. Cheng, R. Fan, H. Zhou, *Sol. RRL* **2017**, *1*, 1700045.
[512] J. W. Jung, C.-C. Chueh, A. K.-Y. Jen, *Adv. Energy Mater.* **2015**, *5*, 1500486.
[513] P. You, Z. Liu, Q. Tai, S. Liu, F. Yan, *Adv. Mater.* **2015**, *27*, 3632.
[514] F. Fu, T. Feurer, T. Jäger, E. Avancini, B. Bissig, S. Yoon, S. Buecheler, A. N. Tiwari, *Nat. Commun.* **2015**, *6*, 8932.
[515] F. Fu, T. Feurer, T. P. Weiss, S. Pisoni, E. Avancini, C. Andres, S. Buecheler, A. N. Tiwari, *Nat. Energy* **2016**, *2*, 16190.
[516] J. Zhao, K. O. Brinkmann, T. Hu, N. Pourdavoud, T. Becker, T. Gahlmann, R. Heiderhoff, A. Polywka, P. Görrn, Y. Chen, B. Cheng, T. Riedl, *Adv. Energy Mater.* **2017**, *7*, 1602599.
[517] B. Chen, Y. Bai, Z. Yu, T. Li, X. Zheng, Q. Dong, L. Shen, M. Boccard, A. Gruverman, Z. Holman, J. Huang, *Adv. Energy Mater.* **2016**, *6*, 1601128.
[518] Q. Xue, Y. Bai, M. Liu, R. Xia, Z. Hu, Z. Chen, X.-F. Jiang, F. Huang, S. Yang, Y. Matsuo, H.-L. Yip, Y. Cao, *Adv. Energy Mater.* **2017**, *7*, 1602333.
[519] C.-Y. Chang, K.-T. Lee, W.-K. Huang, H.-Y. Siao, Y.-C. Chang, *Chem. Mater.* **2015**, *27*, 5122.
[520] O. Ergen, S. M. Gilbert, T. Pham, S. J. Turner, M. T. Z. Tan, M. A. Worsley, A. Zettl, *Nat. Mater.* **2017**, *16*, 522.
[521] G. W. P. Adhyaksa, E. Johlin, E. C. Garnett, *Nano Lett.* **2017**, *17*, 5206.
[522] F. Sahli, B. A. Kamino, J. Werner, M. Bräuninger, B. Paviet-Salomon, L. Barraud, R. Monnard, J. P. Seif, A. Tomasi, Q. Jeangros, A. Hessler-Wyser, S. De Wolf, M. Despeisse, S. Nicolay, B. Niesen, C. Ballif, *Adv. Energy Mater.* **2018**, *8*, 1701609.
[523] Y. H. Jang, J. M. Lee, J. W. Seo, I. Kim, D.-K. Lee, *J. Mater. Chem. A* **2017**, *5*, 19439.
[524] Y. Zhou, Y.-H. Jia, H.-H. Fang, M. A. Loi, F.-Y. Xie, L. Gong, M.-C. Qin, X.-H. Lu, C.-P. Wong, N. Zhao, *Adv. Funct. Mater.* **2018**, *28*, 1803130.

[525] T. Duong, H. K. Mulmudi, Y. Wu, X. Fu, H. Shen, J. Peng, N. Wu, H. T. Nguyen, D. Macdonald, M. Lockrey, T. P. White, K. Weber, K. Catchpole, *ACS Appl. Mater. Interfaces* **2017**, *9*, 26859.
[526] S. J. Yoon, M. Kuno, P. V. Kamat, *ACS Energy Lett.* **2017**, *2*, 1507.
[527] G. F. Samu, C. Janáky, P. V. Kamat, *ACS Energy Lett.* **2017**, *2*, 1860.